DEPARTAMENTO DE ASTROFISICA

Universidad de La Laguna

UNVEILING THE CHEMO-DYNAMICAL PROPERTIES AND ORIGIN OF THICK DISKS IN GALAXIES

Thesis submitted by
D. Francesca Pinna
As a requirement for the degree of
Doctor by University of La Laguna

INSTITUTO Đ ASTROFISICA Đ CANARIAS
July 2018

Examination date: September 17, 2018
Thesis supervisor: Dr. Jesús Falcón-Barroso

ISBN: xx-xxx-xxxx-x
Depósito legal: TF-xxxx/2018

...a Sarita y a Wisky..

Acknowledgements

Acknowledgements/Agradecimientos/Ringraziamenti

I would like to thank all the living creatures who have made this thesis possible, directly or indirectly, even those who are not specifically named in this acknowledgements.

Visto che non so da dove cominciare, cercherò di seguire un ordine cronologico.

Grazie Fede (e il Piccolo Principe) per condividere quell'interesse per l'ignoto e per ciò che c'è lassù lontano, per ciò che non si vede oltre a ciò che si vede...

Las compañeras de la UB, en especial Maricarme, que me motivaron a seguir con esto. Gracias Luzma por todas las comidas y conversaciones al solecito, durante la carrera.

Les agradezco a Jordi y Gerard de los CCiTUB, por haberme dado la oportunidad de disfrutar del nanomundo, trabajar con ellos de esa forma tan llevadera, y apoyarme con clases y exámenes.

A l@s profesor@s de la carrera y del master (María Jesus, Rosario, Cesar, Mercedes, Jose,...), por haber valorado mi trabajo y haberme motivado a seguir en la astrofísica con una tesis doctoral.

Gracias a mis tutores de las prácticas externas y beca de verano en el IAC, Roger y Haresh, por su ayuda, disponibilidad, por aumentar mi interés por la instrumentación astrofísica.

Quiero agradecerle a quien hizo tan agradable mi breve pero muy enriquecedora etapa de operadora de telescopios (l@s compañer@as, astronom@s de soporte, Alex, todo el personal del OT).

A mi director de tesis Jesús, por su disponibilidad y flexibilidad constante, por darme todas las facilidades para hacer y obtener lo mejor para mi, oportunidades para participar en eventos y proyectos importantes. Gracias por ser tan comprensivo y entender que muchas veces las cosas no van como tienen que ir. Gracias por ser muchas veces práctico y eficiente. Por hacer de todo para acabar la tesis en tres años. Por confiar en mi.

Thank you, Marie, for appreciating what I am as a person and as a woman, for you faith in me as a scientist. Thanks for the numerous and productive scientific discussions which make you a second (unofficial) supervisor of my thesis. Thank you also for the conversations about

our non-scientific concerns, which make us human being, not only scientists. I am very grateful for your kindness and welcome in Liverpool.

I wish to thank Glenn for his contribution to this thesis and for giving me the opportunity to spend a month at the MPIA with his group.

Gracias Inma por tu disponibilidad y dedicación, por tu aportación importante a mi primer artículo, sin que tuvieras porque hacerlo.

Thank you Ryan for all the time you spent revising my papers and giving me many helpful comments and suggestions.

I would like to express my appreciation to my referees Paola and Nacho, for being so efficient in helping me to improve the thesis manuscript.

I would like to thank the members of my research group TRACES, for the never-ending discussions at the meetings, that have shaped our knowledge, and for the support given to students.

The Fornax 3D collaboration, for giving me the opportunity of being part of the project and for your valuable comments and suggestions on Chapter 3.

Grazie Enrica per la tua disponibilità ed aiuto, e per le nostre discussioni su Fornax.

Grazie Lodo per la tua velocità ed efficienza nella riduzione dei dati di MUSE, sapendo che era fondamentale per finire la mia tesi in tempo.

Thank you, Tim, for your support and for helping things to go as planned.

I am grateful to Piet van der Kruit and Richard de Grijs for kindly providing their individual measurements shown in Chapter 2.

Especial agradecimiento a mi amiga Cris, que siempre ha sobrevalorado mi forma de trabajar, cosa que se agradece enormemente en los momentos de inseguridad.

A Jorge por nuestras conversaciones, casi nunca de astrofísica, pero muchas veces sobre el mundo donde viven los astrofísicos, otras veces sobre como va el mundo y como intentar cambiarlo.

Muchas gracias Carina por haber sido mi gemela durante el camino de nuestras tesis.

Gracias Lourdes y Eva por su comprensión, disponibilidad y eficiencia en todo momento.

Un agradecimiento también a Joaquín, Elito e Isabel del CAU, siempre preparad@s para resolver nuestros problemas informáticos de forma eficiente.

Agradezco a la Fundación La Caixa su soporte económico en forma de contrato como astrofísica residente y al MINECO por su soporte al proyecto RAVET (AYA2016-77237-C3-1-P).

...ed alla fine, dulcis in fundo, le persone più importanti: la famiglia.

Rayco por tu apoyo, cariño, paciencia, alegría y ayuda constantes. Por haber cuidado de mi entorno cuando yo no podía. Por tu curiosidad sobre lo que hago.

Wisky y Sarita, por haberme dado y pedido todo el cariño del mundo durante la escritura de la tesis, y haberme pisado el teclado cada vez que me descuidaba...

A mis plantas, permitiéndome desconectar de la tesis cuando lo necesitaba y siendo siempre tan agradecidas conmigo!

A Giuseppe e Pinella, per il loro sostegno e la loro fiducia nonostante la stravaganza delle mie scelte. Per avermi trasmesso, da quando ero bambina, la curiosità e la passione per la scienza e la conoscenza in genere. Grazie per avermi insegnato ad arrangiarmi da sola. Comunque sono sempre stati pronti ad aiutarmi in tutti i sensi, e l'hanno fatto.

A Plafony, per essersi sorbita la varie presentazioni su dischi, mergers ed ellissoidi ed avermi fatto riderci sopra. Per avermi appoggiato quando ero una povera studentessa spiantata.

A nonno Ovidio, per la reciproca e profonda ammirazione che ci collegava e la testardaggine che mi permette di andare sempre avanti in quello che faccio.

Francesca Pinna
La Laguna, June 2018

Abstract

In the last decades, the astrophysics community has made a big effort to understand galaxy formation and evolution. In spite of the abundance of advanced theoretical studies in this field, more numerous and detailed observational works are required to test these models. In nearby galaxies, several observational studies have attempted to confirm the theoretical predictions about how their different structures form. However, further research needs to be done about the faintest structural components, such as thick disks, whose origin is still uncharted waters. While photometric studies are more abundant in the literature, thick-disk spectroscopy can be extremely challenging due to its low surface brightness. This is nonetheless necessary to extract the kinematics, which brings the footprint of the dynamical history of the galaxy. Even more challenging it is to perform the analysis of the stellar populations in these thick disks, requiring data with high signal-to-noise ratio. Only with this kind of studies we can assess the different theoretical scenarios. This thesis aims to contribute in this field, taking advantage of the bi-dimensional view given by integral-field spectroscopy.

Theoretical models have shown that disk thickness can be produced via different mechanisms. One possibility is that thick-disk stars were formed *in-situ* at high redshift, from gas already dynamically hot probably because of the turbulence during a multiple-merger phase. These stars, born with velocity dispersions as high as the gas, would have formed a disk already thick. Alternatively, thick-disk stars or a fraction of them could have an extragalactic origin. They would be born in satellites and later be directly accreted. On the other hand, thick disks could have been thinner in previous times and could have been thickened via dynamical heating processes. Disk dynamical heating has been a matter of debate since the correlation between stellar velocity dispersion and age was discovered in the Milky Way. Different candidates were proposed as dynamical heating sources in the literature. The disk stellar velocity ellipsoid (SVE), defined by the radial, azimuthal and vertical components of the stellar velocity dispersion, has been often used as indicator of the predominant heating mechanisms. These can be classified as isotropic heating agents, increasing the stellar velocity dispersion in the three directions, or anisotropic heating agents, acting only in the galactic plane. The most invoked sources of three-dimensional heating are encounters with giant molecular clouds and mergers, while non-axisymmetric features, such as spiral structures and bars, have been usually proposed as planar heating agents.

In this thesis, we first focus on disk heating. We review earlier studies both in the Milky Way and in external galaxies and we gather an exhaustive compilation of observational measurements of the SVE from the literature. Some of these studies suggested a strong anti-correlation between the shape of the disk SVE and Hubble type and related this trend to the different nature of

the disk heating agents in different types of galaxies. Late-type galaxies, with more prominent spiral structures, displayed more anisotropic ellipsoids. Early-type disk galaxies displayed more isotropic velocity dispersions, probably affected by previous three-dimensional heating sources.

Revisiting this relation considering all the previous results, we do not find any clear trend between the SVE shape and galaxy morphology. While in observational studies one could argue that velocity-dispersion measurements could be affected by the methods used to recover them, in N-body simulations they can be measured directly in the particles. We analyze the SVE-Hubble type relation also in simulations, confirming that no clear trend is evident. Especially for late-type galaxies, all kinds of shapes seem to be possible for the SVE. This points to a quite complicated picture where different disk heating agents can be predominant in the same Hubble type, while the same agents can act in different galaxy types. The time evolution of the SVE in simulations shows that different heating histories can result in the same final ellipsoid, but also the same heating mechanisms can affect in a different way depending on the specific situation. Moreover, several processes can heat the disk simultaneously, so that the observed SVE is the result of their combination. We discuss about the helpfulness of the SVE shape to trace back the disk heating history, suggesting that better indicators of the main heating sources should be proposed.

With the main goal of assessing the different formation scenarios proposed for thick disks, we present and discuss the stellar kinematics and populations of a sample of three S0 galaxies: FCC 170, FCC 177 and FCC 153. The selected sample includes the three edge-on galaxies in the Fornax 3D survey, which provides deep MUSE data of bright galaxies within the virial radius of the Fornax cluster. We use this high-quality data to extract the maps of the first four moments of the stellar line-of-sight velocity distribution and of the mass-weighted mean stellar age, metallicity and [Mg/Fe] abundance ratio. Furthermore, we perform a structural decomposition in order to analyze the star formation history of the individual components of the galaxies in our sample. Our kinematic maps, of unprecedented spatial resolution, unveil the structure of the three galaxies described in previous publications. The three galaxies display a fast-rotating and dynamically cooler thin disk and a slower-rotating and dynamically hotter thick disk. In addition, FCC 170 displays a nuclear disk and a bar seen as a prominent boxy bulge with a clear higher-velocity-dispersion X shape. The boxy bulge does not leave a clear imprint in the mean velocity map of FCC 177 and is not visible in FCC 153. Stellar-population maps reveal a nuclear star cluster in the center of FCC 153 and FCC 177.

In addition to the differences in the structure of the three galaxies, the difference between them is striking in the age maps. Whereas FCC 170 appears overall old, with no clear age distinction between the thin and the thick disk, FCC 153 and FCC 177 show relatively young stars in their thin disks and nuclear star clusters. However, a clear-cut distinction separates in the three galaxies the metal-rich and less [Mg/Fe]-enhanced populations in the thin disk and more metal-poor and [Mg/Fe]-enhanced stars in the thick disk. Since the three galaxies are located at different distances from the Fornax cluster center and in regions of different intra-cluster density, we discuss possible evolutionary paths in relation to their environment. Although in FCC 170 it is difficult to claim differences in the formation epoch of the thin and the thick disks, we propose a slightly longer formation timescale for the thin disk, necessary to allow a chemical evolution. FCC 170 is located in the densest region of the Fornax cluster and we discuss the possibility of a "pre-processing" in a subgroup, before falling into the present-day cluster, which could have accelerated and then quenched the star formation. FCC 177 and FCC 153 live

in a less dense environment and their star formation was only recently quenched. These two galaxies also show some peculiarities in their thin disk (i.e. the shape and the properties of the flares), which we suggest they are related to the difference in density between their locations.

In spite of the global differences between the three galaxies in the sample, their thick disks share a composite star formation history. Apart from the higher-metallicity component from the thin-disk flaring in their outer region, thick disks show a significant fraction of younger stars co-existing with a main older population. The younger sub-population is characterized by the galaxy lowest metallicity and the highest [Mg/Fe] abundance, suggesting that its stars were formed later but faster in a less chemically enriched satellite. We propose a complex formation scenario for thick disks in our sample. This involves an *in-situ* formation at high redshift for the oldest component, accretion for the younger most metal-poor populations and dynamical heating to explain the thin-disk flaring affecting the outer region of the geometrically-defined thick disk.

Resumen

En las últimas décadas, la comunidad astrofísica ha realizado un gran esfuerzo para entender la formación y evolución de las galaxias. A pesar de la gran cantidad de estudios teóricos en este campo, se requieren trabajos observacionales más numerosos y detallados para testear estos modelos. En galaxias cercanas, varios estudios observacionales han intentado confirmar las predicciones teóricas sobre como se forman sus diferentes estructuras. Sin embargo, se necesitan investigaciones más profundas sobre las componentes estructurales más débiles, como los discos gruesos, cuyo origen es aún terreno inexplorado. Mientras que los estudios fotométricos de discos gruesos son más abundantes en la literatura, sus estudios espectroscópicos pueden ser un gran desafío debido a su bajo brillo superficial. No obstante, la espectroscopía es necesaria para extraer la cinemática, que lleva la huella de la historia dinámica de la galaxia. Aún más desafiante es el análisis de las poblaciones estelares en los discos gruesos, ya que requiere datos de alta relación señal a ruido. Solo con este tipo de estudios podemos evaluar los diferentes escenarios teóricos. Esta tesis quiere contribuir en este campo, aprovechando la visión bidimensional dada por la espectroscopía de campo integral.

Modelos teóricos han mostrado que el grosor de los discos de galaxias puede ser producido por diversos mecanismos. Una posibilidad es que las estrellas del disco grueso se formaran *in-situ* a alto redshift, a partir de gas ya dinámicamente caliente posiblemente debido a la turbulencia durante una fase de fusiones múltiples de galaxias (mergers). Estas estrellas, nacidas con una dispersión de velocidades tan alta como la del gas, habrían formado un disco ya grueso desde el principio. En alternativa, las estrellas del disco grueso o una fracción de ellas podrían tener un origen extragaláctico. Habrían nacido en galaxias satélites y habrían sido acretadas más tarde. Por otro lado, los discos gruesos podrían haber sido más finos anteriormente y haber sido espesados mediante procesos de calentamiento dinámico. El calentamiento dinámico de discos ha sido un tema muy debatido desde que la correlación entre dispersión de velocidades y edad de las estrellas fue descubierta en la Vía Láctea. En la literatura, varios candidatos han sido propuestos como fuentes de calentamiento dinámico. El elipsoide de velocidades estelar (SVE) del disco, definido por las componentes radial, azimutal y vertical de la dispersión de velocidades estelar, ha sido utilizado a menudo como indicador de los mecanismos de calentamiento predominantes. Estos pueden ser clasificados como agentes de calentamiento isótropos, que aumentan la dispersión de velocidades estelar en las tres dimensiones, o anisótropos, que actúan solo en el plano galáctico. Las fuentes de calentamiento tridimensionales a las que más se ha recurrido son los encuentros con nubes moleculares gigantes y los mergers, mientras que estructuras no axisimétricas como los brazos espirales y las barras han sido normalmente elegidas como agentes de calentamiento en el plano de la galaxia.

En esta tesis, nos enfocamos primero en el calentamiento del disco. Revisamos estudios anteriores tanto en la Vía Láctea como en galaxias externas y recopilamos el conjunto de las medidas observacionales del SVE en la literatura. Algunos de estos estudios sugerían una anti-correlación fuerte entre la forma del elipsoide del disco y el tipo de Hubble y relacionaron esta tendencia con la diferente naturaleza de los agentes de calentamiento que actúan en los diferentes tipos de galaxias. Galaxias de tipo tardío, con estructuras espirales más destacadas, mostraban elipsoides más anisótropos. Galaxias de disco de tipo más temprano mostraban dispersiones de velocidades más isótropas, habiendo sido probablemente afectadas por anteriores fuentes de calentamiento tridimensionales.

Reexaminando esta relación después de considerar todos los resultados en trabajos anteriores, no encontramos ninguna fuerte tendencia del SVE respecto a la morfología de la galaxia. Mientras en estudios observacionales alguien podría argumentar que las medidas de dispersión de velocidades podrían estar afectadas por los métodos utilizados, en simulaciones de N cuerpos estas pueden ser medidas directamente en las partículas. Analizamos la relación SVE-tipo de Hubble también en las simulaciones, confirmando que ninguna clara tendencia es evidente. En particular en galaxias de tipo tardío, todo tipo de forma (isótropa y anisótropa) parece ser posible para el SVE. Esto apunta a una situación bastante complicada en la que agentes de calentamiento de disco diferentes pueden ser predominantes para el mismo tipo morfológico, mientras que los mismos agentes pueden actuar in tipos diferentes de galaxias. La evolución en el tiempo del SVE en las simulaciones muestra que historias de calentamiento diferentes pueden resultar en el mismo elipsoide, pero también los mismos mecanismos de calentamiento pueden afectar de forma diferente dependiendo de la situación específica. Además, varios procesos pueden calentar el disco simultáneamente, de forma que el SVE observado es el resultado de la combinación de ellos. Se discute la utilidad de la forma del SVE para trazar la historia de calentamiento del disco, sugiriendo que deberían de proponerse mejores indicadores de las fuentes principales de calentamiento.

Con el objetivo de evaluar los diferentes escenarios de formación propuestos para los discos gruesos, presentamos y discutimos la cinemática y poblaciones estelares de una muestra de tres galaxias S0: FCC 170, FCC 177 y FCC 153. La muestra seleccionada incluye las tres galaxias vistas de canto en el cartografiado Fornax 3D, que ofrece datos profundos tomados con el instrumento MUSE en el VLT, sobre galaxias brillantes contenidas en el radio virial del cúmulo de Fornax. Utilizamos estos datos de gran calidad para extraer los mapas de los primeros cuatro momentos de la distribución de velocidades en la linea de visión y la edad, metalicidad y abundancia de [Mg/Fe] estelares medias y pesadas en masas. Realizamos además una descomposición estructural para analizar la historia de formación estelar de las componentes individuales de las galaxias en nuestra muestra. Nuestros mapas cinemáticos, de una resolución espacial sin precedentes, revelan la estructura de las tres galaxias, ya descrita en publicaciones anteriores. Las tres galaxias muestran un disco fino en rotación rápida y dinámicamente frío y un disco grueso en rotación más lenta y dinámicamente caliente. A esto, en FCC 170, se añade un disco nuclear y una barra vista de canto con un bulbo "boxy" que destaca en su forma de X con alta dispersión de velocidades. Este tipo de bulbo no deja en cambio una clara marca en el mapa de velocidad media de FCC 177 y no es visible en FCC 153. Las poblaciones estelares desvelan un cúmulo nuclear de estrellas en el centro de FCC 153 y FCC 177.

Además de las diferencias en la estructura de las tres galaxias, estas se diferencian muy claramente en sus mapas de edad. Mientras que FCC 170 aparece vieja en toda la zona obser-

vada, sin clara distinción entre los discos fino y grueso, FCC 153 y FCC 177 muestran estrellas relativamente jóvenes en sus discos finos y cúmulos estelares nucleares. Sin embargo, una clara distinción separa en las tres galaxias las poblaciones ricas en metales y bajas en [Mg/Fe] del disco fino de las del disco grueso que son mucho menos metálicas y contienen más [Mg/Fe]. Dado que las tres galaxias se encuentran a distancias diferentes del centro del cúmulo de Fornax y en regiones de densidad intergaláctica distinta, discutimos los posibles caminos de evolución de estas galaxias en relación a su entorno. Aunque en FCC 170 las diferencias en las épocas de formación de los discos fino y grueso son difíciles de afirmar, proponemos una escala temporal de formación ligeramente más larga para el disco fino, necesaria para permitir la evolución química. FCC 170 se encuentra en la región más densa del cúmulo de Fornax. Discutimos la posibilidad de un "preprocesado" de esta galaxia en un subgrupo, antes de caer en lo que es actualmente el cúmulo, que podría haber acelerado y luego frenado la formación estelar. FCC 177 y FCC 153 habitan un entorno menos denso y su formación estelar fue suprimida solo recientemente. Estas dos galaxias también muestran algunas peculiaridades en sus discos finos (su forma y las propiedades de sus "flares"), que podrían estar relacionadas con la diferencia en las densidades de su entorno específico.

A pesar de las diferencias globales entre las tres galaxias de la muestra, sus discos gruesos comparten una historia de formación estelar compuesta. Además de la componente de más alta metalicidad dada por el flare del disco fino y localizada en sus zonas más exteriores, estos discos gruesos muestran una fracción significativa de estrellas jóvenes que coexisten con la población principal más vieja. La subpoblación más joven se caracteriza por la metalicidad más baja y la abundancia de [Mg/Fe] más alta de la galaxia donde se encuentra. Esto sugiere que sus estrellas se formaron más tarde pero más rápidamente en una galaxia satélite menos enriquecida químicamente. Proponemos un escenario de formación complejo para los discos gruesos en nuestra muestra. Este escenario incluye una formación *in-situ* a alto redshift para la componente más vieja, acreción para la población más joven y más pobre en metales y calentamiento dinámico para explicar el flare del disco fino que afecta la zona exterior del disco grueso, definido geométricamente.

Riassunto

Negli ultimi decenni, la comunità astrofisica ha realizzato grandi sforzi per capire la formazione e l'evoluzione delle galassie. Nonostante la grande quantità di studi teorici avanzati in questo campo, sono richiesti lavori osservazionali più numerosi e dettagliati per verificare questi modelli. In galassie vicine, vari studi osservazionali hanno cercato di confermare le previsioni teoriche su come si formano le loro diverse strutture. Sono richieste comunque ricerche più profonde sulle componenti più deboli, come i dischi spessi, l'origine dei quali è ancora terreno inesplorato. Mentre gli studi fotometrici di dischi spessi abbondano nella letteratura, i loro studi spettroscopici possono presentare gravi difficoltà, dovute alla loro bassa luminosità superficiale. Comunque sia, la spettroscopia è necessaria per ricavarne la cinematica, che porta l'impronta della storia dinamica della galassia. L'analisi delle popolazioni stellari nei dischi spessi si presenta ancora più difficoltosa per il fatto che richiede dati con un alto rapporto segnale/rumore. In ogni caso, solo con questo tipo di studi possiamo valutare i diversi scenari teorici. Questa tesi ha lo scopo di dare un contributo in questo campo, sfruttando la visione bidimensionale data dalla spettroscopia di campo integrale.

Modelli teorici hanno mostrato che lo spessore dei dischi galattici può essere prodotto da diversi meccanismi. Una delle possibilità è che le stelle del disco spesso si siano formate *in-situ* ad alto redshift, a partire da gas già caldo dinamicamente, probabilmente grazie alla turbolenza durante una fase di molteplici fusioni di galassie (mergers). Queste stelle, nate con una dispersione di velocità alta tanto quanto quella del gas, avrebbero formato un disco già spesso dall'inizio. Alternativamente le stelle del disco spesso o una loro frazione potrebbero avere un'origine extragalattica. Sarebbero nate in galassie satelliti e sarebbero state aggregate più tardi. D'altra parte, i dischi spessi potrebbero anche essere stati più sottili nel passato ed essere stati ispessiti mediante processi di riscaldamento dinamico. Il riscaldamento dinamico dei dischi è stato un tema molto dibattuto da quando la correlazione tra la dispersione di velocità e l'età delle stelle fu scoperta nella Via Lattea. Diverse possibili fonti di riscaldamento dinamico sono state proposte nella letteratura. L'ellissoide di velocità stellare (SVE) del disco, definito dalle componenti radiale, azimutale e verticale della dispersione di velocità, è stato spesso utilizzato come indicatore dei meccanismi di riscaldamento predominanti. Questi ultimi possono essere classificati come agenti di riscaldamento isotropi, che aumentano la dispersione di velocità stellare nelle tre dimensioni, o anisotropi, che agiscono solo nel piano galattico. Le fonti di riscaldamento tridimensionali più evocate sono gli scontri con nubi molecolari giganti e i mergers, mentre strutture non assisimmetriche come i bracci di spirale e le barre sono stati generalmente scelti come agenti di riscaldamento nel piano della galassia.

In questa tesi, ci concentriamo prima sul riscaldamento del disco; ripassiamo studi precedenti

tanto sulla Via Lattea come su galassie esterne e riuniamo le misure osservazionali dello SVE nella letteratura. Alcuni di questi studi hanno suggerito una forte anticorrelazione tra la forma dell'ellissoide e il tipo di Hubble e hanno collegato questa tendenza con la natura diversa degli agenti di riscaldamento che agiscono sui diversi tipi di galassie. Galassie di tipo avanzato (late), con strutture a spirale più evidenti, mostravano ellissoidi più anisotropi. Galassie di primo tipo (early) mostravano dispersioni di velocità più isotrope, probabilmente in seguito all'azione precedente di fonti di riscaldamento tridimensionali.

Riesaminando questa relazione dopo aver considerato tutti i risultati in lavori precedenti, non troviamo nessuna tendenza forte dello SVE con rispetto alla morfologia delle galassie. Mentre in studi osservazionali si potrebbe affermare che le misure della dispersione di velocità potrebbero essere condizionate dai metodi utilizzati, queste possono essere effettuate direttamente sulle particelle nelle simulazioni di N corpi. Analizziamo la relazione SVE-tipo di Hubble anche nelle simulazioni, per poi confermare che non appare nessuna chiara tendenza. In particolare, in galassie di tipo avanzato tutte le forme (isotrope e anisotrope) sembrano essere possibili per lo SVE. Questo indica una situazione abbastanza complessa nella quale diversi agenti di riscaldamento del disco possono essere predominanti per uno stesso tipo morfologico, oltre che gli stessi agenti possono operare in tipi diversi di galassie. L'evoluzione nel tempo dello SVE nelle simulazioni mostra che storie di riscaldamento diverse possono dare come risultato lo stesso ellissoide. Succede anche che gli stessi meccanismi di riscaldamento possono influire in modo diverso a seconda della situazione specifica. Inoltre, vari processi possono riscaldare il disco simultaneamente, in modo che lo SVE osservato è il risultato della loro combinazione. Trattiamo qui anche il tema dell'utilità della forma dello SVE per tracciare la storia di riscaldamento del disco e suggeriamo che sarebbe di grande utilità proporre indicatori migliori delle fonti di riscaldamento principali.

Con l'obbiettivo di valutare i diversi scenari di formazione proposti per i dischi spessi, presentiamo e discutiamo la cinematica e le popolazioni stellari di un campione composto da tre galassie: FCC 170, FCC 177 e FCC 153. Il campione selezionato include le tre galassie viste di taglio (edge-on) nel survey Fornax 3D, che offre dati profondi, presi con lo strumento MUSE installato nel VLT, su galassie brillanti contenute nel raggio viriale dell'ammasso galattico di Fornax. Utilizziamo questi dati di alta qualità per estrarre le mappe dei primi quattro momenti della distribuzione di velocità nella linea di visione e l'età, la metallicità e l'abbondanza di [Mg/Fe] stellari medie e pesate in massa. Realizziamo inoltre una scomposizione strutturale per analizzare la storia di formazione stellare delle componenti individuali delle galassie nel nostro campione. Le nostre mappe di cinematica, di una risoluzione spaziale senza precedenti, svelano la struttura delle tre galassie, già descritta anteriormente in altri studi. Le tre galassie mostrano un disco sottile in rotazione rapida e dinamicamente freddo e un disco spesso in rotazione più lenta e dinamicamente caldo. A questo si aggiunge, in FCC 170, un disco nucleare e una barra vista di taglio con un bulge "boxy" che si nota per la sua forma a X con alta dispersione di velocità. Questo tipo di bulge non lascia una traccia chiara nella mappa di velocità media di FCC 177 e non è visibile in FCC 153. Le popolazioni stellari svelano un ammasso nucleare di stelle nel centro di FCC 153 e FCC 177.

Oltre alle differenze nella struttura delle tre galassie, queste ultime si differenziano molto chiaramente nelle mappe dell'età. Mentre FCC 170 appare vecchia in tutta la zona osservata, senza nessuna chiara distinzione tra i dischi sottile e spesso, FCC 153 e FCC 177 mostrano stelle relativamente giovani nei loro dischi sottili e negli ammassi stellari nucleari. In ogni modo, una

chiara distinzione separa nelle tre galassie le popolazioni ricche di metalli e scarse in [Mg/Fe] del disco sottile da quelle del disco spesso che sono molto meno metalliche e contengono più [Mg/Fe]. Visto che le tre galassie si trovano a distanze diverse dal centro dell'ammasso di galassie di Fornax, e in regioni di densità intergalattica distinta, discutiamo i possibili percorsi evolutivi di queste galassie in relazione al loro ambiente circostante. Anche se in FCC 170 le differenze nell'epoca di formazione dei dischi sottile e spesso sono difficili da affermare, proponiamo una scala temporale di formazione leggermente più lunga per il disco sottile, necessaria per permettere l'evoluzione chimica. FCC 170 si trova nella regione più densa dell'ammasso di Fornax. Discutiamo sulla possibilità di una "pre-trasformazione" di questa galassia in un sottogruppo, prima di cadere in ciò che è attualmente l'ammasso di Fornax, che potrebbe avere accelerato e dopo frenato la formazione stellare. FCC 177 e FCC 153 abitano in un ambiente meno denso e la loro formazione stellare è stata soppressa solo recentemente. Queste due galassie mostrano anche alcune peculiarità nei loro dischi sottili (nella loro forma e nelle proprietà dei loro "flares"), che potrebbero essere collegate alla differenza nelle densità del loro ambiente specifico.

Nonostante le differenze globali tra le tre galassie del campione, i loro dischi spessi condividono una storia di formazione stellare composta. Oltre alla componente di più alta metallicità data dal flare del disco sottile e situata nelle sue zone più esterne, questi dischi spessi mostrano una frazione significativa di stelle giovani che convivono con la popolazione principale più vecchia. La sottopopolazione più giovane è caratterizzata dalla metallicità più bassa e l'abbondanza di [Mg/Fe] più alta della galassia dove si trova. Questo suggerisce che le sue stelle si formarono più tardi ma più velocemente in una galassia satellite meno arricchita chimicamente. Proponiamo uno scenario di formazione complesso per i dischi spessi nel nostro campione. Questo scenario include una formazione *in-situ* ad alto redshift per la componente più vecchia, accrescimento per la popolazione più giovane e più povera in metalli, e riscaldamento dinamico per spiegare il flare del disco sottile che interessa la zona esterna del disco spesso, definito geometricamente.

Contents

1

Introduction

The goal of this dissertation is to assess the potential processes responsible for the formation of thick disks in nearby galaxies. With this Introduction, we aim to put the reader in context. We first give some general concepts on galaxy classification and morphology, reviewing the structural components of galaxies with a special emphasis on thick disks. Secondly, we revise the current models on galaxy formation and evolution. Third, we examine the properties of disks focusing on thick disk and the formation scenarios proposed in the literature so far. Finally, we introduce the techniques used in this work.

1.1 Galaxies: classification and morphology

The word "galaxy", meaning "milky", has its origin from the name given by the Greek to our Galaxy, [1]. Nowadays, this term is used more in general to indicate massive systems made up mainly of stars, gas and dark matter (e.g. Sparke & Gallagher, 2007). However, depending on the relative amounts of these three ingredients and their properties and distribution, galaxies assume a large variety of shapes. In spite of the extreme peculiarity of each galaxy, classifications have been used to group these systems in different types sharing common features. The first morphological classification was conceived by Hubble (1926, 1936) and represented as a "tuning fork" (shown in Fig. 1.1). This classification was based on the visual appearance of galaxies in the sky and was later extended by de Vaucouleurs (1959).

The "tuning fork" visualized an evolutionary path from the left to the right side of the diagram, which nowadays is no longer considered valid. However, it set the present-day morphological distinction between early-type galaxies (on the left side of the diagram), including ellipticals and lenticulars (S0s), and late-type galaxies including spirals, on the right side of the diagram. Ellipticals were ordered with increasing apparent ellipticity from left to right. Spirals were located in the diagram according to the apparent size and luminosity of their central mass concentration, called bulge. The latter loses importance from Sa galaxies, more on the left, to

[1] e.g., `https://en.oxforddictionaries.com/definition/galaxy`

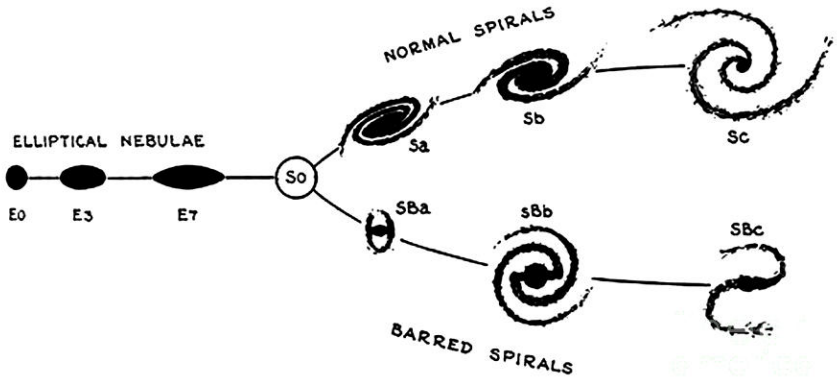

FIGURE 1.1— "Tuning fork" diagram illustrating the original morphological classification by Hubble (1936).

Sc, on the right end. Sa have also more tightly wound spiral arms than later types, where they are looser. The spiral structure becomes more prominent towards later types, in terms of gas and dust fraction and bluer colors due to young stars (e.g. Sparke & Gallagher, 2007). Spiral arms can be organized into a *grand design*, where they are very well defined and can be traced as a continuous spiral over a large angle, or can be *flocculent*, made by many short segments. The arm-class parameter quantifies the strength and symmetry of the spiral structure, on the base of the orderliness: from flocculent in class 1 to grand design in class 12 (Elmegreen & Elmegreen, 1987). Lenticular galaxies, still considered early types, are in between ellipticals and spirals. Their color is more similar to ellipticals but they display a prominent stellar disk, with no spiral structure. de Vaucouleurs (1959) introduced irregulars and further classified lenticulars and spirals according to their internal structures as bars, rings or spiral arms.

1.1.1 Disk galaxies

Lenticular and spiral galaxies present a prominent stellar *disk* containing an important fraction of their baryonic matter (e.g. van der Kruit & Freeman, 2011). For this reason they are also called disk galaxies. In their disk, stars rotate around the galaxy center approximately in the same plane. Disk galaxies are dominated by rotation, which stabilizes their structure. On the contrary, in elliptical galaxies, stars orbit the center following more random patterns with high velocity dispersions, more important than the rotation velocity and responsible for supporting the system (e.g. Sparke & Gallagher, 2007).

Disk galaxies usually show a central *bulge*. Bulges are also classified depending on their different appearances. *Classical bulges* have a spheroidal shape and kinematics more similar to elliptical galaxies than to the disk (with larger random velocities than the disk), although in general they rotate more rapidly than ellipticals (e.g. Kormendy & Illingworth, 1982). Their brightness radial profiles are usually fitted using a Sérsic function (Sersic, 1968). *Pseudo-bulges*

were, in contrast, described by Kormendy (1993) and Kormendy & Kennicutt (2004) as structures with similar appearance to classical bulges, but common properties with disks. They look flatter than classical bulges, have more disk-like orbits and lower velocity dispersions, while their brightness profiles are more similar to disks.

Athanassoula (2005) added *boxy* or *peanut bulges* as a third type, showing in numerical simulations the same morphological, photometrical and kinematical properties as bars viewed edge-on. Apart from a box or a peanut shape, they can also show an X-shape. *Bars* are common non-axisymmetric features of disk galaxies, as well as spiral arms (e.g. Saha & Naab, 2013). They are characterized by different lengths and strengths, being the latter defined as its deprojected axis ratio (Martinet & Friedli, 1997). Cylindrical rotation is one of the kinematical properties of bars observed in boxy bulges (e.g. Kormendy & Illingworth, 1982; Molaeinezhad et al., 2016), showing that they are cylinders rotating differentially.

One more spheroidal component has been detected in the Milky Way and in external galaxies: the *halo*. It is the most extended and also the faintest. It is composed by stars (e.g. Helmi, 2008), hot gas (e.g. Savage et al., 2000) and dark matter (e.g. Frenk et al., 1985).

1.2 Galaxy formation and evolution

Galaxy formation and evolution is one of the most active fields of research in extragalactic astrophysics and cosmology. The *Big-Bang* theory is very well established in the modern cosmology, thanks to several observational evidences (e.g. Dodelson, 2003): the Hubble law, indicating the expansion of the Universe (Hubble, 1929b,a), the observed abundance of light elements (especially helium) in agreement with Big-Bang nucleosynthesis (e.g. Sparke & Gallagher, 2007), and the cosmic microwave background discovered by Penzias & Wilson (1965). According to the current state-of-the art cosmology, the Universe is made up of three main components: the *baryonic matter*, forming the "visible" Universe and including protons, neutrons and electrons, the *dark matter* and the *dark energy*. The nature of dark matter and dark energy is still uncharted waters, but it is believed that they make up more than 95% of the Universe (e.g. Mo et al., 2010). The most popular cosmological framework is currently the Λ-Cold Dark Matter model (ΛCDM), supporting a flat Universe. The $\sim$75% of the energy density is due to a cosmological constant Λ related to dark energy, $\sim$21% is identified with the (cold) dark matter and only $\sim$4% is contributed by the baryonic matter.

In this framework, the formation of the first structures was possible thanks to quantum fluctuations, coupled to density perturbations that are associated to the observed large scale structures. According to inflationary models, an exponential expansion phase (inflation) of the Universe after the Big Bang, was responsible for these fluctuations. Density perturbations grew with time via gravitational instability. Regions with slightly higher density attracted the surrounding matter and became even more dense, while lower-density regions became even more rarefied. The cold dark matter drove the formation of galaxies and clusters (e.g. Blumenthal et al., 1984). Thanks to its collisionless nature and as a result of the fluctuations, dark matter violently collapsed forming the dark matter halos (e.g. Mo et al., 2010). Baryons were well mixed with dark matter in the density fluctuations and they accumulated under the influence of the dark matter potential. Gas associated to dark matter halos cooled down via radiation related to particle collisions. This cooling is another key factor to explain galaxy formation. Dark matter halos and the associated baryonic matter had some angular momentum that was

conserved during the cooling process. Therefore flowing-inwards gas started to spin up and formed cold disks in the center of the halos (Fall & Efstathiou, 1980). The gas cloud cooled down and flowed towards the center of the halo until it collapsed under its own gravity, probably fragmenting in different high density cores that ended up forming stars.

Different scenarios were proposed to explain how this primordial phase of star formation ended up with the observed galaxies, with their variety of morphologies. Eggen et al. (1962) suggested that the Milky Way was formed through a primordial violent collapse, during the time when the first stars were formed, occurred in a very fast timescale. Also called *monolithic collapse*, it implies that all stars were formed at once. The final galaxy was assembled during this stage and had a passive evolution from that time on (e.g. Mo et al., 2010). Similar models were extended to galaxies in general, especially the ones with spherical symmetry, e.g. by Larson (1974) and Silk (1977). During many years this scenario was adopted for elliptical galaxies, formed by homogeneous and old stellar populations. However, observations indicated that ellipticals had a lower mass in the past than now (e.g. Bell et al., 2004). Therefore, they were not assembled in a unique fast event. Kormendy (1982) reviewed the galaxy formation and evolution considering that different processes played an important role at the same time. Apart from the early collapse, external and internal processes would have shaped the present-day galaxies. This was confirmed by van Dokkum et al. (2008), who did not find fully assembled early-type galaxies at $z \sim 2.3$, disagreeing with a simple monolithic collapse and suggesting that additional processes such as mergers were necessary.

Mergers as alternative formation mechanisms were originally proposed by Toomre (1977) to explain the formation of elliptical galaxies. Searle & Zinn (1978) suggested that small structures could merge to form a unique galactic halo and this *hierarchical clustering* was adopted by Fall & Efstathiou (1980) to explain the formation of disk galaxies. According to Toomre (1977), star formation would occur in galaxy disks and ellipticals would come from mergers of disk galaxies. Disks would be seriously affected by scrambling caused by mergers and disk stars would acquire too large velocity dispersions to keep the disky shape. Observational evidence that ellipticals can result from a merger of two late-type galaxies was more recently found in the remnant NGC 7252 by Schweizer et al. (2013). Naab et al. (1999) and Naab & Burkert (2001, 2003) studied with N-body simulations the relation between the mass ratio (between 1:1 and 4:1) of two merging galaxies with the shape of the resulting elliptical (e.g. presenting disky or boxy structures). Simulations by Bournaud et al. (2005) extended the analysis and showed a transition in the shape of the remnants for mass ratios between 4.5:1 and 10:1, leading to systems with hybrid properties between ellipticals and late types. They classified mergers into:

- *major*, with mass ratios from 1:1 to 4:1, forming elliptical galaxies;
- *intermediate*, from 4:1 to 10:1 mass ratios, leading the formation of hybrid remnants with the same appearance as S0 galaxies, that could be their progenitors. If they are multiple, they are also capable of forming ellipticals;
- *minor*, whose remnants would be disturbed spiral galaxies.

Although hierarchical assembling led to an evolutionary path opposite to the one suggested by Hubble's tuning fork, it was proved to be unavoidable in the ΛCDM cosmogony (e.g. Frenk et al., 1988; Cole, 1991; Kauffmann et al., 1993; Navarro et al., 1996, 1997; Abadi et al., 2003;

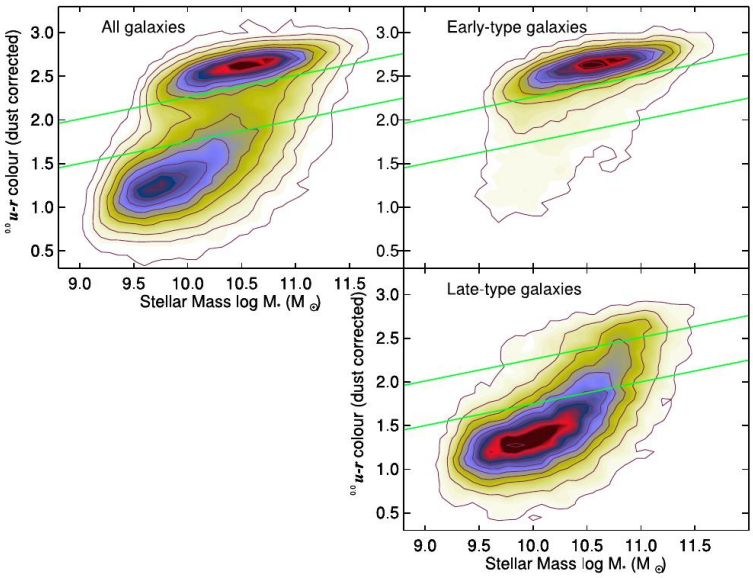

FIGURE 1.2— Reddening-corrected $u - r$ color-mass diagram by Schawinski et al. (2014). Early-type galaxies form the red sequence, while late types form the blue cloud. The green valley region is marked by green lines. The contours on this figure are linear and scaled to the highest value in each panel.

Vogelsberger et al., 2014; Schaye et al., 2015). Bell et al. (2004) found a bimodality in the color-magnitude plane of the sample from the COMBO-17 survey (Classifying Objects by Medium-Band Observations in 17 filters, Wolf et al. 2003), including $\sim 25\,000$ galaxies at $0.2 < z \leq 1.1$ and in all kind of environments. Early-type galaxies formed the *red sequence*, separated from the *blue peak* or *blue cloud* of late types. Since $z \sim 1$, galaxies became redder and more luminous and the number of blue luminous galaxies decreased with time. A truncation of star formation was necessary to explain this. The red-sequence luminosity evolution corresponded to an increase of a factor two in stellar mass, interpreted as a consequence of mergers. In Fig. 1.2 we show the color-mass diagram plotted by Schawinski et al. (2014), for the Galaxy Zoo sample (Lintott et al., 2008), where we can clearly see the red sequence drawn by early types and the blue cloud by late types. A transition between them, called the *green valley*, was indicated with green lines. The evolutionary path proposed by Bell et al. (2004) is from bottom-left to top-right in the top-left diagram of Fig. 1.2. However, Schawinski et al. (2014) warned that only few late-type galaxies cross the green valley in a short timescale. Many of them, keep their disks while their star formation declines slowly. They proposed two different scenarios for the suppression of star formation (*quenching*) in early and late-type galaxies. For late types, the gas supply could have been stopped and quenching would have happened when the gas reservoir was exhausted. In early types, both processes would have happened in a much faster timescale, probably as a consequence of the major merger which would have also changed the morphology from a

disk to a spheroid. Several other candidates have been proposed as causes of the star-formation suppression, such as morphological quenching (e.g. Martig et al., 2009), environmental quenching (see § 1.2.2), and quenching by AGN (active galactic nucleus) feedback (e.g. Bongiorno et al., 2016).

Kormendy & Kennicutt (2004) drew a complete picture of galaxy formation and evolution combining violent processes, occurred predominantly at high redshift as the primordial collapse and the hierarchical clustering, with slow long-term processes leading to secular evolution, occurring now and in the future. Depending on which kind of processes are predominant, galaxies assume one or another shape. Not only ellipticals, but also classical bulges of disk galaxies are thought to be formed through hierarchical clustering of smaller objects (e.g. Athanassoula, 2005). Different versions of this scenario have been proposed for classical bulges. In some models the bulge forms before the disk formation (e.g. Samland & Gerhard, 2003; Sommer-Larsen et al., 2003) and vice versa in others (e.g. Steinmetz & Navarro, 2002; Immeli et al., 2004). The connection between morphology and merger history (and gas accretion) was confirmed also by FIRE-2 simulations (Hopkins et al., 2018) of Milky Way-mass galaxies (Garrison-Kimmel et al., 2017). Gas-rich mergers of compact disks produced the most massive bulges at high redshift, while internal processes dominated more recent bulge formation. In contrast, box/peanut bulges are a result of secular evolution in barred galaxies (Athanassoula, 2005). Stellar disks are on the verge of instability according to the Toomre criterion (see § 1.3). Therefore, they are sensitive to certain disturbances which tend to form massive condensations in its same plane (Toomre, 1964). These instabilities are thought to cause the density waves responsible for forming non-axisymmetric structures (Toomre, 1981), such as bars and spiral arms.

In N-body simulations bars develop naturally from disk instabilities (e.g. Combes & Sanders, 1981; Sellwood & Wilkinson, 1993; Athanassoula, 2003; Martinez-Valpuesta et al., 2006; Saha & Naab, 2013; Di Matteo et al., 2014). This explains why they are observed in about 70% of galaxies (e.g. Knapen et al., 2000). Combes & Sanders (1981) showed that it is possible to form bars within a certain range of halo-to-disk mass ratios (between 0.25 and 2), which determine the evolution timescale of these features. If the disk mass is larger than the halo mass, the bar is developed quickly, while in systems with much larger halo masses the bar strength evolves longer with time. After its early growth, the velocity distribution of bar stars becomes anisotropic due to the dynamical instability called vertical buckling (e.g. Martinez-Valpuesta et al., 2006). Some stars acquire larger vertical motions, especially within half bar length, thickening the bar and giving the box/peanut shape when observed edge-on (Pfenniger, 1984). This first vertical buckling weakens the bar, which after that starts to grow again, causing later a second (and probably recurrent) buckling instability (Martinez-Valpuesta et al., 2006). This formation scenario predicts stellar population properties, for the box/peanut whose material came from the inner disk, similar to it (Athanassoula, 2005). Saha & Naab (2013) explained with different halo rotation why not all galaxies are barred. In their simulations, disk-halo corotation seemed to favor bar formation, increasing dynamical friction so that dark matter particles acquired more angular momentum and formed the inner bar structure. On the contrary, counter-rotating halos seemed to suppress the bar formation.

Spiral arms are believed to be due to a spiral density wave pattern. The observed mass density distribution of gas and stars follows the spiral gravitational field associated to these quasi-static waves (Lin & Shu, 1964). Lindblad (1963, 1964) was the first to propose that the Milky Way spiral structure was quasi-stationary, although the first density wave theory was

developed by Lin & Shu (1964). Lindblad deduced from observations that disk stars rotated differentially, faster in the inner regions than in the outskirts. He related this with the exchange of angular momentum with the spiral arms when stars crossed them. The spiral pattern would have the same angular velocity (*pattern speed*) everywhere. The density wave theory explained the long lifetime of the spiral structures in galaxies, solving the so called "winding problem". If spiral arms were material, they would wind up very quickly because the inner regions rotate faster. They would be more tightly wound than observed and would be dissolved (e.g. Mo et al., 2010). If they are density waves, crossed by stars and gas, they can keep approximately the same shape for a long time. This theory can also explain why star formation is concentrated in the spiral arms. When gas crosses the density waves, it is compressed favoring instabilities causing the formation of giant molecular clouds (GMCs). Recent strong evidence that stars cross arms has been found in the ridges of the detailed velocity distribution presented by Quillen et al. (2018) for the solar neighborhood.

1.2.1 Chemical evolution and stellar populations

Galactic archaeology try to reveal the history of (nearby) galaxies in the same way as archaeologists unveil the customs of ancient civilizations from the available clues (Roškar & Debattista, 2012). Observationally, we can only analyze the remnants of the processes occurred during the Universe's lifetime and interpret these "fossil records" as signatures of these past events. Present-day stellar populations and kinematics of nearby galaxies are some of these fossils. Star motions are the result of the galaxy's dynamical history. Ages, chemical composition and their spatial distribution tell us about galaxies' past (e.g. Sparke & Gallagher, 2007). The primordial nucleosynthesis produced hydrogen, helium, lithium and a very small quantity of other metals. The rest of elements were formed later thanks to nuclear reactions in stars. They ended up enriching the inter-stellar medium (ISM) as a consequence of processes such as stellar winds or supernovae (SNe) explosions (e.g. Mo et al., 2010). These metals, once released into the ISM, were used to form the next generations of stars. Chemical composition can be used as a clock for galaxy aging and abundance ratios, in particular, give information about star formation and its timescale. Since different elements are produced by different processes, abundances display the predominance of a process over others.

Massive stars ($\gtrsim 8M_\odot$), with final core-collapse explosions as SNe type II after a short lifetime, produce mainly α-elements such as O, Ne, Mg, Si and S (e.g. Worthey et al., 1992; Mo et al., 2010; Peletier, 2013). SNe type Ia (whose progenitors were C-degenerate white dwarfs) are the main producers of iron and have much longer lifetimes. Because of this timescale difference, in the early universe there must have been a delay in the production of Fe with respect to the α-elements. As a consequence, the abundance ratio between an α-element and iron can be used as a "star formation clock". In the simple *closed-box model*, there is no mass flows in or out the system. If we think of a coeval population of stars in this closed box, the ISM metallicity [Fe/H] increases with time. In a first phase, when only SNe type II could give their contribution, the abundance [α/Fe] must have been high and roughly constant. Only later, when contribution from SNe type Ia was significant, [α/Fe] started to decrease with time while [Fe/H] increased. Hence, [α/Fe] gives valuable information about the formation timescale of a galaxy or some specific populations. This ratio would be higher if stars were formed rapidly (*starburst*), since α-elements are mostly produced by SNe type II, than if they were formed slowly (*quiescent star*

formation), giving time to SNe type Ia to produce Fe-peak elements.

However, [α/Fe] not only depends on the star formation history, but also on the shape of the *Initial Mass Function (IMF)*, the mass distribution of stars at their birth. If the IMF is $\phi(m)$, $\phi(m)\mathrm{d}m$ is the number of stars with masses in the range $m \pm \mathrm{d}m/2$. Salpeter (1955) was the first to estimate the IMF in the Milky Way, as a single power law:

$$\phi(m)\mathrm{d}m \propto m^{-b}\,, \tag{1.1}$$

with $b = 2.35$ and for masses $0.4\,\mathrm{M}_\odot \leq m \leq 10\,\mathrm{M}_\odot$. Later determinations proposed broken curves with different slopes depending on the mass range (Scalo, 1986; Kroupa, 2002a; Chabrier, 2003). If the IMF is *top-heavy*, massive stars have more weight and more SNe type II can eject α-elements to the ISM. Therefore, a top-heavy IMF can also enhance [α/Fe], with no need to invoke a faster timescale (e.g. Martín-Navarro, 2016).

Historically, the IMF has been thought to be universal, similar for systems with different properties (e.g. Kroupa, 2002a; Bastian et al., 2010). However, numerous more recent studies have proposed a non-universal IMF to solve different dilemmas, including the excess of low-mass stars and the unrealistically short formation timescale derived from [Mg/Fe] abundances in early-type galaxies (e.g. Kuntschner, 2000; Treu et al., 2010; van Dokkum & Conroy, 2010; Spiniello et al., 2015; Martín-Navarro et al., 2015a; Martín-Navarro, 2016; Lyubenova et al., 2016). IMF was proposed as a galaxy local property (rather than global) by Martín-Navarro et al. (2015a), who measured higher slopes in the central regions of massive galaxies (see also La Barbera et al. 2016 and van Dokkum et al. 2017). A tight correlation of the IMF slope with metallicity was also found in the CALIFA survey (Martín-Navarro et al., 2015b). A time-varying IMF slope, furthermore, would resolve the existing tension between the observed chemical composition in early types (high metallicity and α-enhancement, settled by massive stars) and their measured steep IMF (related to the current larger fraction of low-mass stars) (e.g. Vazdekis et al., 1996; Martín-Navarro, 2016). First generations would have been dominated by massive stars (flatter IMF) and following generations by low-mass stars (steeper slope).

1.2.2 Environment

On large scales, the Universe is made of a complex web of filaments and sheets, where galaxies are concentrated, and large empty voids (e.g. Mo et al., 2010). This kind of distribution is shown in Fig. 1.3, from the EAGLE (Evolution and Assembly of GaLaxies and their Environment) set of simulations (Schaye et al., 2015). This gives galaxies the possibility of living in a large variety of environments. Clusters are thought to grow aligned along filaments, from which they accrete mass (e.g. van de Weygaert & Bertschinger, 1996; Faltenbacher et al., 2005; Noh & Cohn, 2011). Environmental density is one of the factors that can trigger or stop some characteristic processes of galaxy evolution.

While direct mergers are rare in present-day clusters, because the high velocity dispersions of galaxies in general prevented them (e.g. Dressler, 1984; Moore et al., 1996), other types of gravitational interactions are quite common. These are known to both increase and quench star formation (e.g. Fujita & Nagashima, 1999; Quilis et al., 2000; Kronberger et al., 2008; Cohen et al., 2014; Hwang et al., 2018). *Ram pressure* can trigger or enhance efficient star formation in molecular clouds, during the interaction of a galaxy with the hot intra-cluster medium (Bekki & Couch, 2003). In particular, during the galaxy first infall into the cluster, the fast increase in

the external pressure can trigger a starburst (e.g. Evrard, 1991). In addition, Byrd & Valtonen (1990) and Hwang et al. (2018) showed that tidal and hydrodynamic interactions with the neighbor galaxies are more than sufficient to enhance star formation by induced collisions and compression of disk gas clouds.

On the other hand, several processes have been proved to strip the gas from galaxies in dense environments, as confirmed by the detection of molecular gas in tidal tails (e.g. Kenney & Koopmann, 1999; Braine et al., 2000; Verdugo et al., 2015). Quilis et al. (2000) and Abadi et al. (1999), among other authors, claimed that ram pressure and viscous stripping are very effective at removing the disk gas in a relatively short timescale. In a longer timescale, *harassment* is another process that can strip material from galaxies, forming tidal tails (e.g. Moore et al., 1996). Finally, the stripping of the hot galaxy-halo gas causes *strangulation*, i.e. the slow decline in the infall of fresh gas into the galaxy disk, gradually truncating the star formation (e.g. Balogh et al., 1999, 2000; Balogh & Morris, 2000; Bekki, 2009; Bekki & Couch, 2010). Fujita & Nagashima (1999) found that the star formation rate can even double in the initial approach of the galaxy to the center of a dense cluster, but then drops fast due to the gas depletion from stripping mechanisms, when the galaxy has reached the cluster core.

1.3 Disks in galaxies

Evolutionary paths in disk galaxies are very often related to the formation and evolution of their disks. Secular evolution and star formation are mainly driven by disks, as well as the formation of spiral arms, bars, rings and other structures (e.g. van der Kruit & Freeman, 2011). This is related to the fact that disks contain or contained, apart from stars, large amounts of gas and dust. Disks present a large variety of thicknesses and shapes, and they can display peculiar morphological structures, such as warps or flares. The latter, given by an increase of the scale height with radius, are of special interest for this thesis. We will mention in § 1.3.2 their potential different origins. Since this thesis is based on the study of stars, we will focus on the stellar properties. Several models were used to describe the stellar luminosity density distribution of disks. Camm (1950) approximated disks as isothermal sheets, to describe their vertical luminosity density distribution, while Freeman (1970) proposed exponentials to fit their radial surface-brightness profiles. In general, expressions like the following are used to describe the disk luminosity density distribution $L(R, z)$ (e.g. Freeman, 2007):

$$L(R, z) = L_0 \exp\left(-R/h_R\right) \operatorname{sech}^2\left(z/h_z\right) , \tag{1.2}$$

where L_0 is the disk central luminosity density. Alternatively, a good approximation is also

$$L(R, z) = L_0 \exp\left(-R/h_R\right) \exp\left(z/h_z\right) . \tag{1.3}$$

h_R is called the (radial) scale length and h_z the scale height. These two parameters are extensively used to describe the size or the radial extent and the thickness of a disk or a disk galaxy. Their ratio h_R/h_z indicates the flatness of a galaxy and appears to be by and large correlated with the Hubble type (e.g. van der Kruit & Freeman, 2011).

The dynamics of disks has been described with a variety of models. Given the complexity of the problem, all of them need a set of assumptions, though. If we assume axial symmetry and

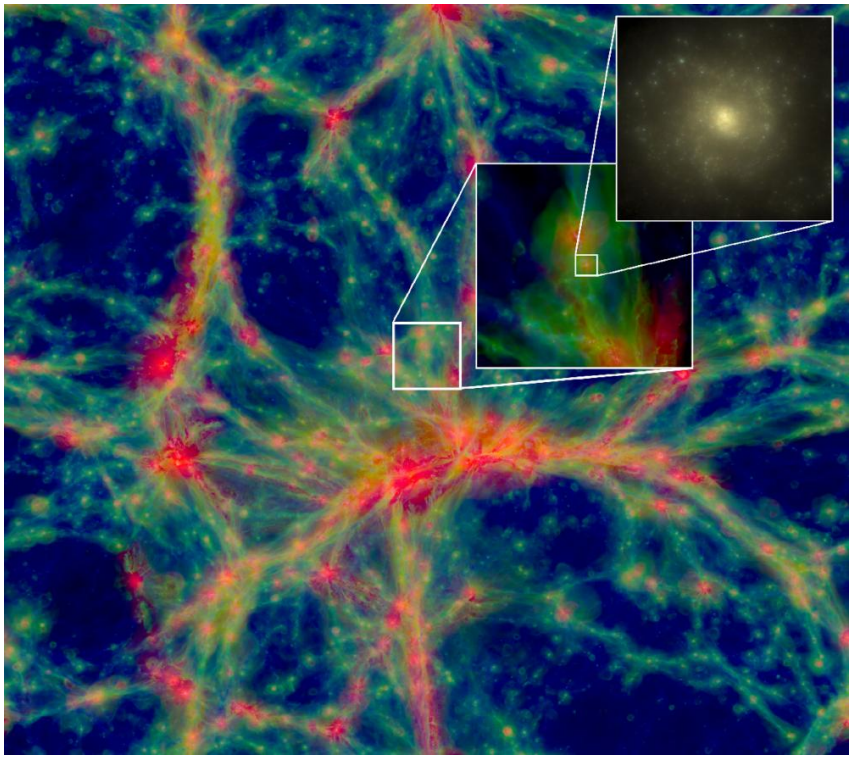

FIGURE 1.3— $100 \times 100 \times 20\,\mathrm{cMpc}$ slice at $z = 0$ from the Ref-L100N1504 simulation of the EAGLE set of simulations (Schaye et al., 2015).

flat rotation curve and we use the plane-parallel layers approximation, the Poisson and Jeans equation simplify to (e.g. van der Kruit, 1988; van der Kruit & Freeman, 2011)

$$\frac{dK_z}{dz} = -4\pi G\rho\,(z) \tag{1.4}$$

$$\frac{d}{dz}\left[\rho(z)\sigma_z^2(z)\right] = \rho(z)K_z\,, \tag{1.5}$$

where K_z is the gravitational force in the vertical direction z, ρ the mass density and σ_z the velocity dispersion along z. The velocity dispersion is by definition the statistical dispersion of the velocities from the mean and consequently indicates the degree of "disorder" in stellar motions. The term *dynamically hot* indicates that disks have large velocity dispersions, while *dynamically cool* disks have low dispersions.

Schwarzschild (1907) introduced the ellipsoidal three-dimensional distribution of the stellar velocity dispersions. The stellar velocity ellipsoid (SVE) is defined, in cylindrical coordinates, by

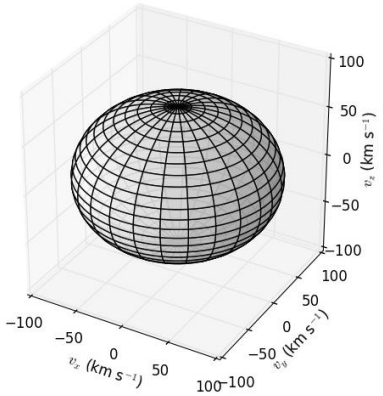

FIGURE 1.4— Illustration of a realistic Stellar Velocity Ellipsoid, in cylindrical coordinates. The semi-axes are the stellar velocity dispersions in the radial, azimuthal and vertical directions.

the vertical (σ_z), radial (σ_R) and azimuthal (σ_ϕ) components of the stellar velocity dispersion. The ratios σ_z/σ_R, σ_ϕ/σ_R and σ_z/σ_ϕ define its shape. Fig. 1.4 illustrates an example of SVE.

Rubin & Ford (1970) and Freeman (1970) observed for the first time that disk rotation curves were affected by the presence of undetected matter. After them, new observational and theoretical evidences were presented to propose the existence of optically invisible massive halos enclosing the disks (e.g. Ostriker & Peebles, 1973; Ostriker et al., 1974). This discussion led to the introduction of the mass-to-light ratio (M/L) as a parameter to quantify the discrepancy between the dynamical mass, calculated from its effect on the kinematics, and the luminous mass (e.g. Faber & Gallagher, 1979; Bosma & van der Kruit, 1979).

Another hypothesis sometimes necessary is the *maximum disk*. This concept is based on approximating the disk mass to the maximum mass allowed by the rotation curve (e.g. van Albada et al., 1985). Bershady et al. (2011) found that disks are submaximal in real galaxies and their mass contributes only the $15-30\%$ of the dynamical mass.

The equation for hydrostatic equilibrium, obtained by combining Eqs. 1.4 and 1.5 (e.g. van der Kruit, 1988), constrains the relation of σ_z (integrated over all the vertical coordinate z) with the mass surface density $\Sigma(R)$ and h_z. For an exponential disk,

$$\sigma_z(R) = \sqrt{\frac{3}{2}\pi G \Sigma(R) h_z}\,. \tag{1.6}$$

If M/L and h_z are constant with radius and the radial distribution of mass density is exponential, $\sigma_z(R)$ of the disk stars will be proportional to the square root of the surface density Σ. It would be an exponential with an e-folding $h_{\sigma,z} \simeq 2h_R$, called kinematic scale length. Martinsson et al. (2013) showed that this is true on average, but only until certain radius. Outside that radius, the velocity dispersion stops declining and becomes flat. In some galaxies it even starts to rise. This difference between the inner and outer scale lengths of σ was called the *kinematic flaring* of the disk.

The velocity dispersions in the plane (σ_R and σ_ϕ) are usually assumed to fulfill the asymmetric-drift equation and the epicycle approximation, respectively (e.g. Gerssen et al., 1997)

$$V_c^2 - \bar{V}^2 = \sigma_R^2 \left[\frac{R}{h_R} - R\frac{\partial}{\partial R} \ln\left(\sigma_R^2\right) - \frac{1}{2} + \frac{R}{2V_c}\frac{\partial V_c}{\partial R} \right] - R\frac{\partial \sigma_{Rz}^2}{\partial z} \tag{1.7}$$

$$\frac{\sigma_\phi^2}{\sigma_R^2} = \frac{1}{2}\left(1 + \frac{\partial \ln V_c}{\partial \ln R}\right) . \tag{1.8}$$

The asymmetric drift (Eq. 1.7) indicates the average speed by which stars lag behind circular orbits (V_c is the circular velocity) (e.g. Sparke & Gallagher, 2007). Small epicycles are used to explain the observed motions of stars in Eq. 1.8 (e.g. Binney & Tremaine, 1987).

The analysis of the local stability of differentially rotating disks, gaseous as well as stellar disks, is usually carried out by means of the parameter Q, first derived byToomre (1964). For stars, the Toomre parameter is defined as

$$Q = \frac{\sigma_R \kappa}{3.36 G \Sigma} , \tag{1.9}$$

This is to say that the stability of a stellar galactic disk against local axisymmetric disturbances depends on σ_R, the epyciclic frequency κ and the local mass surface density Σ. On small scales, a Jeans-type stability is provided locally. The kinetic energy related to random motions balances the tendency to collapse, but only up to a certain (Jeans) scale (van der Kruit & Freeman, 2011). On larger scales, stability is provided by the shear resulting from differential rotation. According to the Toomre criterion, the disk is stable at all scales when $Q > 1$. In real galaxies, stellar velocity dispersions are only slightly larger than the critical values, $Q = 1.5 - 2.5$ and disks are stable but close to instability. The Toomre criterion also suggests that too low values of radial velocity dispersions will not be expected as results, unless balanced by lower values of Σ. A further physical interpretation sees the Toomre parameter as a thermometer for galactic disks. Dynamically hotter disks have higher Q, while cooler disks have lower Q. Hot disks are therefore more stable than cool disks (e.g. Binney & Tremaine, 1987).

1.3.1 Thick disks

More than one disk component can be observed in most galaxies and identified in the brightness distributions or kinematics. The brightest disky component, nowadays called *thin disk*, was the first to be detectable since the birth of extragalactic astronomy. For this reason, with the more general word "disk" we have historically referred to it. More recently, with larger telescopes and better instruments, we have been able to detect the fainter *thick disk*, as well as smaller structures, e.g. nuclear disks. The study of thick disk is currently one of the "hottest" topics in galaxy formation and evolution. The extragalactic scientific community consider their origin an important piece of the puzzle, necessary to understand the assembly of disk galaxies.

Thick disks were discovered, in external galaxies, several decades ago (Burstein, 1979), but their existence was confirmed after discovering that the same Milky Way had one (Gilmore & Reid, 1983). In the Solar neighborhood it was possible to observe, both photometrically and spectroscopically, individual stars, showing that the thick disk is an actual distinct component. Gilmore & Reid (1983) identified three different populations: the young and the old thin disks,

and the thick disk. While the young and old thin disks have scale heights of 100 and 300 pc, the thick disk's stars are older, more metal-poor and kinematically hotter with a scale height of ~ 1.5 kpc. They are also more α-enhanced than the stars in the thin disk (e.g. Prochaska et al., 2000; Cheng et al., 2012), suggesting a different evolution history and timescale. Afterwards, thick-disk observation in all morphological types of edge-on galaxies has proved their ubiquity (e.g. Dalcanton & Bernstein, 2002; Yoachim & Dalcanton, 2006; Comerón et al., 2018), suggesting that they are a generic by-product of galaxy formation. In external galaxies, the thick disk appears as a low-surface brightness red envelope, with similar color and geometry to the Milky Way's thick disk (Dalcanton & Bernstein, 2002). In several works attempting to fit the galaxy surface brightness profiles, two exponentials with different scale lengths were necessary for the disk region (e.g. Burstein, 1979; van der Kruit & Searle, 1981; Yoachim & Dalcanton, 2006; Comerón et al., 2012, 2018).

Definitions

Previous studies of thick disks have been based on different decompositions. Depending on how we define the thick disk, we can find slightly different properties and depending on what exactly we want to study one or another definitions can be more useful. The different definitions were briefly reviewed by Martig et al. (2016). The most used definitions are two and are based on the chemical composition or on the morphology.

The *chemical* definition is based on the resolved stellar-population properties, in general abundance of α-elements, and it is the most used for the Milky Way. Two sequences in the [α/Fe]-[Fe/H] diagram for stars in the solar neighborhood were identified by Fuhrmann (1998) as the thin and the thick disk. Very similar distributions were later found by other several authors with a larger number of stars(e.g. Fuhrmann, 2011; Bovy et al., 2012). In this case, the thick disk is defined as the α-rich component in that diagram.

The *geometrical* (or *morphological*) definition is based on a photometrical decomposition performed fitting vertical brightness profiles with two disky components (e.g. Yoachim & Dalcanton, 2006; Comerón et al., 2012, 2018). This way, we can determine at what average distance from the midplane thick disk starts to dominate. This is mostly done in external galaxies, where we cannot resolve the individual stars. However, this definition has been used also in the Milky Way, in early studies (e.g. Gilmore & Reid, 1983) or more recently (e.g. Jayaraman et al., 2013).

It is also possible to use kinematics to perform a decomposition (e.g. Morrison et al., 1990), while a decomposition based on age has also been proposed (e.g. Haywood et al., 2013). We have to be cautious when we compare geometrically-defined thick disks in external galaxies with the Milky Way, if its thick disk was defined with a different criterion. In fact, in our galaxy, thick-disk properties clearly depend on the definition used to extract them (e.g. Bovy et al., 2012; Jayaraman et al., 2013).

Formation scenarios

The origin of the thick disk has been a matter of debate especially in the last decade. Different formation scenarios were proposed to fit its generally old ages and high velocity dispersions. If their stars were born a long time ago, were they born already with the present-day dispersions or did they acquire their high dispersions with time? This is to say, was the thick disk born

already thick or was it thin and was it dynamically heated later? The literature offers diverse theoretical studies pointing towards one or the other direction.

Brook et al. (2004) proposed that thick disks were formed during an epoch of violent interactions at high redshift, before the formation of the thin disk, as suggested by their chemodynamic simulations. An important amount of the accreted gas came from the protogalactic cloud, carrying high angular momentum and giving the disk shape to the galaxy. At the same time, gas-rich multiple mergers triggered the star formation and stars were formed with the high velocity dispersions of the turbulent star-forming gas, building the thick disk. Also one-dimensional simulations by Forbes et al. (2012) supported a "born hot" scenario, where thick disk was formed already thick. Starting with an unstable disk with dynamically-hot star-forming gas, the gravitational stability criterion itself leads to a decrease of gas velocity dispersion with time, when the accretion rate declines. Abadi et al. (2003) supported an extragalactic origin for the thick-disk stars, since more than 60% of them were accreted in their simulation (in the ΛCDM cosmogony). The orbital angular momentum of the disrupted satellites would have been responsible for the high angular momentum of the thick disk. Other authors admitted the possibility that a certain fraction of thick-disk stars came from accretion, while the bulk of the thick disk would have had another origin (e.g. Wyse, 2004).

Disk heating has been extensively studied and the potential mechanisms that produce it will be reviewed in the following section (§ 1.3.2). From the thick-disk formation point of view, only some of these mechanisms seem to be capable of heating the disk up to the observed thicknesses. For instance, secular processes are not usually invoked since they would produce only a slow and mild disk thickening (e.g. Lacey & Ostriker, 1985). Aumer et al. (2016) found unlikely that the Milky Way thick disk formed by the development of non-axisymmetries in the thin disk. On the other hand, fast thickening could easily explain thick-disk properties. Minor mergers can heat the disk with multiple events over time or in a violent single event (Toth & Ostriker, 1992; Quinn et al., 1993; Sellwood et al., 1998; Benson et al., 2004; Kazantzidis et al., 2008; Bournaud et al., 2009; Villalobos & Helmi, 2009; Qu et al., 2011; Di Matteo et al., 2011; Martig et al., 2014a,b; Pinna et al., 2018), apart from accreting at the same time a certain amount of stars.

In most of simulations by Qu et al. (2011), large scale heights are dominated by stars originally coming from the primary (thin) disk, vertically heated and radially redistributed by minor mergers. In some galaxies stars coming from merging satellites dominate. In this set of simulations, secular processes were unable to reproduce realistic thick disks. According to simulations of gas-rich young galaxies by Bournaud et al. (2009), thick disks could have formed by the dynamical heating of a pre-existing thin disk during turbulent phase at high redshift. Minor mergers were not the only mechanism, but also the formation of internal clumps could thicken the disk by scattering stars. However, the difference between thick disks formed by internal processes and the ones made by minor-merger heating is that, while the first ones show a constant scale height, the second ones flare. Minchev et al. (2015) claimed that, in an inside-out formation scenario, mono-age stellar populations unavoidably flare, but at different radii depending on their age. This could explain why observed disks, composition of the different mono-age populations, do not flare.

Additional scenarios (e.g. Brook et al., 2004; Gilmore et al., 1989), not usually invoked in recent times, are also fast dynamical heating by violent relaxation of the galactic potential (Jones & Wyse, 1983), extended kinematic diffusion of thin-disk stars to high energy orbits (Norris, 1987), pressure-supported collapse following the formation of Population II stars in the halo

(Larson, 1976) and collapse related to enhanced cooling due to metallicity above certain value, causing a rapid increase of dissipation and star formation rate (Wyse & Gilmore, 1988).

The origin of the Milky Way thick disk

Numerous works in the literature proposed different scenarios for the Milky Way thick disk. Dierickx et al. (2010) compared the distribution of orbital eccentricity in Milky Way thick-disk stars to simulations. These observations were compatible with an in-situ formation for most stars, related to gas accretion during satellite mergers, while stars accretion could explain higher eccentricities. Radial migration and disk heating, probably present at the same time, were not able to cause such eccentricities alone. Di Matteo et al. (2011) recovered these orbital eccentricities by N-body/SPH simulations, heating the thin disk with minor mergers in direct orbits. Following now a definition based on thick-disk chemical properties, Haywood et al. (2013) claimed that the star formation took place in an already assembled turbulent gas disk and lasted for $4-5$ Gyr, leading to a uniform chemical composition. In favor of this scenario, Haywood et al. (2015) measured homogeneous abundances of α-elements in (inner) thick-disk stars of all ages. These would have formed in a large scale process, as predicted by the two-infall model by Chiappini et al. (1997), explaining the formation of the halo and the thick disk. Snaith et al. (2014) measured the Milky Way star formation history and suggested that the thick disk formed during the most intense star formation epoch in the universe (from 12.5 and 9 Gyr ago), from large quantities of gas probably coming from previous accretions. Robin et al. (2014) agreed with a thick disk formation at high redshift, from gravitational collapse of well-mixed turbulent gas (following Bournaud et al. 2009). The star formation would have increased in intensity with time and extended between 12 and 10 Gyr ago, as recently confirmed by Robin et al. 2017. However, the chemo-orbital properties found by Liu & van de Ven (2012) pointed to a double origin for the Milky Way thick disk stars. Some of them would have formed through gas-rich mergers at high redshift, whilst others would have migrated from the thin disk.

Thick disks in external galaxies

Elmegreen & Elmegreen (2006) observed disks already thick in spiral galaxies of the Hubble Space Telescope Ultra Deep Field (up to redshift $z \sim 5$), characterized by giant star-forming clumps, probably produced by gravitational instabilities in a highly turbulent phase. The thin disk would have formed later in these galaxies. However, in the Hubble Space Telescope Frontier Fields, an anti-correlation between the mid-plane brightness and the scale height suggested the early presence of two components, a faint thick disk and a bright thin disk, in clumpy spiral galaxies at high redshift (up to $z = 3$) (Elmegreen et al., 2017). Wisnioski et al. (2015) showed a $1 + z$ evolution of gas velocity dispersion with cosmic time, leading to an increase in a factor of two from redshift $z \sim 1$ to $z \sim 2$.

Most of studies on thick disks in nearby external galaxies are photometry based. Imaging has been able to prove the existence and ubiquity of these disks (e.g. Dalcanton & Bernstein, 2002), and it has given an important contribution to characterize them. Rejkuba et al. (2009) extracted, using images from the Advanced Camera for Surveys on the Hubble Space Telescope, the color-magnitude diagram for thick disk stars of the Milky Way analogue NGC 891. The thick disk in NGC 891 looks more chemically evolved and presents a larger dispersion in metallicities,

with no radial gradient, than the Milky Way thick disk at solar galactocentric distances. This suggests a more active accretion history than in our Galaxy.

Yoachim & Dalcanton (2006), fitting the surface brightness profiles of 34 very late-type edge-on galaxies with two disk components, extracted some general properties for them. They compared the disks' properties showing that thick disk scale heights are approximately twice larger than the thin disk's, and in general the former have also more extended scale lengths than the latter. They found a correlation of the scale heights and scale lengths of both disks, but an anticorrelation of the thick-to-thin disk luminosity ratios, with circular velocity V_c (i.e. galaxy total mass). Whereas in high mass galaxies ($V_c > 120\,\mathrm{km\,s^{-1}}$) the thick disk's luminosity is only around 10% of the total, in lower masses it rises up to 40% and in very-low mass systems ($50\,\mathrm{km\,s^{-1}} < V_c < 70\,\mathrm{km\,s^{-1}}$) the thick disk can even dominate. A very similar trend was found for thick-to-thin disk stellar mass ratios as function of circular velocities. The baryon fraction confirmed that the thick disks become more important in low-mass galaxies. The authors believed that these results argued in favor of scenarios where thick-disk stars have an extragalactic origin. They considered a hierarchical scenario in which galaxy formation comes from multiple mergers contributing both stars and gas. The stars would have end up in the thick disk, while thin-disk stars would have formed from the accreted gas.

Their trends with V_c were confirmed by Comerón et al. (2012), who found thick-to-thin disk (stellar) mass ratios $0.2 < M_\mathrm{T}/M_\mathrm{t} < 0.7$ for galaxies with $V_c > 120\,\mathrm{km\,s^{-1}}$ and up to 2.0 for lower-mass galaxies. By and large, the latter displayed thick and thin disks masses comparable to one another (Comerón et al., 2018). However, Comerón et al. (2011b) had previously found in their sample larger $M_\mathrm{T}/M_\mathrm{t}$ and a much higher percentage of thick-disk-dominated galaxies. These studies, displaying a different behavior in high and low-mass galaxies, pointed towards a different thick disk origin for the two mass ranges. As e.g. Elmegreen et al. (2017) explained in their introduction, this can be due to the dependence of the star formation rate on galaxy mass (see also Comerón et al. 2012, 2014). Massive galaxies probably formed quickly at high redshift and are expected to be overall old (including the thick and the thin disk, see examples in Comerón et al. 2016; Kasparova et al. 2016) and more α-enhanced in their thick disks. Low-mass galaxies might be observed just as an α-poor thick component.

In this context, spectroscopy is needed to extract the stellar kinematics and populations of the thick disks, giving more insights about their properties and a better opportunity to understand their origin. Nevertheless, this kind of analysis is extremely challenging due to the very low surface brightness of thick disks. For this reason, few spectroscopic studies extracted the stellar kinematics and even fewer the stellar populations. Yoachim & Dalcanton (2005) studied the kinematics of the thin and the thick disks of two edge-on galaxies, using spectroscopy with long slit placed parallel to the major axis and in two different positions with respect to the galaxy plane. While one galaxy displayed a rotation lag (of the thick-disk region compared to the thin-disk region) similar to the one observed in the Milky Way, the second galaxy showed a much slower rotation above than in the midplane. The authors proposed the presence of a counterrotating component to explain this behavior. The analysis was extended to nine late-type galaxies in Yoachim & Dalcanton (2008a). They observed globally a wide variety of thick-disk kinematics and strong differences with thin disks in low-mass galaxies. After comparing with formation models, they supported accretion as the only formation mechanism capable of explaining the observations. Yoachim & Dalcanton (2008b) analyzed for the first time unresolved stellar populations in the thick disks. They used Lick indices to extract luminosity-weighted ages

and metallicities of nine low-mass late-type galaxies. They found generally old thick disks, with ages between 4 and 11 Gyr depending on the galaxy, and much younger thin disks, with ages lower than 5 Gyr. Thin disks had strong radial gradients, showing younger stars in the outer regions (younger than 1 Gyr). Both disks showed similar metallicities, though.

Kasparova et al. (2016), using a full spectral fitting technique on long-slit data, studied the stellar populations of three early-type edge-on disk galaxies. They found a variety of abundances and age distributions, suggesting different pictures for different environments. In NGC 4111, living in a dense group, they found an initially thick disk growing until low redshift, very similar to the thin disk. In NGC 4710, in the outskirts of the Virgo cluster, they observed a younger, more metal rich and α-poor thin disk than the thick disk. This was interpreted as a sign of a more intense star formation and chemical evolution, probably thanks to the additional gas coming from the environment. Since both disks flare at large radii, the authors suggested that those stars where formed when the star formation in the midplane was already quenched. Finally, they found a single thick disk in NGC 5422, with a rapid formation during a turbulent phase at high redshift. This galaxy belongs to a sparse group of very old lenticular galaxies which might have consumed their gas early after the thick disk formation.

While long-slit studies have provided valuable information and hints about the thick disk origin, only integral field spectroscopy (§ 1.4.1) allows us to extract stellar kinematics and populations maps, look for gradients more easily and have a global view of galaxies and their disks. The first study of this kind was done by Comerón et al. (2015) with the VIsible Multi-Object Spectrograph (VIMOS) at the Very Large Telescope (VLT), on ESO 533-4, an almost edge-on high mass S0 with a small central mass concentration. For the first time, velocity, age and metallicity maps were shown, although with low spatial resolution and a single bin for the thick disk dominated region. No counterrotation was necessary to explain the observed kinematics and the thin and the thick disks appeared to be made up by different populations. They displayed a distinction in the age-metallicity diagram, being the thick disk older and more metal poor. A fast internal or external event was proposed as responsible for forming the thick disk of ESO 533-4 at high redshift.

This was followed by a second bi-dimensional study by Comerón et al. (2016), this time using deeper IFU data from the Multi Unit Spectroscopic Explorer (MUSE) mounted on VLT, allowing several bins in the thick disk region. The analyzed galaxy was one more high-mass S0, ESO 243-49, located in the Abell 2877 cluster. Maps of the mean velocity, velocity dispersion, age and metallicity were shown with an unprecedented spatial resolution. ESO 243-49 showed old and similar ages in both the thin and the thick disk, whilst some difference in metallicity was detected (the thick disk was more metal poor). This study supported an internal origin for thick disks in high-mass galaxies, with a fast formation during a high-redshift turbulent phase inmediately followed by the thin-disk formation or through fast disk heating. They described the global formation process of this galaxy as a monolithic collapse which would have produced, in a very fast timescale, the different generations of stars of both disks. Just after that, the star formation was totally quenched.

1.3.2 Disk heating

The origin of the disk heating has been a matter of study for many years, since the correlation of velocity dispersion with age was discovered in the Milky Way (e.g. Strömberg, 1946; Spitzer &

Schwarzschild, 1951; Wielen, 1977; Carlberg et al., 1985; Holmberg et al., 2009). This trend was later called the age-velocity dispersion relation or the age-velocity relation (AVR) (e.g. Martig et al., 2014a,b; Aumer et al., 2016) and was confirmed also in external galaxies (e.g. Beasley et al., 2015; Dorman et al., 2015). Observations of edge-on galaxies reveal that disks have a finite extent perpendicular to their plane, which can be attributed to the excursion that stars acquire in this vertical direction, due to their random motions (Merrifield et al., 2001). In this scenario, stars were formed with dynamically cold orbits from a thin layer of gas. Therefore, random velocities would have increased later, due to some sources of kinematic heating which several candidates have been proposed for. On the one hand, these include slow processes. In the solar neighborhood, the Geneva-Copenhagen survey showed that the square of the vertical velocity dispersion increases linearly with age, indicating that gradual processes (probably related to secular evolution) played an important role in the disk history (Nordström et al., 2004). On the other hand, the disk heating can be produced in a faster timescale (e.g. Quinn et al., 1993; Kazantzidis et al., 2008; Martig et al., 2014b; Grand et al., 2016).

The AVR, whose shape is closely connected to the past heating events, can provide good observable hints about the disk evolution (Grand et al., 2016). One diagnostic for the possible predominant heating sources can be provided by the relative amplitudes of the random motions in different directions, which are a measure of the relative importance of the different mechanisms (e.g. Jenkins & Binney, 1990; Merrifield et al., 2001). The three-dimensional distribution of the stellar velocity dispersions, which defines the SVE, is thus the result of the dynamical history of the disk. In an axisymmetric disk with stellar orbits not too far from circular (the epicycle approximation, see Eq. 1.8 and Binney & Tremaine 1987), σ_ϕ/σ_R depends only on the circular velocity and not on any disk heating mechanisms. However, measurements of σ_z/σ_R and of the orbital anisotropy parameter

$$\beta_z = 1 - \left[\frac{\sigma_z(R)}{\sigma_R(R)}\right]^2 , \tag{1.10}$$

(e.g. Cappellari et al., 2007) can be used to assess the shape of the SVE and constrain the predominant heating processes in galactic disks (e.g. Gerssen & Shapiro Griffin, 2012). Vertical and radial dispersions similar to each other would reveal an approximately *isotropic heating*, whereas *anisotropic heating* would be displayed by a significant difference between those velocity dispersion components. Depending on their influence on the shape of the SVE, the candidates as sources of disk heating can be classified as:

1. *three-dimensional agents*, responsible for increasing both vertical and radial (and azimuthal) dispersions, although not necessarily at the same rate. The most invoked examples in the literature are stochastic processes such as encounters with GMCs and mergers.

2. *radial (or planar) agents*, involved only in radial (planar) heating, with no effect on the vertical component of the velocity dispersion. The most invoked candidate is the spiral structure, typical of most disk galaxies.

Spitzer & Schwarzschild (1951) showed that star-cloud encounters could be responsible for the increase of the velocity dispersion with advancing spectral type (and age) along the star main sequence. Spitzer & Schwarzschild (1953) agreed that this could be possible thanks to the large-scale fluctuations in the interstellar medium density, indicated as density inhomogeneities by previous extinction observations. Moreover, clustered star formation may add kinematically

hot components to pre-existing populations, thanks to the expulsion of the residual gas by the massive stars, thickening the disk (Kroupa, 2002b). Recent N-body simulations by Aumer et al. (2016) confirmed that GMCs are capable of heating the disks vertically as well as horizontally. If their influence was significantly higher in the past than now, due to higher mass and/or number densities, they could explain the observations in the solar neighborhood (see also Lacey 1984). Hence, the heating efficiency would have declined during time, not only due to a decline in the star-formation rate (SFR), but also because a GMC is individually more effective at heating when it represents a large fraction of the not-fully-grown disk mass. The rate at which an individual GMC heats scales with its mass relative to the mass of the Galaxy interior to its orbit. As a consequence, we probably need to invoke other heating agents to explain the vertical/isotropic heating in the later stages of the disks, when they are already massive (as suggested by Lacey 1984).

The dynamical heating caused by galaxy mergers was analyzed by numerous theoretical studies. Toth & Ostriker (1992) showed, with an analytical model, how the satellite infall helps to explain the observed scale height of the Milky Way disk. Disks respond thickening to mergers, according to Quinn et al. (1993). Due to satellite accretions, which deposit kinetic energy into random motions of stars, disk stars spread both vertically and radially. Sellwood et al. (1998), on the basis of N-body simulations, claimed that mergers with satellites couple closely to oscillations that can be excited in the vertical direction. Direct vertical heating of disk stars by the gravitational perturbations would be negligible if compared to the one caused by dissipation of large-scale bending waves, excited by satellites decaying orbits at resonances with stellar orbits. On the other hand, Benson et al. (2004) developed an analytical model, ignoring the effect of resonances, which predicted a median thickening of the disks by satellite accretions, which deposit kinetic energy into disk stars. This model was compatible with the thickness observations in the Milky Way and the abundance of substructures in dark matter haloes predicted by the ΛCDM model of galaxy formation. Velazquez & White (1999), using N-body simulations, studied the amount and distribution of the heating caused by interactions with merging satellites. They found that the effect depends strictly on the masses of the disk, the bulge and the satellites relative to each other, and on the coupling of their orbits with each other (prograde or retrograde). In simulations by Kazantzidis et al. (2008, 2009), vertical, radial and azimuthal velocity dispersions increased at the same time during mergers with satellites, without affecting significantly the shape of the velocity ellipsoid. This is in agreement with this kind of interactions being proposed as three-dimensional heating agents.

Roškar et al. (2013) claimed that the change in the radial positions of stars would have an important effect on the final disk scale height. On the other hand, numerous other authors showed that the contribution of this so-called radial migration might be insignificant (e.g. Minchev et al., 2012a,b,c, 2013; Bird et al., 2013; Vera-Ciro et al., 2014; Grand et al., 2016).

Regarding the dynamical heating in the disk plane, numerous studies have pointed to spiral arms as the most efficient source. Disk stars usually receive, from the spiral density waves, kicks at a frequency which is close to their natural oscillation frequency in the radial direction (Merrifield et al., 2001; Minchev & Quillen, 2006, e.g). Therefore, radial random motions can be increased rapidly by this near-resonant process. At the same time, this does not happen in the vertical direction, so that σ_r will be made significantly grater than σ_z (Jenkins & Binney, 1990). Sellwood & Carlberg (1984) argued that the transient spiral patterns are self-regulating features, since they tend to stability rising secularly the radial velocity dispersion, until the Toomre

parameter (Toomre, 1964) has risen to a value around 2. This would make the spiral patterns fainter in later times, unless any cooling process ensures that the disk does not completely stabilize and exhibits a recurrent spiral structure. Concerning the effect of bars, Grand et al. (2016) claimed that they are important contributors to disk heating, after associating the bar buckling to a sudden increase in vertical kinetic energy. Saha et al. (2010) found an explanation for the vertical heating in the inner region of the disk (within a scale-length) in the instabilities caused by the bar growth. On the contrary, in the outer disk, the radial heating overtook the vertical heating in presence of bars evolved to saturation (in the sense that its amplitude cannot grow anymore). Saha et al. (2013) related the buckling instability with a drop in σ_z/σ_R and warned about the difficulty of tracking stars subject to rapid changes during the buckling phase.

The disk heating in the Milky Way has been extensively studied. Dehnen & Binney (1998) used the absolute parallaxes and proper motions of 11 865 stars from the *Hipparcos* Catalogue ESA 1997 (Perryman et al., 1997) to measure the kinematics in the local solar neighborhood. They suggested that both spiral structure and scattering by molecular clouds have contributed essentially to the local disk heating. However, they found a hint of a slightly more isotropic ellipsoid for redder stars, in agreement with the expectation that the dynamically hotter stellar populations are less sensitive to heating by spiral structure. This study, preceded by Wielen (1977), was followed by Nordström et al. (2004), Aumer & Binney (2009), Casagrande et al. (2011), and Aumer et al. (2016). In spite of slightly different results depending on the selected sample, these studies were in agreement with the same disk heating scenario: a combination of encounters with GMCs and spiral density waves.

Few observational studies have tried to assess the predominant heating mechanisms in external galaxies. Different methods were used to constrain σ_z/σ_R, all of them affected by several assumptions and large uncertainties. The scientific community generally expected a trend of the shape of the SVE with the Hubble type. Following the picture drawn by Jenkins & Binney (1990), later types should present more important spiral structures, leading to a more anisotropic SVE. The first galaxy, other than the Milky Way, for which the shape of the SVE was determined, was NGC 488 (Gerssen et al., 1997). They decomposed the line-of-sight velocity dispersion, measured in the major and the minor axes with long-slit spectroscopy, into the three components in the radial, azimuthal and vertical direction. This was possible thanks to the intermediate inclination of the galaxy. They compared their result for σ_z/σ_R with the value for the Milky Way previously calculated by Wielen (1977). Their galaxy was a slightly earlier type than the Milky Way and they interpreted its more isotropic SVE as a lower contribution from the spiral density waves to the disk heating. This early study was followed by the one by van der Kruit & de Grijs (1999). They used a method based on surface photometry, to constrain the SVE of 40 edge-on late-type galaxies of different morphological types. They remarked the lack of any trend as function of the Hubble type in their sample. Gerssen et al. (2000), Shapiro et al. (2003) and Gerssen & Shapiro Griffin (2012) extended the sample of Gerssen et al. (1997) to 8 galaxies, finding a clear trend of the SVE shape with the morphological type. The earlier type the galaxy, the more isotropic the ellipsoid, having the three-dimensional agents dominated the disk heating. Probably these galaxies had suffered from mergers or encounters with other systems such as giant molecular clouds. On the contrary, for later types and more important spiral structures, more flattened ellipsoids were found. In this case, radial (planar) agents could have predominantly heated the galactic disk, likely the same spiral density waves.

Gerssen & Shapiro Griffin (2012) also argued that GMCs could be only marginally consistent

with being the three-dimensional agent, since they found no correlation between the molecular gas surface mass density and the ratio σ_z/σ_R, in their sample. They moreover suggested that alternative mechanisms had to be invoked, such as the accretion of satellites. Finally, they investigated the role of spiral arms in the disk heating, looking for correlations between the three velocity dispersions and the arm-class parameter. A strong correlation was found with σ_R, as expected from the Toomre criterion. The parameter Q is proportional to σ_R, so that larger radial velocity dispersions create more stable systems which are less rensponsive to the spiral density waves. That is why, for the largest values of σ_R, the most flocculent structures were found, and the most clear spirals in the galaxies corresponded to lowest radial dispersion. In conclusion, spiral transient are excellent candidates as radial agents.

There were later studies of the SVE shape in other galaxies, not all of them in agreement with the trend plotted by Gerssen & Shapiro Griffin (2012). We send the reader to Chapter 2 for more details about studies on the SVE. There, we describe more extensively the works in the literature and we plot their results as function of the galaxy Hubble type in Fig. 2.1. We revisit all the literature on this issue and we compare the observational results with simulations.

Disk flares

In general, disk flaring has been related to the dynamical heating processes. In particular, pronounced flares were found in simulated minor mergers (e.g. Walker et al., 1996; Kazantzidis et al., 2008; Qu et al., 2011; Martig et al., 2014b), showing that they are a generic property of disks after being heated via gravitational interactions (Villalobos & Helmi, 2008; Bournaud et al., 2009). Due to the lower density of the external region of the disk, this is more affected by the disturbances caused by minor mergers. According to Martig et al. (2014a), mergers increase the flaring. Only minor flares are created by star scattering by giant clumps (Bournaud et al., 2009). Minchev et al. (2012c) studied the effect of radial migration on flaring. They found that stars that migrate outwards lose velocity dispersion to match the energy typical of stars in their new region. Nonetheless, they retain some of this energy, in a larger amount if they come from farther. However, Grand et al. (2016) found exactly the opposite in their simulations, where radial migration disfavored the flaring, due to the cooling effect provided by stars migrating outwards (see also Minchev et al. 2014). Minchev et al. (2015) proposed that all mono-age populations flare, but since they flare at different galactocentric distances their composition do not flare. Therefore flaring is unavoidable, but we do not observe it in all galaxies. Lastly, a dynamical origin of the flare was proposed by Narayan & Jog (2002a), taking into account the gas potential. Narayan & Jog (2002b) showed the match of their model with observations in the Milky Way, where not only stars but also atomic and molecular gas flare (e.g. Wouterloot et al., 1990; Kent et al., 1991; Burton et al., 1992).

Recent results from the Gaia mission (second data release) showed a clear flare in velocity dispersion (Gaia Collaboration et al., 2018). This structure was attributed to two factors: the radial evolution of the relative importance of the thick and the thin disk (the second one with larger scale length) and the weakening of the vertical gravitational force causing that, for the same velocity, stars could go farther from the midplane. Regarding the kinematic flaring mentioned at the beginning of Section 1.3, its astrophysical origin has been questioned during years. Possible explanations proposed so far for this behavior include an increase in the disk M/L ratio, in the importance of the thick disk, and a heating of the thin disk for instance by

halo substructures (Martinsson et al., 2013).

1.4 Techniques

The opportunity to study the distribution of light in different wavelengths, which contains an enormous amount of information about astronomical objects, has made spectroscopy the optimal observational technique to study their physical properties. Stellar spectra have been the main source of knowledge about the physics of stars (e.g. Rutten, 2003). Since the visible mass of galaxies is made of stars (and gas), their spectra give us a great opportunity to study their properties and origin. If the galaxy distance is sufficient to prevent us to resolve the individual

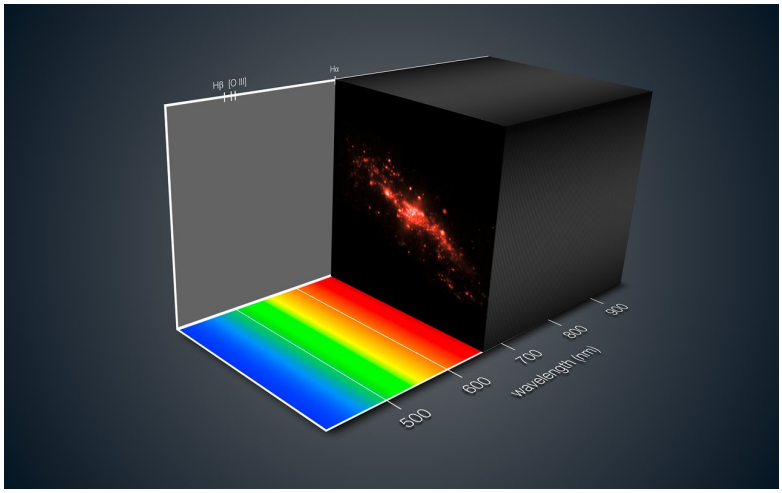

FIGURE 1.5— Illustration of the three-dimensional MUSE data cube of the galaxy NGC 4650A from `http://www.eso.org/public/images/eso1407a/` (Credit: ESO/MUSE consortium/R. Bacon/L. Calçada).

stars, we do not have other option than observing the integrated light of stars. Stellar-population synthesis is based on galaxy integrated spectra in the line of sight (e.g. Peletier, 2013). Only with a spectroscopic analysis we can extract kinematics and stellar populations, that allow us to infer about the history of a galaxy as we have seen in the previous sections (e.g. § 1.2.1, 1.3.1 and 1.3.2).

The main part of this thesis (Chapters 3 and 4) makes use of MUSE integral-field data from the Fornax 3D survey.

1.4.1 Integral field spectroscopy

Integral field spectroscopy (IFS) is the state-of-the-art technique to study extended objects such as nebulae or galaxies, since it allows to map the information extracted from the spectra, such as kinematic or chemical properties. The light from each spatial pixel (*spaxel*) is sent

to a spectrograph which produces the spectrum. An integral field unit (IFU) organizes these spectra into a *datacube* as the example illustrated in Fig. 1.5. For each spaxel of the galaxy we have a spectrum. We keep the two-dimensional spatial information and wavelength plays as a third dimension in the datacube. For this reason IFS is also called three-dimensional (3D) spectroscopy. This is the main advantage of IFS compared to the more traditional long-slit spectroscopy, which loses the second spatial dimension in its one-dimensional spectra. IFS allows us to analyze the spatial distribution of stellar properties and reveals structures that sometimes do not stand out in images. Another advantage of IFUs is the fact that an accurate positioning of the source in the field of view (FoV) is no longer necessary. In contrast, this is essential in long-slit spectroscopy. Moreover, IFUs usually have a relatively small spaxel size with respect to the seeing, assuring a constant spectral resolution.

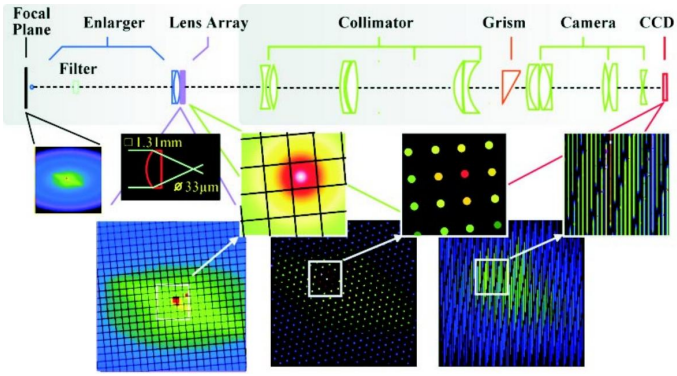

FIGURE 1.6— Optical design of the instrument SAURON (Bacon et al., 2001). The image of a galaxy is shown successively at the telescope focal plane, at the entrance plane of the lens array, at the exit plane of the lens array and at the detector plane.

Since the first developments of 3D spectroscopy in the 80s-90s (e.g. Gray et al., 1982; Vanderriest & Lemonnier, 1988; Arribas et al., 1991), instruments have gone through a significant evolution. Spatial resolution has considerably improved and the size of FoV has increased. Different types of IFUs have been used so far, using different techniques to separate the FoV in different areas and split the light before feeding the spectrographs. The main three types of IFU are:

- *microlens array*, placed in the slit plane before the spectrograph. The light from each microlens go through the corresponding dispersive element and produces a spectrum. The instrument SAURON (Spectroscopic Areal Unit for Research on Optical Nebulae), which operated at the William Herschel Telescope (WHT) on the Roque de los Muchachos Observatory in la Palma, is shown as an example in Fig. 1.6. An image of a galaxy is shown at different steps of the processing. Each lenslet forms a small image which is separated in different wavelengths creating a spectrum in the CCD (Charge-Coupled Device). Spectra are slightly inclined in the CCD in order to avoid overlapping. Other examples are TIGER (Bacon, 1995) mounted on CFHT (Canada France Hawaii Telescope, at Mauna Kea ob-

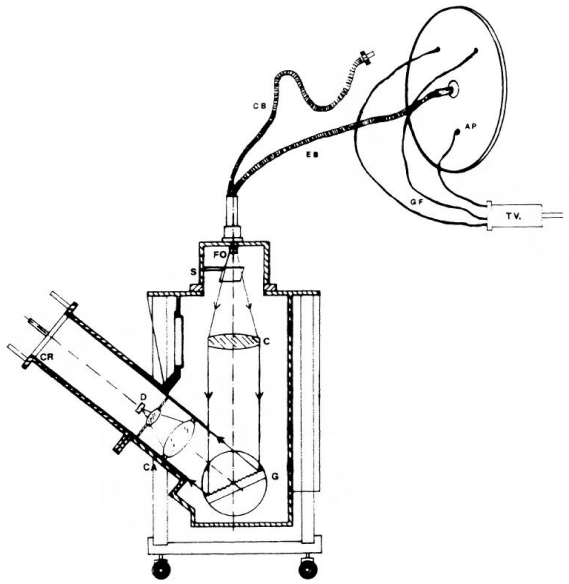

FIGURE 1.7— Scheme of the optical fiber spectrograph designed by Arribas et al. (1991). The notation is as follows. AP: aperture plate, GF: guiding fibers, TV : TV acquisition system, CB: compact bundle, EB: extended bundle, FO: optical fibers at the entrance of the spectrograph, S: shutter, C: collimator, G: grating, CA: camera, D : detector, and CR: cryostat.

servatory in Hawaii), and SPHERE (Claudi et al., 2008) on VLT (Very Large Telescope, at Paranal observatory in Chile).

- *fiber bundle*, where an array of optical fibers is positioned in the slit plane. In the simple illustration of Fig. 1.7 from Arribas et al. (1991) we can see one possible design. The fiber bundle conducts the light into the spectrograph. More modern designs combine microlens arrays and fibers, as illustrated in Fig. 1.8. In this case, the fibers are placed after the microlens array. Examples of this kind of IFU were INTEGRAL (Arribas et al., 1998) mounted on WHT and PMAS/PPak (Kelz et al., 2006) on the Calar Alto 3.5 m telescope.

- *image slicer*, whose functioning is shown in Fig. 1.9. The image, for example of a galaxy, is divided in different slices and each slice plays the role of a slit. The light is fed from each of them into a spectrograph. The spectra of the different slices are then recombined in the two spatial dimensions to form the 3D datacube. The instruments MUSE (Bacon et al. 2010, described next) and SINFONI (Eisenhauer et al., 2003) on VLT, for instance, use this kind of technology.

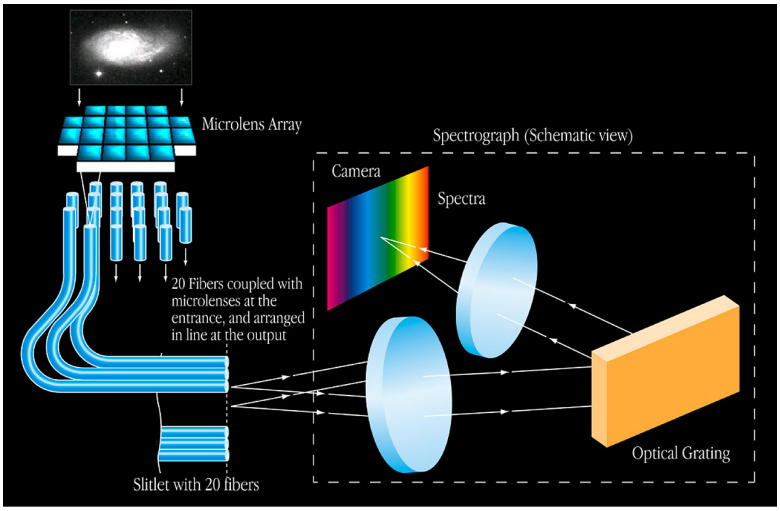

FIGURE 1.8— Illustration of an IFU combining lenslets and fibers, from `http://www.eso.org/public/images/eso0203c/` (Credit: ESO).

MUSE

The Multi Unit Spectroscopic Explorer (MUSE, Bacon et al. 2010) was designed for the Nasmyth focus of the UT4, one of the four Unit Telescopes (UTs) of the Very Large Telescope (VLT) at ESO Paranal observatory in Chile [2]. The four UTs have a main mirror of 8.2 m of diameter. A picture of MUSE mounted on the UT4 is shown in Fig. 1.10. MUSE is a panoramic integral-field spectrograph composed by 24 IFUs using the image slicer technology (e.g. Henault et al., 2004; Bacon et al., 2004, 2010; Kosmalski et al., 2011). The FoV is splitted into 24 subFoVs, each one divided into 48 "mini slits" rearranged into a pseudo-slit.

MUSE will offer two different FoV magnifications. The Wide Field Mode (WFM), currently offered, has a $1' \times 1'$ FoV sampled at $0.2''$, while the Narrow Field Mode (NFM), not offered yet, will have a FoV of $7.5'' \times 7.5''$ sampled at $0.025''$. The spatial resolution at FWHM (Full Width Half Maximum) is $0.3'' - 0.4''$ for the WFM and $0.03'' - 0.05''$ for the NFM. MUSE operates in the visible and near infrared with a large spectral range between 4650 and 9300 Å and an average spectral resolution R $\sim$ 3000 ($\sim$ 2000 at 4650 Å, $\sim$ 3000 at 7000 Å and $\sim$ 4000 at 9300 Å).

The main scientific goal driving the design of MUSE was the study of galaxies out to redshift $z \sim 6$, in order to identify progenitors of nearby galaxies. Other aims were the study of very faint sources, the detection of Ly_α emission to study the reionization, the search for population-III stars, the observation of AGNs and mapping of the growth of dark matter haloes. Some remarkable scientific results have already been achieved with MUSE, such as the detection of the visible counterpart of a gravitational wave source and the observation of possible first signs of self-

[2] `http://www.eso.org/public/teles-instr/paranal-observatory/vlt/`

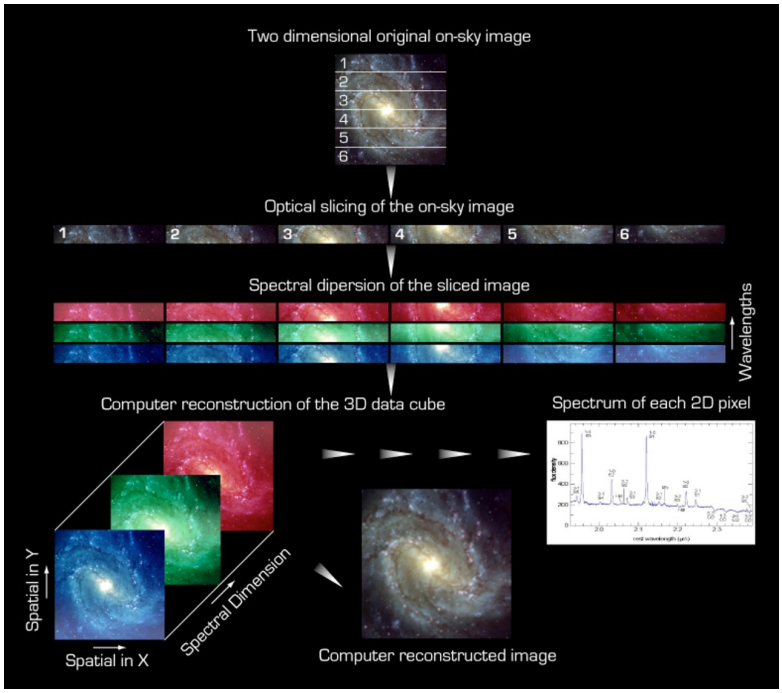

FIGURE 1.9— Functioning scheme of an image slicer, from `http://www.eso.org/public/images/eso0426i/` (Credit: ESO).

interacting dark matter (`http://www.eso.org/public/teles-instr/paranal-observatory/vlt/vlt-instr/muse/`). MUSE superb spatial resolution allows detailed studies of nearby galaxies.

1.4.2 The Fornax 3D project

The Fornax 3D project (Sarzi et al., 2018) is a comprehensive study of bright galaxies in the Fornax cluster, based on MUSE deep high quality observations. The goal of the project is in general to contribute new insights to the formation and evolution of galaxies in dense environments. More in details, the project aims to characterize the disk components of the fast-rotating early-type galaxies but also their outskirts and the very faint stellar haloes, by means of kinematic and stellar-population analysis. Spatially resolved IMF studies are also planned in order to constrain radial variations. In addition, the distribution of globular clusters and planetary nebulae is being mapped, and emission-line analysis is being performed in late-type galaxies.

The Fornax 3D survey includes a sample of 33 galaxies (23 of them early types), shown in Fig. 1.11, within (or close to) the virial radius of the Fornax cluster ($R_{\rm vir} \sim 0.7$ Mpc, Drinkwater

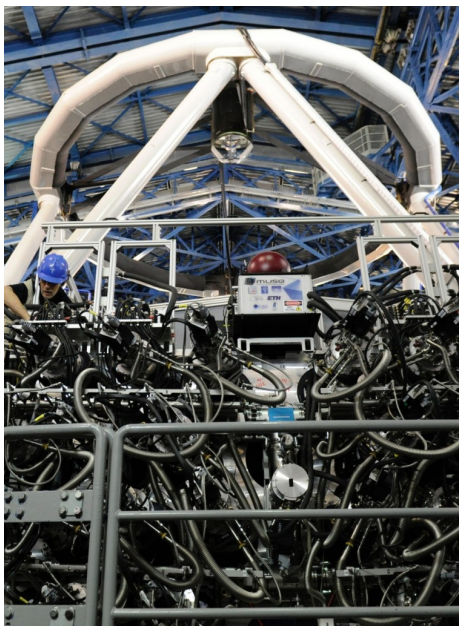

FIGURE 1.10— Picture of MUSE mounted on the UT4, from `http://muse-vlt.eu/science/cropped-dsc0194-jpg/` (Credit: R. Bacon).

et al. 2001). Only galaxies brighter than $m_B = 15\,\mathrm{mag}$ (in the B-band) were selected, excluding dwarf galaxies. The outskirts of early-type galaxies were observed down to a surface brightness in the B-band of $\mu_B \geq 25\,\mathrm{mag\,arcsec^{-2}}$, corresponding to a radial extent out to $R \geq 4R_\mathrm{e}$ (where R_e is the effective radius).

1.5 Thesis outline

The main goal of this thesis is to contribute to our knowledge about thick-disk origin. Particular emphasis is given to the analysis of dynamical heating as origin for the disk thickness. Given the low number of advanced analyses on thick-disk stellar populations in external galaxies, such as high-resolution integral-field studies, and some discrepancy between them, many questions remain still unanswered. Does the diversity of observed thick disks mean different origins for different galaxies? Were thick-disk stellar populations formed through only one of the proposed scenarios or more than one of them could have played an important role? Which factors favor one or another formation scenario? Galaxy mass? Environment? Internal or external processes? This thesis aims to use cutting-edge observations to characterize thick disks and answer some of these open questions.

Chapter 2 reviews the previous observational measurements of the SVE in galaxies, from

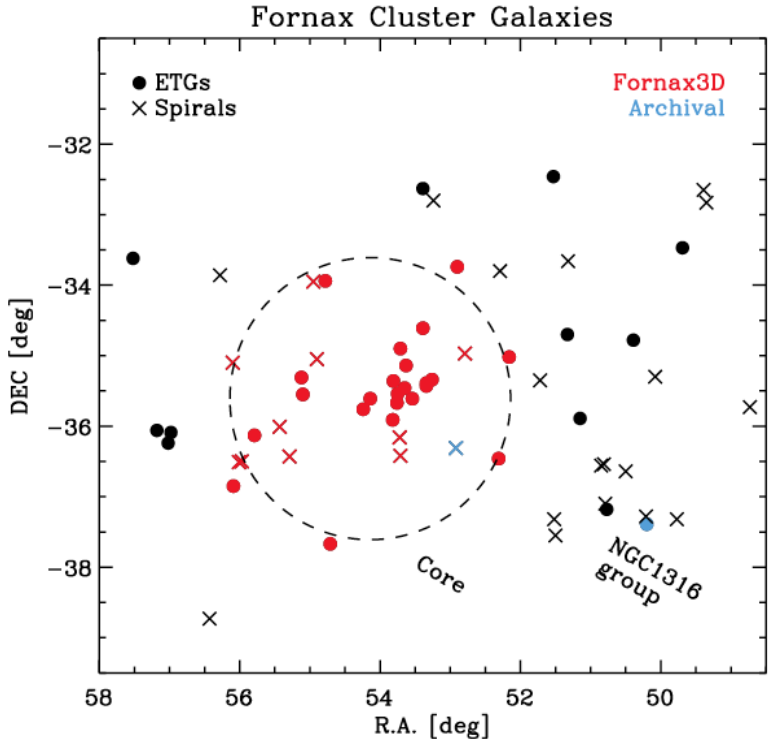

FIGURE 1.11— Identification of the Fornax 3D sample in the sky (red symbols), from Sarzi et al. (2018). Circles indicate early-type galaxies. Crosses indicate late-type galaxies. The dashed circle marks the virial radius of the cluster. The blue symbols correspond to NGC 1316 (filled circle) and NGC 1365 (cross) for which MUSE data are already available in the ESO Science Archive Facility.

the point of view of the disk dynamical heating. In particular, we revisit the relation between the shape of the SVE and the Hubble type, using not only results from the literature, but also N-body simulations of different kinds. Simulations help us to study the effect of different heating agents, in particular mergers and bar formation, on the SVE. In addition, with a time evolution analysis of the SVE in simulations, we assess the short and long-term capability of some heating sources, in particular mergers, to thicken the disk, taking into account the counteracting agents such as the contribution of young dynamically cool stars. Finally, we discuss the goodness of the SVE shape as indicator of the predominant disk heating mechanisms.

In Chapters 3 and 4, we analyze a sample of three S0 galaxies in the Fornax cluster, concentrating on their stellar kinematics and populations. We present maps of the first four moments of the line-of-sight velocity distribution, age, metallicity and [Mg/Fe] abundance, extracted from deep MUSE data from the Fornax 3D survey. We extract the star formation history and the

average chemical properties for the different structural components of the galaxies in the sample. In particular, we focus on the properties of thick disks also in light of previous studies in other galaxies. We propose formation and evolution scenarios for the three galaxies and for their thick disks, taking into account the different scenarios proposed in this Introduction. Eventually, we infer about possible environmental processes which could have affected their evolution. Since the galaxies are located in different positions of the cluster, we compare the three galaxies with each other and discuss the potential reasons for their similarities and differences.

We sum up the conclusions drawn from this thesis in Chapter 5, where we also propose a future outlook.

2

Revisiting the Stellar Velocity Ellipsoid – Hubble type relation: observations versus simulations

The material included in this chapter has been published in:
Pinna F., Falcón-Barroso J., Martig M., Martínez-Valpuesta I., Méndez-Abreu J., van de Ven G., Leaman R., Lyubenova M., 2018, Monthly Notices of the Royal Astronomical Society, 475, 2697.

The stellar velocity ellipsoid (SVE) in galaxies can provide important information on the processes that participate in the dynamical heating of their disk components (e.g. giant molecular clouds, mergers, spiral density waves, bars). Earlier findings suggested a strong relation between the shape of the disk SVE and Hubble type, with later-type galaxies displaying more anisotropic ellipsoids and early types being more isotropic. In this chapter, we revisit the strength of this relation using an exhaustive compilation of observational results from the literature on this issue. We find no clear correlation between the shape of the disk SVE and morphological type, and show that galaxies with the same Hubble type display a wide range of vertical-to-radial velocity dispersion ratios. The points are distributed around a mean value and scatter of $\sigma_z/\sigma_R = 0.7 \pm 0.2$. With the aid of numerical simulations, we argue that different mechanisms might influence the shape of the SVE in the same manner and that the same process (e.g. mergers) does not have the same impact in all the galaxies. The complexity of the observational picture is confirmed by these simulations, which suggest that the vertical-to-radial axis ratio of the SVE is not a good indicator of the main source of disk heating. Our analysis of those simulations also indicates that the observed shape of the disk SVE may be affected by several processes simultaneously and that the signatures of some of them (e.g. mergers) fade over time.

2.1 Introduction

Ever since its discovery in the Milky Way, the relation between stellar random motions and age has been a matter of intense study (e.g. Spitzer & Schwarzschild, 1953; Wielen, 1977; Carlberg et al., 1985; Holmberg et al., 2009). There are two main invoked scenarios, explaining why old stars display larger velocity dispersions than young stars. On the one hand, an increasing gas velocity dispersion with redshift has been observed in disk galaxies (Wisnioski et al., 2015). This suggests that old stars, born from this turbulent and dynamically hot gas, would have already high dispersions when they were young. Such cases were shown both in House et al. (2011) and Bird et al. (2013). Some galaxies, in the N-body hydrodynamical simulations sample from the former study, maintained the same dispersions until the end of the simulations. In galaxies with a highly turbulent interstellar medium (from mergers or internal processes), old stars were already dynamically hot at birth. The latter study analyses the Eris cosmological simulation (Guedes et al., 2011) and agrees with an "upside-down" evolution for the Milky Way disk. The oldest stars would have been formed in an early active merger phase and quickly scattered into kinematically hot orbits by these mergers (Bird et al., 2013).

On the other hand, in a disk heating scenario, stars were born in a very thin layer of gas with (dynamically) cold orbits and observed random velocities would have appeared more recently (e.g. Merrifield et al., 2001). This occurs in other galaxies of the simulations sample from House et al. (2011), where disk stars were born dynamically cold and acquired higher dispersions later, thanks to various disk heating mechanisms. A number of candidate sources for dynamical heating have been identified. These include encounters with giant molecular clouds (GMCs), perturbations from irregular and transient spiral structures or from stellar bars, dissolution of young stellar clusters, scattering by dark halo objects or globular clusters, and disturbances by satellite galaxies or mergers (e.g. Gerssen & Shapiro Griffin, 2012).

The shape of the stellar velocity ellipsoid (SVE), defined by the ratios σ_z/σ_R, σ_ϕ/σ_R and σ_z/σ_ϕ, is the result of the balance between agents acting in the different directions (e.g. Merrifield et al., 2001). Therefore, it is the "footprint" of the predominant heating mechanisms. Several authors have used the measurements of the σ_z/σ_R ratio to make predictions about the predominant heating processes in galactic disks (e.g. Gerssen & Shapiro Griffin, 2012). Three-dimensional or isotropic heating agents would lead to a vertical and radial dispersions similar to each other, while radial (or planar) agents would be related to an anisotropic heating and a lower σ_z/σ_R.

Numerous studies, since the discovery of the age-velocity relation in the Milky Way, attributed the increase of the three components of the stellar velocity dispersion with age to encounters with GMCs (e.g. Spitzer & Schwarzschild, 1951, 1953; Lacey, 1984; Kroupa, 2002b; Aumer et al., 2016). However, larger GMCs masses in the past are required to recover the observed kinematics (e.g. Aumer et al., 2016), or other heating mechanisms were also important (Lacey, 1984). Several articles in the literature have already proposed mergers as responsible for enhancing σ_z relative to σ_R (Toth & Ostriker, 1992; Quinn et al., 1993; Sellwood et al., 1998; Benson et al., 2004). They are another stochastic agent and their effect on the disk heating seems to depend on the specific properties of the interaction. Velazquez & White (1999) found a relation of the strength of the heating not only with the disk-satellite mass ratio, but also with the type of orbit of the satellite relative to the disk (prograde or retrograde).

Several N-body simulations (e.g. Grand et al., 2016) and analytical models (e.g. Jenkins

& Binney, 1990; Sellwood & Carlberg, 1984) have indicated that spiral arms and bars are efficient at increasing the velocity dispersion in the planar directions. Spiral density waves were associated with a fast increase of the radial velocity dispersions, due to near-resonant processes (e.g. Merrifield et al., 2001; Minchev & Quillen, 2006). While bar instabilities seemed to increase the vertical velocity dispersion in the disk inner region (Saha et al., 2010; Grand et al., 2016), bar buckling was found to decrease σ_z/σ_R (Saha et al., 2010, 2013).

There are very limited observational works in the literature constraining the shape of the SVE in external galaxies since it is, still nowadays, an arduous task. One of the most successful studies is that of Gerssen & Shapiro Griffin (2012). They fitted the stellar velocity ellipsoids of 8 intermediately-inclined galaxies and studied their shapes as a function of the Hubble type. They found a strong trend with early-type galaxies having more isotropic SVE than later types, suggesting three-dimensional agents are the main contributors to the heating of their disk. On the contrary, in late-type disks, they proposed that their flatter ellipsoids were due to the action of radial agents, most likely the spiral density waves. This trend was in agreement with expectations from some previous studies (e.g. Jenkins & Binney, 1990), but not others (e.g. van der Kruit & de Grijs, 1999). Globally, there is no consensus in the literature about the shape of late-type ellipsoids, in the sense that different results have been found for different galaxies of the same morphological type. Even for our Galaxy, where the properties of individual stars can be measured directly, a wide range of values of the vertical-to-radial velocity dispersion ratio were observed in the solar neighborhood (e.g. Wielen, 1977; Dehnen & Binney, 1998; Casagrande et al., 2011; Aumer & Binney, 2009; Bond et al., 2010; Smith et al., 2012; Binney et al., 2014b; Büdenbender et al., 2015; Aumer et al., 2016). As suggested by Büdenbender et al. (2015), these results might be affected by the tilt of the SVE, implying a coupling between the vertical and the radial velocity dispersion that is not taken into account in most studies.

The aim of this chapter is to revisit the SVE–Hubble type relation and try to reconcile the different results in the literature with the help of state-of-the-art simulations. We present, in § 2.2, observational results for a sample of 55 galaxies gathered from published observational analyses and we describe the methods used to study their ellipsoids. Section 2.3 revises the SVE–Hubble type relation from the observational datasets presented here. In § 2.4 we introduce the set of numerical simulations used in this work. Section 2.5 makes use of the numerical work to elaborate on the sources of disk heating and their effect on the shape of the SVE. We sum up our conclusions in § 2.6.

2.2 Observational Data

In this section, we describe the observed subsamples gathered from the literature. They are organized according to the methods used to calculate the shape of their SVE. Unfortunately, each subsample was analyzed only with one method. So, we do not have the possibility of comparing the different techniques or verifying that they are consistent with each other. Nonetheless, we consider all the methods equally valid since they are all based on reasonable assumptions. We think that the general results of our study are robust to possible biases in individual methods.

2.2.1 The solar neighborhood ellipsoid

Numerous works have been carried out for the SVE of the Milky Way disk in the solar neighborhood, with many of them leading to slightly different results depending on the specific sample. The study from Dehnen & Binney (1998) involved stars in a wide range of populations, although representative only of the local solar neighborhood. They selected a kinematically unbiased sample of 11 865 stars from the *Hipparcos* catalog ESA 1997 (Perryman et al., 1997), which included also young stars. The *Hipparcos* astrometry mission did not provide radial velocities for this big sample. They determined the kinematics from the absolute parallaxes and proper motions provided by this catalog and using the deprojection technique described in Dehnen & Binney (1998). The velocity dispersion tensor was calculated in nine different bins in the $B-V$ color, all with equal number of stars. Their result was confirmed and updated by Aumer & Binney (2009), who used the new reduction of *Hipparcos* data (van Leeuwen, 2007) and a 27 per cent larger sample, with more blue stars. They re-calculated the velocity dispersion ratios as function of color and found a very good agreement also with the results from radial velocities from the Geneva-Copenhagen Survey (Nordström et al., 2004), in the range of red stars.

Some authors have recently extended the study of the stellar velocity ellipsoid of the Milky Way disk to a larger volume of the solar neighborhood. Smith et al. (2012) made use of SDSS Stripe 82 proper motions (Bramich et al., 2008) of 7280 dwarf stars, which they divided into three ranges in metallicity. They fitted the radial and vertical velocity distributions using maximum likelihood methods for different distances $|z|$ from the mid-plane (up to 2 kpc). Other 16 276 stars from SDSS, this time G-dwarfs from *SEGUE* (Yanny et al., 2009), were used by Büdenbender et al. (2015). They constructed Jeans models to fit the orbital properties derived by Liu & van de Ven (2012). They studied the shape of the SVE in the meridional plane, between 0.5 and 3.0 kpc away from the Galactic plane, for different metallicities. Binney et al. (2014b) analyzed the kinematics of $\sim 400\,000$ stars from the RAVE survey (Steinmetz et al., 2006), in a region within ~ 2 kpc of the Sun. Probability density functions in distance modulus were determined by Binney et al. (2014a). Proper motions were drawn from the UCAC4 catalog (Zacharias et al., 2013). Binney et al. (2014b) mapped σ_z/σ_R for different distances from the Galaxy plane.

In this context, light-weighted SVE measurements in external galaxies might be dominated by the young and more metal-rich thin disk. Nevertheless, the light is still integrated over the line of sight so that the thick disk has probably an important contribution (Yoachim & Dalcanton (2006) estimated the thick disk contribution to be between 10% and 40% of the total luminosity of the galaxy, depending on its mass). Since we do not have any fair criterion to weight the different populations, we have decided to adopt, for the shape of the Milky Way disk ellipsoid, an average of the results of all the mentioned studies.

2.2.2 Velocity dispersions of edge-on galaxies: surface photometry

For edge-on galaxies, it is not possible to measure directly (with spectroscopy) the vertical component of the velocity dispersion. van der Kruit & de Grijs (1999) proposed a method for its indirect estimate from surface photometry. They showed how to calculate the radial and vertical stellar velocity dispersions, with simple equations, knowing the radial scale length and the scale height of the disk. The following assumptions were necessary: exponential disk surface brightness radial profile, self-gravitating stellar disk (which can be approximated by an isothermal sheet), constant mass-to-light ratio (M/L) and flat rotation curves. They applied

their model to 40 edge-on late-type galaxies, most of them selected from the sample of de Grijs (1998), (e.g. inclination $i \geq 87°$, angular blue diameters $D_{25} \geq 2.2$ arcmin, non-interacting, and discarding S0 and Sa because the assumptions needed in this method were not valid, in particular the self-gravitating disk). The surface photometry and the structural parameters were already available, as well as HI observations which were used to estimate the gas-to-total disk mass.

They used the relations between the radial velocity dispersion, the radial scale length, the vertical dispersion and the scale height as explained in van der Kruit & de Grijs (1999). The radial component of the velocity dispersion tensor (σ_R) was measured, at one photometric scale length in the $B-$band, using the empirical relations of Bottema (1993). The vertical component (σ_z), was computed (also at one scale length) assuming a Toomre parameter of $Q \approx 2$ (Toomre, 1964). While they published the results by combining the individual measurements by morphological type, they kindly gave us access to values for 31 galaxies in the de Grijs (1998) sample.

2.2.3 σ_{LOS} decomposition from spectroscopic data

After the Milky Way, the first object with a measurement of the vertical-to-radial velocity dispersion ratio was the Sb galaxy NGC 488 (Gerssen et al., 1997). They presented a new way of extracting the three components of the velocity ellipsoid, from long-slit spectroscopic observations of the line-of-sight velocity dispersion (σ_{LOS}) along the major and minor axes in intermediate-inclined disks. It used the epicycle approximation to relate σ_ϕ with σ_R and the asymmetric drift equation to connect the circular velocity (described by a power-law) to the stellar rotation curve. Exponential radial profiles, with the same scale length, were assumed for both the radial and the vertical velocity dispersions. This implied that σ_z/σ_R was assumed constant with radius in the disk-dominated region. The model had five free parameters which were fitted simultaneously to the major and the minor axes data. Since it was designed for the disk, it was applied only to the disk-dominated regions.

Later, Gerssen et al. (2000) used the same procedure to study the SVE of the Sab NGC 2985 (see also Noordermeer et al. 2008). The circular velocity, obtained from emission-line measurements in the gas disk, was included in the procedure. Shapiro et al. (2003) added four more galaxies and improved the previous results by Gerssen et al. (1997, 2000) for NGC 488 and NGC 2985. Their study of the SVE along the Hubble sequence was completed with two later-type galaxies (NGC 2280 and NGC 3810) in Gerssen & Shapiro Griffin (2012). The same methodology was also applied by several authors to long-slit and integral-field observations (see e.g. Westfall et al., 2005, 2011; Gentile et al., 2015).

2.2.4 Dynamical models: Schwarzschild, three integral and Jeans methods

Two-integral and three-integral models were used by Emsellem et al. (1999) to fit the photometry and kinematics of the S0 NGC 3115. Given that this galaxy has a double disk structure (e.g. Emsellem et al., 1999), for the outer Freeman type II disk they constructed a three-integral model and recovered the σ_z/σ_R ratio in the meridional plane. In this work, we use the mean value from ~ 12 kpc, where the outer disk starts to dominate the surface brightness.

Cappellari et al. (2006) built dynamical models, based on the Schwarzschild (1979) numerical orbit-superposition method, for 24 elliptical and lenticular galaxies part of the SAURON sample (de Zeeuw et al., 2002). This subsample was selected because it had accurate distance

determination, availability of *HST* photometry, and did not present strong evidence of bars. The global anisotropy in the meridional plane (parametrized as in Eq. 1.10) was determined in Cappellari et al. (2007). From the set of 24 galaxies, we include 8 lenticular galaxies in this work. The values of β were calculated within one effective (half-light) radius, including not only the disk but also the central region of the galaxies. Following Gerssen & Shapiro Griffin (2012), we decided to include those results in our compilation, as the SAURON measurements should be biased towards the equatorial plane and also disk regions (given the extent of the aperture used).

Tempel & Tenjes (2006) produced a model, based on Jeans equations, of the Sombrero galaxy (M 104, NGC 4594). They used the averaged major-axis kinematics from previous literature works (Kormendy, 1982; Carter & Jenkins, 1993; Hes & Peletier, 1993; van der Marel et al., 1994; Emsellem et al., 1996; Kormendy et al., 1996) and they determined the σ_z and σ_R radial profiles, as well as the orientation of the stellar velocity ellipsoid. In this work we adopt the mean value of σ_z/σ_R in the disk-dominated range, between 2 and 10 kpc approximately. In a recent work, Kipper et al. (2016) studied the SVE of our neighbor galaxy M 31. It is a well known galaxy and its major axis kinematics had been measured several times (McElroy, 1983; Kormendy, 1988; van der Marel et al., 1994; Kormendy & Bender, 1999). The mass distribution was taken from Tamm et al. (2012), who used a three-component model with a stellar bulge, a stellar disk and a dark matter halo. Jeans equations were used by Kipper et al. (2016) with an approach similar to Tempel & Tenjes (2006). The ellipsoid axis ratios were plotted in two different radial profiles for the bulge and the disk. We consider the mean value of σ_z/σ_R in the disk for the purpose of this work.

2.3 The observed SVE - Hubble type relation

As mentioned in § 2.1 and § 2.2, several works in the literature (e.g. Dehnen & Binney, 1998; Merrifield et al., 2001; Gerssen & Shapiro Griffin, 2012; Aumer & Binney, 2009; Aumer et al., 2016) have suggested that the shape of the stellar velocity ellipsoid can be used to unveil different heating mechanisms. In addition, if the sources of disk heating were different for early and late-type galaxies, their SVE should have different shapes and show a trend along the Hubble sequence. We revisit these claims here by analyzing all the observational results we could find in the literature on this issue. We present all these values of σ_z/σ_R in Table A.1.

Figure 2.1 shows all the literature σ_z/σ_R values as a function of morphological type. Data points have been divided and represented with different colors and symbols according to the method used, as described in § 2.2. The first thing to notice is that no clear correlation is found, opposed to the strong trend found by Gerssen & Shapiro Griffin (2012). A linear regression to all the points[1] (weighting by their uncertainties) yields a slope of -0.03 ± 0.02, with a coefficient of determination (R^2, defined as the square of the correlation coefficient) of 0.15. This indicates a very poor correlation between the axis ratio of the SVE and the morphological type. Gerssen & Shapiro Griffin (2012) sample gives a slope of -0.11 ± 0.02 with an R^2 of 0.86.

The lack of a strong correlation is apparent in several individual datasets. The van der Kruit & de Grijs (1999) sample is the largest and does not show any trend for their 31 galaxies, mostly very late types. One could argue that the (photometry based) technique employed is the cause

[1] Upper-limit values, as indicated in Table A.1 and Figure 2.1, have not been taken into account.

for such discrepancy. Nonetheless, it uses approximations similar or common to other methods (e.g. exponential disk and isothermal sheet). Furthermore, the kinematics of 15 galaxies (11 in common with van der Kruit & de Grijs 1999) was modeled, now using spectroscopy (Kregel et al., 2004), by Kregel & van der Kruit (2005). Their vertical-to-radial velocity dispersion ratios, plotted in Fig. 6(a) of Kregel et al. (2005), range between ~ 0.5 and ~ 0.9 for Hubble types between Sb and Scd[2]. Therefore, spectroscopic and photometric samples are compatible with each other and both point towards a picture where late types can have nearly isotropic SVE.

Westfall et al. (2005) and Gentile et al. (2015) data points were computed using the same methodology as Gerssen & Shapiro Griffin (2012), and yet they present very different values at a given morphological type. Two of these late-type galaxies display rather prolate ellipsoids (with $\sigma_z/\sigma_R > 1$) suggesting that vertical agents must have been predominant. In their work, Gentile et al. (2015) excluded important recent mergers as responsible for this heating, due to the regular morphology and kinematics. While these prolate ellipsoids may seem odd, there are several examples in our compilation, all of them coming from different sources and methodologies (see Table A.1). They might be related to a real phenomenon that we cannot explain yet, or be unreal and due to a general failure, common to the different methods, in reproducing the disk physics. Even Gerssen & Shapiro Griffin (2012) found a slightly vertically elongated ellipsoid for NGC2775, but considered the value of σ_z/σ_R an upper limit. The two galaxies from Westfall et al. (2005) come from an unrefereed publication and hence they are indicated with different symbols (diamonds) in Fig. 2.1. We decided to include them because they were obtained using the same σ_{LOS} method as others and they are in agreement with others.

For the Milky Way we indicate in Table A.2 the individual results for σ_z/σ_R, from the different studies mentioned in § 2.2.1. They have been averaged over the different regions and ranges indicated in the third and the last columns of the Table, weighting with the number of stars in each bin or group when this was available. Errors have been estimated as the (weighted) standard deviations of the samples. Dehnen & Binney (1998) believed that their value for the local solar neighborhood was the result of the contributions of both spiral structure and scattering by molecular clouds to the disk heating. For reference, Aumer & Binney (2009) found σ_z/σ_R from ~ 0.33 for the bluest to ~ 0.6 for the reddest stars in the *Hipparcos* catalog. For the extended solar neighborhood, an increase in the kinematic isotropy for lower metallicities and larger distances z from the Galactic plane was generally found. Binney et al. (2014b) gave 0.6 as approximation for σ_z/σ_R of giant and cool dwarf stars in the sample. For hot dwarfs, we have adopted the value given for the plane (~ 0.48) since the velocity dispersions increased slowly with distance from the plane.

The range of values in Table A.2 shows the lack of universal agreement on the global value of σ_z/σ_R in the solar neighborhood. Different SVE shapes can be found even in the same galaxy, depending on the analyzed populations. Results are sensitive to differences in color, metallicity, distance from the mid-plane and type of stars. We averaged the different results in Table A.2, weighting with the number of stars (in the second column of Table A.2), to find the value indicated in Table A.1 for the Milky Way. The uncertainty has been estimated as the weighted standard deviation of the ensemble of samples. This value is represented with a purple star in Fig. 2.1, where the purple shade shows the range of σ_z/σ_R where the results in Table A.2 lie.

[2] They could not provide us the individual values of the plotted points nor the Hubble types they corresponded to. For this reason we have not been able to include them in Table A.1 and Figure 2.1.

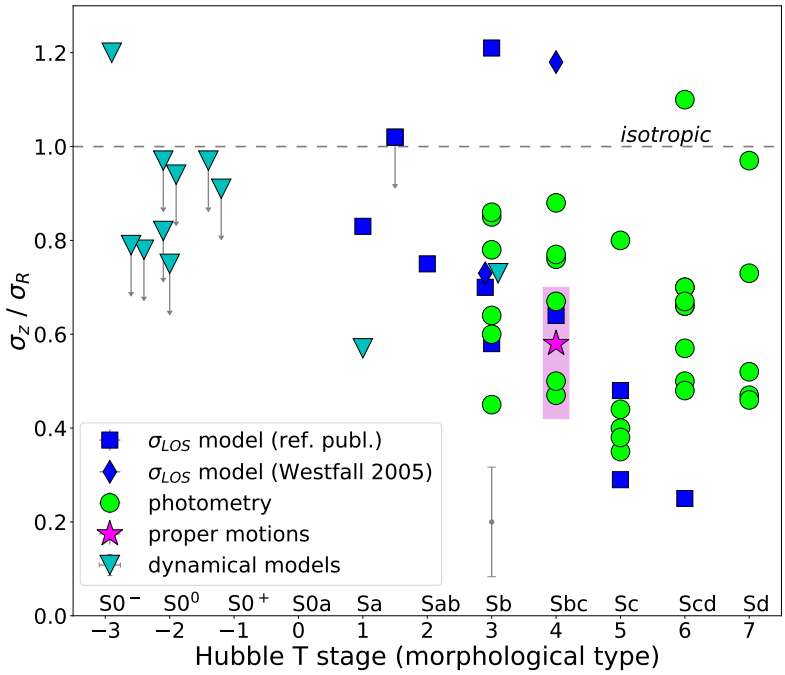

FIGURE 2.1— The flattening of the disk SVE, indicated by its axis ratio σ_z/σ_R, as function of Hubble types from observations of 55 galaxies. Different symbols and colors are used for different techniques and methods (see § 2.2 for details). *Dark blue points* were computed from σ_{LOS} models (squares for Westfall et al. 2011; Gerssen & Shapiro Griffin 2012; Gentile et al. 2015 and diamonds for Westfall et al. 2005, see § 2.2 for more details). In *green (circles)* results from surface photometry by van der Kruit & de Grijs (1999). In *purple* the Milky Way in the solar neighborhood: the *shade* shows the range where all the results mentioned in § 2.2 and § 2.3 lie, while the *star* indicates their average value. Finally, dynamical models (*light blue triangles*) include Schwarzschild (Cappellari et al., 2007), three integral (Emsellem et al., 1999) and Jeans models (Tempel & Tenjes, 2006; Kipper et al., 2016). Vertical arrows indicate upper limits. A mean error bar is indicated on the right of the legend. See Table A.1 for more details. An horizontal line indicates the shape of the SVE when this is exactly isotropic ($\sigma_z = \sigma_R$).

Kipper et al. (2016) plotted the radial and vertical profiles of σ_R, separately for the bulge and for the disk of M 31, showing that the bulge has radial velocity dispersions far larger than the disk. They also determined the orientation and axial ratios of the velocity ellipsoids of the two structural components along a meridional plane of the galaxy. While the ellipsoid stays almost spherical throughout the bulge component, the disk ellipsoid is nearly isotropic only near the rotation axis, and flattens out towards the most external radii.

For completeness, we also show the SVE values for the early-type galaxies in the SAURON survey (Cappellari et al., 2007). They have nearly isotropic ellipsoids, which is expected as they are the average within one effective radius (R_e), and thus include the bulge component. They should be considered as upper limits to the real σ_z/σ_R of their disks.

The main conclusion one can draw from Fig. 2.1 is that the relation between the shape of the SVE (using the σ_z/σ_R ratio) and Hubble type is much weaker than previously reported. The earliest-type disk galaxies do not have necessarily isotropic ellipsoids and the latest types show a wide range of values. Therefore there must be different factors affecting the shape of the SVE of galaxies of the same morphological type. At the same time, different Hubble types can have the same ellipsoid shape. It is thus logical to wonder whether they are affected by the same heating mechanism or if different mechanisms can lead to the same σ_z/σ_R ratios. However, since the region of late-type galaxies (in Fig. 2.1) is completely dominated by the results from van der Kruit & de Grijs (1999), who used photometry, more results from spectroscopic observations would be necessary to confirm this picture.

2.4 Numerical simulations

We describe here the two sets of numerical simulations used in this work. We use them to extract information of the SVE shape for comparison with the observational data and to explore the impact of different mechanisms.

2.4.1 Disk galaxies from zoom-in cosmological simulations

We determine the SVE information from the stellar kinematics of 26 simulated Milky-Way-mass spiral galaxies by Martig et al. (2012), created with the purpose of studying galaxy evolution in a cosmological context. Martig et al. (2012) used a method that consisted in coupling cosmological with galactic scale simulations at much higher resolution. The technique is based on two steps: extracting the merger and gas accretion histories (and geometry) of dark matter halos in a large-scale Λ-CDM cosmological simulation, and then re-simulating these histories at very high resolution, replacing each halo by a realistic galaxy.

The cosmological simulation was performed with the Adaptive Mesh Refinement code RAMSES (Teyssier, 2002). The simulation box had a comoving length of 20 h^{-1} Mpc and contained 512^3 dark matter particles of $6.9 \times 10^6\,\mathrm{M}_\odot$ each. The cosmological constants in the Λ-CDM were set as follows: $\Omega_m = 0.3$, $\Omega_\Lambda = 0.7$, $H_0 = 70$ km s^{-1} Mpc^{-1} and $\sigma_8 = 0.9$. The merger and diffuse accretion histories of a halo were extracted by tracking halos and diffuse particles (not gravitationally bound with any halo). The position, velocity and spin of each incoming satellite were recorded as well as the date of the interaction.

Each halo of the cosmological simulation (i.e. the main halo as well as all the interacting satellites) was then replaced with a realistic galaxy, made up of gas, stars and dark matter

particles. The diffuse particles were replaced by a blob of gas and dark matter particles of lower mass and higher resolution. The total mass of the galaxy was divided in 20% of baryons and 80% of dark matter (the mass of dark matter being given by the cosmological simulation). The new simulation followed the evolution of the main galaxy from redshift $z = 5$, included an area of 800 kpc, to $z = 0$. The re-simulation was done by means of the Particle-Mesh code described in Bournaud & Combes (2002), with a spatial resolution of 150 pc, a time step of 1.5 Myr and a particle mass of $1.5 \times 10^4\,M_\odot$ for gas, $7.5 \times 10^4\,M_\odot$ for stars and $3 \times 10^5\,M_\odot$ for dark matter. A sticky-particle model was used for gas dynamics, and a Schmidt-Kennicutt law (Kennicutt, 1998) for star formation, while supernovae feedback was introduced in the form of kinetic energy. In each galaxy substituting the dark matter halo from cosmological simulation, particles were already distributed in the morphological components. The disk, made of gas and star particles, was modeled with a Toomre profile (Toomre, 1963), while the bulge, made of stars, as a Plummer sphere (Plummer, 1911). A Burkert profile (Burkert, 1995) was used for the dark matter halo.

Finally, the targeted galaxies were chosen to have a $z = 0$ halo mass between 2.7×10^{11} and $2 \times 10^{12}\,M_\odot$ and to be relatively isolated. They were distributed all across the cosmological simulation box, but avoiding the densest regions. They had different evolution histories, but most of them underwent mergers at some stage of their life-time. They have a wide range of bulge-to-total (B/T) ratios and morphological types.

2.4.2 Idealized *N*-body simulations

In order to enrich our simulation sample with extremely late types and establish the influence of purely secular evolution processes in galaxies in total isolation, we also added to our study a small sample from idealized N-body simulations by Martinez-Valpuesta et al. (2006, 2017). They used the FTM-4.4 version of the N-body code from Heller & Shlosman (1994) and Heller (1995). The initial density distribution was derived from the disk-halo analytical model of Fall & Efstathiou (1980). The disk was created exponential, with an initial scale length of 1.36 kpc and a Toomre parameter fixed at 1.5. Regarding the velocity dispersion calculations, the initial σ_R was set from the Toomre parameter and the surface brightness profile. The initial σ_z/σ_R ratio was fixed to 0.6, a value commonly adopted in the literature (e.g. van der Kruit & Freeman, 1984; Bershady et al., 2011), to define the initial σ_z.

We considered here a sample of six simulated galaxies. Four of them, identified by labels from I0 to I3, were allowed to evolve in isolation during the full simulation lifetime (14 Gyr). All of them are bulgeless and were made with a disk and a dark matter halo, each one with 5×10^5 particles at the beginning of the simulation. They differ from each other in the mass and dark matter fraction. The total mass decreases from I0 to I3, in a range between $3.9 \times 10^{10}\,M_\odot$ (I3) and $2.0 \times 10^{11}\,M_\odot$ (I0). I0 contains 80% of dark matter of the total mass budget within a sphere of radius 5 kpc, while I1 contains 57%. The I2 and I3 simulations have 38% and 7% of dark matter fraction within 5 kpc, respectively.

These simulations were created with the purpose of studying the mechanisms triggering the formation of bars, both in isolation and induced by interactions. For this reason, the two simulations I0 and I1 were redone but now with a galaxy fly-by and then left in isolation for ~ 5 Gyr. The interaction was modeled with the impulse approximation (see Martinez-Valpuesta et al., 2017). This means assuming that the energy exchanged during the interaction had been injected as kinetic energy to the host galaxy, whose reorganization within its potential happened

after the fly-by had finished. The tidal approximation (Binney & Tremaine, 1987) was also used. The perturber galaxy was assumed to have the same mass and size of the host and to orbit hyperbolically in the disk plane of the host.

2.4.3 Adequacy of numerical simulations

The balance between the three-dimensional and the radial heating, the birth of new cooler young stars and how hot the older stars were born, determines the evolution of the stellar velocity ellipsoid shape. We have assessed these factors in our simulations, in order to assure ourselves that the results were adequately modeled. While other authors opted for only GMCs as vertical heating source (e.g. Aumer et al., 2016), in our zoom-in cosmological simulations we have instead a large variety of mergers, of different mass ratios and occurring in different planes and at different times.

As non-axisymmetric heating sources, bars in our idealized N-body simulations match very well to real galaxies. Although not made for this purpose, Martinez-Valpuesta & Gerhard (2011, 2013) and Gerhard & Martinez-Valpuesta (2012) showed how one of these simulated galaxies (here called I1) reproduces the Milky Way bar and the corresponding boxy-bulge vertical metallicity gradient. These simulations have been also compared to nearby galaxies, by different authors. Seidel et al. (2015, 2016) quantified the influence of bars on stellar kinematics and populations. Molaeinezhad et al. (2016, 2017) studied bulge properties and cylindrical rotation in barred galaxies. Font et al. (2017) analyzed bar rotation and evolution. All of them found a good agreement between these simulations and observed galaxies. Kraljic et al. (2012) studied bar formation and evolution in our zoom-in cosmological simulations, as well as the bar fraction in spiral galaxies, performing an analysis whose results were totally compatible with properties of real bars (e.g. length and strength).

A study on the effect of bars on the disk SVE shape was carried out by Martinez-Valpuesta et al. (2006), based on a disk simulation similar to our idealized N-body simulations sample. In Fig. 6 of their paper, the disk is affected very locally by the early evolution of the bar. A first bar growth just after its formation flattens the SVE by increasing σ_R. Then isotropy is rapidly reached thanks to the buckling (what they call "first buckling"). In our study, we take into account only the disk-dominated region, in order to perform an analysis as similar as possible to observational works. Therefore, these early effects on the inner disk do not leave any signature on our final SVE. Nevertheless, according to Martinez-Valpuesta et al. (2006), the later bar evolution does affect the kinematics of the outer disk. The final result comes from a trade-off between a potential secondary buckling, heating vertically, and the bar secular growth, heating radially. In our full simulations sample, no considerable effect of the buckling has been detected in the disk SVE, while an increase in σ_R can be easily related to the secular growth of the bar.

Spiral arms, another non-axisymmetric feature affecting the SVE, have not been studied in our simulations yet. The measurement of their strength, or any other further analysis to quantify their impact on the disk heating, is beyond the scope of this work. However, similar dynamical processes dominate the formation of both bar and spiral arms. For this reason we expect spiral arms to be as realistic as bars in both zoom-in cosmological and idealized N-body simulations. Disk kinematics in our simulations are comparable to observations of real galaxies (as shown in Fig. 2.5 to 2.9 for zoom-in cosmological simulations). This points towards a good modeling of the disk heating. Martig et al. (2014b) compared the age-velocity relation (AVR) of some of

their simulations with observations for the solar neighborhood, finding a very good match.

The birth of new stars can counteract the heating by other sources, and affect σ_z/σ_R if their ellipsoid shape is considerably different from the pre-existing populations. If the star-forming gas has cooled down and no new process has heated it, recently born stars are expected to be dynamically cooler than the ones born in the past. We have checked that new stars are born with lower velocity dispersions in the three directions, in our zoom-in cosmological simulations (see § 2.5.3 for more details). In addition, Leaman et al. (2017) have recently compared (in Fig. 7 of their paper) the AVR in the Milky Way to one simulated galaxy from Martig et al. (2014b). The latter not only matched the AVR in the solar neighborhood, but the velocity dispersion of its stars at birth, at different time steps, also matched the one of open clusters of different ages in the Milky Way disk.

However, very young stars in these simulations seem to be still too dynamically hot in their very first Myr of life, due mainly to the limited resolution and the gas density threshold for star formation, according to Martig et al. (2014b). Some tests confirmed that an increase in resolution or in the star formation threshold does not affect the shape of the AVR. After the first 500 Myr, stars recover velocity dispersions similar to the Milky Way. In addition, a different balance between the vertical and radial velocity dispersions, in recently born stars with respect to the rest of the galaxy, would be necessary to change the global σ_z/σ_R. For this reason, resolution and star formation recipe might not affect the shape of the SVE drastically. Very young stars are expected to have almost circular orbits and fulfill the epicycle approximation, with a typical azimuthal-to-radial velocity dispersion ratio around 0.7 (Binney & Tremaine, 1987). This is true in these simulations and indicates that our modeling of the disk dynamics is reasonable.

In our idealized N-body simulations, we do not have either mergers nor star formation. The purpose of including these simulations was to reproduce the behavior of simple disks that are left to evolve by themselves. The only agents capable of modifying the shape of the SVE are the ones related to secular evolution, giving reasonable values of σ_z/σ_R similar to zoom-in cosmological simulations and observations.

2.5 Insights from numerical simulations

We now turn our attention to the predictions from the numerical simulations to get a better insight into the mechanisms underlying the SVE of spiral galaxies.

2.5.1 The simulated SVE - Hubble type relation

We present in Fig. 2.2 the vertical-to-radial velocity dispersion ratio as a function of the Hubble type for all the simulated galaxies. For zoom-in cosmological simulations, we assigned them a morphological type visually, by comparison with the observational sample classification. For all idealized N-body simulations, given that they are bulgeless galaxies, we approximated their Hubble type to Sd, i.e. the latest type.

The individual numerical values in Fig. 2.2 are shown in Tables A.3 and A.4. They are the medians computed within the disk-dominated region of the radial profiles, at the last time step of the simulations. The errors were computed as $\pm 1\sigma$ of the (radial) distribution. The disk radial range was defined as the one where the surface brightness profile could be fitted with an exponential. Thus, bulge and bar regions were excluded similarly to most observational results.

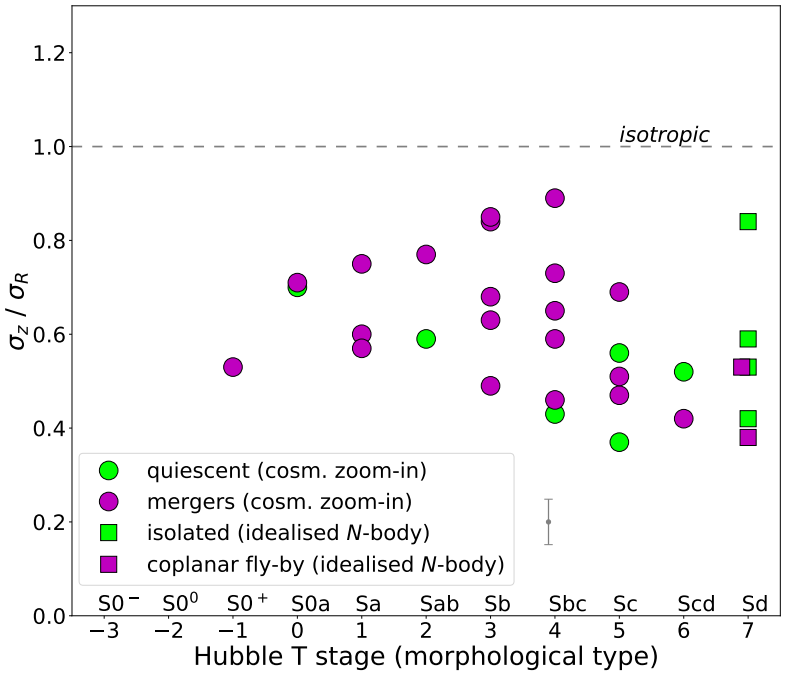

FIGURE 2.2— The flattening of the disk SVE, indicated by the ratio σ_z/σ_R, as function of Hubble types from simulations of 32 galaxies. The points have been divided with different colors and symbols. *Light green circles* for quiescent (or merger with a mass ratio lower than 1:20) and *purple circles* for interacting galaxies in zoom-in cosmological simulations (up to 1:3 mass ratio mergers). This first classification was based on the galaxy evolution after its first 5 Gyr of life. *Purple squares* for idealized N-body simulations with fly-by interactions (see § 2.4 for details). *Green squares* come from idealized N-body simulations that have evolved in complete isolation. The uppermost green square is a particular case in this sample (see § 2.4 and 2.5 for details). A mean error bar is indicated on the right of the legend. The individual errors were computed as $\pm 1\sigma$ of the disk radial distribution. See Tables A.3 and A.4 for more details. An horizontal line indicates the shape of the SVE when this is exactly isotropic ($\sigma_z = \sigma_R$).

The mean radial profiles for the individual dispersions were calculated by radially binning the star particles located at different azimuths. In this way, the effect of azimuthal variations was attenuated. However, we analyzed these variations and verified that they were in general of the order of 5 - 10%, although larger in the outer disk of some galaxies with pronounced spiral structure.

Figure 2.2 shows that no major trend is found with Hubble type. In these simulations, we have the possibility of looking for correlations between events or processes undergone by the galaxy and the shape of the SVE. For this reason, we have color-coded quiescent and non-quiescent galaxies, for both types of simulations. In zoom-in cosmological simulations none of the galaxies has evolved in total isolation. The galaxies plotted with light green circles are relatively quiescent, in the sense that they have not had mergers larger than 1:20 in mass of the satellite versus host galaxy, after the first 5 Gyr of its lifetime (when we already had a stable disk).

No strong trend is seen globally for any given evolutionary path, although the light green circles suggest that quiescent galaxies SVE tend to be more isotropic for earlier types. A linear regression to these six points gives a slope of -0.04 ± 0.03 with an R^2 of 0.52, but more points would be needed to confirm this mild trend. Moreover, note that this relation is not observed in isolated galaxies in idealized N-body simulations (green squares). Like in observations, the lowest values of σ_z/σ_R correspond to late-type spirals, which however show values in a wide axis ratio range. Quiescent and non-quiescent galaxies can have exactly the same ellipsoid shape. This is in agreement with the study by Martig et al. (2012) on the same set of zoom-in cosmological simulations. For disk-dominated galaxies, they found a correlation of the bulge-to-total light fraction not only with the merger history at $z < 1$, but also with the gas accretion at $z > 1$. More prominent bulges correspond to more active merger and/or gas accretion histories. Curiously, some of the bulges with the highest Sérsic indexes were formed in absence of strong merger activity but with an early intense gas accretion together with an early bar formation or other disk instabilities. This suggests that there are different possible pathways to form a bulge, as Bell et al. (2017) confirmed observationally. In their sample, small pseudobulges were consistent with a quiet merger history and pointed to other formation mechanisms like gas accretion, disk instabilities or secular evolution. Some massive classical bulges were compatible with a merger origin, but others needed to invoke alternative mechanisms. Therefore, no strong trend is expected between merger activity and morphological types, either.

While in observations, including early-type disk galaxies, the distribution of σ_z/σ_R has a slightly higher mean value of 0.7 ± 0.2, these simulations suggest that the vast majority of spiral galaxies have a vertical-to-radial axis ratio around 0.6 ± 0.2. This would partly justify the common adoption of similar values in the literature (e.g. van der Kruit & Freeman, 1984; Kregel et al., 2005; Bershady et al., 2011; Martinsson et al., 2013). It is important to remember that idealized N-body simulations had this 0.6 as an initial condition, perhaps affecting somewhat the resulting ratios to be around this value, though with large scatter. On the contrary, no similar initial condition was set in zoom-in cosmological simulations. This simple result indicates that the vertical-to-radial axis ratio of the velocity ellipsoid appears to be a poor predictor of the dominant mechanism driving its shape. This finding is in agreement with the observational results presented in § 2.3, and highlights the complexity of interpreting the σ_z/σ_R ratio.

Also in idealized N-body simulations, disks evolved in total isolation have σ_z/σ_R ratios extending in a wide range of values. We have not found a direct correlation of the values with

the dark matter fraction. A particular case is the isolated galaxy I0_no_bar (see Table A.4) which, with an 80% of dark matter in the central 5 kpc, did not have the conditions to form any bar (Martinez-Valpuesta et al., 2017). The cool disk of this galaxy, with low absolute values of the individual velocity dispersion components, has one of the most isotropic SVE in the full simulations sample. Nonetheless, if this same disk undergoes a fly-by in the galaxy plane (with 1:1 mass ratio), this triggers the bar formation, causes a disturbance in the same plane which enhances σ_R, and flattens the ellipsoid (i.e. I0_inter in Table A.4). The same happens to the galaxy I1, where σ_z/σ_R jumps down after the same interaction (I1_inter).

2.5.2 Disentangling different processes from the SVE shape

Here we study in more detail the impact of some disk heating agents on the final shape of the SVE. This is shown in Fig. 2.3 and 2.4, where the top panel shows the average axis ratios at the end stage of zoom-in cosmological simulations. The bottom panel presents the average of the square individual components, normalized by the square total dispersion defined as: $\sigma^2 = \sigma_R^2 + \sigma_\phi^2 + \sigma_z^2$. In this way, it becomes clearer what is the most prominent axis of the SVE and helps us to remove any potential dependence on the galaxy mass. Our zoom-in cosmological simulations allow us to specifically study the effect of mergers and also the action of bars. The effect of spiral arms is more complex to isolate, but will be discussed to some extent in the next section.

We focus first on the effect of mergers on the shape of the SVE (Fig. 2.3). We divided the zoom-in cosmological simulations into three groups according to their evolution after the first 5 Gyr of life, a time when in general the disk appearance starts to be similar to the final one. The first group (in blue) is made of relatively quiescent galaxies, with no mergers with mass ratios larger than 1:20 (i.e. light green points in Fig. 2.2). The second group (in green) includes galaxies with "low-mass" mergers (i.e. 1:20 to 1:10 mass ratios). Finally, the third group is plotted in red and corresponds to the strongest mergers, with mass ratios larger than 1:10 (up to 1:3). The distributions of the second and third groups are not substantially different in Fig. 2.2, hence we plot them together in purple - only their average values are somewhat different from one another, as shown in Fig. 2.3.

We see in both panels that, on average, stellar velocity ellipsoids are more isotropic (i.e. axis ratios closer to 1 and individual components similar in amplitude to each other) when high-mass ratio mergers have taken place (red triangles). For σ_z/σ_R in particular, high-mass mergers have a ratio $\sim 8\%$ larger than low-mass mergers. For the same axis ratio, a substantial difference is observed between galaxies with mergers and more quiescent galaxies. For the latter, σ_z/σ_R is $\sim 14\%$ lower than for galaxies affected by 1:20-to-1:10-mass-ratio mergers. The bottom panel shows that the (normalized) vertical component (σ_z/σ) is larger when high-mass-ratio encounters have occurred, and lower for more quiescent systems, where the radial component (σ_R) is more prominent (perhaps highlighting the prevalence of spiral arms or bars). Low-mass mergers can increase the contribution of σ_z to the total dispersion, being an intermediate case with respect to the high-mass mergers and quiescent galaxies. However, the contribution of σ_R in these galaxies is similar to the quiescent group.

To complete our analysis, we assess the influence of bars in Fig. 2.4. Galaxies have been classified into two groups according to the bar-to-total light ratio, based on the photometric decomposition. Components with bar-to-total ratio above 10% are considered strong bars and

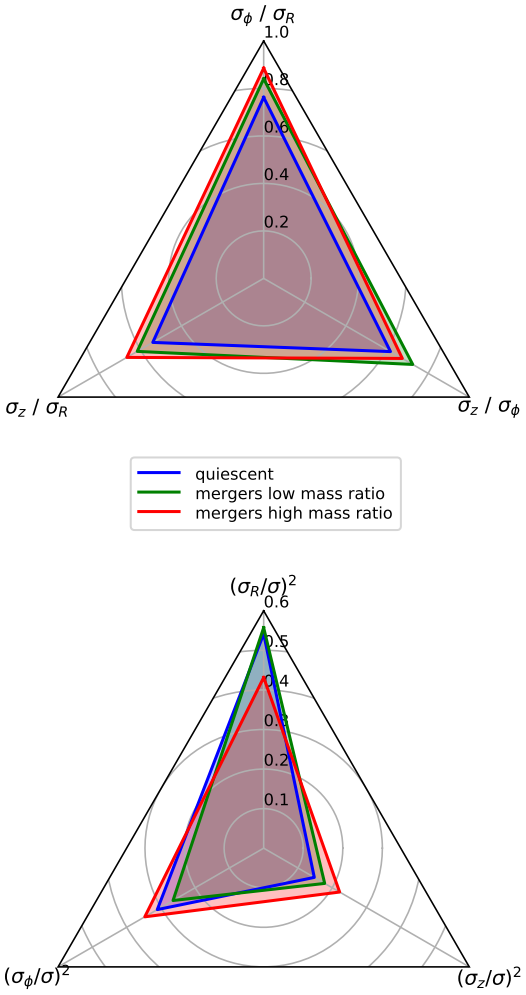

FIGURE 2.3— Radar plots of the average three axis ratios of the SVE (top) and normalized square velocity dispersions (bottom), for the zoom-in cosmological simulations sample, divided into three different groups according to their evolution after the first 5 Gyr of life: 6 relatively quiescent galaxies, in *blue* (no mergers with mass ratio higher than 1:20), 6 galaxies with "low-mass" mergers (i.e. 1:20 to 1:10) in *green*, and 14 galaxies with "high-mass" mergers (i.e. 1:10 to 1:3) in *red*. σ is the three-dimensional composition of the velocity dispersions defined as $\sigma^2 = \sigma_R^2 + \sigma_\phi^2 + \sigma_z^2$.

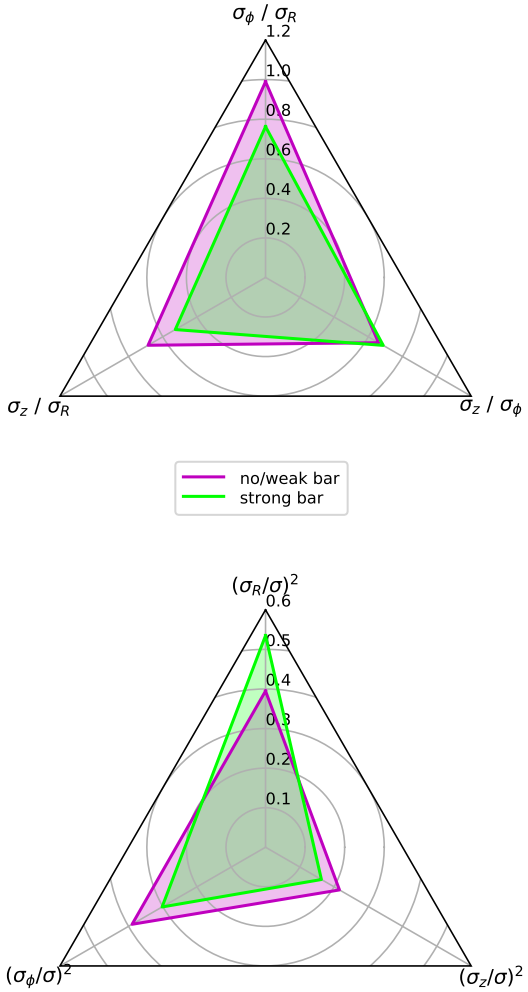

FIGURE 2.4— Radar plots of the average three axis ratios of the SVE (top) and normalized square velocity dispersions (bottom), for the zoom-in cosmological simulations sample, divided into barred and unbarred galaxies. 16 of them have a bar-to-total light ratio above 10% (*strong bars*) and 10 are below 6%, having *no or weak bars*. σ is the three-dimensional composition of the velocity dispersions defined as $\sigma^2 = \sigma_R^2 + \sigma_\phi^2 + \sigma_z^2$.

weak or no bars for values below 6%. The figure suggests that bars (on average) are related to an enhancement of the radial component of the velocity dispersion. Consequently, galaxies with bars tend to have flatter ellipsoids (with σ_z/σ_R and σ_ϕ/σ_R ratios smaller than in unbarred galaxies). The idealized N-body simulations sample, with the only unbarred galaxy with a remarkably higher σ_z/σ_R, is also in agreement with this trend.

While simulations allow us to see somewhat more clearly the effects of distinct mechanisms on the shape of the SVE, this is more difficult to capture in observations as differences are often subtle. In addition, different agents could have acted simultaneously in real galaxies. The high scatter of the points even in groups with similar mergers history (presented in Fig. 2.2) emphasizes this issue. Also, fly-by encounters can be important in enhancing one or another component of the velocity dispersion, as we have seen in idealized N-body simulations. It is therefore likely that the particular dominance of one mechanism over others depends on the specific situations, which makes the shape of the SVE a not so obvious diagnostic to unveil the main mechanism influencing the dynamical heating of disks.

2.5.3 Time evolution of the SVE shape

Another interesting aspect to analyze in our simulations is the evolution of the shape of the SVE with time. This gives us information about how long a particular disk heating mechanism (e.g. mergers) influences the SVE shape. In Fig. 2.5 to 2.9 we plot the changes of the individual components and axis ratios of the SVE as a function of time, for five galaxies representative of the variety of cases. Of each group in Fig. 2.2, we show one of the most and one of the least isotropic SVEs. Finally, we added one more quiescent galaxy as an example of continuously changing σ_z/σ_R. The shaded areas mark the 16% and 84% percentiles of the values calculated over the disk radial profiles. They are, at each specific time, the mean value in the radial profile and its $1\,\sigma$ error bar. The radial profiles are the mean of all the star particles. Therefore these plots include, at a specific time, disk stars of all the previously born populations. In addition, we plot snapshots of the face-on and edge-on views of the simulated galaxies in order to determine the potential link between the shape of the SVE and galaxy morphology.

Mergers happen at different times in the life of different galaxies. In Fig. 2.5 we show the evolution of an Sbc galaxy (galaxy_48). We see that the three dispersions, especially σ_z, after declining around the age of 6 Gyr, increased steeply when the galaxy suffered from a 1:8 and a 1:4 mergers between the age of 7 and 8.5 Gyr, indicated with vertical lines. Consequently, σ_z/σ_R also increased to a value of ~ 0.9. After the age of 9.2 Gyr, the disk globally cooled down for little more than one Gyr and then the dispersions stayed approximately constant. In spite of this cooling, the vertical-to-radial ratio ended in $0.73^{+0.12}_{-0.04}$, much higher value than the initial (~ 0.55 at 4.7 Gyr). This is not the case of galaxy_106, a barred Sc type, with a final σ_z/σ_R of $0.47^{+0.13}_{-0.06}$, much lower than the initial value (~ 0.8 at 4.7 Gyr). Although this galaxy went through a long 1:5 merger from 6 to 7 Gyr, it ended up with a quite flattened ellipsoid, as shown in Fig. 2.6. The disk cooled down until 8 Gyr, then dispersions stayed approximately constant.

Martig et al. (2014b) studied the effect of mergers on the age-velocity relation (AVR) of a sample including galaxy_48 and galaxy_106. In Fig. 2 of their paper, both galaxies exhibit jumps in their AVR at the age corresponding to the end of the mergers. For galaxy_48 the jump is more pronounced and the gas took much longer to cool down and give birth to cooler young populations. This is probably due to the fact that the mergers happened later, when the disk

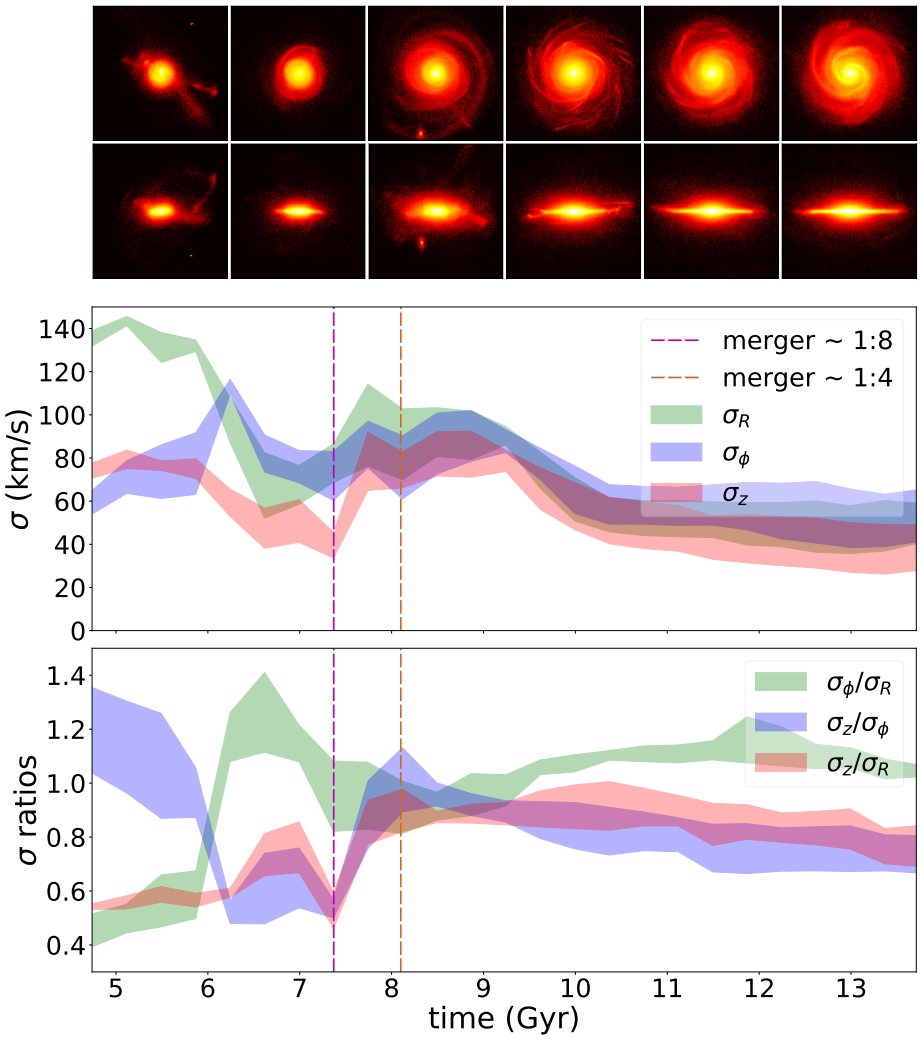

FIGURE 2.5— Evolution in time of galaxy_48: snapshots of stars (top panel, face-on in the first line, edge-on in the second line), stellar velocity dispersions (middle panel) and SVE axis ratios (bottom panel). The shaded areas mark the 16% and 84% percentiles of the values calculated over the disk radial profiles (see §2.5.3 for details). Displayed on the horizontal axis is time since the Big Bang. The galaxy had a 1:8 and a 1:4 merger around the ages of 7.3 and 8.1 Gyr respectively, both indicated by vertical dashed lines.

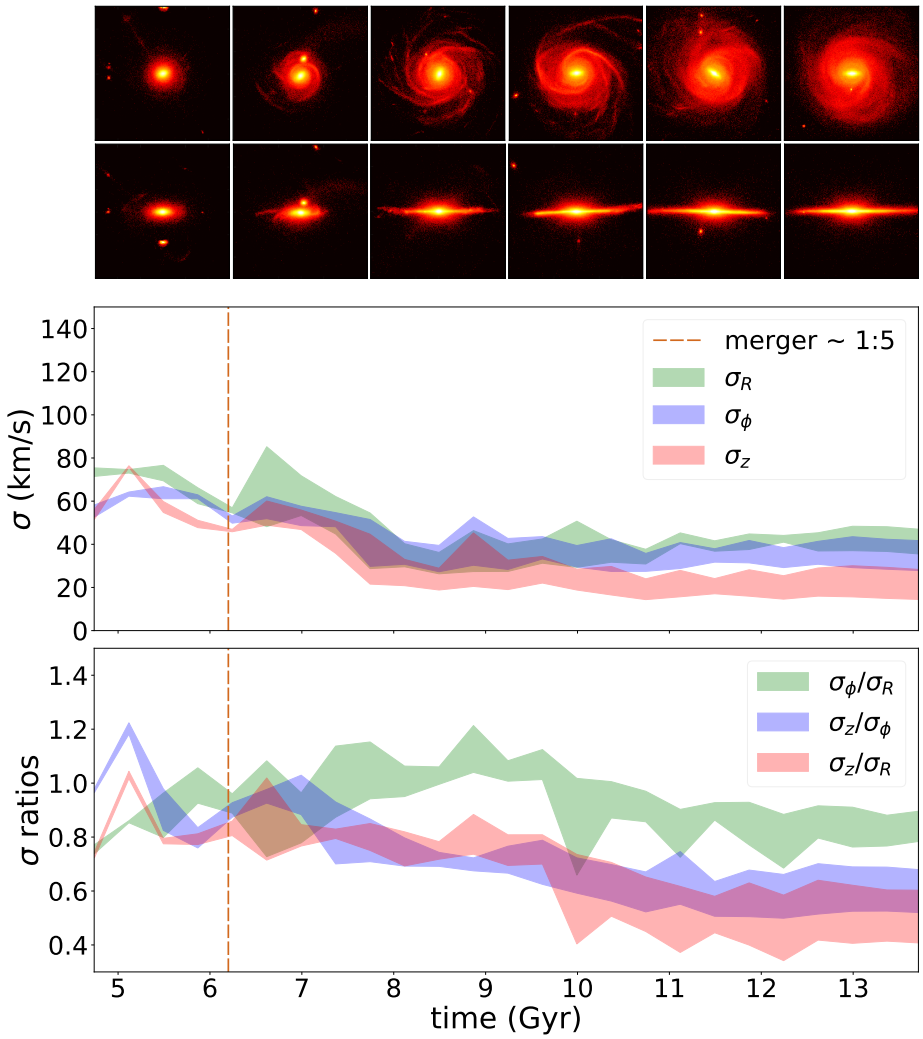

FIGURE 2.6— Evolution in time of galaxy_106: snapshots of stars (top panel, face-on in the first line, edge-on in the second line), stellar velocity dispersions (middle panel) and SVE axis ratios (bottom panel). The shaded areas mark the 16% and 84% percentiles of the values calculated over the disk radial profiles (see § 2.5.3 for details). Displayed on the horizontal axis is time since the Big Bang. The galaxy had a long 1:5 merger from the age of 6 to 7 Gyr, indicated by a vertical dashed line.

had already cooled down and new populations had a lower σ_z, being more sensitive. A small thin disk was also appearing, but during the merger epoch it became even thicker than before (see snapshots). In contrast, in galaxy_106 the merger happened when the stellar disk was still thick and dynamically hot. In that time, internal as well as external perturbations had little effect so that the merger did not affect visibly the mean SVE shape. In addition, an almost imperceptible increase of the radial plus decrease of the vertical dispersions, was sufficient to make σ_z/σ_R drop, between $\sim$9.5 and $\sim$11.5 Gyr, from $\sim$0.8 to $\sim$0.47 (Fig. 2.6). The origin of this gentle process could reside in the spiral density waves of this very late-type galaxy or the bar evolution, since it took place just after the spiral arms and the bar appeared (see snapshots in Fig. 2.6). This picture provides a potential explanation for the differences in the SVE evolution of the two galaxies.

We also show two examples of quiescence in Fig. 2.7 and 2.8, galaxy_128 being barred and galaxy_86 unbarred. The first one, an Sc, exhibits the flattest ellipsoid in the sample (at the final step of the simulation). After a disk cooling already finished at $\sim$7.3 Gyr, velocity dispersions remained approximately constant, if only with a slight increase of σ_R over time. This was likely related to the development of the bar, the spiral structure and the thin disk (see snapshots in Fig. 2.7). It was in fact enough to transform the ellipsoid from initially quite isotropic to much flatter, as seen in the bottom panel of the figure. The ellipsoid of galaxy_86, one of the earliest types, on the contrary was quite isotropic from the start, and it barely changed during its quiescent path. Between its 6 and 8 Gyr of life, the disk cooled down at the same rate in the vertical and the radial direction, but it heated remarkably in the azimuthal direction. This means that stars rotation became more disordered instead of ordered (as we have seen, disks typically cool down in the three directions meanwhile they acquire their final appearance). The peculiar properties of this disk are probably related to its morphology: it is photometrically smaller and thicker than galaxy_128, with almost no spiral arms (see snapshots in Fig. 2.8).

Finally, in Fig. 2.9, we show a relatively quiescent disk, born with an isotropic ellipsoid which became oblate and then flattened. During the disk cooling around 8 Gyr, σ_R dropped faster than σ_z, making the vertical-to-radial ratio larger than one. The snapshots indicate that the morphology of the galaxy drastically changed at that moment in time, from a small galaxy with no clear evidence of a disk to a fully grown spiral galaxy. From that time on, the σ_z/σ_R ratio has decreased steadily to a value of $0.59^{+0.04}_{-0.03}$.

These examples lead us to some general deductions. First, all the disks seem to cool down before they acquire their final appearance (e.g. extended, fully formed and with spiral arms). The contribution of recently born stars can help us to understand the nature of this cooling. We have compared the kinematics of stars younger than 300 Myr to the composition of all populations. The former have a degree of cooling that depends on the specific galaxy and time, if no mechanism heats dynamically the gas. During the mergers, they reach the velocity dispersions of the global galaxy, but afterwards they recover the previous values very soon. Thus, a merger can delay the forthcoming cooling or make it more gentle, but cannot prevent it. Its signature can be erased by the appearance of new stars when enough time has passed.

The cooling observed in Fig. 2.5 to 2.9 was driven by the increasing contribution of new cooler stars. The latter were characterized by an earlier and faster drop (in around one Gyr) in the individual dispersions, during the formation of the thin disk. A delay was seen between the cooling of gas (new stars) and the cooling of the global galaxy stellar component. An increase in the radial dispersion, driven by secular evolution, was also clearer in newly born

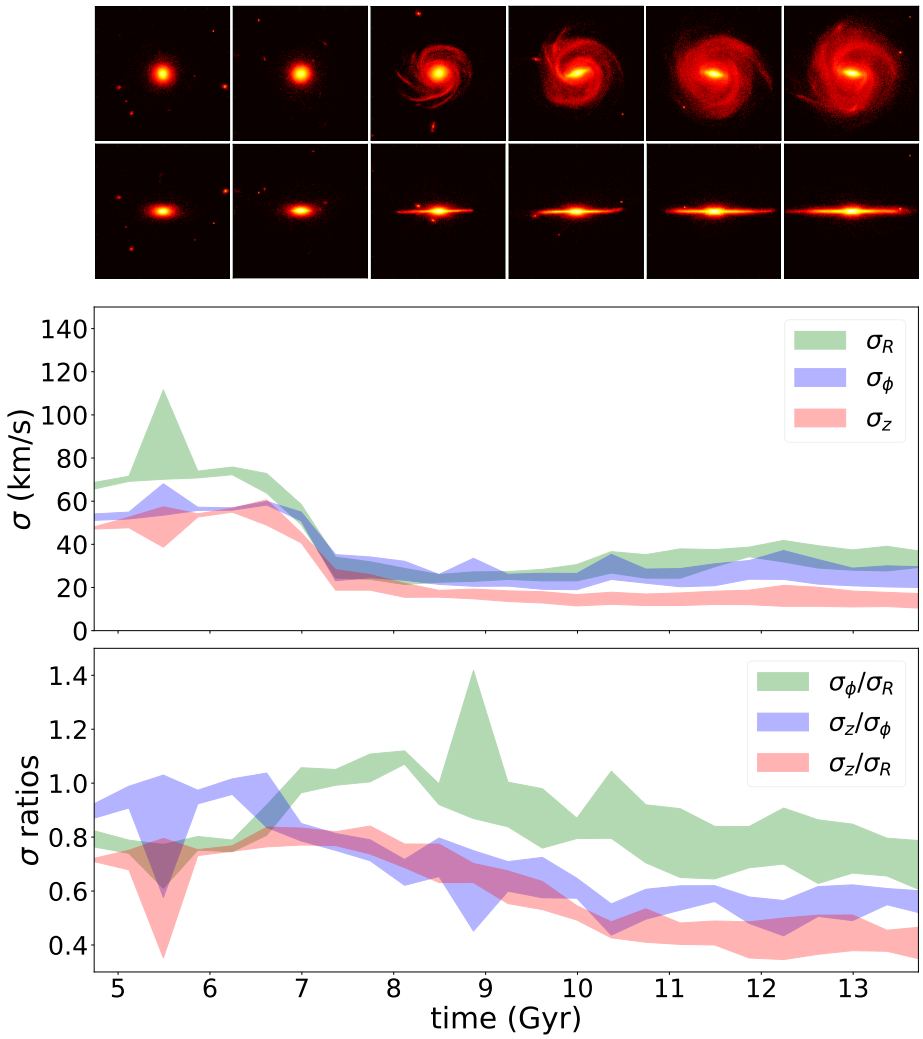

FIGURE 2.7— Evolution in time of galaxy_128: snapshots of stars (top panel, face-on in the first line, edge-on in the second line), stellar velocity dispersions (middle panel) and SVE axis ratios (bottom panel). The shaded areas mark the 16% and 84% percentiles of the values calculated over the disk radial profiles (see §2.5.3 for details). Displayed on the horizontal axis is time since the Big Bang.

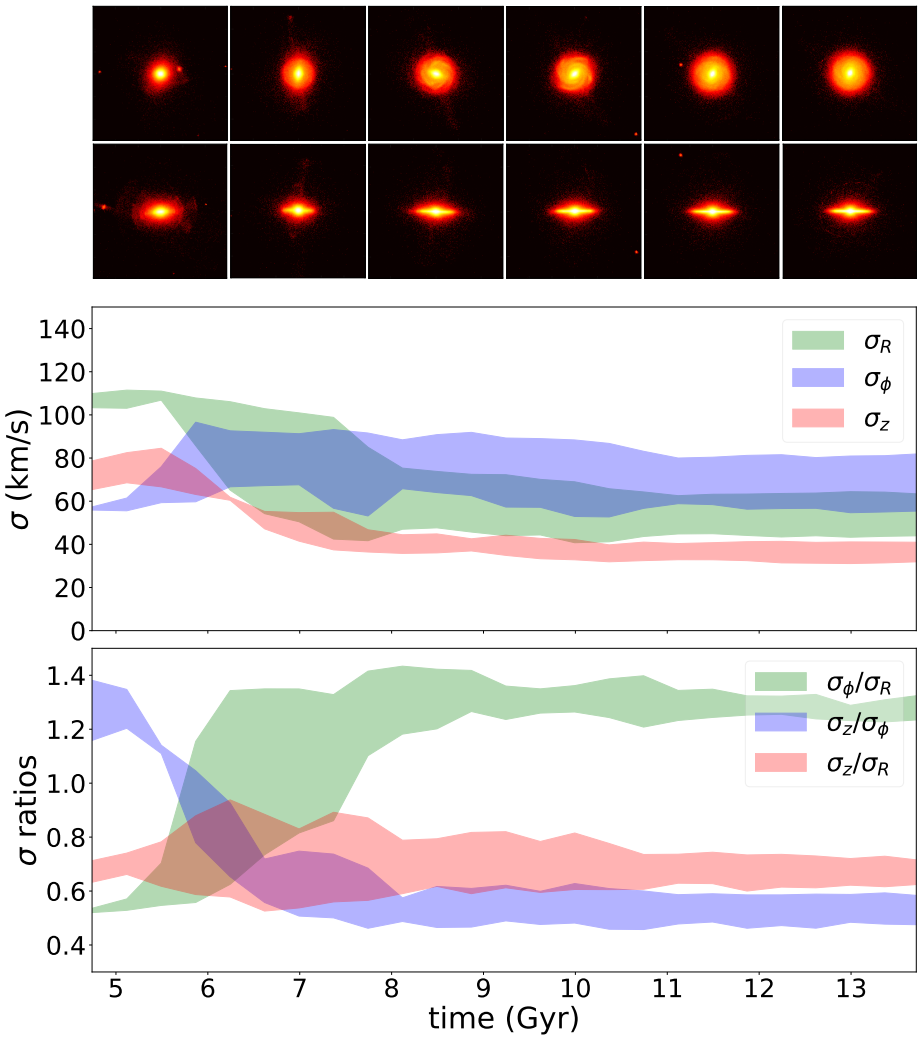

FIGURE 2.8— Evolution in time of galaxy_86: snapshots of stars (top panel, face-on in the first line, edge-on in the second line), stellar velocity dispersions (middle panel) and SVE axis ratios (bottom panel). The shaded areas mark the 16% and 84% percentiles of the values calculated over the disk radial profiles (see § 2.5.3 for details). Displayed on the horizontal axis is time since the Big Bang.

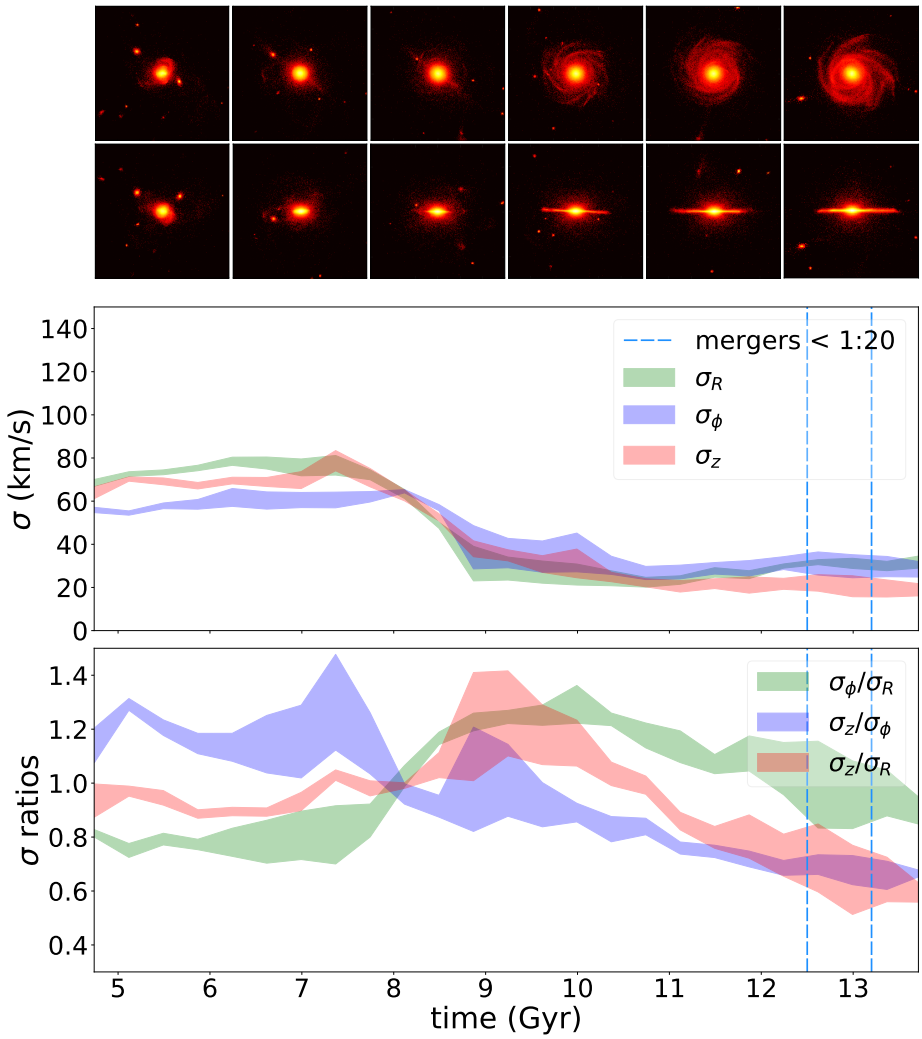

FIGURE 2.9— Evolution in time of galaxy_146: snapshots of stars (top panel, face-on in the first line, edge-on in the second line), stellar velocity dispersions (middle panel) and SVE axis ratios (bottom panel). Two mergers with very low mass ratios (<1:20) are indicated with dashed vertical lines. The shaded areas mark the 16% and 84% percentiles of the values calculated over the disk radial profiles (see §2.5.3 for details). Displayed on the horizontal axis is time since the Big Bang.

stars compared to stars of all ages, where it was smoothed. Despite this, the shape of the ellipsoid is not necessarily less isotropic for recently born populations. The shape comes from the balance between cooling or heating in the different directions, and therefore can be quite varied. For the two quiescent galaxies, galaxy_128 and galaxy_86, the same values of σ_z/σ_R are measured for very young stars and for all populations. The remaining three galaxies analyzed in this subsection have globally a more isotropic ellipsoid than recently born stars alone.

Secondly, the time in which we look at the ellipsoid is relevant. In some galaxies (e.g. galaxy_48, galaxy_106, galaxy_128 and galaxy_146) we would find an isotropic or anisotropic ellipsoid depending on when we look at it. Although at the final step of the simulations we do not have values of σ_z/σ_R either larger than one or much smaller than 0.4, we do have them during the evolutionary path of some galaxies, in agreement with the observational results in those ranges. Third, changes in the SVE shape are not necessarily related to disk heating, understood as an increase in velocity dispersions. These changes can also be caused by a decrease in radial or vertical dispersions, or an increase in both direction but in different amounts. Lastly, the vertical-to-radial ratio is more or less sensitive to small changes of σ_R and σ_z (few km s^{-1}), depending on their absolute values. Therefore in some very late types the slight increase in σ_R, contemporary to the appearance of the spiral structure, is sufficient to flatten the SVE but impossible to detect in observations and very sensitive to any other stronger process. For these reasons σ_z/σ_R might not be the best indicator of a disk heating or cooling, and even less helpful to distinguish between individual heating agents.

2.6 Conclusions

We have gathered all the published studies analyzing the shape of the stellar velocity ellipsoid in galaxies. Aiming to extend the study done by Gerssen & Shapiro Griffin (2012), we have plotted the vertical-to-radial axis ratio as a function of Hubble type for 55 galaxies. No strong correlation has been found and the points are distributed with a large scatter around a mean value of 0.7 ± 0.2.

In general, the other works included in this chapter are not in agreement with Gerssen and Shapiro's trend. This could be partially explained by the fact that their sample was carefully selected, as they explained (e.g. Shapiro et al., 2003), for having "optically regular-looking morphologies" and the typical appearance of their specific Hubble type. Our sample includes 55 galaxies of all kinds and suggests a much more complicated picture. Disk galaxies of early types can have more anisotropic ellipsoids than what their trend predicted, and late types can have ellipsoids covering all shapes. If it is true that different shapes correspond to different heating mechanisms, both early and late-type spirals can be affected by the same processes. At the same time, morphologically similar galaxies can be affected by different sources of disk heating.

We have used two different kinds of simulations to understand better this observational scenario, and they confirmed this picture. The SVE's flattening does not show a clear trend along the Hubble type either in simulations. The average value is around 0.6 with a scatter of ± 0.2. Idealized N-body simulations confirm that late-type galaxies can have different kind of ellipsoids. Their shape does not show any direct relation with the distribution of the dark matter. A relation between bars and the enhancement of the radial velocity dispersion is shown in zoom-in cosmological simulations. According to idealized N-body simulations, a fly-by in the disk plane also enhances σ_R and flattens the SVE. Furthermore, 1:10 to 1:3 mergers in zoom-in

cosmological simulations predict ellipsoids that are more isotropic on average, while quiescent mechanisms (perhaps bars and/or spiral arms) tend to enhance σ_R with respect to the other components.

The scatter of σ_z/σ_R is high also among galaxies with strong recent mergers and similar morphology. Evolution with time suggests that this axis ratio depends on the time when mergers happened and also on which snapshot of the galaxy life we are looking at. For instance, if just after a merger we see an isotropic SVE, its shape could change after some time.

In summary, the disk heating (cooling) scenario is complex and observations of the stellar velocity ellipsoid alone are insufficient to unveil it, due to the following reasons:

- σ_z/σ_R can be sensitive to small variations in one velocity dispersion component or two, perhaps not so relevant in terms of heating (cooling).
- An isotropic ellipsoid can be related not only to an increase of the velocity dispersion in the vertical direction (heating), but also to a decrease in the radial direction (cooling), as well as to a static situation (if the SVE was born already isotropic). Likewise, anisotropy can be caused by a "radial heating" as well as a "vertical cooling".
- When it comes to the different heating processes, the SVE results from the combination of them (e.g. mergers and spiral arms).
- A given heating process can produce a variety of velocity ellipsoid shapes, depending on the time and the conditions in which it occurs.
- Conversely, the same velocity ellipsoid can be achieved via a multitude of heating mechanisms.

The main outcome of this work is that additional information, beyond the stellar velocity ellipsoid, may be required to assess the different disk heating mechanisms in observed galaxies.

3

Unveiling the thick disk origin in FCC 170: signs of accretion?

The material included in this chapter is based on the article:
Pinna F., Falcón-Barroso J., Martig M., Sarzi M., Coccato L., Iodice E., Corsini E. M., de Zeeuw P.T., Gadotti D.A., Leaman R., Lyubenova M., McDermid R.M., Minchev I., Morelli L., van de Ven G., Viaene S., 2018, Astronomy & Astrophysics, submitted.

We present and discuss the stellar kinematics and populations of the S0 galaxy FCC 170 (NGC 1381) in the Fornax cluster, using deep MUSE data from the Fornax 3D survey. We show the maps of the first four moments of the stellar line-of-sight velocity distribution and of the mass-weighted mean stellar age, metallicity and [Mg/Fe] abundance ratio. The high-quality MUSE stellar kinematic measurements unveil the structure of this massive galaxy: a nuclear disk, a bar seen as a boxy bulge with a clear higher-velocity-dispersion X shape, a fast-rotating and flaring thin disk and a slower rotating thick disk. Whereas their overall old age makes it difficult to discuss differences in the formation epoch between these components, we find a clear-cut distinction between metal-rich and less [Mg/Fe]-enhanced populations in the thin-disk, boxy-bulge and nuclear disk, and more metal-poor and [Mg/Fe]-enhanced stars in the thick disk. Located in the densest region of the Fornax cluster, where signs of tidal stripping have been recently found, the evolution of FCC 170 might have been seriously affected by its environment. We discuss the possibility of its "pre-processing" in a subgroup before falling into the present-day cluster, which would have shaped this galaxy a long time ago. The thick disk displays a composite star formation history, as a significant fraction of younger stars co-exist with the main older thick-disk population. The former sub-population is characterized by even lower-metallicity and higher-[Mg/Fe] values, suggesting that these stars formed later and faster in a less chemically evolved satellite, which was subsequently accreted. Finally, we discuss evidence that metal-rich and less [Mg/Fe]-enhanced stars were brought in the outer parts of the thick disk by the flaring of the thin disk.

3.1 Introduction

Little is known about the origin of thick disks. Two main formation scenarios are advocated to explain their general properties: thick disks were born already dynamically hot at high redshift or they formed from the thickening of a pre-existing thin disk, dynamically heated. In the first case, stars could have been born from dynamically hot gas, as suggested by observations of thick disks in high redshift galaxies (Wisnioski et al., 2015; Elmegreen & Elmegreen, 2006), and in agreement with the simulation by e.g. Forbes et al. (2012). In N-body chemodynamic simulations by Brook et al. (2004), the thick-disk stars were born *in situ* at high redshift, before the formation of the thin disk, from gas accreted during the chaotic phase of multiple mergers. Another possibility to form an already hot disk is by direct accretion, as proposed by Abadi et al. (2003). In their simulations, thick-disk stars came from the tidal debris of accreted satellites and have, therefore, an extragalactic origin.

A fast dynamical heating of recently born stars would also form quickly a thick disk. Bournaud et al. (2009) showed that internal clumps in gas-rich young galaxies at high redshift are capable of rapidly scattering disk stars. Violent events are usually associated to mergers, which were proved by numerous sets of simulations to be able to form thick disks by scattering stars (e.g. Kazantzidis et al., 2008; Villalobos & Helmi, 2009; Di Matteo et al., 2011). On the other hand, secular heating might be responsible for a slow thickening of the disk, through scattering off giant molecular clouds or black holes present in the dark halos (e.g. Spitzer & Schwarzschild, 1953; Villumsen, 1985; Lacey & Ostriker, 1985; Hänninen & Flynn, 2002; Benson et al., 2004). However, Lacey & Ostriker (1985) found that this thickening would be too inefficient to explain the observed thick disks, in agreement with Minchev et al. (2012c).

Disentangling between all these possibilities has been one of the aims of the extragalactic scientific community in the last decade. Imaging has given the possibility of characterizing thick disks as structures. For instance, from photometry we have learned about their morphology, size, mass, and trends with global galaxy properties (Yoachim & Dalcanton, 2006; Comerón et al., 2011a,b, 2012, 2018). However, galaxy formation and evolution leaves a clearer imprint on stellar kinematics and populations. Therefore, spectroscopy brought important advances to the study of thick-disk origin. Yoachim & Dalcanton (2005, 2008b,a), with long-slit observations, studied the stellar kinematics and populations of the thin and the thick disks in late-type galaxies. They strongly supported direct accretion of stars from satellites as formation scenario for their thick disks. Kasparova et al. (2016), based on their stellar-population study from long-slit spectroscopy, proposed different pictures for the formation of thick disks in their three galaxies, fitting with the different environments where they live. There are only two contributions from integral-field spectroscopy, so far in the literature. Comerón et al. (2015) presented the stellar kinematics and populations of a single spatial bin covering the observed thick disk. They suggested different origins for the thick and the thin disk and a rapid formation at high redshift for the older more metal-poor thick disk. Not much later, Comerón et al. (2016) proposed a monolithic collapse scenario for the formation of an overall old S0 galaxy in the Abell 2877 cluster, with no significant difference in the age of the thick and the thin disk. Their integral-field observations were deep enough to allow several spatial bins in the thick disk, but not sufficient to cover a large area of this very faint component.

Even deeper data are required to go further from the midplane with larger spatial resolution. Moving in this direction, in this work we use deep MUSE integral-field observations from the

Fornax 3D survey (Sarzi et al., 2018) to measure the stellar kinematics and stellar population properties of the S0 FCC 170 (NGC 1381). We analyze the implications on the origin of the thick disk of this galaxy. Section 3.2 and 3.3 give the relevant information about the galaxy and the data set. In § 3.4 we describe the methods used to extract the stellar kinematics and populations. In § 3.5 we show the results on the first four moments of the velocity distribution, age, metallicity and [Mg/Fe]. These results are discussed in § 3.6, and summed up in § 3.7.

3.2 FCC 170

FCC 170 (NGC 1381) is an S0 galaxy in the Fornax cluster located at a distance of 21.78 Mpc (Tully et al., 2013) (so that 10 arcsec in the sky correspond to ~ 1.06 kpc). This bright galaxy has an effective radius in the B-band of 13.8 arcsec ($\simeq 1.46$ kpc) (Sarzi et al., 2018). Its maximum circular velocity is about 280 km s^{-1} (Bedregal et al., 2006) and its stellar mass has been estimated as 5.19×10^{10} M$_\odot$ (Vaddi et al., 2016). In the context of thick-disk origin, FCC 170 is therefore expected to behave as a massive galaxy (e.g. Yoachim & Dalcanton, 2006, 2008a; Comerón et al., 2011b, 2012, 2014, 2018).

It is edge-on (e.g. Bureau et al., 2006) and symmetric about the major and minor axes (de Carvalho & da Costa, 1987). It is an object of interest in the field of galaxy formation and evolution due to its complex structure. The prominent box-shaped bulge (e.g. Lütticke et al., 2000), with a central X shape (Bureau et al., 2006), was identified as a bar viewed edge-on by Chung & Bureau (2004) and Bedregal et al. (2006). Williams et al. (2011) suggested the presence of a classical bulge and a small disky structure in the center. Comerón et al. (2018) confirmed the existence of a thick disk and used two disky components and a central mass concentration to fit the surface-brightness profile. They determined that the thick-disk light starts to dominate over the thin disk at a distance of 10.8 arcsec ($\simeq 1.1$ kpc) from the midplane.

FCC 170 has no important line emission in the optical range (Bureau & Freeman, 1999). This simplifies the extraction of the stellar populations and makes this galaxy very suitable for studying their vertical distribution. At the same time, the fact that this galaxy does not show clear signs of dust or gas is noteworthy and could be related to the peculiar environment where it lives. FCC 170 belongs to the Fornax cluster, which is the second largest concentration of galaxies relatively close to the Milky Way, after Virgo (e.g. Jordán et al., 2007). Much less massive, Fornax has a core $\sim 40\%$ smaller than Virgo, but twice as dense. FCC 170 is located in this core (at a projected distance of 0.42° from the central galaxy FCC 213, from Iodice et al., private communication), where intra-cluster light (ICL) has been recently found (Iodice et al., 2017b). Hence, this work will provide insights about galaxy evolution and thick disks in dense environments.

3.3 Observations and data reduction

The spectroscopic data used in this work were collected as part of the Fornax 3D survey (Sarzi et al., 2018), a magnitude-limited survey of galaxies within the virial radius of the Fornax cluster (see also § 1.4.2). The deep character of the Fornax 3D data makes them ideal to study also the faint thick-disk regions of edge-on galaxies, such as FCC 170. Fornax 3D observations are detailed in Sarzi et al. (2018). They were performed with the Multi Unit Spectroscopic Explorer

(MUSE) (Bacon et al., 2010), mounted on the UT 4 at the Very Large Telescope (VLT). They made use of high-quality 3D spectroscopy with a spatial sampling of $0\farcs2 \times 0\farcs2$ in a large field of view of $1' \times 1'$ with the Wide-Field Extended mode. The wavelength range covered from 4650 to 9300 Å with nominal spectral resolution of 2.5 Å (FWHM) at 7000 Å and spectral sampling of 1.25 Å pixel^{-1}. The measured spectral resolution was on average 2.8 Å (FWHM), due to the adverse impact of combining different slightly offset exposures taken at different position angles. FCC 170 was observed with two pointings: one in the central region, with single exposures of 720 s and a total on-source time of one hour, and another in the outer part, with single exposures of 600 s and a total on-source time of two hours. The position of the two pointings is indicated in Fig. A.1 of Sarzi et al. (2018). Exposures were few arcseconds dithered and rotated by 90° in order to minimize the signature of the 24 MUSE slices on the field of view. Immediately before or after each science exposure, dedicated sky exposures were carried out in order to perform sky modeling and subtraction on the single spaxels.

The data reduction was performed using the version 1.6.2 of the MUSE reduction pipeline (Weilbacher et al., 2012, 2016). It included bias and overscan subtraction, flat-fielding correction, wavelength calibration, determination of the line-spread-function, and illumination correction. The observation of a spectro-photometric standard star at twilight was necessary to perform the flux calibration and first-order correction of the atmospheric telluric features. The different exposures were aligned using reference sources and then combined in a single datacube (see Sarzi et al. 2018 for more details).

3.4 Analysis methods

3.4.1 Voronoi binning

From the reduced and combined MUSE cube, we produced a spatially binned MUSE cube using the Python version of the Voronoi tessellation software described in Cappellari & Copin (2003)[1]. This method provides an adaptive spatial binning to a target signal-to-noise ratio (SNR) per bin, preserving the maximum spatial resolution. We required a minimum mean SNR of 40 per spatial bin and spectral pixel, in the range from 4750 to 5500 Å. We decided to adopt this value with the purpose of having a very good spatial resolution, after testing that compatible results were obtained with larger target SNR (e.g. 80 or 100). We set at 1 the minimum accepted SNR per spaxel to be considered, in order to extend the maps to a larger region of the faint thick disk. The number of the resulting bins is 10 344, 57% of them with a SNR > 40, only 5% with SNR < 35 and none with SNR ≤ 31. The Voronoi binned MUSE cube included spectra cut to the wavelength range from 4750 to 5500 Å, containing enough spectral features for the extraction of stellar kinematics and populations. We decided not to use the full MUSE spectral range to avoid regions where the sky subtraction could have left residuals. Also, while the used stellar population models (see the next section) cover up to about 7400 Å, age sensitivity weakens towards the red and non-alpha sensitive features are included.

[1] `http://www-astro.physics.ox.ac.uk/~mxc/software/`

3.4.2 Full spectrum fitting

We extracted the stellar kinematics and populations of FCC 170 from full-spectrum fitting, using the Penalized Pixel-Fitting method (pPXF) described in Cappellari & Emsellem (2004) and upgraded in Cappellari (2017) [1]. Based on a maximum penalized likelihood approach, this method makes use of expansions of the line-of-sight velocity distribution (LOSVD) as Gauss-Hermite series, to fit the observed spectra with templates from a stellar library. We used, to fit the MUSE spectra, the [Mg/Fe]-variable version of MILES single stellar population (SSP) models[2] based on BaSTI isochrones (Vazdekis et al., 2015). We assumed a Kroupa Universal IMF, with slope 1.30. These models cover a wavelength range between 3540 and 7410 Å, and are sampled at a spectral resolution of 2.51 Å (FWHM, Falcón-Barroso et al. 2011).

They include 12 values of total metallicity $[\mathrm{M/H}] = [-2.27, +0.40]$ dex, with a resolution between 0.14 and 0.48 dex, 53 values of age between 0.03 and 14.0 Gyr, with a resolution between 0.01 and 0.5 Gyr, and two values of $[\alpha/\mathrm{Fe}] \approx [\mathrm{Mg/Fe}] = 0$ (solar abundance) and 0.4 dex (super-solar). The SSP models are 1272 in total. No models of this kind with more than two values of [Mg/Fe] were available. While this is not optimal, the way how pPXF assigns weights to the models still offers the chance of interpolating between the two [Mg/Fe] values and find intermediate abundances (see § 3.5.2 for more details). For simplicity, in the following sections, with $[\alpha/\mathrm{Fe}]$ we refer to the [Mg/Fe] abundance, the only abundance we can measure among the α elements. Each SSP model has a unit total mass (in solar masses), so that mass-weighted results are obtained from pPXF.

Since this galaxy has hardly any line emission, it was not necessary to mask any lines when fitting the spectra with pPXF. We fitted simultaneously the stellar kinematics and populations, introducing only multiplicative polynomials of 8th order, to correct for uncertainties in the spectral calibration. We avoided additive polynomials, which could cause changes in the absorption line strengths and then bias the results in age and metallicity (see also Guérou et al. 2016). We verified that the kinematic results were not affected by this approach.

Following Cappellari (2017), we regularized the stellar-population weights assigned to the SSP models to obtain the best fit to the data. In this way, the results of age, metallicity and [Mg/Fe] were smoothed. The regularization parameter was chosen by looking for a compromise between smoothing (and purging the solutions from potential noise) and not loosing information. We followed the suggestions given in the same code by the authors as well as in McDermid et al. (2015), to calibrate the regularization for the bin with the highest SNR. First, we rescaled the noise in order to obtain a unit reduced χ^2 with no regularization. Then, we calculated the maximum regularization parameter as the one which increases the χ^2 from the value with no regularization (equal to the number of fitted pixels $N_{good\,pix}$) by the quantity $\Delta\chi^2 \simeq \sqrt{2N_{good\,pix}}$. This value would be the maximum allowed regularization, leading to the smoothest SFH, to give a solution still consistent with the data. After that, we performed tests with different regularization parameters between zero and the maximum value, realizing that some peculiar features in the SFH (see § 3.5.4 for details) disappeared above certain smoothing value. We verified that the position of these maxima in the SFH (i.e. their age, metallicity and [Mg/Fe]) did not change when varying the regularization parameter. This smoothed them changing only the mass fraction assigned to them. Therefore, we decided to select the highest regularization parameter allowing us to see these features, still giving a reasonably smoothed solution. All the

[2]Models and their description are available at `http://miles.iac.es/`

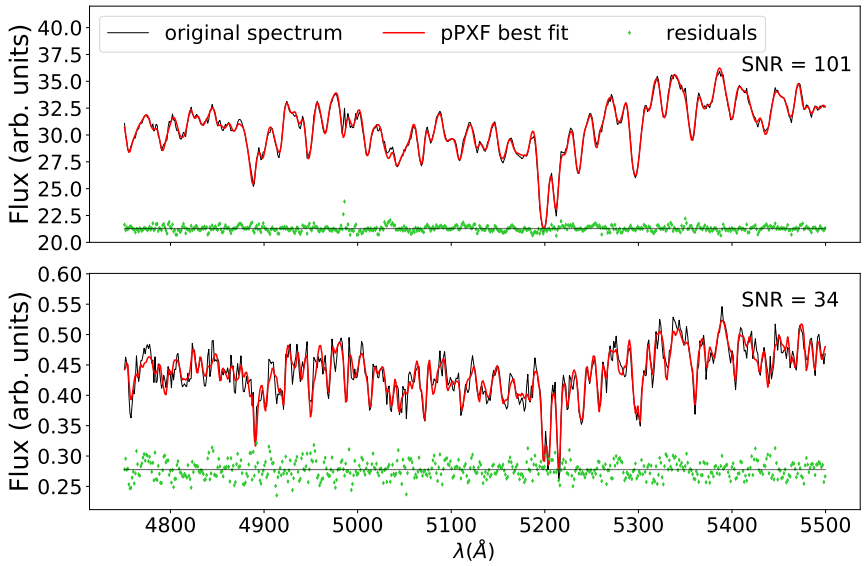

FIGURE 3.1— Examples of two pPXF fits in the wavelength range between 4750 and 5500 Å. On the top, the bin with the highest SNR (SNR = 101). On the bottom, a bin with SNR = 34. The observed spectrum, the best fit and the residuals of the fit are plotted in black, red and green, respectively. The residuals are arbitrarily shifted for displaying purposes.

results shown in this work were obtained using a regularization parameter of 0.05, kept constant for all the spatial bins.

In Fig. 3.1 we show two examples of pPXF best fits of spatial bins with high and low SNR. pPXF gave as output the first four LOSVD moments and the weights given to the individual SSP models to obtain the best fit. 54 bins were discarded because, despite their SNR being within the limits required during the Voronoi binning, their spectra were not good enough to allow good fits or they were contaminated by foreground stars. We kept 10 290 bins for the analysis in the following sections.

3.5 Results

3.5.1 Stellar kinematics

In Fig. 3.2, we show the maps of mean velocity V, velocity dispersion σ and third and fourth-order Gauss-Hermite moments, h_3 (skewness) and h_4 (kurtosis), of the LOSVD. The discarded bins and the two MUSE pointings are plotted in grey. Kinematic uncertainties associated to the SNR range used in this work were estimated in Sarzi et al. (2018). Their mean values are about: $6\,\mathrm{km\,s^{-1}}$, $8\,\mathrm{km\,s^{-1}}$, 0.030 and 0.035, respectively for V, σ, h_3 and h_4. The structural

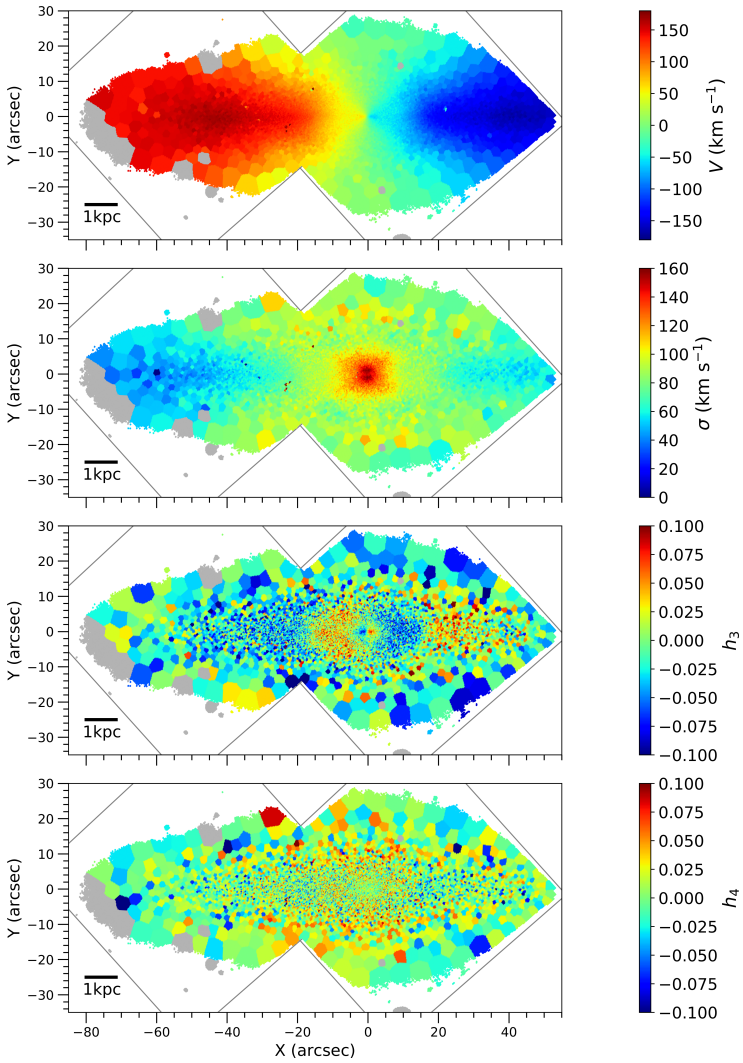

FIGURE 3.2— Maps of the first four moments of the stellar LOSVD. From top to bottom: mean velocity V, velocity dispersion σ, third Gauss-Hermite moment h_3 (skewness) and fourth Gauss-Hermite moment h_4 (kurtosis). The discarded bins and the position of the two MUSE pointings are plotted in grey. A scale bar on bottom-left of each map indicates the correspondence with physical units.

components that will be defined in § 3.5.3 (Fig. 3.4) can be distinguished in the kinematic maps described as follows.

In the velocity map (Fig. 3.2, top panel), a clear spider diagram appears. We easily identify the fast-rotating thin disk and a slower-rotating thick disk at higher distance from the midplane. It is also possible to see a faster-rotating nuclear disk. Signs of cylindrical rotation are visible in the boxy-bulge region, where the spider pattern is blurred and we see similar velocities at different distances from the midplane. Nonetheless, the rotation is not perfectly cylindrical from our line of sight, probably due to the bar orientation angle (e.g. Gonzalez et al., 2016; Molaeinezhad et al., 2016). Velocity dispersion shows a clear X-shaped pattern in the center, formed by a smaller X with higher σ values and a bigger X with lower values. The small X presents a drop in the midplane, probably related to the presence of the nuclear disk. The lowest velocity dispersions are found in the thin disk, although low sigma values appear to extend also out from the mid-plane at larger radii (we show evidence of a thin disk flaring in § 3.5.2 and § 3.6.2). This causes a radial gradient in the thick-disk region (from $\sim$10 arcsec onwards, see § 3.2), which has globally lower σ than the boxy bulge and higher σ than the thin disk.

The skewness map describes the asymmetric deviations of the LOSVD from a Gaussian (van der Marel & Franx, 1993; Gerhard, 1993). It clearly shows the different morphological structures of FCC 170. An anticorrelation of h_3 with respect to the mean velocity is usually associated with disk-like components (e.g. Krajnović et al., 2008; Guérou et al., 2016). It indicates in Fig. 3.2 the positions where the thin and the nuclear disks are located. It also confirms that the box/peanut shape corresponds to a bar viewed edge on, by showing a correlation with the mean stellar velocity (e.g. Bureau & Athanassoula, 2005). It indicates the region where this bar dominates the kinematics. In the kurtosis map in Fig. 3.2, the different structures are barely visible. Positive values, related to a LOSVD with a narrower symmetric profile than a pure Gaussian (van der Marel & Franx, 1993; Gerhard, 1993), are predominant in the box/peanut region and negative values in the (thin) disk region.

3.5.2 Mass-weighted stellar-population maps

From the mass weights given by pPXF to the different SSP models, it is possible to reconstruct age, total metallicity [M/H] and abundance [Mg/Fe] of the stellar populations building the galaxy. Each SSP model corresponds to a combination of these three properties, therefore the weights indicate the importance of each combination in each individual bin. By averaging the different populations making up each bin, with their respective weights, we obtained the mean quantities plotted in Fig. 3.3.

Martig et al. (in preparation) have carried out an analysis on the galaxy NGC 5746, very similar to this work, using the same methods on MUSE data. They performed some Monte Carlo simulations, as suggested by Cappellari & Emsellem (2004), to estimate uncertainties on the mean age, metallicity and [Mg/Fe]. They perturbed a series of spectra (of about 30 spatial bins) with a Gaussian noise, whose level was estimated as the standard deviation of the residuals of a first pPXF fit (the residuals were calculated as the difference between the best fit and the original spectrum). Each spectrum of the series was perturbed with 50 realizations. For each spatial bin, they fitted the 50 perturbed spectra and looked at the distribution of the resulting stellar population parameters, estimating the uncertainties of the mean age, metallicity and

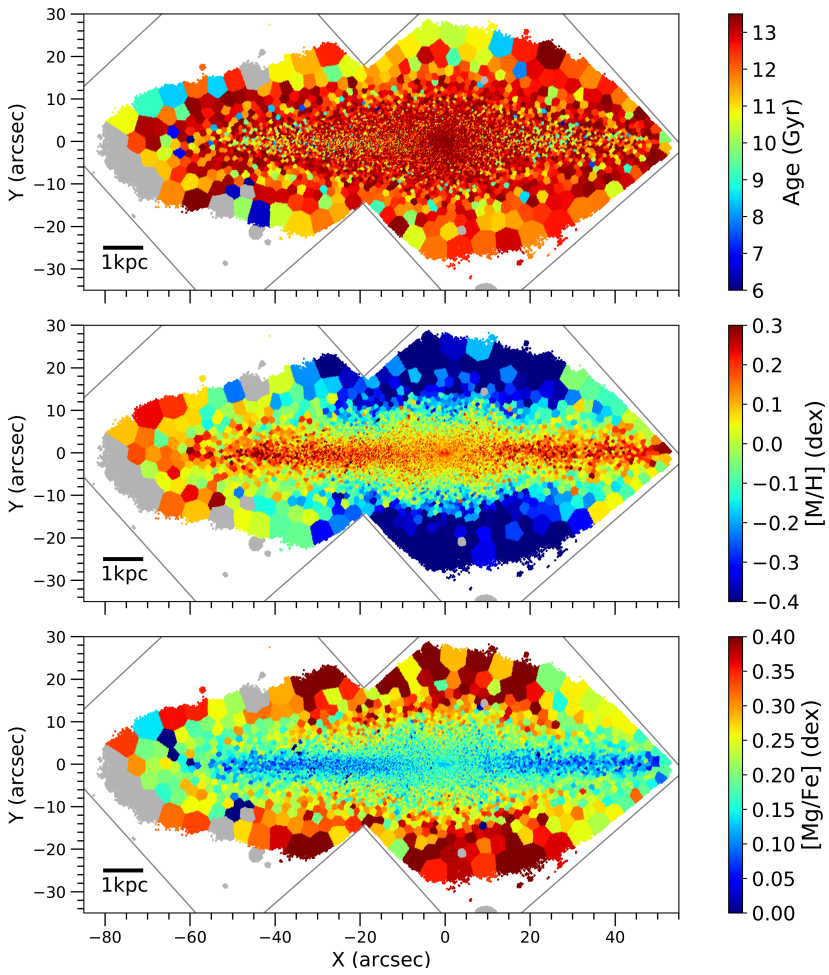

FIGURE 3.3— Maps of the stellar populations of FCC 170. From top to bottom: mean age, total metallicity [M/H] and [Mg/Fe] abundance. The discarded bins and the position of the two MUSE pointings are plotted in grey. A scale bar on bottom-left of each map indicates the correspondence with physical units.

[Mg/Fe]. The maximum estimated uncertainties were, for all the spectra of the series, about 1 Gyr, 0.06 and 0.02 dex respectively. We considered them a good estimate but a lower limit because a white noise was added during the tests. We expect the errors to be larger in real cases, in which the noise depend on wavelength. In addition to these statistical uncertainties, systematic uncertainties may be larger and very difficult to estimate. Factors which could be

affecting them might be the imperfection of the SSP models and fitting method, including IMF variations and the introduced polynomials and regularizations.

From the age map in the upper panel of Fig. 3.3, we see that FCC 170 is overall old, with relatively small variations of age generally in the range between $\sim$8 and $\sim$14 Gyr. For this reason, it is difficult to clearly distinguish the different structures in this age map. It is barely possible to recognize the oldest very central region and the youngest thin disk, while some thick-disk bins look surprisingly younger. However, the transitions between the different structural components are well visible in the mean metallicity map, in the middle panel of Fig. 3.3. A prominent X-shaped feature is traced by the metal-rich stars of the edge-on bar (solar/supersolar metallicities), with the even more metal-rich nuclear disk in the center.

The most metal-rich region appears to be the thin disk, with no prominent radial gradient similarly to what has been found in the Milky-Way inner thin disk (Fragkoudi et al., 2017b). The thin disk of FCC 170 exhibits a metallicity flaring in the outer part and touches the thick-disk region (10 arcsec above the midplane) still with high metallicity. The thick disk displays rather subsolar metallicities in its inner part. In the outer part, a radial metallicity gradient is plainly visible in the map. This could be related to the thin-disk flaring, mixing more metal-rich populations, associated to the thin disk, with the most metal-poor, belonging to the thick disk.

In spite of having only two possible values of [Mg/Fe] in the SSP models, averaging them by their respective weights assigned by pPXF we obtained average [Mg/Fe] values in the full range between 0.0 and 0.4 dex. Several structures are also easily visible in the map of the mean abundance of [Mg/Fe]. In the bottom panel of Fig. 3.3, the X-shape is suggested by the distribution of bins with [Mg/Fe] in the range between $\sim$0.05 and $\sim$0.10 dex. The less α-enhanced tiny nuclear disk is clearly visible. The thin disk appears as the least α-enhanced component, with slightly supersolar values of [Mg/Fe], and a potential flaring connecting to the more [Mg/Fe]-enhanced outer thick disk. The most α-enhanced region is certainly the inner thick disk, with a difference of about 0.30 dex with respect to the thin disk.

3.5.3 Structural decomposition

The kinematics maps, especially the third-order Gauss-Hermite moment h_3, helped us to outline the regions where each structural component dominates. This is necessary to perform the stellar population analysis for each one of these components (see § 3.5.4 and § 3.5.5). It is possible to calculate the mean properties of the individual structures averaging on the bins dominated by it, or collapsing the spectra of these bins to obtain a single spectrum per component. It is important to note that our comparison between components will be only qualitative, given that it is based on the line-of-sight properties. We cannot isolate the values for the individual components where they are superimposed, especially in the central region of the galaxy.

Following Comerón et al. (2018), we consider the bins with $|y| > 10$ arcsec dominated by the thick disk. We also divided the bins into an inner thick disk ($|x| < 25$ arcsec) and an outer thick disk ($|x| > 25$ arcsec), since they appear to have slightly different chemical properties (see § 3.5.2). We define a thin-disk-dominated region between $|y| < 5$ arcsec and $|x| > 20$ arcsec, excluding a transition range between the thick and the thin disk (5 arcsec $< |y| <$ 10 arcsec) and the central region under the influence of the bar ($|x| < 20$ arcsec). To study the boxy-bulge and the nuclear disk, we selected the regions where they dominate h_3. We selected the region with $|y| < 0.8$ arcsec and $|x| < 2.5$ arcsec for the nuclear disk and the region with 5 arcsec $< |y| <$ 10 arcsec and

$|x| < 13$ arcsec for the box/peanut. We observe these two components in the line of sight, overlapped to each other (in the case of the nuclear disk) and to the thin and the thick disk. A quantitative analysis would be strongly influenced by other very bright components such as the thin disk. In particular, the properties obtained for the nuclear disk could be seriously affected by the ones of the box/peanut and the thin disk. Nevertheless, the data allows a qualitative comparison between components.

We show the bins selection for the individual structural components in Fig. 3.4. Martig et al. (in preparation), in their analysis on NGC 5746, compared this decomposition method (based on kinematics) with a morphological decomposition based on surface brightness profiles. They confirmed that the structural decomposition based on kinematics is the most restrictive, in the sense that we are taking into account the regions least affected by the other components.

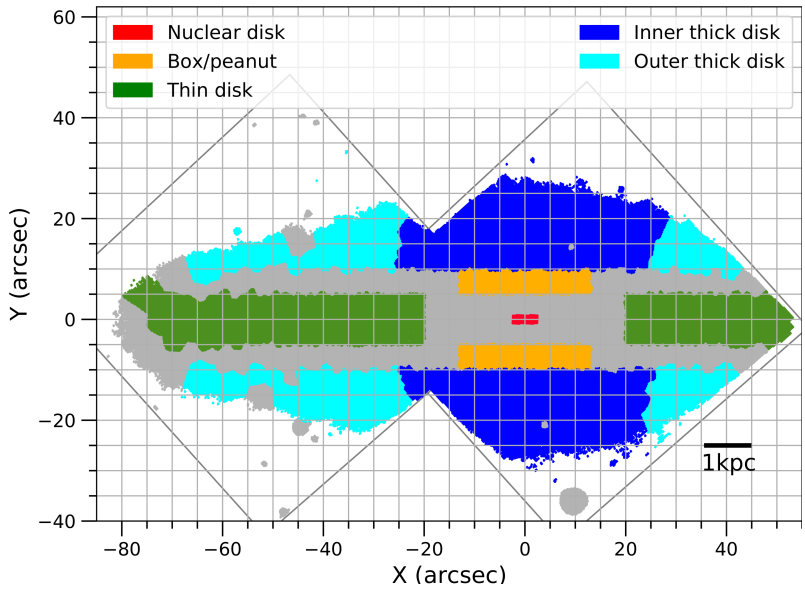

FIGURE 3.4— Map of the structural decomposition used in this work. Each color corresponds to a different component. The thick disk is divided into inner and outer regions. We plotted in grey all the bins not taken into account for the analysis of the single components, as well as the position of the two MUSE pointings. A scale bar on bottom-left indicates the correspondence with physical units.

3.5.4 Star formation history

We reconstructed the star formation history (SFH) of the individual bins of FCC 170 summing the mass fraction of the different coeval SSPs. We calculated the mass in each individual spatial bin, using the mass-to-light ratio in the V-band corresponding to each SSP model [2]. We first converted the g-band surface brightness in an image of the galaxy (from the Fornax Deep Survey,

Iodice et al. 2016) to the V-band in the Vega system. Then, we compared the surface brightness in our MUSE spectra to the V-band surface brightness in the image, in an annulus between 5 and 10 arcsec, to obtain an offset between them. Taking into account this offset and the galaxy distance (§ 3.2), we estimated the V-band absolute surface brightness in each spaxel of our MUSE data. The mean M/L per spaxel was calculated as the weighted average of the M/L corresponding to the models assigned to that spaxel by the pPXF best fit. We used Eq. 1 in Cebrián & Trujillo (2014) to compute the stellar mass per spaxel from the M/L and absolute surface brightness (both in the V-band). This method gave us a total stellar mass of about $5.7 \times 10^{10}\,\mathrm{M}_{\odot}$ in the region of FCC 170 covered by our Voronoi binning, a lower limit for the galaxy stellar mass.

Following the spatial-bins decomposition in § 3.5.3 we averaged, on the different bins of a specific individual structural component, the mass fraction corresponding to the same age. We weighted according to the different masses in the individual spatial bins (for the specific age) when averaging. This method results in the SFHs of the different components shown in Fig. 3.5. The left column, where the mass fraction was normalized to the stellar mass of the corresponding structural component, is more recommended to compare the different populations in the same component. In the right column, where the mass fraction was normalized to the galaxy total mass, we can compare the different components with each other. The thin disk is clearly the most massive for all ages. This SFH is non-cumulative in the sense that it does not show the properties of the global galaxy for a given time, but only the properties of specific stellar populations (with the age indicated in the plots). In each panel, only the average SFH of one component is plotted with a specific color and with upper and lower limits of the same color. These indicate the 1σ dispersion between the individual spatial bins of each component. They were calculated as the 16 % and 84 % percentiles of the mass fraction distribution over the different bins. The average SFH of the other structural components were plotted in each panel in black with different line styles, for reference. We compared these results with those obtained from collapsing all the bins of a component into a single spectrum. We found similar star formation histories with the two methods.

The SFH of the four components peak around 14 Gyr, confirming the predominance of the very old populations in the mean age map in Fig. 3.3. The similarity in the shapes of the curves in Fig. 3.5 is probably favored by the line-of-sight overlapping, in some regions (especially the central region), of stars belonging to different components (see also § 3.5.3). However, the structural components differ in the sharpness of this peak and the extent of the SFH. In the nuclear disk region (green curve in the first row from top of Fig. 3.5), for instance, stars formed in a very early epoch and star formation roughly stopped around 11 Gyr. However, we cannot rule out the presence of an older central component, i.e. a classical bulge, difficult to see in our maps because of its relatively reduced size, mass and brightness. It would be contaminating the SFH of the nuclear disk. The box/peanut (blue curve in the second panel from top) has also a very pronounced peak around 14 Gyr, but a slightly more extended SFH including a very smooth peak around 10 Gyr. This peak is much more pronounced in the thick disk, where the star formation had almost halted around 11 Gyr, when this younger population appeared. This is present in both the red and purple curves in the two bottom rows of Fig. 3.5, corresponding to the inner and outer thick disk, respectively. The red and purple shades show that this bump is present in all the spatial distribution. The thin-disk SFH appears to be more continuous (brown curve in the third row from top), extending down to $\sim$7 Gyr. The fact that the 10 Gyr peak is

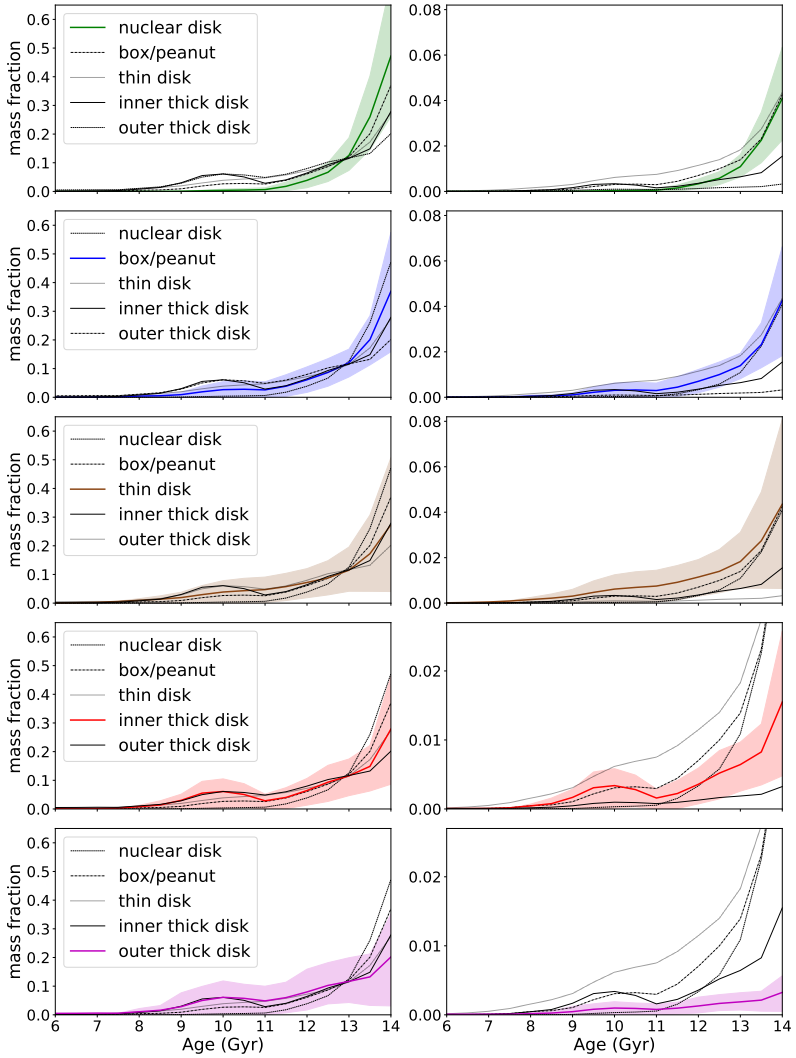

FIGURE 3.5— Weighted average SFH of the different structural components of FCC 170, as defined in Fig. 3.4. The average mass fraction is displayed on the vertical axis, weighted by the mass in each bin. This mass fraction is normalized to the total mass of the component, in the left column, and to the total mass of the galaxy, in the right column. In each panel, only one component is represented in a specific color (*green* for the nuclear disk, *blue* for the box/peanut, *brown* for the thin disk, and *red* and *purple* respectively for the inner and the outer thick disk). For this component, 1σ uncertainties, calculated as 16 % and 84 % percentiles of the spatial-bin distribution, are represented as shades of the same color. The SFH of the rest of components are plotted in black, with different line styles, in each panel.

more pronounced in the inner than in the outer thick disk is probably related to the thin-disk flaring. The outer-thick-disk SFH is compatible with a composition of inner-thick-disk-type populations with thin-disk populations.

3.5.5 Chemical abundances

The chemical composition of the populations appearing in the SFH can help us to understand if they came from different formation processes or if they were simply part of a continuous build-up of the galaxy. For each structural component, in Fig. 3.6 we have plotted histograms of the SFH in the left column of Fig. 3.5, with the mass fraction normalized to the component mass. This time we have color coded the different age bins according to the weighted average of the total metallicity (by weighting on the different SSP models according to their weights and on the spatial bins according to their mass). Most stars formed from an evolved interstellar medium, since in general we measure solar or supersolar metallicities. The most metal-rich structures are the nuclear and the thin disks (first and third panels from top), while the thick disk clearly displays subsolar metallicities (last two panels from top). The most metal-poor stars (reaching $[M/H] \lesssim -0.5$ dex) form the younger peak at ~ 10 Gyr in the thick-disk SFH. These stars formed later but from a less chemically evolved gas. This difference in metallicity might be the hint of a different formation history for this younger population, compared to the older and less metal-poor rest of the thick disk. Comparing the inner and the outer thick disks, the ~ 10 Gyr-old population is clearly more metal-poor, on average, in the former. The metallicity in the outer region reveals again the mixing of the metal-poor populations with the metal-rich stars in the flaring thin disk. The smooth younger peak visible in the second panel from top, in Fig. 3.6, is also more metal-poor than the rest of the box/peanut, suggesting that the same thick disk younger population might be present also here, although to a minor extent.

Dividing the age and metallicity ranges into different bins, it is possible to plot the spatial distribution of the different stellar populations. In Fig. 3.7, we have mapped the mass density of the different stellar populations according to the combination of their age and metallicity. The top-left panel shows that younger (ages ≤ 11.5 Gyr) and more metal-rich ($[M/H] \geq 0.06$ dex) stars are not contained in all spatial bins and are mainly in the thin disk and the box/peanut. Most metal-rich stars are very old (i.e. older than 11.5 Gyr, see top-right panel), contributing about half the total mass. They form almost entirely the box/peanut and their presence is very strong in the inner thin disk too. They are also present in the thick disk in a minor extent. Although most metal-poor stars ($[M/H] \leq 0.06$ dex) dominate the thick disk in mass fraction, their mass is concentrated in the very central region, suggesting a spherical distribution (bottom panels in Fig. 3.7). This could be a small classical bulge that, because of its more reduced size than the bar, is not visible in the other maps. In contrast, in the same region, metal-rich stars followed the shape of the box/peanut (see top panels). The population corresponding to the secondary peak in the thick-disk SFH plot is included in the bottom-left panel of Fig. 3.7, but has been also isolated in Fig. 3.8. Here we see that it is mainly concentrated in the central region and the inner thick disk but present everywhere (top panel). It contributes $\sim 2.5 \times 10^9$ $M_\odot$ in the region under study in this work, approximately the 10% of the galaxy total stellar mass. The bottom panel shows that this population dominates several less dense bins of the inner thick disk, while in the rest of the galaxy it contributes only about the 6% of the bin mass, on average.

The [Mg/Fe] abundance can add some insights to our analysis. In fact, this ratio would be

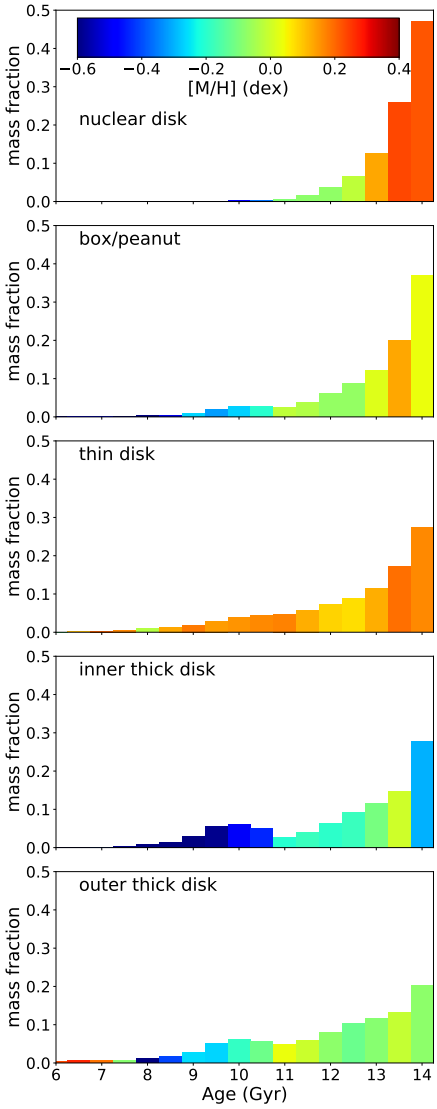

FIGURE 3.6— SFH of the different structural components making up FCC 170. From top to bottom: the nuclear disk, the box/peanut, the thin disk, the inner and the outer thick disk. We have color coded the histogram age bins according to the weighted average total metallicity ([M/H]) of the specific age bin. The average mass fraction is displayed on the vertical axis, weighted by the mass in each bin and normalized to the mass of the component.

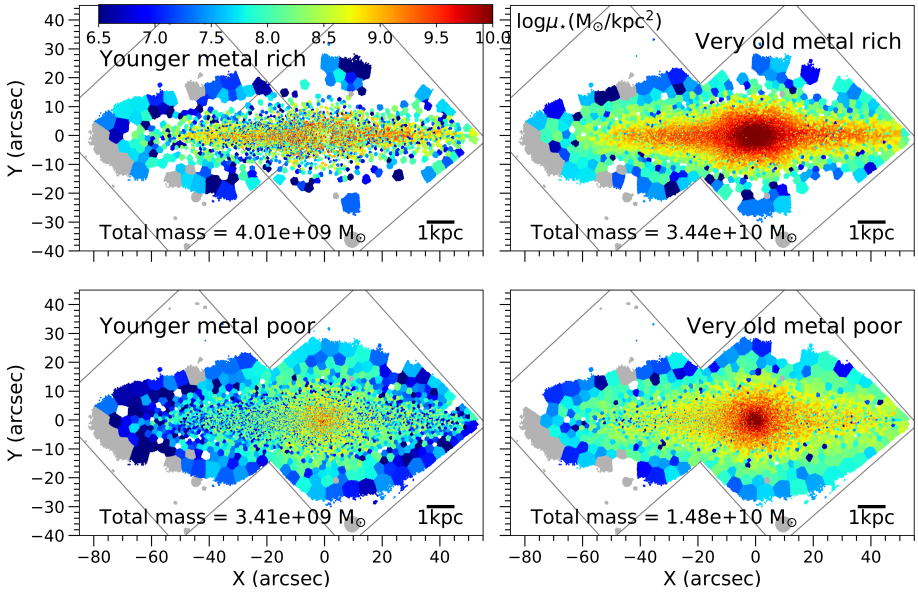

FIGURE 3.7— Maps of some combinations of age and metallicity for the stellar populations in FCC 170. *Top*: most metal-rich populations ([M/H]$\geq$ 0.06 dex). *Bottom*: most metal-poor populations ([M/H]≤ -0.25). *Left*: younger populations (ages $\leq$ 11.5 Gyr). *Right*: oldest populations (ages $\geq$ 11.5 Gyr). The color scale shows the mass density corresponding to the populations in the specific age-metallicity bin. The total mass in the age-metallicity bin is indicated on bottom-left of each map. The position of the two MUSE pointings is plotted in grey. A scale bar on bottom-right of each map indicates the correspondence with physical units.

higher if stars were formed rapidly, since α-elements are mostly produced by supernovae type II, than if they were formed slowly, giving more time to supernovae type Ia to produce Fe-peak elements (see § 1.2.1). In Fig. 3.9 we show the SFH histograms of the different components, this time color coding the different age bins according to the corresponding mean value of [Mg/Fe]. These plots indicate that the α-enhancement increases towards younger populations except in the thin disk, less enhanced in [Mg/Fe] for all ages. The thick disk is globally the most α-enhanced component. In particular, the distinction between the oldest populations and the bump in the SFH (peaking at $\sim$10 Gyr) is emphasized by a jump to a higher [Mg/Fe] abundance, both in the outer and the inner thick disks. This means that these younger stars were formed not only from a less evolved interstellar medium, but also with a different formation timescale, compared to the rest of the thick disk. Our results point to different formation scenarios for this younger population with respect to the dominant very old ones.

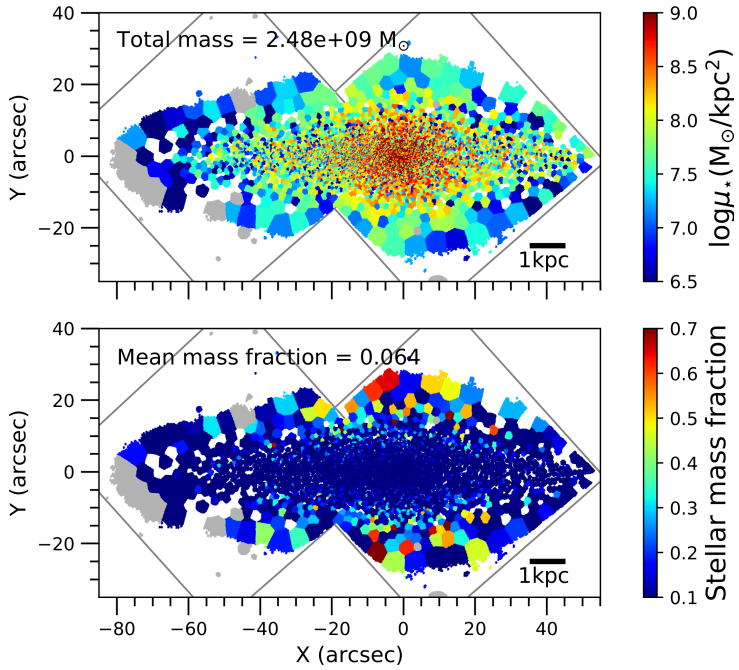

FIGURE 3.8— Distribution of the stellar population with ages between 9 and 11 Gyr, metallicity between -0.96 and -0.06 dex and [Mg/Fe]∼0.4 dex. The color scale shows the stellar mass density in the top panel and the stellar mass fraction in the bottom panel. The total mass or the mean mass fraction per bin, in this specific populations, are indicated on top-left of respectively the top and the bottom maps. In each panel, the position of the two MUSE pointings is plotted in grey and a scale bar on bottom-right indicates the correspondence with physical units.

3.6 Discussion

3.6.1 Comparison with previous works on FCC 170

Our work, making use of integral-field data, shows a two-dimensional view of FCC 170 stellar kinematics and populations. Previous studies used only long-slit observations and are not straightforward to compare to. In their kinematic profiles from long-slit observations, several authors (Chung & Bureau, 2004; Bedregal et al., 2006; Spolaor et al., 2010a; Koleva et al., 2011; Williams et al., 2011) already identified some signatures corresponding to the structures in our kinematics maps, such as humps in the rotation curve or h_3 correlations and anticorrelations with the mean velocity. Therefore, our bi-dimensional results confirm the presence of the structures associated to these kinematic signatures: the nuclear disk, the bar seen as a boxy-bulge, the thin disk. The compatibility of the positions dominated by these components, as determined from our maps and from the rotation curves in previous works, allowed us to define them spa-

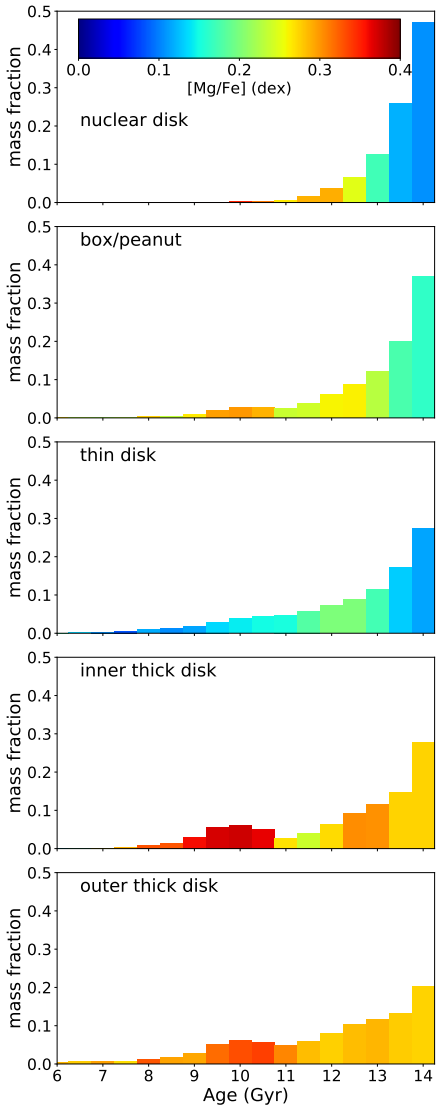

FIGURE 3.9— SFH of the different structural components of FCC 170. From top to bottom: the nuclear disk, the box/peanut, the thin disk, the inner and the outer thick disk. We have color coded the histogram age bins according to the weighted average [Mg/Fe] of the specific age bin. The average mass fraction is displayed on the vertical axis, weighted by the mass in each bin and normalized to the mass of the component.

tially. Williams et al. (2011), in particular, measured the stellar kinematics of FCC 170 with four slits at different distances from the midplane. However they could not measure many points at disk-dominated radii. They found signs of cylindrical rotation, which is visible in our mean velocity map in Fig. 3.2. Their velocity dispersions at the different slit positions also agree very well with our maps, with a central peak of $\sim 160\,\mathrm{km\,s^{-1}}$ and values between 80 and $100\,\mathrm{km\,s^{-1}}$ in the thick disk region. Our maximum rotation velocity and velocity dispersion are also in very good agreement with the rotation curve and σ profile presented in Chung & Bureau (2004).

When it comes to the stellar populations, we have partial agreement with some of the studies in the literature. Spolaor et al. (2010b) found FCC 170 uniformly old along the major axis, with (luminosity-weighted) ages compatible with our Fig. 3.3. Regarding metallicity, they found a radial profile characterized by a steep gradient, spanning from supersolar to subsolar (luminosity-weighted) values. In the same radial extent, the midplane is overall metal rich according to our analysis, instead. Analysing the same data of Spolaor et al. (2010b) with different methods, Koleva et al. (2011) found a more uniform metallicity along the major axis, at about solar [Fe/H], except for the outskirts (from about 60 arcsec on) where it dropped to subsolar [Fe/H] values and where also our [M/H] decreases. Our age results are in a good agreement with Williams et al. (2011), who observed overall old populations in the region covered by their four slits, including the thin disk and up to 12 arcsec above the midplane. They detected a negative vertical gradient from solar to subsolar metallicities, and a positive vertical [α/Fe] gradient, starting from a solar abundance in the midplane up to supersolar. Also, Johnston et al. (2012) found ages in the same range as we did, older than 10 Gyr. Our estimate of the lower limit for stellar mass (§ 3.5.5) is in agreement with the total stellar mass estimated by Vaddi et al. (2016).

3.6.2 Formation and evolution scenarios for FCC170

The absence of structures in the age map of FCC 170 is striking. The spatial correspondence of the different structures in kinematics, metallicity and [Mg/Fe] abundance is not present in the age map. FCC 170 looks overall old. On the one hand, this is surprising given the results in the literature showing, by and large, a younger thin disk than the thick disk (e.g., in the Milky Way, Gilmore & Reid 1983; Prochaska et al. 2000; Cheng et al. 2012; Haywood et al. 2013 and in external galaxies Yoachim & Dalcanton 2008b; Comerón et al. 2015; Guérou et al. 2016; Kasparova et al. 2016). On the other hand, massive galaxies are expected to have been more efficient in forming stars, to have formed them quickly at high redshift, and therefore to be overall old and more α-enhanced in their thick disks (e.g. Elmegreen et al., 2017). Furthermore, they tend to be globally more metal-rich (e.g. Spolaor et al., 2010b). FCC 170 can be considered a massive galaxy in this context.

Other studies also found similar ages in both disks. No important age difference was found in the S0a NGC 4111 by Kasparova et al. (2016). Nevertheless, this galaxy was much younger than FCC 170 (~ 5 Gyr old) and the chemical composition appeared very similar in both disks. Another S0, ESO 243-49, located in the Abell 2877 cluster, did not display important differences in age between the thin and the thick disk. It was analysed by Comerón et al. (2016) using MUSE data. There are some similarities between their maps and the ones we show in this work. ESO 243-49 appeared to be overall old like FCC 170, with no younger thin disk. Differences in metallicity were found between the thin and thick disk regions in ESO 243-49, although less prominent than in FCC 170. In both galaxies these differences were not reflected in age.

Both galaxies are members of a cluster, being the environment potentially important for their evolution. Comerón et al. (2016) adopted a monolithic collapse scenario (e.g. Eggen et al., 1962) to explain the properties of ESO 243-49.

The origin we propose for FCC 170 differs from a simple monolithic collapse, but we do agree with a relatively fast formation at high redshift of both disks, approximately equally old, which stopped forming stars very early. In spite of this, the metal-rich thin disk (as well as the bar and the nuclear disk), had probably little more time to let the gas evolve from subsolar to supersolar metallicities. Moreover, this little time let supernovae type-Ia increase their contribution compared to supernovae type-II, resulting in a lower α-enhancement with respect to the thick disk (e.g. Brook et al., 2004; Yoachim & Dalcanton, 2008b).

Only if star formation in both disks occurred in a relatively short timescale, the age differences between the structural components would have become unrecoverable with our method (Fig. 3.3). The drop in the sensitivity of the Hβ line depth to stellar ages from about 4 Gyr on, in our models (Vazdekis et al., 2010, 2015), together with the age-metallicity degeneracy, makes it arduous to distinguish between different values in the age range of FCC 170. This could also explain why, in Fig. 3.6 and 3.9, nuclear disk, box/peanut and thin disk seem to be born already with high metallicities and low [Mg/Fe], while the Milky Way disk reached supersolar metallicities only after $4-5$ Gyr (Haywood et al., 2013; Snaith et al., 2014). According to the closed-box model (see § 1.2.1), a very high star-formation efficiency would allow an initial almost instantaneous increase of metallicity, even up to supersolar values (Vazdekis et al., 1996). This initial very high star-formation efficiency likely drove the early evolution of FCC 170, since it formed a large stellar mass in a few Gyr. In this case, the initial high metallicity would be expected to be associated to high values of [Mg/Fe], but in this metallicity regime our method could be less sensitive to variations in [Mg/Fe], so that we do not detect them (Vazdekis et al., 2015).

The chemical evolution shown in Fig. 3.6 and 3.9 is somewhat counter-intuitive. After a fast increase in the first Gyr, mean metallicity of recently born stars decreases with time (see e.g. the nuclear disk), contrary to what is usually predicted in a closed box. In addition, we would expect Fe-peak elements to increase with respect to α-elements for later generations of stars. This is not shown in the full age range by our plots, where [Mg/Fe] also increases with time in some epochs depending on the structural component. This behavior might be either real or not (or partially real) due to a combination of the following reasons. On the one hand, the oscillations of [M/H] and [Mg/Fe] with age might be due to technical issues, such as the drop of Hβ sensitivity in the age range of FCC 170. Also line-of-sight effects could be playing a role, in particular in the analysis of nuclear disk and box/peanut. Stars of overlapped structural components, which we are unable to separate, might be dominating specific age bins.

On the other hand we cannot discard the reality of this chemical evolution, counter-intuitive from the point of view of a closed box. It could be due to the accretion of gas less enriched than the host galaxy or accretion of stars with different compositions and ages. They could have happened in several events during the life of FCC 170 or in the single event that brought new populations to the thick disk, as it will be discussed later in this section. Regularization could be responsible for diluting the accreted populations in a wider age range. In the accretion case, the closed-box model could obviously fail. However, a very high star-formation efficiency would allow, even in a closed box, a mild decrease in metallicity related to a hypothetical lack of available gas, after the initial very steep increase of metallicity (Vazdekis et al., 1996).

We advice the reader not to interpret our plots for a quantitative analysis based on the

absolute values. Apart from what explained in the last paragraphs, these might be also affected by the limited age, [M/H] and [Mg/Fe] ranges of the specific SSP models. The fact that the results are mass-weighted should be additionally taken into account. A qualitative analysis based of the mean values per bin should be safe given the spatial coherence between age, metallicity and [Mg/Fe].

FCC 170: in the core of the Fornax cluster

FCC 170 is located in the densest region of the Fornax cluster, where several signs of gravitational interactions have been found. Iodice et al. (2016) found a faint stellar "bridge" between NGC 1399 (FCC 213), the cD galaxy in the center of the cluster, and NGC 1387. This indicates an interaction between the two galaxies, probably stronger in an earlier epoch. In fact, Iodice et al. (2017b) detected intra-cluster light in a quite extended region of the cluster core, including FCC 170. In addition, this light was shown to be the counterpart of previously detected over-densities of blue globular clusters (Bassino et al., 2006; D'Abrusco et al., 2016), indicators of a tidal stream. The morphology, the location and the faintness of this ICL were interpreted by Iodice et al. (2017b) as signs of tidal stripping from the galaxies in this dense region, which would have passed close to the central cD in an earlier epoch. The velocity difference of FCC 170 with respect to NGC 1399 is compatible with tidal interactions with the cluster potential (Iodice et al., 2017b), which could have strongly affected its evolution.

As mentioned in the Introduction (§ 1), Fujita & Nagashima (1999) claimed that the star formation can be enhanced during the first infall of a galaxy into a denser environment and later quenched by stripping processes. However, the intense star formation and the posterior quenching happened in FCC 170 rather early in the life of the Universe, when probably the Fornax cluster was not formed yet as we observe it today. According to Chiang et al. (2013), a Fornax-type cluster would have reached half of the current mass at redshift $z \sim 0.6$, while at $z \sim 2$ it would have had only the 10%. Galaxy clusters have been found up to $z \sim 2$, but protoclusters can be already identified at $z \sim 6$ in cosmological simulations (Overzier, 2016). The progenitors of nowadays's groups and clusters had a very intense star formation, shaping the massive galaxies that we observe today. The more massive the halo, the higher the star formation rate.

As pointed out by Iodice et al. (private communication) FCC 170 has a receding velocity similar to other three galaxies in the same region of the cluster (FCC 167, FCC 182 and FCC 190, see e.g. Ferguson 1989), while $\sim$300 km s^{-1} larger than the central galaxy FCC 213. This suggests that these four galaxies, aligned in the north-south direction, belonged to a primordial (sub-)group, before falling into Fornax. That could be the environment favoring the initial intense star formation in FCC 170, giving rise to a relatively large stellar mass fast and early. Its gas could have been (partially) exhausted, and the remaining amount (if any) could have been stripped out later by interactions of different nature. The star formation was quenched very early. This "pre-processing" before entering the current-day cluster (Haines et al., 2012, 2015) would have given already the observed appearance to FCC 170, with roughly no gas nor dust, nor young populations, and could explain the shape of its SFH (as shown in § 3.5.4). We send the reader to Chapter 4 for a further discussion about the environment of FCC 170 and a comparison to other two S0 galaxies in different locations of the Fornax cluster.

Signs of accretion in the thick disk

In FCC 170, the thick disk is clearly made up by the contributions of different populations, as shown in § 3.5.4 and 3.5.5. The thick-disk main population was probably born already thick. It is old and its composition is different from the rest of the galaxy. Its α-enhancement indicates that it must have formed relatively faster. However, the presence of the second peak in the SFH (Fig. 3.5) calls for a different origin for this younger population. Its chemistry is very different not only from the rest of the galaxy but also from the older population in the thick disk (Figs. 3.6 and 3.9). This population formed later, from a less enriched gas and in an even shorter timescale than the oldest population. An external origin could explain these properties. Stars would have been formed, in a satellite with its own chemistry, about 10 Gyr ago. The satellite would have had a stellar mass of at least $2.5 \times 10^9\,M_\odot$, according to Fig. 3.8, taking into account that this lower limit was obtained only from the region covered by our data and the satellite could have lost material at larger distances from FCC 170 during the early phase of accretion. Its accretion could have preceded the onset of type-Ia supernovae in its stellar population, leaving its stars with the observed high values of [Mg/Fe]. As suggested by Qu et al. (2011), its stars could have been initially distributed with an increasing fraction with height. The bottom panel of Fig. 3.8 indicates that they dominate several bins of the inner thick disk. Nonetheless, the top panel shows that these stars probably had the time to be redistributed overall the galaxy and to migrate mostly to the central region.

FCC 170's formation could have much in common with the "two-phase scenario". This scenario was initially proposed for early-type galaxies by Oser et al. (2010), based on their simulations. It includes a first *in-situ* phase at high redshift ($z \gtrsim 2-3$) followed by a second *ex-situ* phase at intermediate or low redshift ($z \lesssim 2-3$). The first phase would have been dominated by an *in-situ* star formation related to gas inflows. This phase is characterized by an early star formation peak which is relatively extended in time. It could explain the main very old stellar populations in all the components of FCC 170. The second phase would have been characterized by the accretion of stars from satellites and could explain the secondary peak in the SFH of the thick disk and box/peanut of FCC 170. Yoachim & Dalcanton (2005) invoked satellite accretion to explain the thick-disk kinematics of the two galaxies in their sample. In addition, the variety of the kinematics observed by Yoachim & Dalcanton (2008a) confirmed the compatibility with an external origin. In one galaxy in the sample of Yoachim & Dalcanton (2008b), stars appeared to be more α-enhanced at larger radii, also interpreted as a later accretion. We cannot determine the moment when the (minor) merger(s) happened in FCC 170, but we do not expect it to be recent because we do not see morphological disturbances in any of the maps (e.g. Fig. 3.2). In addition, direct mergers would be rare in the very dense environment where we observe FCC 170 now (§ 1.2.2). However, they could have been rather probable in the proposed primordial (sub-)group, where FCC 170 could have lived during the "pre-processing" phase before entering the cluster.

Although we have strong features characterizing each component, they also contain a lower mass fraction of other populations (see Figs. 3.7, B.1 and B.4). This mixing of the different populations, was also probably caused by some merger activity subsequent to the accretion of stars, while we cannot rule out secular mixing processes. Possibly one or both mechanisms distributed the stars of different (younger) populations in the different components, without erasing the global chemical differences. Together with the fact that the accreted stars correspond

only to a modest fraction of the stellar mass, their re-distribution could explain why we do not see any sign of accretion in the kinematics (e.g. we do not see any strong rotation lag).

This mixing culminates in the thin disk metallicity flaring, involving a sufficient amount of stars to make it clearly visible in the velocity dispersion and metallicity maps. The thin-disk flaring was previously detected in the photometric analysis of FCC 170 by Iodice et al. (2017a). A bi-dimensional model of the light distribution was obtained for each early-type galaxy in the core of Fornax. The method, detailed in Iodice et al. (2016), consisted of extracting the azimuthally-averaged intensity profile, fitting isophotes in elliptical annuli with the same position angle and ellipticity. They subtracted the bi-dimensional model to the observed light, obtaining a residual image showing all deviations from pure ellipses in the shape of galaxies outskirts. While for the other galaxies in the sample they detected asymmetric elongations, a thin-disk flaring appeared in FCC 170, as shown in Fig. 3.10. Comparing the scales in Fig. 3.10 and Fig. 3.3, we can confirm that the same flaring shape visible in light is reproduced by the chemical composition.

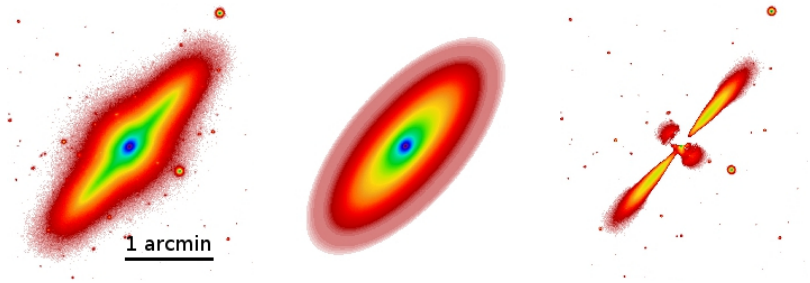

FIGURE 3.10— Isophotal analysis for FCC 170 in the r-band from Iodice et al. (2017a). From left to right: data from the Fornax Deep Survey (Iodice et al., 2016), bi-dimensional model and residual image. The latter was obtained subtracting the model from the data and clearly shows the thin-disk flaring.

Flares have been related with mergers in several previous works (e.g. Walker et al., 1996; Kazantzidis et al., 2008; Villalobos & Helmi, 2008; Read et al., 2009; Bournaud et al., 2009; Qu et al., 2011; Minchev et al., 2015). Bournaud et al. (2009) claimed that the outer regions of disks were more sensitive to the kinematic heating caused by minor mergers, given their lower density. Also, in their simulations, the disruption of the satellite left most of the mass and energy to the outer disks. In FCC 170, the absence of any visible age radial gradient disfavors the inside-out formation scenario proposed by Minchev et al. (2015). We cannot rule out differences of few Gyr, though. Flares do not have to be necessarily related to mergers, they can also have their origin simply in the disk potential, as shown by Narayan & Jog (2002a). However, the specific environment where FCC 170 suffered from gravitational interactions in the past points to them as responsible for this flaring. Because our galaxy mainly formed in a fast early process, mergers probably heated the outer thin disk when it was already formed, whereas the thick disk had formed before. Our MUSE data are not deep enough to go sufficiently far from the midplane and see if the thick disk flares too.

The boxy-bulge and the nuclear disk

An X-shape in the metallicity map was previously observed in NGC 4710 by Gonzalez et al. (2017) and in the Milky Way by Fragkoudi et al. (2018). Gonzalez et al. (2017) explained it with a kinematic fractionation model (Debattista et al., 2017). According to this scenario, stellar populations can be separated by an evolving bar according to their initial radial velocity dispersion (see also Fragkoudi et al. 2017a). (Younger) more metal-rich stars would have been dynamically colder when the bar formed. Therefore they would have been vertically redistributed in the central region of the bar in a way that produces the X-shaped structure. More metal-poor stars, dynamically hotter, would have become vertically thicker in a more uniform (but weaker) box-shaped configuration. An X shape in the age map and age vertical gradients were also predicted by Debattista et al. (2017). They warned, though, that such age differences (of the order of 2 Gyr) could be difficult to detect. In fact, they were not observed in NGC 4710 nor in FCC 170. As also suggested by Gonzalez et al. (2017), the age resolution might not have been sufficient to detect these differences in both galaxies.

To explain observations of a drop in velocity dispersion associated with nuclear disks, Emsellem et al. (2001) proposed a formation scenario from gas inflow along the bar. Emission lines have been found in nuclear disks in other galaxies, supporting this picture (e.g. Chung & Bureau, 2004). On the one hand this scenario might not fit very well to FCC 170, where we do not see any clear correspondence of age with kinematics (and metallicity) and no current star formation is detected. Star formation finished relatively early in both nuclear disk and bar, if we do not consider the minor younger population accreted later to the bar (Figs. 3.6 and 3.9). The nuclear disk must have formed almost contemporarily to the bar. On the other hand, the nuclear disk looks colder than the bar, supporting the gas inflow scenario and an *in-situ* formation (Morelli et al., 2010). It appears also more metal-rich than the bar, likewise the nuclear disks produced by Cole et al. (2014) with simulations of bar-driven gas inflows. Its lower values of [Mg/Fe] than the bar, suggest a slightly slower formation process. It could have formed from fresh cold gas infalling, driven by the forming bar, with differences in timescales that we are not able to detect in age.

3.7 Summary and conclusions

We have observed a small nuclear disk, a prominent central X-shaped structure, a massive thin disk and a complex thick disk in the Fornax-cluster galaxy FCC 170. These structures are clearly distinguishable in the maps of velocity, velocity dispersion, skewness, metallicity and [Mg/Fe]. This massive S0 galaxy looks overall old. Although some younger populations are present, no important differences are detected in the mean age of all the structural components. Regarding the chemical composition, FCC 170 is characterized by metal-rich thin disk, bar and nuclear disk, with solar or slightly supersolar [Mg/Fe] abundances. On the other hand, it displays a more metal poor and α-enhanced thick disk. The star formation history indicates that the thick disk is the mix of different stellar populations. A very old component contributes most of the mass. It has subsolar metallicities and larger [Mg/Fe] abundance than the rest of the galaxy. A secondary younger component, even more metal-poor and α-enhanced, formed around 10 Gyr ago. We have shown a certain level of mixing of the different populations throughout the galaxy. A flaring of the dynamically colder thin disk clearly incorporates metal-rich stars to the

geometrically-defined thick-disk region, corresponding to a potential third component.

Supported by the results of our analysis, we propose a formation scenario for FCC 170 including an *in-situ* formation followed by the accretion of *ex-situ* stars. We suggest that the star formation peaked early, between 13 and 14 Gyr ago, probably accelerated by the "pre-processing" environment (i.e. a preliminary group or sub-group) where the galaxy could have lived before its infall into the Fornax cluster. Almost all the stellar mass was formed rather rapidly, as shown by its overall solar/supersolar [Mg/Fe] abundance. On the one hand stars in the thick disk, the most α-enhanced and metal poor, would have been formed in a shorter time and from gas not chemically enriched yet. The star formation was probably a little slower in the thin disk, bar and nuclear disk. Here, the interstellar medium would have had time to evolve reaching supersolar metallicities. The contribution by supernovae type-Ia would have become noticeable leading to abundance of [Mg/Fe] around solar. Differences in the timescales would have been smaller enough not to be detected with our age resolution, but sufficient to change the dominant processes of the gas enrichment. Star formation would have been globally quenched after few Gyr, probably helped by gas stripping processes. On the other hand, about 10 Gyr ago, another population would have been formed on an even shorter timescale in an even more metal-poor satellite galaxy. Afterwards, the satellite would have been accreted during a minor merger adding this younger population with a different chemistry to FCC 170. The same or other mergers could be also responsible for a relative mixing of the populations and for the thin disk flaring.

4

Thick disks of S0 galaxies in different regions of the Fornax cluster.

The material included in this chapter is based on the article:
Pinna F., Falcón-Barroso J., Martig M. et al., to be submitted to Astronomy & Astrophysics.

We used deep MUSE observations from the Fornax 3D survey to perform the stellar-kinematic and population analysis of FCC 153 and FCC 177, two edge-on S0 galaxies in the Fornax cluster. This allows us to describe the nature of their thick disks. The latter are both old, relatively metal poor and [Mg/Fe]-enhanced, and their star formation history (SFH) reveals a minor younger component whose chemical properties suggest its later accretion. These two galaxies show signs of relatively recent star formation in their thin disks and nuclear star clusters (NSCs). While the thin disks show more continuous SFH, the NSCs display a rather bursty SFH. Given that these two galaxies are located outside of the densest region of the Fornax cluster, where FCC 170 lives, we discuss our results in the light of the previous study presented in Chapter 3. The differences between these three galaxies, at different distances from the cluster center, confirm that the environment can have a strong effect in the galaxy evolutionary path.

4.1 Introduction

Recent works on stellar populations of thick disks in external galaxies have globally shown their diversity. Thick disks of different ages (between 4 and 11 Gyr) were found by both Yoachim & Dalcanton (2008b) and Kasparova et al. (2016) in their samples of late-type and S0-*a* galaxies, respectively. Their thick disks also displayed metallicities in a very wide range. The thick-disk relative properties compared to the respective thin disks display also a certain variety. On the one hand, a clear distinction in age between the thick and the thin disk has been shown in most of analyzed galaxies (see also Comerón et al. 2015). On the other hand, two very old S0 galaxies were found in clusters by Comerón et al. (2016) and us (see Chapter 3). The thin and thick disks of these two galaxies showed approximately the same age, but a clear difference in their chemical properties unveiled the different origins and evolution of the two disks.

This variety of thick disks points to different origins among galaxies with different structures and in different environments. The most invoked scenarios support either a galactic or an extra-galactic origin. Thick disks could have been formed *in-situ* from dynamically hot turbulent gas at high redshift, during the phase of multiple gas-rich mergers (Brook et al., 2004). Alternatively, its stars might have come from the a pre-existing disk, dynamically colder and thinner, which would have been dynamically heated (e.g. Bournaud et al., 2009). This disk thickening could have happened fast at high redshift, being minor mergers the most invoked processes responsible for it (e.g. Quinn et al., 1993; Kazantzidis et al., 2008). Another possibility is that thick-disk stars were formed *ex-situ* and accreted later (Abadi et al., 2003). While Comerón et al. (2015) preferred a "born hot" thick disk for ESO 533-4, and Comerón et al. (2016) proposed a "monolithic collapse" for the formation of both the thin and the thick disks in ESO 243-49, Yoachim & Dalcanton (2005, 2006, 2008a,b) strongly supported accretion as formation scenario for thick disks of their sample. Nonetheless, different mechanisms could follow one another and be responsible for the formation of the thick disks that we observe today. In Chapter 3, we proposed a combination of both stars formed *in-situ* and *ex-situ* to explain the complexity of the thick disk in FCC 170.

Environment, closely connected to the global history of a galaxy, has important consequences also in the nature of its thick disk (Kasparova et al., 2016). The galaxy infall into a cluster could initially accelerate the star formation, which could also be quenched by stripping processes, when approaching to the cluster core (e.g. Fujita & Nagashima, 1999). As proposed for FCC 170, this evolution could also happen during the "pre-processing" phase in galaxy groups before entering the cluster (e.g. Haines et al., 2015). At the same time, mergers could contribute with new populations (Abadi et al., 2003) or create flares in the disks (e.g. Bournaud et al., 2009). The relation between thick-disk origin and galaxy formation and evolution also stresses the importance of thick-disk studies to probe the proposed scenarios in different environments.

Considering the very reduced sample of galaxies whose thick disks have been exhaustively analyzed, this work aims to contribute the stellar kinematics and populations of two more galaxies. We perform the same analysis done in Chapter 3 for two more edge-on S0 galaxies in the Fornax cluster. This chapter is outlined as follows. Section 4.2 describes the sample. Sections 4.3 and 4.4 characterize briefly the data set and the methods, leading to the results presented in § 4.5. In § 4.6 we discuss our results, also in the more general context of the Fornax cluster. Section 4.7 summarizes our conclusions.

4.2 The sample

The sample analyzed in this chapter includes two edge-on S0 galaxies: FCC 153 and FCC 177. Similar to FCC 170, they belong to the Fornax cluster, a dense and dynamically relaxed nearby system (e.g. Sarzi et al., 2018). Thus, the properties of these three galaxies are representative of S0 in clusters and their evolution histories could test the role of environment in shaping lenticular galaxies. Furthermore, their different positions in the cluster, as indicated in Fig. 4.1, make this work an excellent opportunity to discuss the galaxy evolution in different locations of the same cluster. The most relevant properties of FCC 153 and FCC 177 are summed up in Table 4.1 (where we have also added FCC 170 for completeness) and their images in the r-band are shown in Fig. 4.1. Their distances are such that 10 arcsec in the sky correspond to about 0.89 and 0.96 kpc, respectively. FCC 177 is slightly more extended than FCC 153, although the latter is slightly more massive. When it comes to the thick-to-thin luminosity and mass ratios, we expect FCC 153 to behave as a massive galaxy and to be thin-disk dominated ($V_c \sim 165\,\mathrm{km\,s^{-1}}$, see Table 4.1), according to the criterion by Yoachim & Dalcanton (2006). Because of its lower circular velocity ($V_c \sim 120\,\mathrm{km\,s^{-1}}$), FCC 177 is right on the limit to be considered massive.

TABLE 4.1— Relevant properties of the two galaxies in the sample.

FCC[(1)] name	Alternative names	D[(2)] (Mpc)	D_c[(3)] (°)	(Mpc)	R_e[(4)] (″)	(kpc)	$v_{c,max}$[(5)] (km s^{-1})	M_*[(6)] (10^9M$_\odot$)	z_{c1}[(7)] (″)	(kpc)	r_{NSC}[(8)] (″)	(kpc)
153	IC 1963 IC 0335	18.37	1.17	∼ 0.37	11.4	∼ 1.02	∼ 165	∼ 9.5	5.1	∼ 0.5	∼ 0.2	∼ 0.02
177	NGC 1380A PGC 13335	19.86	0.79	∼ 0.27	15.0	∼ 1.44	∼ 120	∼ 7.9	8.4	∼ 0.8	∼ 0.4	∼ 0.04
170	NGC 1381 PGC 13321	21.78	0.42	∼ 0.22	13.8	∼ 1.46	∼ 280	∼ 26.8	10.8	∼ 1.1		

Notes. (1) Galaxy name from the Fornax Cluster Catalog (Ferguson, 1989). (2) Distance from Tully et al. (2013). (3) Projected distance from the cluster central galaxy FCC 213 (Iodice et al., private communication). (4) Effective radius in the B-band (e.g. Sarzi et al., 2018). (5) Maximum circular velocity, from Bedregal et al. (2006). (6) Estimate of the total stellar mass from the morphological components in Comerón et al. (2018). (7) Lower limit of the region where the thick disk dominates, according to the photometrical decomposition by Comerón et al. (2018). (8) Mean radius of the region dominated by the NSC (Turner et al., 2012).

The mid-plane kinematics as extracted by D'Onofrio et al. (1995) and Bedregal et al. (2006) does not show, in both galaxies, any other prominent structure than an edge-on disk, which starts to dominate from very close to the galaxy center. In agreement to this, Johnston et al. (2012) used only a disk component to fit FCC 153 in their spectroscopic bulge-disk decomposition. Lütticke et al. (2000) classified the bulge of FCC 177 as a boxy-bulge, but the one in FCC 153 as an elliptical bulge. Comerón et al. (2018) performed a photometric decomposition using two disk components and a small central mass concentration for both galaxies in our sample. They calculated the height z_{c1} above which most of the light is emitted by the thick disk. Its values, in Table 4.1, indicate a thicker thin disk for FCC 177 than in FCC 153. Turner et al. (2012) identified nuclear star clusters (NSCs) in the center of numerous galaxies of the Fornax cluster, including FCC 153 and FCC 177. Their NSCs were described bluer than their hosts, suggesting the predominance of younger populations of stars. According to their surface brightness analysis, the nucleus dominates over the host up to a mean radius of about 0.4 arcsec in FCC 177 and

0.2 arcsec in FCC 153. Nevertheless, in the latter galaxy, the nucleus is not much brighter than the host even in the center.

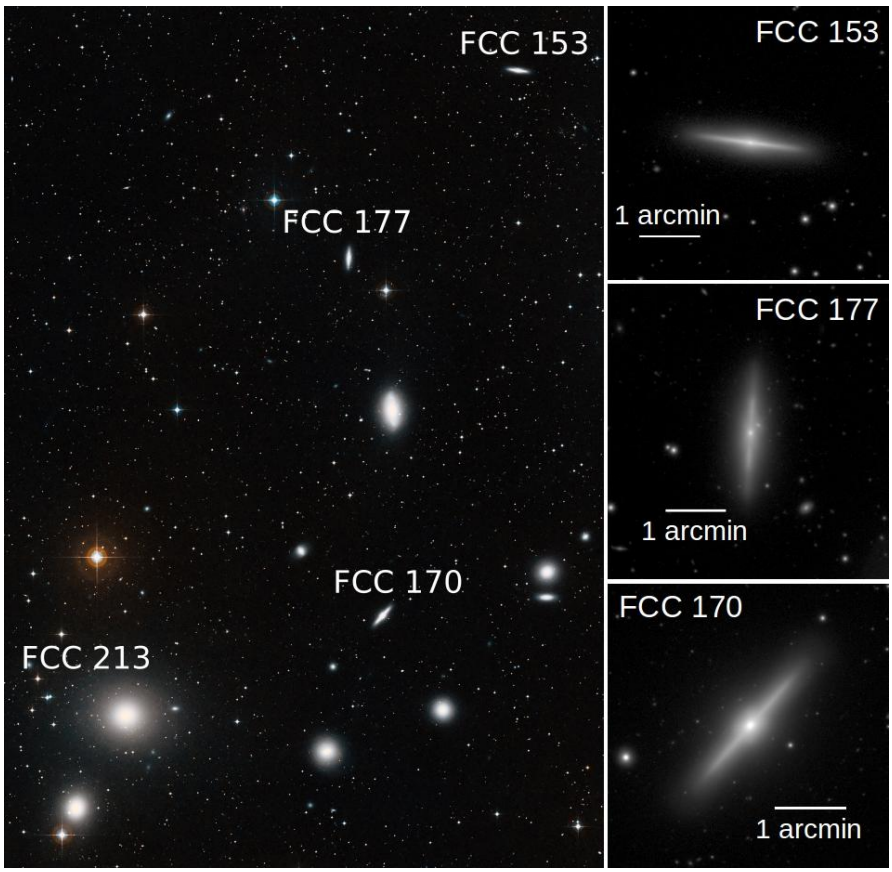

FIGURE 4.1— Left: clipping of the Wide-field view of the Fornax Galaxy Cluster from `http://www.eso.org/public/images/eso0949m/` (credit:ESO and Digitized Sky Survey 2, acknowledgment: Davide De Martin). The three galaxies analyzed in this thesis are indicated with their names. FCC 213 is the central galaxy of the cluster. Right: *r*-band images from the Fornax Deep Survey (Iodice et al., 2016): from top to bottom FCC 153, FCC 177 and FCC 170. A scale bar is indicated in each image.

4.3 Observations and data reduction

Deep high-quality integral-field data from the Fornax 3D survey (Sarzi et al., 2018) were used for the present work. They were collected at the UT 4 at the Very Large Telescope (VLT), by

means of the Multi Unit Spectroscopic Explorer (MUSE) (Bacon et al., 2010). Observations were performed in the same way as for FCC 170. They follow the description in Chapter 3 and are detailed in Sarzi et al. (2018). Two MUSE pointings were used for each one of the two galaxies in our sample. The position of these pointings is indicated in Fig. A.1 of Sarzi et al. (2018). On-source exposure times for the central pointings were the same as for FCC 170 (five exposures of 720 s), but they were only of one hour and half for the outer region (9 exposures of 600 s). Dithering, sky subtraction, data reduction and alignment of the two pointings were performed in the same way as for FCC 170.

4.4 Methods

We used the same methods explained in Chapter 3 for FCC 170 to extract the stellar kinematics and populations for FCC 153 and FCC 177. We give here some specific details, sending the reader to Section 3.4 for a more complete description. Looking for a compromise between a good spatial resolution and keeping the gradients in stellar-population maps (avoiding too "noisy" maps), we chose a target signal-to-noise ratio (SNR) per spatial bin of 60 between 4750 and 5500 Å. We used this value to perform the Voronoi binning using the code described in Cappellari & Copin (2003), with a minimum accepted SNR per spaxel of 1. This resulted in 3583 bins for FCC 153 and 3213 bins for FCC 177. Among them, respectively $\sim 45\%$ and $\sim 41\%$ had SNR < 60, but only $\sim 0.8\%$ and $\sim 0.7\%$ had SNR < 50. We discarded 18 and 259 bins respectively for FCC 153 and FCC 177, because their spectra did not allow good fits or they were contaminated by the light of foreground objects.

We fitted our spectra with the Penalized Pixel-Fitting code detailed in Cappellari & Emsellem (2004) and Cappellari (2017), and MILES single-stellar-population (SSP) models from the BaSTI library, in the version with two values of [Mg/Fe] (Vazdekis et al. 2015, see also Section 3.4.2). After checking (directly in the same spectra) that the two galaxies in the sample have barely any line emission, we decided to perform the full-spectrum fitting by pPXF without masking any lines. We fitted stellar kinematics and populations in the same run, using a multiplicative polynomial of 8th order and regularization parameter of 0.5. We used the same approach as for FCC 170 to select the level of regularization. We verified that the features in the age-metallicity-[Mg/Fe] space did not change their position by changing the level of regularization, but they only change slightly their shape. Since the maximum allowed smoothing gave very similar values for the two galaxies, we selected the same regularization for both of them.

4.5 Results

4.5.1 Stellar kinematics

The first four moments of the line-of-sight velocity distribution (LOSVD) for the two galaxies in the sample are mapped in Fig. 4.2 and 4.3. We assume the same order of magnitude as for FCC 170 for the uncertainties in the kinematic analysis ($\delta V \sim 6\,\mathrm{km\,s^{-1}}$, $\delta\sigma \sim 8\,\mathrm{km\,s^{-1}}$, $\delta h_3 \sim 0.030$ and $\delta h_4 \sim 0.035$, Section 3.5). Spider patterns appear in the velocity maps of both galaxies (top panels). The maximum stellar rotation velocity is larger in FCC 153, about $150\,\mathrm{km\,s^{-1}}$, than in FCC 177, about $100\,\mathrm{km\,s^{-1}}$, following the difference between their masses shown in Table 4.1. Signs of cylindrical rotation are not clear in FCC 153, in agreement with

the fact that its bulge is not a prominent bar seen edge-on. In FCC 177, this cylindrical rotation is visible in a box up to about 10 arcsec of radius, corresponding to the boxy bulge.

None of the two galaxies shows a central peak in velocity dispersion, as seen in the second panels from top in both Figs. 4.2 and 4.3. This confirms that we do not have any massive central concentration of stars. The highest σ values are measured in the thick disk region (dominating above z_{c1} from Table 4.1). In FCC 153, the dynamically cold thin disk is well defined with a narrow transition to the dynamically hotter thick disk. It displays a clear flare which starts not far from the galaxy center, implying a radial gradient in the thick-disk velocity dispersion. The thin disk also shows a negative σ gradient up to a certain galactocentric distance, while a little increase in suggested farther in radius. In contrast, the dynamically cold region is much thicker in FCC 177, where a σ vertical gradient is still present above $\sim z_{c1}$. A flaring is not clear, probably also because our data does not go farther enough from the midplane in the external part, where this flaring seems to be suggested.

In the two bottom panels of Fig. 4.2 we can see the anticorrelation of h_3 with V associated to FCC 153's disk (e.g. Krajnović et al., 2008; Guérou et al., 2016). h_4 assumes positive values in the central radii and negative values in the more external radii near the midplane. In FCC 177, no structures are clearly seen in the h_3 and h_4 maps (see two bottom panels of Fig. 4.3) and even the disk $h_3 - V$ anticorrelation is barely suggested.

4.5.2 Mass-weighted stellar populations

The full-spectrum-fitting method used in this work allows us to extract age, total metallicity ([M/H]) and [Mg/Fe] abundance. Since [Mg/Fe] is an indicator of α-element abundances, for simplicity we will refer to its enhancement also as "α-enhancement". We show the mean stellar-population properties of the individual spatial bins of FCC 153 and FCC 177 in Fig. 4.4 and 4.5, where the different structural components of the two galaxies are remarkably clear. We assume uncertainties of the same order of magnitude as for FCC 170 (respectively about 1 Gyr, 0.06 and 0.02 dex for age, [M/H] and [Mg/Fe], see Section 3.5.2 for more details).

In both top panels, there is a clear age distinction between the thin and the thick disk, being the latter very old (about 13 Gyr). Young stars are present close to the midplane, in a much narrower band in FCC 153 than in FCC 177. In addition, the thin-disk youngest stars are concentrated in a certain radial range and a positive age gradient is visible in both galaxies along the thin disk. Younger spatial bins in the thick-disk outer region are probably connected to the thin-disk flaring detected in the velocity dispersion map of FCC 153. The youngest stars are distributed in the center of both galaxies, in a spherical/elliptical shape much larger than the NSC detected by Turner et al. (2012) (see also Table 4.1). This is very likely due to the much larger PSF (Point Spread Function) in our MUSE data than in data from the Advanced Camera for Surveys mounted at the Hubble Space Telescope, used by Turner et al. (2012). We have measured ages down to $\sim$4 Gyr in FCC 153, and down to $\sim$2 Gyr in FCC 177 in their NSCs, while their thin disks appear approximately coeval with one another ($\sim 4-5$ Gyr old in their youngest region).

In the sample analyzed in this chapter, there is a clear correspondence between age and metallicity (top and middle panels in Fig. 4.4 and 4.5), being younger stars more metal rich and vice versa. The NSCs are clearly visible in the metallicity maps, where they assume the highest (supersolar) values. The thin disk is very thin and well defined in FCC 153's metallicity

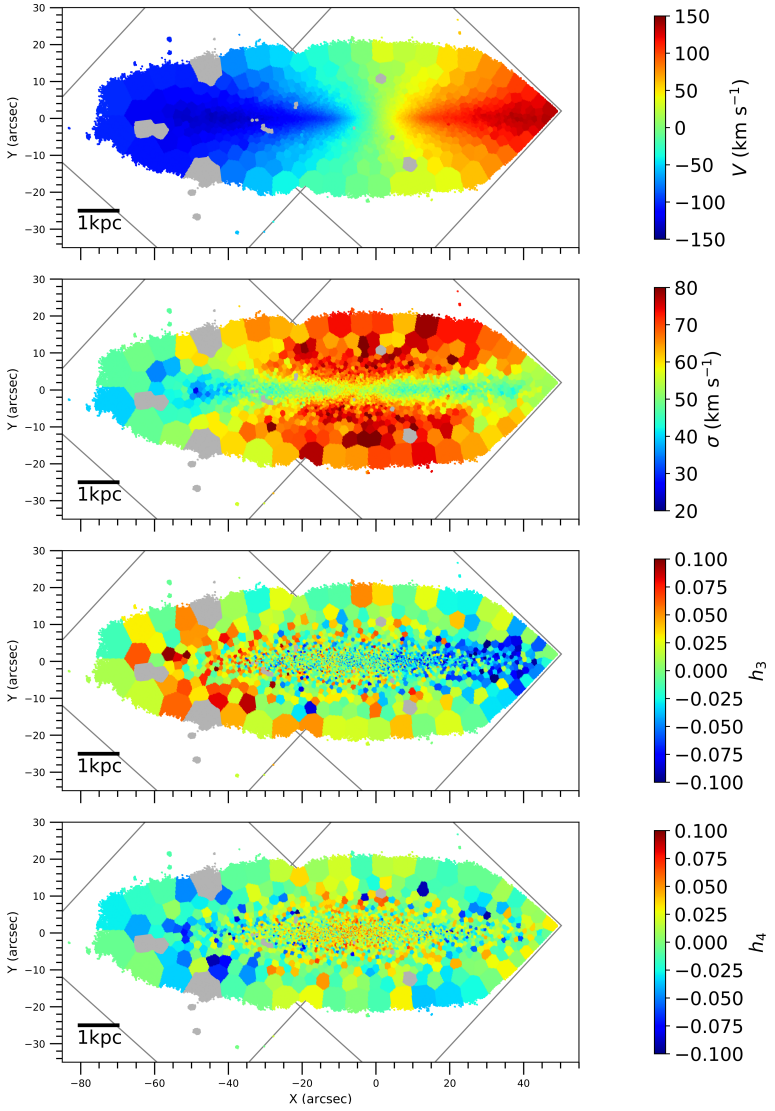

FIGURE 4.2— Maps of the stellar kinematics of FCC 153. From top to bottom: mean velocity V, velocity dispersion σ, skewness h_3 and kurtosis h_4. The discarded bins are plotted in grey, as well as the two MUSE pointings. The physical units are indicated by the scale bar on bottom-left of each panel.

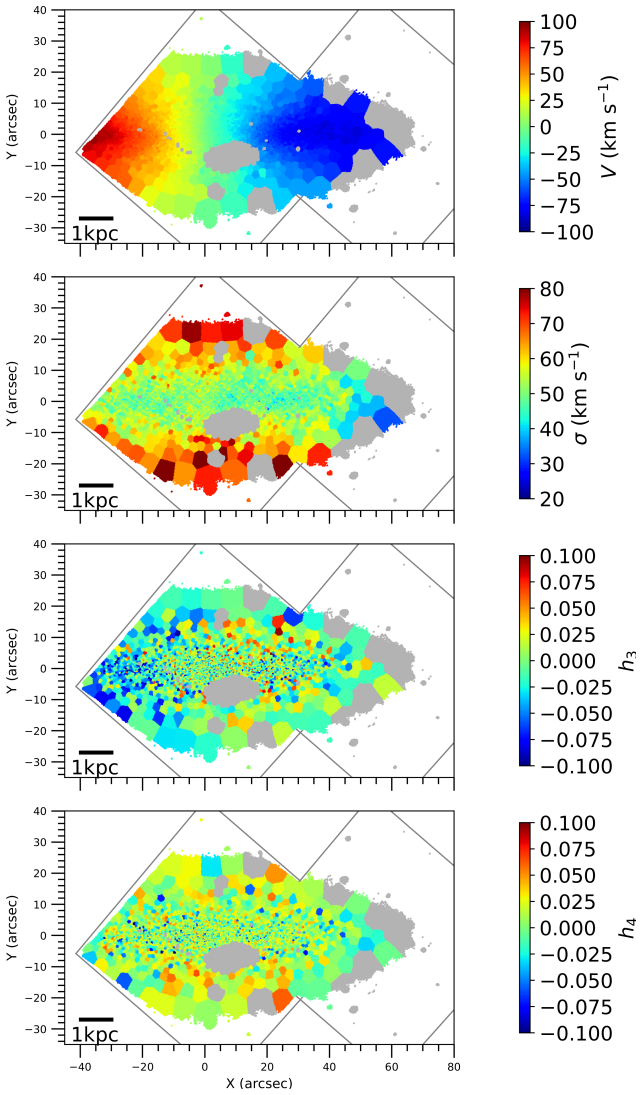

FIGURE 4.3— Maps of the stellar kinematics of FCC 177. From top to bottom: mean velocity V, velocity dispersion σ, skewness h_3 and kurtosis h_4. The discarded bins are plotted in grey, as well as the two MUSE pointings. The physical units are indicated by the scale bar on bottom-left of each panel.

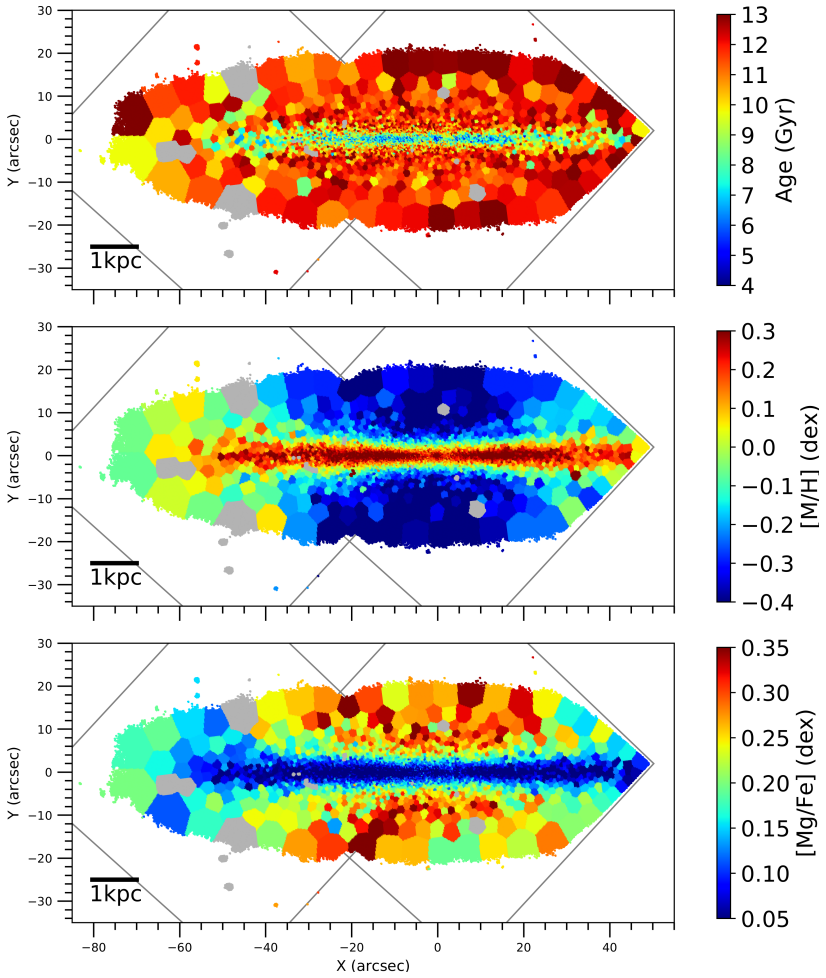

FIGURE 4.4— Stellar-population maps for FCC 153. From top to bottom: mean age, total metallicity [M/H], [Mg/Fe] abundance. The discarded bins are plotted in grey, as well as the two MUSE pointings. The physical units are indicated by the scale bar on bottom-left of each panel.

map. It is thicker and fuzzier in FCC 177. Radial gradients are present in disks of both galaxies. A negative metallicity gradient is seen in thin disks, while the thick-disk subsolar metallicities increase towards the outskirts. The variation of this gradient with height in FCC 153, suggests that it is strongly related to the thin-disk flare. We found similar values of the total metallicity in the thick disks of the two galaxies, while FCC 153's thin disk appears more metal rich than

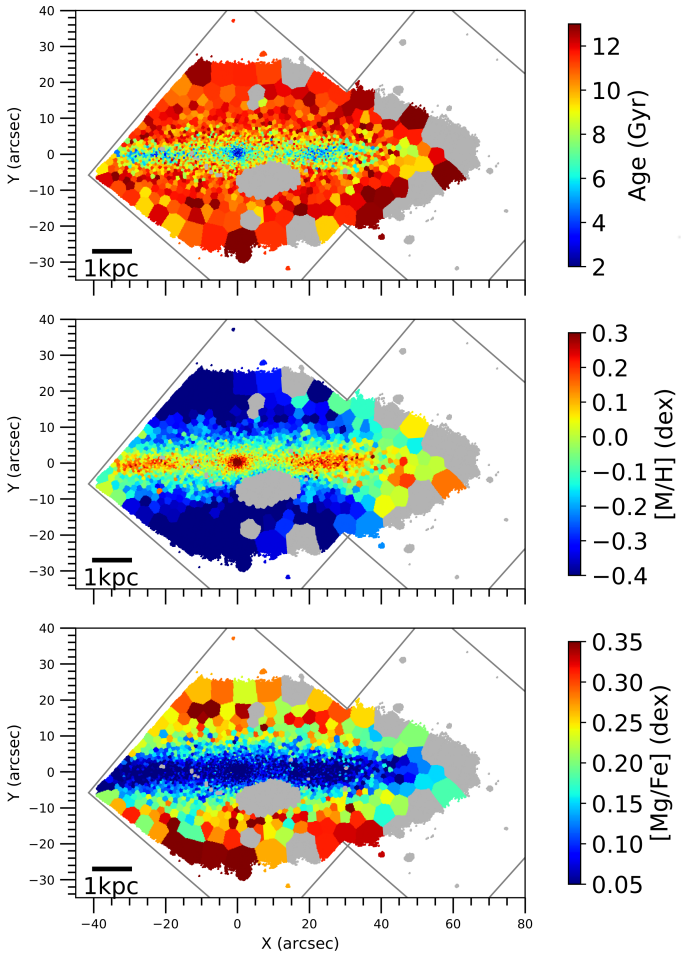

FIGURE 4.5— Stellar-population maps for FCC 177. From top to bottom: mean age, total metallicity [M/H], [Mg/Fe] abundance. The discarded bins are plotted in grey, as well as the two MUSE pointings. The physical units are indicated by the scale bar on bottom-left of each panel.

the one in FCC 177.

The maps of [Mg/Fe] follow age and metallicity (bottom panels in Figs. 4.4 and 4.5). Mid-plane stars display abundances around solar (including the thin disk and the NSC), while thick-disk stars are quite α-enhanced. Also, the metallicity radial gradients correspond to "inverted" [Mg/Fe] gradients: positive in the outer thin disk, but negative in the thick disk (one more time, very clear in FCC 153 and not so clear in FCC 177).

4.5.3 Structural decomposition

We based our structural decomposition on the previous photometric analysis by Comerón et al. (2018) and Turner et al. (2012) (see also Section 4.2), using a similar approach as for FCC 170 (Section 3.5.3) and being somewhat more restrictive for the thick disk than the limits in Table 4.1. We divided the spatial bins according to which of the three main components dominates: NSC, thin disk and thick disk. We excluded a region of transition between the thin and the thick disks, based on our population maps. Given that we could not distinguish the stellar populations of the bulges in our maps, we considered that it was not possible to analyze their properties with the line-of-sight data. However, from the kinematic maps, we were able to define a central region which could be influenced by the bulges (mainly where the mean-velocity spider pattern was not clear). We discarded this region from the analysis of the thin and thick disks in both galaxies. We also divided the thick-disk bins into inner and outer regions, given that they have different kinematic and chemical properties. We selected these two regions according to the maps of σ, [M/H] and [Mg/Fe], defining the inner thick disk as the region where properties were approximately (spatially) constant. In this way, we got rid of the thin-disk flaring in the inner thick disk, while we expect the outer thick disk to be contaminated by thin-disk populations. The limits between the components are indicated in Table 4.2 and mapped in Fig. 4.6.

TABLE 4.2— Structural decomposition of FCC 153 and FCC 177 into NSC, thin disk, inner and outer thick disk.

FCC	NSC		Thin disk		Thick disk			
					Inner		Outer	
	$\lvert x\rvert$ ($''$)	$\lvert y\rvert$ ($''$)	$\lvert x\rvert$ ($''$)	$\lvert y\rvert$ ($''$)	$\lvert x\rvert$ ($''$)	$\lvert y\rvert$ ($''$)	$\lvert x\rvert$ ($''$)	$\lvert y\rvert$ ($''$)
153	< 0.2	< 0.2	> 6	< 2	< 20	> 6	> 20	> 6
177	< 0.4	< 0.4	> 13	< 4	< 25	> 10	> 25	> 10

4.5.4 Star formation history

The structural decomposition in Section 4.5.3 allows us to analyze individually the star formation history (SFH) of the NSC, the thin and the thick disk of the two galaxies. We calculated the SFHs of FCC 153 and FCC 177 using the same method as for FCC 170 (Chapter 3). From the mass in every spatial bin, we estimated the total mass of the two galaxies within the regions covered by our MUSE pointings (discarded bins excluded). This lower limit for the total galaxy mass is $\sim 2.2 \times 10^{10}\,M_\odot$ for FCC 153 and $\sim 8.6 \times 10^{9}\,M_\odot$ for FCC 177, consistent with the literature values in Table 4.1 (resulting, however, from different methods). We show the SFH of the two galaxies in Fig. 4.7, where the mass fraction was normalized to the total mass of the component and it is easier to compare the different populations in the same component, and in Fig. 4.8, where the mass fraction was normalized to the total mass of the galaxy and we can compare between the different components.

The NSCs exhibit "bursty" star formation histories, in the sense that they formed during different intense episodes (green curves in the top panels of Figs. 4.7 and 4.8). The nucleus appears younger in FCC 177 than in FCC 153. It formed relatively few stars in a stable rate between 6 and 12 Gyr ago, but had a later intense burst between 2 and 4 Gyr. FCC 153 formed more stars in its NSC in an early epoch, although had some other recent peaks in the star

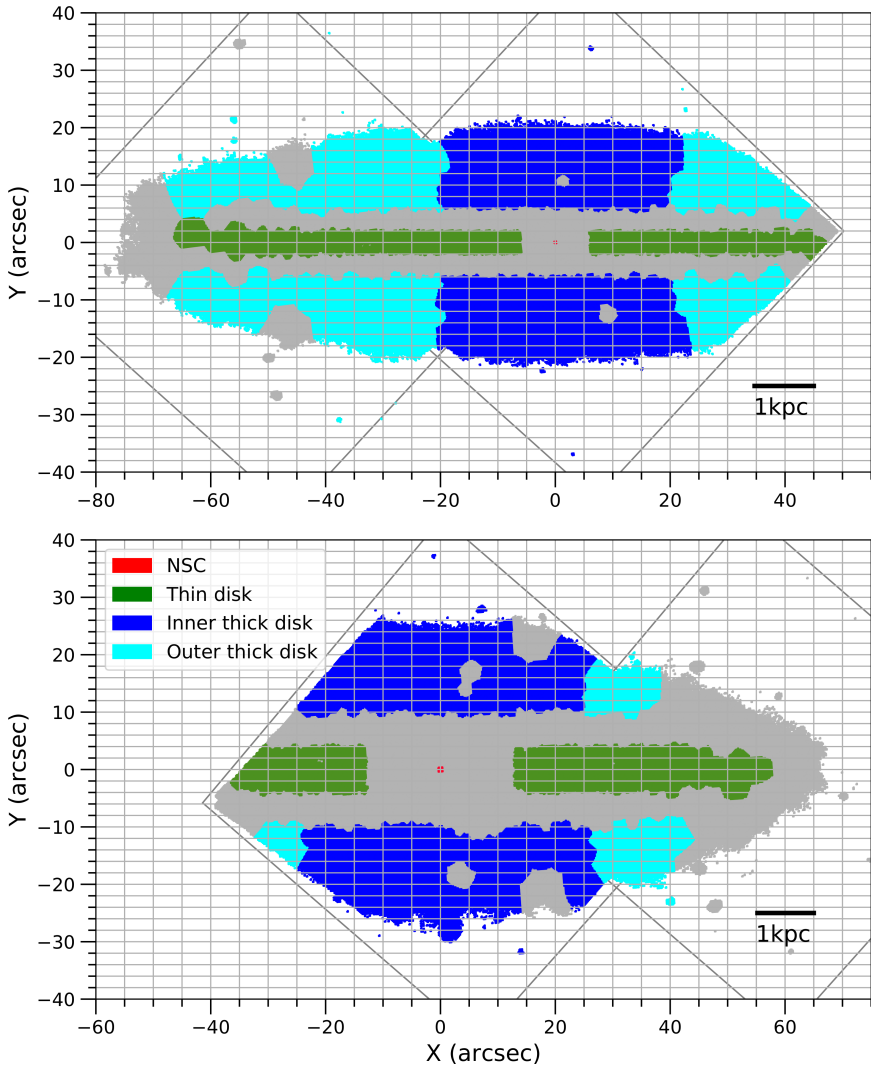

FIGURE 4.6— Structural decomposition for FCC 153 (top panel) and FCC 177 (bottom panel). We have color coded the spatial bins for each one of the components. We divided the thick disk into inner and outer regions. We plotted in grey the spatial bins not taken into account for the study of the individual components (bad bins or bins in the transition where more than one components are important).

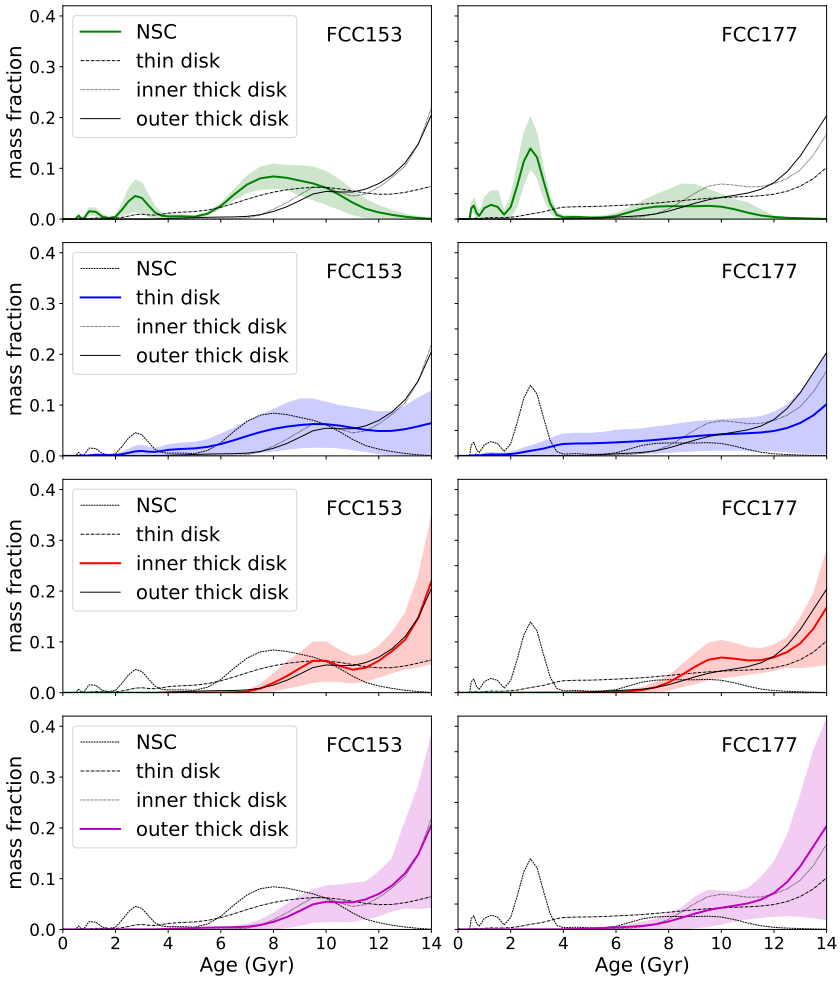

FIGURE 4.7— SFH of the structural components of FCC 153 (left column) and FCC 177 (right column) defined in Fig. 4.6. The average mass fraction, calculated weighting with the mass in the different spatial bins, is displayed on the vertical axis. This mass fraction is normalized to the total mass of the component. In each panel, only one component is represented in a specific color (*green* for the NSC, *blue* for the thin disk, and *red* and *purple* respectively for the inner and the outer thick disk). For the colored component, 1σ uncertainties, calculated as 16 % and 84 % percentiles of the spatial-bin distribution, are represented as shades of the same color. The SFH of the rest of components are plotted in black, with different line styles, in each panel.

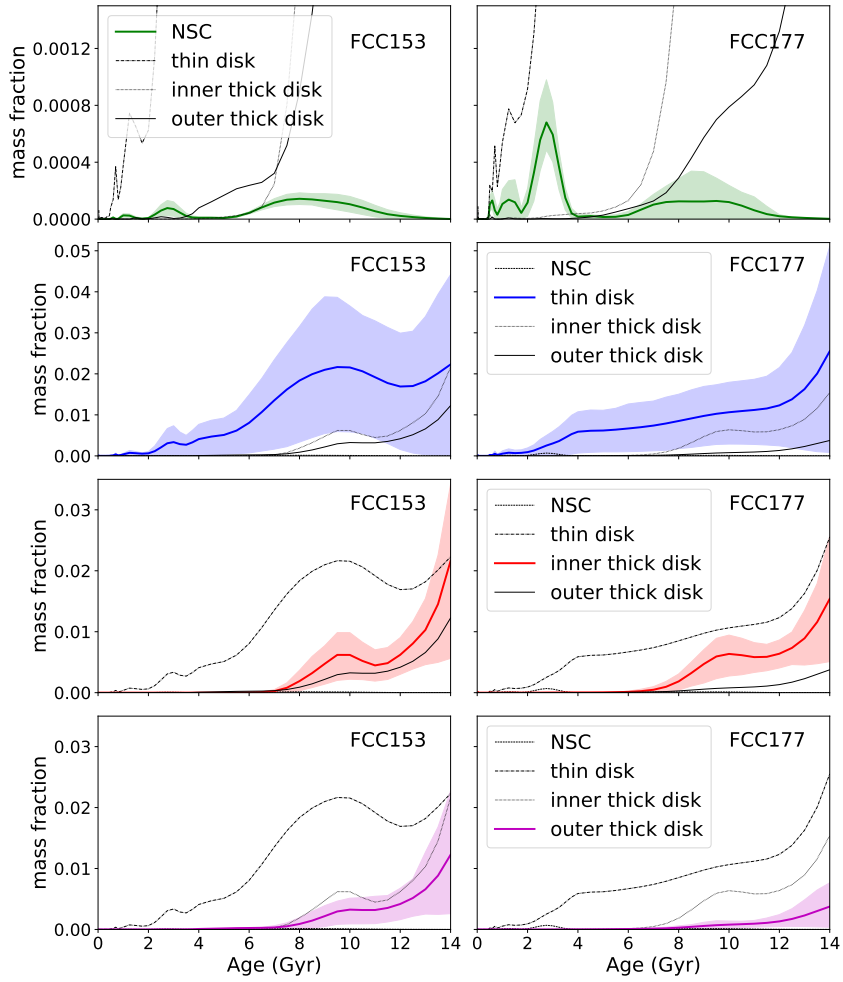

FIGURE 4.8— SFH of the structural components of FCC 153 (left column) and FCC 177 (right column) defined in Fig. 4.6. The average mass fraction, calculated weighting with the mass in the different spatial bins, is displayed on the vertical axis. This mass fraction is normalized to the total mass of the galaxy. In each panel, only one component is represented in a specific color (*green* for the NSC, *blue* for the thin disk, and *red* and *purple* respectively for the inner and the outer thick disk). For the colored component, 1σ uncertainties, calculated as 16 % and 84 % percentiles of the spatial-bin distribution, are represented as shades of the same color. The SFH of the rest of components are plotted in black, with different line styles, in each panel.

formation. The thin disks present a continuous SFH, as shown in the second from top panels of Figs. 4.7 and 4.8. In both galaxies, either they started to form stars very early or line-of-sight effects make the thick disk stars contribute for the oldest ages. FCC 177 seems to have had a more stable star formation in the thin disk than FCC 153. Anyway, thin disks continued to grow their stellar mass up to recent times (about 2 Gyr). The thick disks have very similar SFH in the two galaxies (two bottom panels in Figs. 4.7 and 4.8). They formed early, with a main component $12 - 14$ Gyr old. However, an additional population came later, with 10-Gyr-old stars, indicated by a peak in the SFH. This second younger component is more prominent in the inner thick disk than in the outer thick disk, where we probably have a mixing with other populations due to the thin-disk flaring. This makes the SFH appear slightly smoother in the outer thick disk.

4.5.5 Chemical abundances

We performed a chemical analysis of the different populations color coding the age bins of the SFH histograms, according to their chemical properties. In Fig. 4.9 and 4.10, we show the SFH of FCC 153 (left panels) and FCC 177 (right panels), indicating the mean [M/H] and [Mg/Fe], respectively. We followed the same normalization as in Fig 4.7, to the mass of the structural component. The NSCs, the most metal-rich components, display slightly higher metallicities for the youngest ages (top panels in Fig. 4.9). They display also the lowest [Mg/Fe] abundance, around solar values (top panels in Fig. 4.10). NSCs does not show a strong time evolution in the mean [M/H] and [Mg/Fe]. Thin disks present different initial (average) metallicities for the two galaxies (second panels from top, in Fig. 4.9). FCC 153 started already with a metal-rich thin disk (at older ages), whose interstellar medium seems not to have evolved much since then. On the contrary, FCC 177's thin disk exhibits a clear positive metallicity gradient with time, from about solar values to clearly supersolar. This indicates a gradual chemical enrichment. In relation to their [Mg/Fe], both thin disks display uniform slightly supersolar values along time (see second panels from top, in Fig. 4.10). The extended chemical evolution of FCC 177's thin disk is not visible in the [Mg/Fe] abundance.

Inner thick disks are the most metal-poor and [Mg/Fe]-enhanced components in both galaxies (third from top panels in Figs. 4.9 and 4.10), with a big difference in values if compared to the respective NSCs and thin disks. Similarly to what we found for FCC 170 (Section 3.5.5), the thick disks in FCC 153 and FCC 177 display a dominant very old population and a smaller peak of younger stars. The oldest populations were born with relatively low metallicity, but the gas was slightly enriched during time, increasing a little the mean metallicity of later stars. Then, the new younger populations were added to the thick disks. These components have similar properties in the two analyzed galaxies. They are approximately 10 Gyr old (probably slightly younger in FCC 153) and they have similar metallicities and [Mg/Fe] abundances. These populations brought a new chemistry to the galaxies: the lowest metallicity and the highest [Mg/Fe]. The outer regions of the thick disks (bottom panels in Figs. 4.9 and 4.10), which include the spatial bins located in the thin-disk flare, appear in general slightly less metal-poor and α-enhanced than the inner regions. Probably related to the flare, the difference in the [Mg/Fe] abundance between the inner and the outer thick disk is more pronounced in FCC 153 than in FCC 177.

We can look at the spatial distribution of the different populations mapping the stars in different age and metallicity ranges. We used this approach to produce Figs. 4.11, 4.12, B.2, B.3,

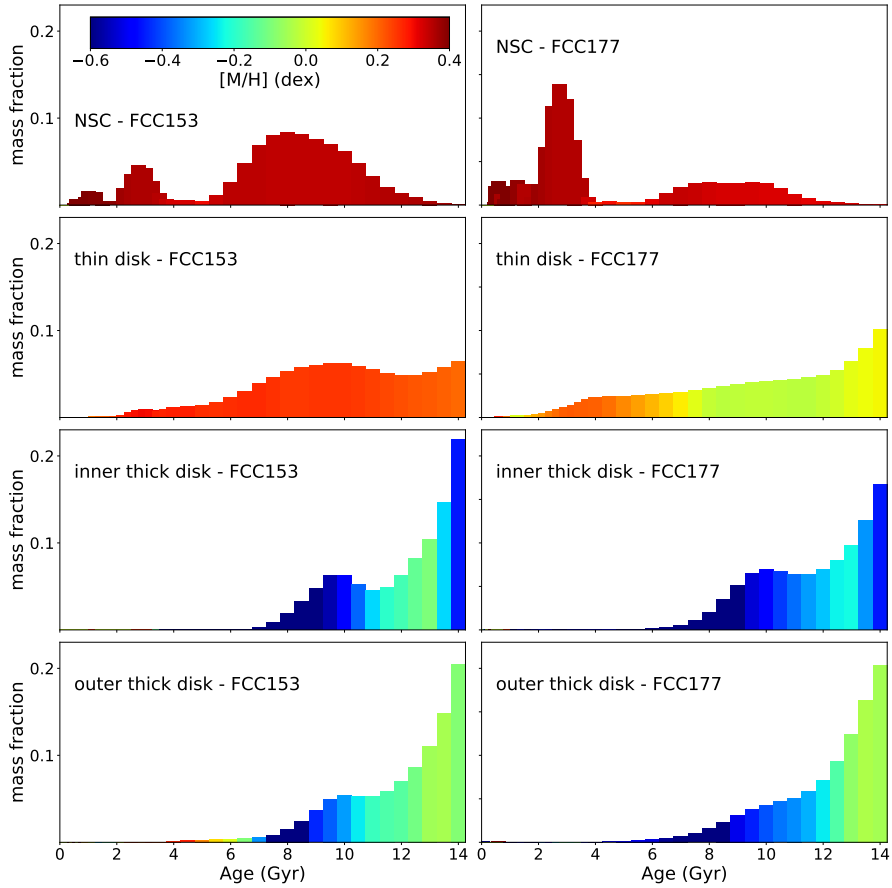

FIGURE 4.9— SFH of the different structural components of FCC 153 (left panels) and FCC 177 (right panels). From top to bottom: the NSC, the thin disk, the inner and the outer thick disk. We color coded the histogram age bins according to the weighted average total metallicity ([M/H]) of the specific age bin. The average mass fraction is displayed on the vertical axis, weighted by the mass in each bin and normalized to the mass of the component.

B.5 and B.6. In FCC 153, we see the metal-rich stars concentrated in the thin disk (supersolar metallicity, top panels of Fig. 4.11). In particular, the relatively young populations (younger than 11 Gyr, top-left panel) are concentrated right in the midplane and absent in numerous bins of the inner thick disk, while the older are denser at a certain (small) height. The populations with subsolar metallicity (bottom panels of Fig. 4.11) are distributed everywhere but with higher density close to the galaxy center, avoiding the midplane where the youngest stars are (especially

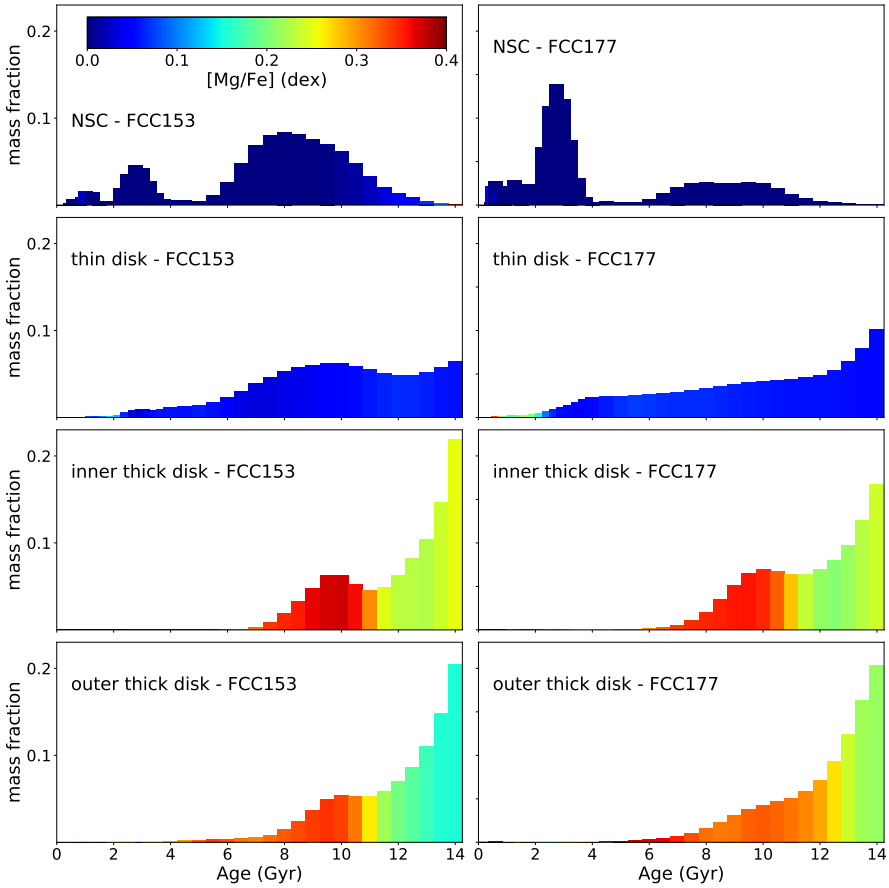

FIGURE 4.10— SFH of the different structural components of FCC 153 (left panels) and FCC 177 (right panels). From top to bottom: the NSC, the thin disk, the inner and the outer thick disk. We color coded the histogram age bins according to the weighted average [Mg/Fe] of the specific age bin. The average mass fraction is displayed on the vertical axis, weighted by the mass in each bin and normalized to the mass of the component.

in the bottom-right panel). Similar results are obtained for FCC 177 (Fig. 4.12). However, the younger metal-rich stars are located mainly in the nucleus, and in a minor extent in the thin disk (top-left panel). The metal-rich but older stars have a more uniform density in a much thicker region aligned with the major axis (top-right panel), than in FCC 153.

In addition, we mapped in Fig. 4.13 and 4.14 the density distribution of the metal-poor and α-enhanced peaks of younger stars, found in the SFHs of the thick disks. In none of the two

galaxies these populations are present in the dynamically coldest region of the thin disks (the closest to the midplane). They are spread over the rest of both galaxies, mainly in a box-shaped region concentric with the galaxy (top panels). The bottom panel of Fig. 4.13 indicates that in FCC 153 the mass fraction of this population is more important at a certain height from the midplane. In FCC 177 (Fig. 4.14), this is more clear and the mass of this population is more prominent in most bins of the inner thick disk than in the rest of the galaxy. The estimates of the mass contribution by these younger populations, in the regions covered by our MUSE data of FCC 153 and FCC 177, were respectively of $\sim 9 \times 10^8\,M_\odot$ and $\sim 4 \times 10^8\,M_\odot$.

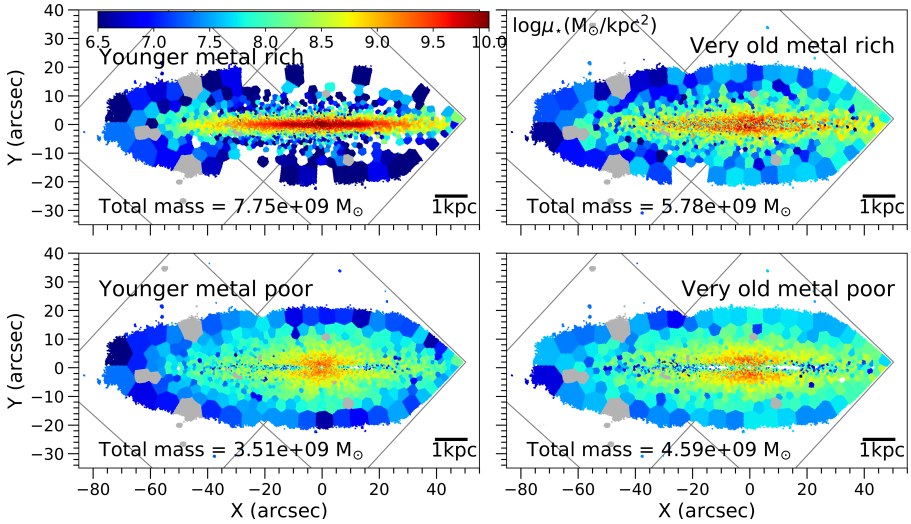

FIGURE 4.11— Spatial distribution of stars of a given range of age and metallicity, in FCC 153. *Top*: most metal-rich populations ([M/H]$\geq$ 0.06 dex). *Bottom*: most metal-poor populations ([M/H]≤ -0.25). *Left*: little younger populations (ages $\leq$11.0 Gyr). *Right*: oldest populations (ages $\geq$11.5 Gyr). The color scale shows the mass density corresponding to the populations in the specific age-metallicity bin. The total mass in the age-metallicity bin is indicated on bottom-left of each map. The position of the two MUSE pointings is plotted in grey. A scale bar on bottom-right of each map indicates the correspondence with physical units.

4.6 Discussion

4.6.1 Comparison to previous results

FCC 153 ans FCC 177 are not well-known galaxies, but previous long-slit studies revealed the stellar kinematics or the stellar populations along the major axis. Our velocity maps in Figs. 4.2 and 4.3 follow the rotation curves plotted by D'Onofrio et al. (1995). Nonetheless, we found lower values for σ in both galaxies. On the other hand, our kinematics are in very good agreement with Bedregal et al. (2006), who attributed their discrepancy in σ with D'Onofrio et al. (1995) to a resolution issue in the previous work. Bedregal et al. (2006) also found no peculiarities

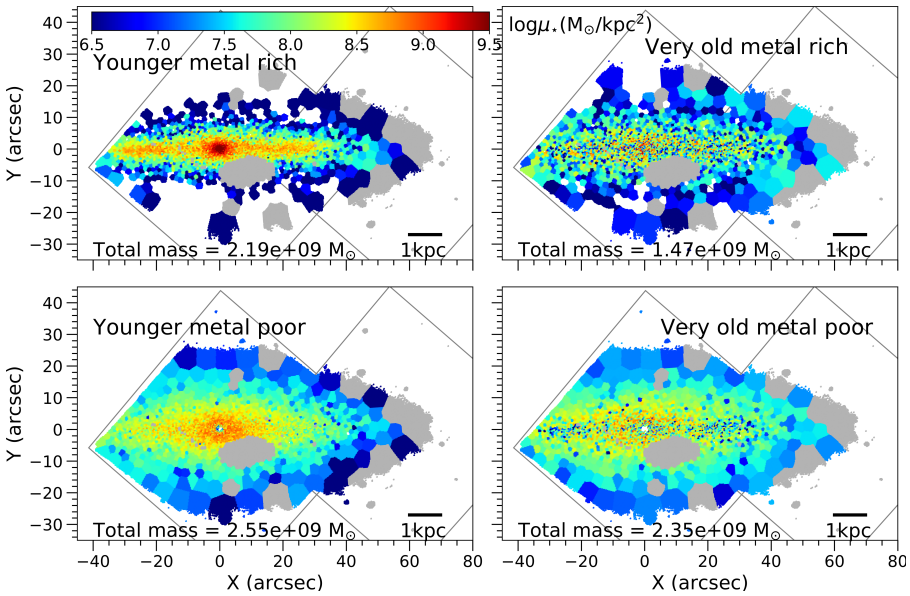

FIGURE 4.12— Spatial distribution of stars of a given range of age and metallicity, in FCC 177. *Top*: most metal-rich populations ([M/H]$\geq$ 0.06 dex). *Bottom*: most metal-poor populations ([M/H]≤ -0.25). *Left*: little younger populations (ages $\leq$11.0 Gyr). *Right*: oldest populations (ages $\geq$11.5 Gyr). The color scale shows the mass density corresponding to the populations in the specific age-metallicity bin. The total mass in the age-metallicity bin is indicated on bottom-left of each map. The position of the two MUSE pointings is plotted in grey. A scale bar on bottom-right of each map indicates the correspondence with physical units.

in h_3 and h_4, as in our Figs. 4.2 and 4.3, confirming the simple velocity structure shown by the mean velocity. Stellar populations extracted by Spolaor et al. (2010b), Koleva et al. (2011) and Johnston et al. (2012) give slightly younger luminosity-weighted ages in the midplane of FCC 153 and FCC 177, compatible with our results.

4.6.2 Formation and evolution of S0 galaxies in the Fornax cluster

In this thesis we analyzed a sample of three S0 galaxies within the virial radius of the Fornax cluster. In Chapter 3, we described an overall old S0, with no clear age distinction between the thin and the thick disk. In this chapter, we analyzed two galaxies quite similar to each other, but very different from FCC 170. They do show a clear age distinction between the thin and the thick disk, in agreement with literature on the Milky Way and external galaxies (e.g. Gilmore & Reid, 1983; Yoachim & Dalcanton, 2008b; Comerón et al., 2015). This age difference is sharper in FCC 153, but remarkable in both galaxies suggesting a different formation process for the two geometrically defined disks. While their thick disks formed faster during the early stages of the life of these two galaxies, from the initial metal-poor gas, thin-disk formation was probably slightly delayed (although we cannot see this small age difference in our SFHs). This would

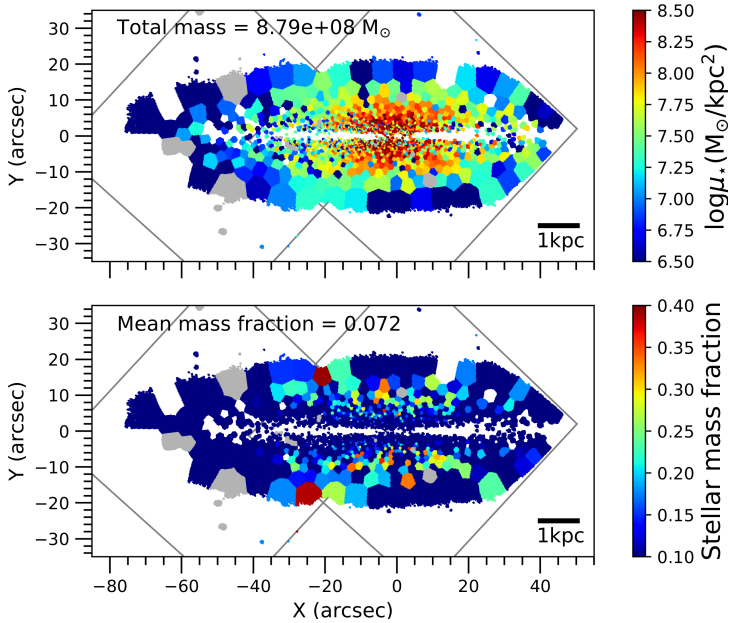

FIGURE 4.13— Distribution in FCC 153 of the stellar population with ages between 6 and 11 Gyr, metallicity between -0.6 and -0.35 dex and [Mg/Fe]∼0.4 dex. The color scale shows the stellar mass density in the top panel and the stellar mass fraction in the bottom panel. The total mass or the mean mass fraction in this specific population are indicated on top-left of respectively the top and the bottom maps. In each panel, the position of the two MUSE pointings is plotted in grey and a scale bar on bottom-right indicates the correspondence with physical units.

explain the presence of old stars with already higher metallicities and lower [Mg/Fe] abundance than in the thick disk (especially in FCC 153, more massive, probably initially evolved in a shorter timescale than FCC 177) and was discussed for FCC 170 in § 3.6.2. In FCC 153 and FCC 177, the bulk of thin disks would have formed slowly in an extended time, following the chemical enrichment.

Our stellar-population analysis points clearly to different evolutions for FCC 170 from FCC 153 and FCC 177. To disentangle between the potential reasons, we analyze the differences between these galaxies. First of all, they have different total masses. FCC 170 is the most massive, followed by FCC 153 and then FCC 177, according to their maximum circular and rotation velocities. Their stellar masses follow the same order (see Table 4.1). Koleva et al. (2011) observed the down-sizing phenomenon in the Fornax cluster. The star formation was shifted to galaxies with lower mass along time. We observe this trend in our sample, since FCC 177 has the lowest mass and the youngest stars, while the most massive FCC 170 hosts only old stars. Kuntschner (2000) confirmed in Fornax a correlation between luminosity and age in lenticulars, previously found in Coma (Terlevich et al., 1999). This means that the systems

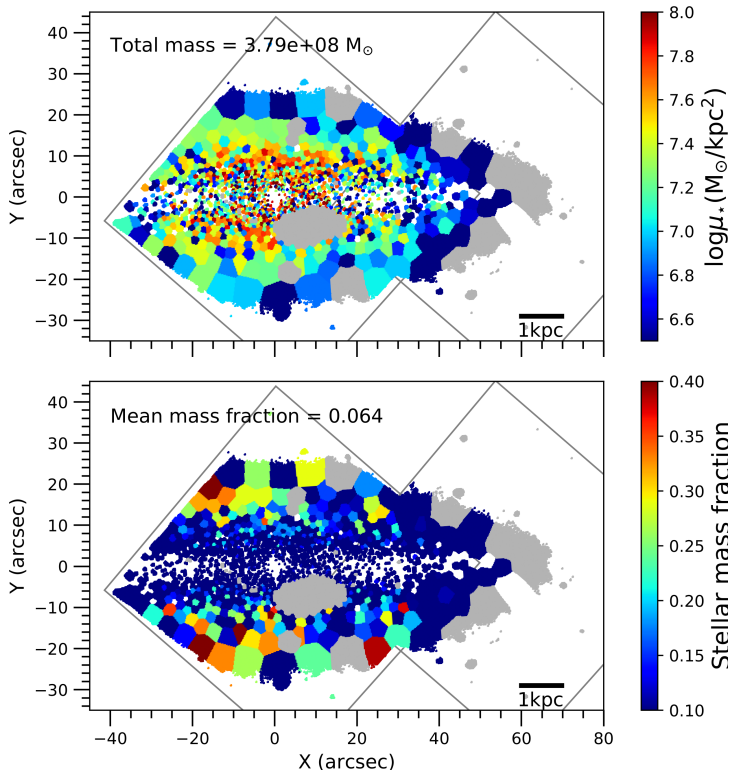

FIGURE 4.14— Distribution in FCC 177 of the stellar population with ages between 6 and 11 Gyr, metallicity between -0.6 and -0.35 dex and [Mg/Fe]∼0.4 dex. The color scale shows the stellar mass density in the top panel and the stellar mass fraction in the bottom panel. The total mass or the mean mass fraction in this specific population are indicated on top-left of respectively the top and the bottom maps. In each panel, the position of the two MUSE pointings is plotted in grey and a scale bar on bottom-right indicates the correspondence with physical units.

hosting younger populations are predominantly fainter S0 galaxies. In addition, Kuntschner (2000) and Bedregal et al. (2008) recovered some stellar-population properties of ellipticals in the central regions of brightest lenticulars, including FCC 170. They proposed a faster timescale formation for the more massive S0 galaxies, which are older and more α-enhanced. This pointed towards different formation scenarios for bright and faint S0 galaxies. The authors suggested that the former (at least their central regions) would have a similar origin to ellipticals, since they have similar SFHs, while the latter would be more likely the results of spirals after loosing their gas. The properties of FCC 170 from our analysis correspond to the description of bright S0s. FCC 153 and FCC 177, defined as "intermediate" (brightness) S0s by Bedregal et al. (2006), already harbor young populations and their global SFH is noticeably different from FCC 170.

As indicated in Fig. 4.1 and Table 4.1, the three galaxies are located at different distances from the cluster central galaxy FCC 213: FCC 170 is the closest, while FCC 153 is the farthest. FCC 170 lives within the highest density region of Fornax, where tidal interactions were proposed as the stripping mechanism traced by the spatial distribution of intra-cluster light (Iodice et al., 2017b) and blue globular clusters (D'Abrusco et al., 2016; Cantiello et al., 2017). Moreover, as suggested in Chapter 3, FCC 170 could have belonged to a primordial subgroup, before falling into the Fornax cluster. There, its star formation could have been accelerated, forcing to form a large mass in a short time. The rest of gas (if any) would have been later stripped out causing an early quenching. The higher mass of FCC 170 (compared to the other two galaxies) and the presence of a massive bar in it, not displayed prominently by FCC 153 and FCC 177, could also be related to its past environment different from the other two galaxies. For instance, bar formation can be triggered by gravitational interactions (e.g. Martinez-Valpuesta et al., 2017). The fact that FCC 153 and FCC 177 are located in a lower density intra-cluster medium, out of this very dense central region of the cluster, in addition to the lack of a pre-processing phase in a previous subgroup, probably marked the difference in the SFH of their thin disks. Unlike FCC 170, they could form stars in an extended time, until few Gyr ago. According to Kuntschner (2000), young S0 could have been accreted recently to the Fornax cluster, since they tend to be in the periphery.

Although FCC 153 and FCC 177 display common properties in contrast to FCC 170, they show some individual peculiarities. Iodice et al. (private communication) studied the photometric properties of early-type galaxies in the Fornax cluster, in relation to their locations. They found a clear correlation of galaxy morphology and color with environmental density, which is shown in Fig. 4.15. Red galaxies are distributed in a wide region where X-ray emission, indicating high hot-gas density, was detected (Paolillo et al., 2002). Bluer galaxies are located farther from the center. Fig. 4.15 shows that galaxies in our sample are not located in regions with the same density and display different colors. FCC 177 and FCC 170 are redder and located within the region traced by the X-ray emission. FCC 153, still within the cluster virial radius, lives in a lower intra-cluster density region and is bluer. Some properties of the thin disks could be related to this segregation. FCC 153's thin disk is very thin and its chemical properties are spatially well defined. In FCC 177 it is thicker and fuzzier. Some mixing between stars with slightly different stellar-population properties might be suggesting disk heating processes happened to red galaxies in their denser environment.

Iodice et al. also found thin-disk flaring structures in the three galaxies, both in the r-band, subtracting a bi-dimensional model as shown in Fig. 3.10 for FCC 170, and in $g-i$ color images. Of similar morphology in FCC 170 and FCC 153, the thick flare appeared more extended in the former, while FCC 177 showed a thinner flaring structure. However, only the flares of FCC 153 and FCC 177 were found to be prominent in $g-i$. Their colors are different and could be suggesting different flaring-formation mechanisms, related to the different locations of the two galaxies. FCC 153 displays bluer colors in its outskirts, while FCC 177 is redder especially in the flaring region. FCC 170 displays a less pronounced flare in $g-i$.

In our stellar-population maps, the best spatially defined flaring is found in FCC 153. Slightly more confused in [Mg/Fe] and only suggested in age, "mono-metallicity" flares of progressively more metal-rich and dynamically-colder populations are sharply evident in the metallicity and velocity dispersion maps, from a certain radius towards the outskirts. The stellar-population properties of the flares in FCC 170 and FCC 177, on the contrary, look more mixed and no age

radial gradient is hinted. This could be another indicator of the different flare origins suggested by the colors from Iodice et al. (the flare is bluer in FCC 153). While for FCC 170 and FCC 177 gravitational interactions could have dynamically heated the thin-disk stars forming the observed more "disordered" flares, the composition of FCC 153's flare by several "mono-metallicity" flares could be suggesting a secular-evolution origin. The striking anticorrelation between metallicity and velocity dispersion seems to be suggesting a flaring of dynamical origin (Narayan & Jog, 2002a,b). However, although spatial bins in the flare display younger ages, we do not see in FCC 153 the age radial gradient predicted by the inside-out formation proposed by Minchev et al. (2015).

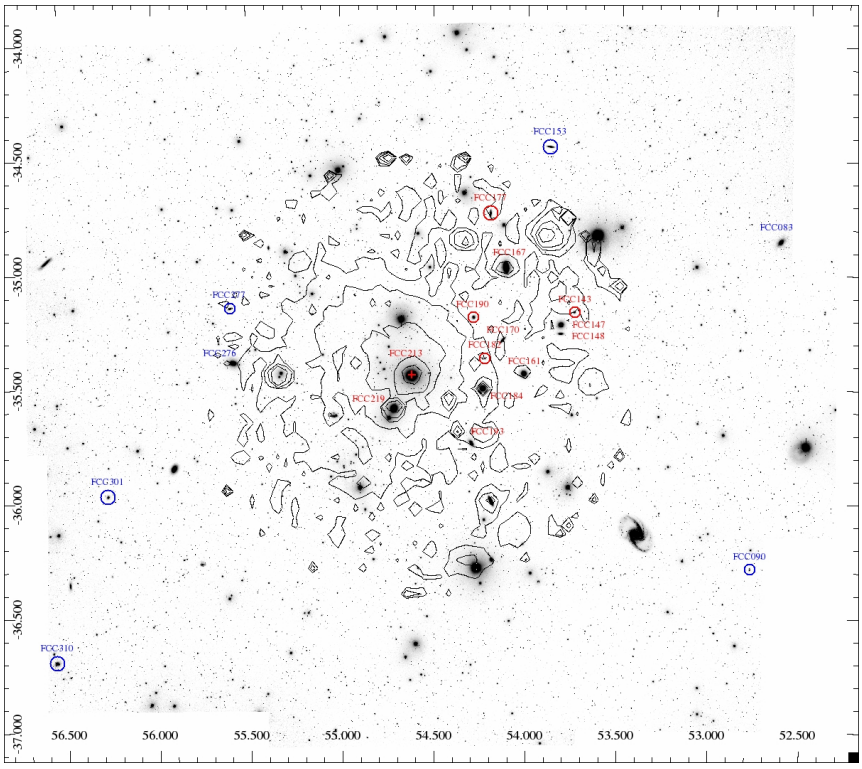

FIGURE 4.15— Mosaic of the Fornax cluster in the g-band, from Iodice et al. (private communication). X-Ray emission from ROSAT is superposed with black contours. Galaxies listed in blue are blue early-type galaxies ($g - i \leq 0.8$ mag and $g - r \leq 0.4$ mag) and the one listed in red are red galaxies.

Thick disks

For the thick disks in FCC 153 and FCC 177, we propose the same two-phases formation as for FCC 170. In a first phase, $2-4$ Gyr long, most of thick-disk stars were quickly formed *in-situ*, still allowing some chemical evolution until the second *ex-situ* components came up. The oldest *in-situ* population, given its chemical composition, could have been formed already as a thick component, in a fast timescale, from turbulent gas. However, an alternative origin could be possible, especially for FCC 177. Here, dynamically colder stars extend well above z_{c1} and the transition between thin and thick-disk populations is not as clear as in FCC 170 and FCC 153. Vertical gradients cover a thick region in the maps of σ, [M/H] and [Mg/Fe]. Because of these (only hinted) continuity between the properties of the thin and the thick disk, we cannot rule out pictures as disk heating or upside-down formation of an unique (thick) disk component in FCC 177.

The younger *ex-situ* populations have roughly similar properties in the three thick disks (seen as bumps in the SFHs), in spite of being hosted by galaxies with different properties and in different locations of the cluster. They show mean ages between 8 and 11 Gyr, [M/H] ~ -0.6 and [Mg/Fe] $\sim 0.34-0.36$. We consider accretion the best possibility to explain that these additional components formed later and with their peculiar chemical properties, when the rest of the host galaxies were already forming more chemically enriched stars. Accreted satellites could have been more metal poor according to their much lower mass compared to the host galaxies. We have checked what stellar mass these satellites should have had, corresponding to their [Fe/H], according to the stellar mass-metallicity relation for Local Group dwarfs, in Fig. 9 of Kirby et al. (2013). Using our approximate mean values of [M/H] and [Mg/Fe] to calculate [Fe/H]=[M/H]-0.75 [Mg/Fe] (Vazdekis et al., 2015), we roughly estimated a stellar mass of about $10^9\,M_\odot$ for the satellites. Our lower-limit estimates of the accreted masses for FCC 153 and FCC 170 were of the same order of magnitude (Sections 3.5.5 and 4.5.5). In proportion to the host galaxy mass, the contribution of the accreted population in FCC 153 approximately double the one in FCC 170 and FCC 177. For FCC 177 we found only $\sim 4\times10^8\,M_\odot$. In this case, this lower limit excludes a relatively wide region near the galaxy center (we discarded its spatial bins due to the presence of a foreground object), where this population is more concentrated (Fig. 4.14). For this reason, we could be missing even more mass than in the other two galaxies. In FCC 153 the satellite would have contributed about the 10% of the total stellar mass, and the 4 and 5% respectively in FCC 170 and FCC 177.

We should be cautious in associating these accreted masses to the initial satellite masses. These galaxies, before being accreted, could have had a total mass rather larger than the contribution that we see now in their hosts. They could have lost a significant mass fraction, still at large distances from the host galaxy, during the early stages of their accretion. Although we discourage a quantitative comparison to other studies based on absolute values (see § 3.6.2), our values of [Mg/Fe] are in general higher than what expected from previous works on galaxies of about $10^9\,M_\odot$ with comparable total metallicities (e.g. the Large Magellanic Cloud, Van der Swaelmen et al. 2013, with a stellar mass of about $8.7\times10^9\,M_\odot$, van der Marel 2006). A larger initial satellite mass, together with the dense environment where these satellites could have lived, could help to explain this chemical abundances (see e.g. dwarfs and ellipticals in clusters, Sybilska et al. 2017).

In the three galaxies, the accreted stars were formed (in the satellite) before the host-galaxy

quenching, as shown by the SFHs. For FCC 170, not much time passed in between and we propose that these satellites were accreted soon after their formation. This would not give them time for contamination from supernovae type-Ia and could explain their α-enhancement. We suggest that they were accreted before that cluster velocity dispersions were high enough to prevent direct mergers, probably before the infalling of these galaxies into the Fornax cluster. It could have happened during the intense merger epoch around redshift $1 - 1.5$ (e.g. Brook et al., 2004).

The difference in metallicity and [Mg/Fe] abundance between the old (*in-situ*) and the young (*ex-situ*) populations looks much sharper in the SFH of FCC 170 than in FCC 153 and FCC 177 (Figs. 3.6, 3.9, 4.9 and 4.10). In the thick disks of the latter, the transition towards the most metal-poor and α-enhanced youngest stars is rather gradual. On the one hand, this smoothing could be (at least partially) real, given that our SFHs represent the mean properties of all populations of a certain age. Therefore, in the transition between the old and the younger components, we go (more or less gradually) from ages still dominated by the *in-situ* populations to the *ex-situ*-dominated populations. On the other hand, we should also consider this apparent (second) chemical evolution to be an artifact caused by the regularization used in pPXF. In general, this introduces a smoothing between different-population ages, metallicities and [Mg/Fe], probably reproducing the real behavior in most cases, but maybe sometimes introducing unreal or excessive smoothing, if the real transition between populations is sharper (as expected from accretion). These two interpretations (regularization and mixing of *in-situ* and *ex-situ* stars) could explain also the similar chemical evolution towards higher [Mg/Fe] in the nuclear and thin disks and in the box/peanut of FCC 170 (Fig. 3.9). An alternative speculation could be the "wet" nature of the satellite merger, which would have accreted less evolved gas resetting the [Mg/Fe] "clock". These and other interpretations were discussed for FCC 170 in § 3.6.2.

Another explanation for the α-enhancement in the thick disks and especially in their younger populations would be a varying IMF (Martín-Navarro et al., 2015a,b; La Barbera et al., 2016; Lyubenova et al., 2016; Martín-Navarro, 2016). In our sample, an interpretation of the IMF slope as a local property could explain the differences among the structural components in their chemistry, in spite of the similarities in their SFH shapes (especially in FCC 170). In addition, a time evolution of the IMF shape would explain the chemistry evolution in individual regions without invoking a timescale change (see e.g. Fig. 3 in Martín-Navarro 2016). In a similar way, a different IMF in the accreted satellites could justify its chemical composition. Current studies on the IMF in the Fornax 3D galaxies will probably add helpful insights to this discussion.

NSCs in the Fornax cluster

NSCs were detected in the three galaxies of our sample by Turner et al. (2012). Their blue colors are in agreement with the young ages we found in the central regions of FCC 153 and FCC 177. However, given their reduced size and the prominent boxy bulge in the center of FCC 170, the NSC in this galaxy was not visible in our maps.

The two most invoked scenarios to form NSCs are the star-cluster infall towards the galaxy center, due to dynamical friction, and the inflow of gas to the nuclear region, triggering star formation *in-situ*. Turner et al. (2012) preferred the second one for the galaxy-mass range of our sample, capable to form the observed young populations. The bursty SFH measured in our stellar-population analysis fits well with different phases of gas accretion. This gas could

have come from previous mergers, from supernova winds or from disk instabilities (e.g. Ordenes-Briceño et al., 2018). Kuntschner (2000) suggested that galaxy harassment could have driven some disk gas towards the galaxy center of young S0s in the Fornax cluster, causing a final burst. In the case of FCC 153 and FCC 177, still keeping a young extended disk, the bulge would have stabilized the disk preserving part of its gas.

The low [Mg/Fe] since the formation of the first stars in the nuclei could be the hint of a bottom-heavy IMF. We can speculate that if the gas was accreted in different stages in low-mass amounts and immediately formed stars, exhausting the gas until a new accretion, massive stars were never enough to enhance the [Mg/Fe] abundance. Nevertheless, the most enriched gas was driven towards the center, forming stars probably with a steeper IMF.

4.7 Summary and conclusions

This work completes the study of thick disks in the three edge-on S0 galaxies of the Fornax cluster, started in Chapter 3. FCC 153 and FCC 177, located in a less dense intra-cluster medium compared to FCC 170, appear very different from it, indicating a different evolution history. Unlike FCC 170, the stellar kinematics and populations of FCC 153 and FCC 177 reveal structures composed by relatively young thin disks embedded in old thick disks, and small, young NSCs in the central regions. A clear spatial correspondence is shown between mean stellar age and chemical properties. Youngest stars are the most metal-rich and least α-enhanced, concentrated in the mid plane and the very central region. The thick disks are the most metal poor and α-enhanced components.

Both galaxies display bursty SFHs in their NSCs until very recent times, suggesting a nuclei growth driven by gas infall in different events. Thin disks formed their mass in an extended time and did not suffered from an early quenching as FCC 170 did. FCC 153's thin disk appears very thin and well geometrically defined, with a flaring clearly seen in velocity dispersion, [Mg/Fe] and especially metallicity. Radial gradients are seen in these properties both in the thin and thick disks. FCC 177 has a more fuzzy and thick thin disk. The transition towards the thick disk is less clear and the thin-disk flaring is not obvious. The differences between the two galaxies could reside in the different density in their locations. While FCC 177 and FCC 170 live in the red galaxies higher-density area traced by the X-ray emission, FCC 153 is bluer and is located outside of this hot dense gas.

Thick-disk SFHs fit the same two-phase formation scenario that we proposed for FCC 170: in a first *in-situ* phase the old component would be formed, while in the later phase a second younger component, formed *ex-situ* with different chemical properties, would have been accreted.

5

Conclusions and future work

THICK disks were discovered only some decades ago and have been proved to be ubiquitous in galaxies relatively recently. Since they are one of the oldest components in galaxies, they have raised a growing interest in the community, who thinks that understand their origin could be of great importance to understand more globally the history of galaxies.

The present thesis was motivated by the low number of detailed studies on thick disks and the lack of agreement about their origin in the literature. First, we analyzed specifically one of the mechanisms potentially forming the thick disks, the disk dynamical heating, which had enjoyed previous extensive studies especially in the Milky Way. However, the main purpose of this thesis is to present our contribution to the characterization of thick disks in S0 galaxies in dense environments, providing a comprehensive possible picture for their formation and evolution.

We revisit the main conclusions of this work in § 5.1, already summarized at the end of each one of the three previous chapters, and we describe the future plans to follow up in § 5.2.

5.1 Conclusions

Aiming to extend the study done by Gerssen & Shapiro Griffin (2012), where they showed a clear trend in the SVE-Hubble type relation, we gathered results on the disk vertical-to-radial velocity dispersion ratio for 55 galaxy disks from observational publications. We added 26 galaxies from N-body simulations, which also allowed us to assess some of the proposed disk heating scenarios and analyze the time evolution of the SVE. We drew the following conclusions:

- No strong correlation, between the disk SVE shape and the galaxy morphological type, is found globally in the sample from the literature, either in simulations. This suggests a much more complicated picture. Early-type disk galaxies do not have necessarily isotropic ellipsoids and late types can have ellipsoids as isotropic as early types and as anisotropic as possible.

- In previous studies, it was suggested that different SVE shapes correspond to different heating mechanisms. If this is true, not only galaxies with similar morphology can be

affected by different sources of disk heating, but also the same mechanisms can act both on early and late types.

- Bars reveal themselves to be a good radial heating agent in our numerical simulations.
- Mergers with mass ratios 1:10 to 1:3 provide, on average, isotropic heating in our zoom-in cosmological simulations, while quiescent mechanisms (e.g. spiral structures) tend to flatten the SVE.
- The present-day shape of the ellipsoid, in galaxies with past mergers, depends on the time when they happened. This could explain the scatter of σ_z/σ_R in the SVE-Hubble type relation among galaxies with strong recent mergers and similar morphology. The strength of mergers' impact depend on how dynamically cool were stars when these mergers happened and how long has passed since the last merger. Moreover, mergers' signatures in the SVE can fade with time.

The main general conclusion of this first part of the thesis is that the assessment of the disk dynamical heating mechanisms is quite complicated. Therefore a satisfactory analysis cannot be achieved only with observational measurements of the SVE shape. We specify the main reasons in the following:

- σ_z/σ_R is sensitive to small velocity dispersion variations which do not mean necessarily that the disk has been dynamically heated.
- A present-day more isotropic ellipsoid could have been produced by different situations not necessarily related to the disk heating: an increase of σ_z but also a decrease of σ_R or a disk born already thicker and that did not change. Similarly, anisotropy can be related to different heating or cooling processes.
- The present-day SVE results from the combination of different heating (cooling) processes.
- A variety of velocity ellipsoid shapes can be produced by the same heating mechanism in different specific situations.
- In turn, different heating histories can generate the same SVE shape.

With the purpose of contributing to the characterization of thick disks in external galaxies, we analyzed the stellar kinematics and populations of three edge-on S0 galaxies in the Fornax cluster, by means of deep MUSE data from the Fornax 3D survey. The study led to the following results and conclusions.

- The kinematics of our sample revealed different structures.
  - FCC 170 has a complex structure: fast-rotating nuclear disk and thin disk, slower-rotating thick disk and prominent X-shaped bulge with the highest values of velocity dispersion.
  - FCC 153 and FCC 177 do not display any prominent central mass concentration in the velocity dispersion maps.

  - The distinction between the dynamically-hotter thick disk and the cooler thin disk is clearer in FCC 153, with a much thinner thin disk than in FCC 177.

- These structures are recovered by stellar-population maps in different ways.
  - In FCC 153 and FCC 177, relatively young, metal-rich and less α-enhanced thin disks are embedded in old, more metal-poor and α-enhanced thick disks. Young nuclear star clusters stand out in the central regions with their high metallicity and slightly supersolar [Mg/Fe].
  - In FCC 170, thin disk, box/peanut and nuclear disk display much higher values of metallicity and lower [Mg/Fe] abundance than the thick disk. However, these structural components are not clearly distinct in the age map, although the thin disk seems to show slightly younger ages. This galaxy looks overall very old.
- These differences in the properties of the galaxies, also shown by their star formation histories, are clearly related to different evolution histories.
  - The bulk of the star formation occurred very fast and early in FCC 170, peaking between 13 and 14 Gyr ago and being quenched about 5 Gyr later. All structural components were formed with similar timescales. Differences would be small enough not to be detected with our age resolution, but sufficient to allow a (fast) chemical evolution in the thin disk, bar and nuclear disk.
  - Both FCC 153 and FCC 177 show recent star formation in their thin disks and nuclear star clusters. Whereas thin disks were assembled during a long time while their chemical enrichment took place, nuclear star clusters were affected by several bursts of star formation suggesting different episodes of gas inflow.
- These different evolution histories could be related to the different locations of the three galaxies in the Fornax cluster, corresponding to different environmental densities.
  - FCC 170 is located in the densest region of the Fornax cluster, close to the central galaxy. Moreover, its receding velocity suggests that it could have been member of a primordial subgroup before entering the present-day cluster. Its very fast star formation and posterior quenching could have been caused by the preliminary "processing" of this galaxy in the environment where it spent its earlier stages.
  - FCC 153 and FCC 177 are located farther from the cluster center and in a less dense intra-cluster medium compared to FCC 170. Their extended star formation history suggests that they missed early gas-stripping processes.
- The three galaxies display some specific peculiarities in their thin disks. In particular, the thin disk appears thinner and better geometrically defined in FCC 153. The same happens to its flare, which is also bluer. These properties could be due to the fact that FCC 153 lives in an even lower density region than FCC 177.

Main Conclusions of the Thesis

From this work, aimed to unveil the origin of thick disks, we draw the following final conclusions.

Thick disks share common properties in our whole sample. The three of them show a complex structure, result of the composition of different stellar populations.

1. The main component is very old and was probably formed *in-situ* at high redshift. It is remarkably more metal poor and α-enhanced than the rest of the galaxy.

2. A second younger component (formed around 10 Gyr ago) is even more metal-poor and α-enhanced. We proposed that this populations were formed (*ex-situ*) in a satellite with a different chemical evolution, which was later accreted.

3. A third component made of more metal-rich and less α-enhanced stars is incorporated to the geometrically-defined thick-disk region by the thin-disk flare, probably caused by the dynamical heating of stars close to the midplane at large radii.

We cannot rule out any of the thick-disk formation scenarios presented in the introduction, as observations suggest that they may have contributed, at different times, to the mass assembly of the thick disk of a galaxy. Although the bulk of the mass seems to have been formed at high redshift in a "born hot" scenario, the role played by accretion was almost surely of certain importance.

5.2 Future work

This thesis addressed numerous questions regarding thick-disk formation and galaxy evolution. However, we propose here some future research to provide a complete answer to all of them.

- Larger samples could populate the SVE-Hubble type plane. Cutting-edge observations, e.g. deep MUSE data, could be used to measure the disk SVE in galaxies with intermediate inclination. This would also require improvements in the theoretical models used to perform the fitting of the observed velocity dispersions.

- Apart from the SVE, additional information would probably help to disentangle the heating agents in kinematic observations of galaxy disks. A potential way forward is to measure the velocity anisotropy separately for different stellar populations, to distinguish different events which happened at different moments along the life of a galaxy.

- This work is part of a more extended study on the origin of thick disks in external galaxies, based on bi-dimensional stellar kinematic and population analysis. We aim to achieve a more global view to be set in a general context of galaxy formation and evolution, by gathering more complete samples including field galaxies of different morphological types.

- Promising results are expected from IMF measurements in early-type galaxies of the Fornax cluster. Since these will include the three galaxies analyzed in this thesis, we will be able to quantify the effects of a varying IMF on the stellar-population analysis.

- More efforts need to be done to improve our understanding of galaxy evolution in clusters and protoclusters. We expect that new studies will shed light on these issues.

6

Conclusiones y trabajo futuro

Los discos gruesos se descubrieron hace sólo algunas décadas y más recientemente se ha podido probar su ubicuidad en las galaxias. Dado que son una de sus componentes más viejas, han levantado un interés creciente en la comunidad científica, según la cual su origen podría ser de gran importancia para comprender más globalmente la historia de las galaxias.

Esta tesis está motivada por la escasez de estudios detallados sobre los discos gruesos y la falta de una concordancia sobre su origen en la literatura. Primero, analizamos en específico uno de los potenciales mecanismos que forman los discos gruesos, el calentamiento dinámico, que ha disfrutado de estudios extensivos sobretodo en la Vía Láctea. Sin embargo, el objetivo principal de esta tesis es presentar nuestra contribución a la caracterización de los discos gruesos en galaxias S0 en entornos densos, ofreciendo una posible imagen completa de su formación y evolución.

Repasamos las conclusiones principales de este trabajo en § 6.1, y describimos los planes futuros a seguir en § 6.2.

6.1 Conclusiones

Con el propósito de extender el estudio hecho por Gerssen & Shapiro Griffin (2012), en el cual se mostraba una tendencia clara del elipsoide de velocidades estelar (SVE) versus el tipo de Hubble, reunimos resultados de trabajos observacionales para 55 galaxias de disco, sobre el cociente de la dispersión vertical de velocidades frente a la radial. A esta muestra añadimos 26 galaxias de simulaciones de N cuerpos, que además nos permitieron analizar el impacto de algunos de los escenarios de calentamiento de disco y la evolución del SVE en el tiempo. Llegamos a las conclusiones siguientes:

- No se encuentra globalmente ninguna correlación entre el SVE del disco y el tipo morfológico, ni en la muestra de la literatura ni en las simulaciones. Esto sugiere una situación mucho más complicada que la descrita en estudios anteriores. Galaxias de tipo temprano no tienen necesariamente elipsoides isótropos y los tipos tardíos pueden tener elipsoides tan isótropos como los tipos tempranos y tan anisótropos como posible.

- En estudios anteriores, se sugería que formas diferentes del SVE correspondían a mecanismos de calentamiento diferentes. Si esto es cierto, no solo galaxias de morfología similar pueden ser afectadas por fuentes diferentes de calentamiento, sino que también los mismos mecanismos pueden actuar a la vez en tipos tempranos y tardíos de galaxias.
- Las barras se revelan como un buen agente de calentamiento radial en nuestras simulaciones numéricas.
- Fusiones de galaxias (mergers) con cocientes en masa de 1:10 a 1:3 aportan, en media, un calentamiento isótropo en nuestras simulaciones zoom-in, mientras que mecanismos internos como los brazos espirales tienden a aplanar el SVE.
- La forma actual del elipsoide, en galaxias que han sufrido mergers en el pasado, depende del momento en que estas fusiones ocurrieron. Esto puede explicar la dispersión de los puntos de σ_z/σ_R en la relación SVE-tipo de Hubble entre galaxias con mergers fuertes recientes y morfología parecida. El impacto de los mergers depende de cómo dinámicamente frías estaban las estrellas de la galaxia huésped al momento del encuentro con la otra galaxia, y cuanto tiempo ha pasado después. Además, las trazas dejadas por estos mergers en el elipsoide pueden desaparecer en el tiempo.

La principal conclusión general de esta primera parte de la tesis es que la evaluación de los mecanismos de calentamiento del disco es bastante complicada. Por lo tanto, es muy improbable alcanzar un análisis satisfactorio solo con medidas observacionales del elipsoide de velocidades. Especificamos las razones principales como sigue:

- σ_z/σ_R es sensible a pequeñas variaciones de la dispersión de velocidades que no necesariamente significan que el disco ha sido calentado dinámicamente.
- Un elipsoide actual más isótropo puede haber sido producido por situaciones diferentes no necesariamente relacionadas con el calentamiento del disco: por ejemplo un aumento de σ_z, pero también una disminución de σ_R o un disco desde el principio grueso y que no ha sufrido cambios. De forma parecida, la anisotropía puede estar relacionada con procesos diferentes de calentamiento o enfriamiento.
- El SVE actual es el resultado de la combinación de mecanismos de calentamiento (enfriamiento) diferentes.
- El mismo mecanismo de calentamiento puede producir una variedad de formas del elipsoide, en situaciones específicas diferentes.
- En cambio, historias de calentamiento diferentes pueden generar la misma forma en el SVE.

Con el objetivo de contribuir a la caracterización de los discos gruesos en galaxias externas, analizamos la cinemática y poblaciones estelares de tres galaxias S0, vistas de canto, en el cúmulo de Fornax. Utilizamos datos profundos de MUSE que son parte del cartografiado Fornax 3D. El estudio ha llevado a los siguientes resultados y conclusiones.

- La cinemática de nuestra muestra revela diferentes estructuras.

  - FCC 170 tiene una estructura compleja: un disco fino y un disco nuclear en rotación rápida, un disco grueso en rotación más lenta y un bulbo prominente con forma de X y con los valores más altos de dispersión de velocidades.
  - FCC 153 y FCC 177 no muestran ninguna concentración central de masa prominente en los mapas de dispersión de velocidades.
  - La distinción entre el disco grueso dinámicamente caliente y el disco fino más frío es más clara en FCC 153, que tiene un disco fino mucho más fino que el de FCC 177.

- Estas estructuras se recuperan en los mapas de poblaciones estelares de diferentes maneras.
  - En FCC 153 y FCC 177, relativamente jóvenes, los discos finos ricos en metales y menos abundantes en [Mg/Fe] son envueltos por los discos gruesos viejos, más pobres en metales y acentuados en [Mg/Fe]. Un cúmulo estelar nuclear joven destaca en la región central de ambas galaxias, con su alta metalicidad y unas abundancias de [Mg/Fe] apenas sobresolares.
  - En FCC 170, el disco fino, el bulbo "box/peanut" y el disco nuclear muestran valores mucho más altos de metalicidad y valores más bajos de [Mg/Fe] con respecto al disco grueso. De todas formas, estas estructuras no se distinguen claramente en el mapa de edades, a pesar de que el disco fino parezca ligeramente más joven. Esta galaxia aparece globalmente vieja.

- Estas diferencias en las propiedades de las galaxias, confirmadas por las historias de formación estelar, están claramente relacionadas con historias evolutivas diferentes.
  - El grueso de la formación estelar sucedió muy rápido y temprano en FCC 170, con su pico hace entre 13 y 14 Gyr y terminando alrededor de 5 Gyr después. Todas las componentes estructurales se formaron en escalas de tiempo parecidas. Diferencias en ellas serían demasiado pequeñas para ser detectadas con nuestra resolución en la edad, pero suficientes para permitir una evolución química rápida en el disco fino, la barra y el disco nuclear.
  - Ambas FCC 153 y FCC 177 muestran signos de formación estelar reciente en su discos finos y cúmulos estelares nucleares. Igualmente, mientras que los discos finos se ensamblaron durante un tiempo extendido y su enriquecimiento químico ocurrió entretanto, los cúmulos nucleares sufrieron varios brotes de formación estelar intensa, que sugieren varios episodios de afluencia de gas.

- Estas historias evolutivas diferentes podrían estar relacionadas con las ubicaciones de estas galaxias en el cúmulo de Fornax, a las que corresponden densidades diferentes del entorno.
  - FCC 170 se encuentra en la región más densa del cúmulo de Fornax, relativamente cerca de la galaxia central. Además, su velocidad de recesión sugiere que podría haber sido un miembro de un subgrupo primordial antes de entrar en el cúmulo actual. Su formación estelar muy eficiente y su consiguiente supresión podrían haber sido causadas por un "procesado" preliminar de esta galaxia en el entorno en el que pasó sus primeras etapas.

  - FCC 153 y FCC 177 se encuentran más lejos del centro del cúmulo y en un medio intergaláctico menos denso comparado con FCC 170. Su formación estelar extendida apunta a que estas galaxias no sufrieron procesos tempranos de sustracción del gas.

- Las tres galaxias muestran algunas peculiaridades específicas en sus discos finos. En particular, el disco fino aparece más delgado y mejor definido geométricamente en FCC 153. lo mismo ocurre a su "flare", que es además más azul. Estas propiedades podrían ser debidas al hecho de que FCC 153 habita un región aún menos densa que FCC 177.

Conclusiones principales de la tesis

De este trabajo, orientado a desvelar el origen de los discos gruesos, extraemos las siguientes conclusiones.

Los discos gruesos comparten propiedades comunes en la muestra entera. Los tres muestran una estructura compleja, resultado de la composición de varias poblaciones estelares.

1. La componente principal es muy vieja y fue probablemente formada *in-situ* a alto redshift. Esta componente es notablemente más pobre en metales y acentuada en [Mg/Fe] que el resto de la galaxia.

2. Una segunda componente (formada alrededor de hace 10 Gyr) es aún más pobre en metales y acentuada en [Mg/Fe]. Proponemos que esta población se formara (*ex-situ*) en una galaxia satélite con una evolución química diferente, y fuera luego acretada.

3. Una tercera componente compuesta por estrellas más ricas en metales y menos abundantes en [Mg/Fe] es incorporada al disco grueso definido geométricamente por el flare del disco fino, posiblemente causado por el calentamiento dinámico de las estrellas cerca del plano de la galaxia en radios externos.

No podemos descartar ninguno de los escenarios de formación presentados en la introducción, ya que nuestras observaciones indican que todos ellos podrían haber contribuido, en momentos diferentes, al ensamblaje del disco grueso de una misma galaxia. Aunque parece que el grueso de la masa se formara a alto redshift en un escenario de tipo "born hot", el papel jugado por la acreción fue casi seguramente de cierta importancia.

6.2 Trabajo futuro

Esta tesis aborda numerosas cuestiones sobre la formación de los discos gruesos y la evolución de galaxias. Sin embargo, proponemos aquí algunas potenciales investigaciones futuras orientadas a aportar respuestas a todas esas cuestiones.

- Muestras más amplias podrían poblar el plano dado por la forma del SVE y el tipo de Hubble. Observaciones punteras, como por ejemplo datos profundos de MUSE, podrían usarse para medir el SVE del disco en galaxias de inclinación intermedia. Esto requeriría también mejoras en los modelos teóricos usados para realizar el ajuste de las dispersiones de velocidades observadas.

- Aparte el SVE, información adicional ayudaría quizás a distinguir entre los agentes de calentamiento en observaciones de la cinemática de los discos galácticos. Un posible camino hacia adelante sería medir la anisotropía de velocidades separadamente para las diferentes poblaciones estelares, para separar los eventos diferentes que ocurrieron en momentos diferentes a lo largo de la vida de la galaxias.
- Este trabajo es parte de un estudio más extenso sobre el origen de los discos gruesos en galaxias externas, basado en el análisis bidimensional de la cinemática y poblaciones estelares. Pretendemos llegar a una visión más global a situar en el contexto de la formación y evolución de galaxias, juntando muestras más completas que incluyan galaxias de campo y de morfologías diferentes.
- Se esperan resultados prometedores de las medidas de la función inicial de masa (IMF) en el cúmulo de Fornax. Dado que estos incluirán las tres galaxias analizadas en esta tesis, podremos cuantificar los efectos de una IMF que varíe sobre el análisis de poblaciones estelares.
- Se necesitan más esfuerzos científicos para mejorar nuestra comprensión de la evolución de galaxias en cúmulos y protocúmulos. Esperamos que estudios nuevos aclaren estos temas.

7

Conclusioni e lavoro futuro

I dischi spessi sono stati scoperti solo qualche decennio fa ed ancora più recentemente si è potuta provare la loro ubiquità nelle galassie. Dato che sono una delle componenti più vecchie, hanno suscitato un interesse in aumento nella comunità , secondo la quale la loro origine potrebbe essere di grande importanza per capire più globalmente la storia delle galassie.

Questa tesi è motivata dalla carenza di studi dettagliati sui dischi spessi e dalla mancanza di concordanza sulla loro origine negli studi precedenti. Innanzitutto, abbiamo analizzato in modo specifico uno dei potenziali meccanismi che formano i dischi spessi, il riscaldamento dinamico, che ha goduto di ampi studi in particolare nella Via Lattea. Tuttavia, l'obiettivo principale di questa tesi è presentare il nostro contributo alla caratterizzazione dei dischi spessi in galassie S0 in ambienti circostanti densi, offrendo un possibile ritratto completo della loro formazione ed evoluzione. Ripassiamo le principali conclusioni di questo lavoro nella § 7.1, e descriviamo nella § 7.2 dei possibili piani futuri da seguire.

7.1 Conclusioni

Con lo scopo di estendere lo studio realizzato da Gerssen & Shapiro Griffin (2012), nel quale si mostrava una chiara tendenza dell'ellissoide stellare di velocità (SVE) rispetto al tipo di Hubble, raccogliamo i risultati di lavori osservazionali per 55 galassie a disco, sul quoziente della dispersione verticale di velocità rispetto a quella radiale. A questo campione abbiamo aggiunto 26 galassie di simulazioni a N corpi, che inoltre ci hanno permesso di analizzare l'impatto di alcuni degli scenari di riscaldamento del disco e l'evoluzione dello SVE nel tempo. Siamo arrivati alle seguenti conclusioni:

- Non si trova una correlazione globale tra lo SVE del disco e il tipo morfologico, nè nel campione della letteratura nè nelle simulazioni. Questo suggerisce una situazione molto più complicata di quanto descritto negli studi precedenti. Galassie di primo tipo non hanno necessariamente ellissoidi isotropi e quelle di tipo avanzato possono avere ellissoidi isotropi tanto come i primi tipi, ma anche ellissoidi il più anisotropi possibile.

- In studi precedenti, è stato suggerito che diverse forme dello SVE corrispondono a meccanismi di riscaldamento diversi. Se questo è vero, non solo le galassie di morfologia simile possono essere interessate da diverse fonti di riscaldamento, ma anche gli stessi meccanismi possono agire sia nei primi tipi che nei tipi avanzati di galassie.
- Le barre si sono rivelate un buon agente di riscaldamento radiale nelle nostre simulazioni numeriche.
- Le fusioni di galassie (mergers) con rapporti di massa da 1:10 a 1:3 forniscono, in media, un riscaldamento isotropo nelle nostre simulazioni di tipo zoom-in, mentre i meccanismi interni come le braccia a spirale tendono ad appiattire lo SVE.
- La forma attuale dell'ellissoide, nelle galassie che hanno subito mergers nel passato, dipende dal momento in cui si sono verificate queste fusioni. Questo può spiegare la dispersione dei punti di σ_z/σ_R, nella relazione SVE-tipo di Hubble, tra galassie con mergers forti e recenti e con morfologia simile. L'impatto dei mergers dipende da quanto fossero dinamicamente fredde le stelle della galassia ospite al momento dell'incontro con l'altra galassia, e quanto tempo sia passato dopo. Inoltre, le tracce lasciate da questi mergers nell'ellissoide possono scomparire nel tempo.

La principale conclusione generale di questa prima parte della tesi è che la valutazione dei meccanismi di riscaldamento del disco è piuttosto complicata. Pertanto, raggiungere un'analisi soddisfacente solo con misure osservazionali dell'ellissoide di velocità è altamente improbabile. Specifichiamo le ragioni principali qui di seguito:

- σ_z/σ_R è sensibile a piccole variazioni della dispersione di velocità che non per forza significano che il disco è stato riscaldato dinamicamente.
- Un ellissoide attuale più isotropo potrebbe essere stato causato da diverse situazioni non necessariamente prodotte dal riscaldamento del disco: ad esempio un aumento di σ_z, ma anche una diminuzione di σ_R o un disco già spesso dall'inizio e che non ha subito cambiamenti fino ad ora. Allo stesso modo, l'anisotropia può essere dovuta a processi diversi di riscaldamento o raffreddamento.
- L'attuale SVE è il risultato della combinazione di meccanismi di riscaldamento (raffreddamento) diversi.
- Lo stesso meccanismo di riscaldamento può produrre una varietà di forme dell'ellissoide, in diverse situazioni specifiche.
- Al contrario, diverse storie di riscaldamento possono generare la stessa forma nello SVE.

Con l'obiettivo di contribuire alla caratterizzazione dei dischi spessi in galassie esterne, abbiamo analizzato la cinematica e le popolazioni stellari di tre galassie S0, viste di taglio, nell'ammasso galattico di Fornax. Abbiamo utilizzato dati profondi presi con lo strumento MUSE che fanno parte del survey Fornax 3D. Lo studio ha portato ai seguenti risultati e conclusioni.

- La cinematica del nostro campione rivela diverse strutture.

  - FCC 170 ha una struttura complessa: un disco sottile e un disco nucleare in rotazione rapida, un disco spesso in rotazione più lenta e un notevole bulge a forma di X che presenta i valori più alti di dispersione della velocità.
  - FCC 153 e FCC 177 non mostrano alcuna prominente concentrazione centrale di massa nelle mappe di dispersione di velocità.
  - La distinzione tra il disco spesso dinamicamente caldo e il disco sottile più freddo è più chiara in FCC 153, che ha un disco sottile molto più fine di quello di FCC 177.

- Queste strutture sono recuperate nelle mappe delle popolazioni stellari in modi diversi.
  - In FCC 153 e FCC 177, relativamente giovani, i dischi sottili ricchi di metalli e con un'abbondanza di [Mg/Fe] più alta sono avvolti dai dischi spessi che sono vecchi, più poveri di metalli e con il [Mg/Fe] più accentuato. Un giovane ammasso nucleare di stelle si distingue nella regione centrale di entrambe le galassie, con la loro elevata metallicità ed un'abbondanza di [Mg/Fe] a malapena soprasolare.
  - In FCC 170, il disco sottile, il bulge "box/peanut" e il disco nucleare mostrano valori molto più alti di metallicità e valori più bassi di [Mg/Fe] rispetto al disco spesso. Ad ogni modo, queste strutture non si distinguono chiaramente sulla mappa delle età, anche se il disco sottile sembra leggermente più giovane. Questa galassia appare globalmente vecchia.

- Queste differenze nelle proprietà delle galassie, confermate dalle storie della formazione stellare, sono chiaramente collegate con diverse storie evolutive.
  - La maggior parte della formazione stellare è avvenuta molto velocemente e presto in FCC 170, con il suo picco tra 13 e 14 Gyr fa e cessando intorno a 5 Gyr più tardi. Tutte le componenti strutturali si sono formate su scale temporali simili. Le differenze tra di loro sarebbero troppo piccole per essere rilevate con la nostra risoluzione nell'età, ma sufficienti per consentire una rapida evoluzione chimica nel disco sottile, nella barra e nel disco nucleare.
  - Sia FCC 153 che FCC 177 mostrano segni di formazione stellare recente nei loro dischi sottili ed ammassi stellari nucleari. In ogni caso, mentre i dischi fini si sono assemblati durante un tempo prolungato e nel frattempo si è verificato il loro arricchimento chimico, gli ammassi nucleari hanno subito diversi eventi di intensa formazione stellare, che suggerisce diversi episodi di afflusso di gas.

- Queste diverse storie evolutive potrebbero essere correlate alle posizioni di queste galassie nell'ammasso galattico di Fornax, a cui corrispondono diverse densità dell'ambiente circostante.
  - FCC 170 si trova nella regione più densa di Fornax, relativamente vicino alla galassia centrale. Inoltre, la sua velocità di recessione suggerisce che potrebbe essere stata un membro di un sottogruppo primordiale prima di entrare nell'attuale ammasso. La formazione stellare molto efficiente e la sua conseguente soppressione potrebbero essere state causate da una trasformazione preliminare di questa galassia nell'ambiente in cui ha passato le sue prime fasi.

  - FCC 153 e FCC 177 sono più distanti dal centro dell'ammasso e si trovano in un mezzo intergalattico meno denso rispetto a FCC 170. La loro formazione stellare estesa suggerisce che queste galassie non hanno subito processi precoci di sottrazione del gas.

- Le tre galassie mostrano alcune peculiarità specifiche nei loro dischi sottili. In particolare, il disco sottile appare più fine e definito meglio geometricamente in FCC 153. Lo stesso accade al suo "flare", che inoltre è più blu. Queste proprietà potrebbero essere dovute al fatto che FCC 153 abita in una regione ancora meno densa rispetto a FCC 177.

Conclusioni principali della tesi

Da questo lavoro, volto a rivelare l'origine dei dischi spessi, possiamo trarre le seguenti conclusioni.

I dischi spessi condividono proprietà comuni nell'intero campione. Tutti e tre mostrano una struttura complessa, risultato della composizione di diverse popolazioni stellari.

1. La componente principale è molto vecchia e probabilmente è stata formata *in-situ* ad alto redshift. Questa componente è notevolmente più povera di metalli con un [Mg/Fe] più abbondante rispetto al resto della galassia.

2. Una seconda componente (formata attorno a 10 Gyr fa) è ancora più povera di metalli e presenta un'abbondanza di [Mg/Fe] più alta. Sosteniamo che questa popolazione si sia formata (*ex-situ*) in una galassia satellite con un'evoluzione chimica diversa, e poi sia stata aggregata.

3. Una terza componente composta da stelle più ricche di metalli e con un [Mg/Fe] meno abbondante è incorporata nel disco spesso (definito geometricamente) dal flare del disco sottile, essendo questo probabilmente causato dal riscaldamento dinamico delle stelle vicino al piano della galassia nei raggi più esterni.

Non possiamo escludere nessuno degli scenari di formazione presentati nell'introduzione, poichè le nostre osservazioni indicano che tutti potrebbero avere contribuito, in momenti diversi, all'assemblaggio del disco spesso della stessa galassia. Anche se sembra che la maggior parte della massa si sia formata ad alto redshift in uno scenario di tipo "born hot", il ruolo svolto dall'accrezione è stato quasi certamente di una certa importanza.

7.2 Lavoro futuro

Questa tesi affronta numerose questioni sulla formazione dei dischi spessi e l'evoluzione delle galassie. Tuttavia, proponiamo qui alcune potenziali ricerche future orientate a procurare risposte a tutte quelle domande.

- Campioni più grandi potrebbero popolare il piano dato dalla forma dello SVE e il tipo di Hubble. Osservazioni all'avanguardia, come dati profondi di MUSE, potrebbero usarsi per misurare lo SVE del disco in galassie con inclinazione intermedia. Ciò richiederebbe anche dei miglioramenti nei modelli teorici utilizzati per riprodurre le dispersioni delle velocità osservate.

- Oltre allo SVE, informazioni aggiuntive potrebbero aiutare a distinguere tra gli agenti di riscaldamento nelle osservazioni della cinematica dei dischi galattici. Una via possibile potrebbe essere misurare l'anisotropia delle velocità separatamente per le diverse popolazioni stellari, per separare i diversi eventi che si sono verificati in momenti diversi durante la vita delle galassie.
- Questo lavoro fa parte di uno studio più ampio sull'origine dei dischi spessi in galassie esterne, basato sull'analisi bidimensionale della cinematica e delle popolazioni stellari. Puntiamo a raggiungere una visione più globale da inserire nel contesto della formazione ed evoluzione delle galassie, riunendo campioni più completi che includono galassie di campo e di diverse morfologie.
- Risultati promettenti sono attesi dalle misure della funzione iniziale di massa (IMF) nell'ammasso di Fornax. Poichè questi risultati includeranno le tre galassie analizzate in questa tesi, potremo quantificare gli effetti di una IMF variabile sull'analisi delle popolazioni stellari.
- Sono necessari ulteriori sforzi scientifici per migliorare la nostra comprensione dell'evoluzione delle galassie in ammassi e proto-ammassi. Ci aspettiamo che nuovi studi chiariscano questi argomenti.

A

Appendix A: tables for Chapter 2

TABLE A.1— SVE shape for 55 galaxies calculated with different methods.

Galaxy name	Hubble type	σ_z/σ_R (1)	References	Method	radial range
Milky Way	Sbc (2)	0.58 ± 0.06	(3)	(3)	solar nbhd
ESO-LV 026-G06	Sd	0.52 ± 0.08	van der Kruit & de Grijs (1999)	photometry	at 1 scale length
ESO-LV 033-G22	Sd	0.47 ± 0.07	van der Kruit & de Grijs (1999)	photometry	at 1 scale length
ESO-LV 041-G09	Scd	0.70 ± 0.10	van der Kruit & de Grijs (1999)	photometry	at 1 scale length
ESO-LV 141-G27	Scd	0.66 ± 0.10	van der Kruit & de Grijs (1999)	photometry	at 1 scale length
ESO-LV 142-G24	Sd	0.73 ± 0.11	van der Kruit & de Grijs (1999)	photometry	at 1 scale length
ESO-LV 157-G18	Scd	0.66 ± 0.10	van der Kruit & de Grijs (1999)	photometry	at 1 scale length
ESO-LV 201-G22	Sc	0.44 ± 0.07	van der Kruit & de Grijs (1999)	photometry	at 1 scale length
ESO-LV 202-G35	Sb	0.60 ± 0.09	van der Kruit & de Grijs (1999)	photometry	at 1 scale length
ESO-LV 235-G53	Sb	0.64 ± 0.10	van der Kruit & de Grijs (1999)	photometry	at 1 scale length
ESO-LV 240-G11	Sc	0.40 ± 0.06	van der Kruit & de Grijs (1999)	photometry	at 1 scale length
ESO-LV 269-G15	Scd	0.70 ± 0.10	van der Kruit & de Grijs (1999)	photometry	at 1 scale length
ESO-LV 286-G18	Sbc	0.67 ± 0.10	van der Kruit & de Grijs (1999)	photometry	at 1 scale length
ESO-LV 288-G25	Sbc	0.88 ± 0.13	van der Kruit & de Grijs (1999)	photometry	at 1 scale length
ESO-LV 322-G87	Sb	0.78 ± 0.12	van der Kruit & de Grijs (1999)	photometry	at 1 scale length
ESO-LV 340-G08	Scd	1.10 ± 0.17	van der Kruit & de Grijs (1999)	photometry	at 1 scale length
ESO-LV 340-G09	Sd	0.97 ± 0.15	van der Kruit & de Grijs (1999)	photometry	at 1 scale length
ESO-LV 383-G05	Sbc	0.76 ± 0.11	van der Kruit & de Grijs (1999)	photometry	at 1 scale length
ESO-LV 416-G25	Sb	0.85 ± 0.13	van der Kruit & de Grijs (1999)	photometry	at 1 scale length
ESO-LV 435-G14	Sc	0.80 ± 0.12	van der Kruit & de Grijs (1999)	photometry	at 1 scale length
ESO-LV 435-G25	Sc	0.35 ± 0.05	van der Kruit & de Grijs (1999)	photometry	at 1 scale length
ESO-LV 435-G50	Scd	0.67 ± 0.10	van der Kruit & de Grijs (1999)	photometry	at 1 scale length
ESO-LV 444-G21	Scd	0.57 ± 0.09	van der Kruit & de Grijs (1999)	photometry	at 1 scale length
ESO-LV 446-G18	Sb	0.45 ± 0.07	van der Kruit & de Grijs (1999)	photometry	at 1 scale length
ESO-LV 446-G44	Scd	0.50 ± 0.07	van der Kruit & de Grijs (1999)	photometry	at 1 scale length
ESO-LV 460-G31	Sc	0.38 ± 0.06	van der Kruit & de Grijs (1999)	photometry	at 1 scale length
ESO-LV 487-G02	Sb	0.86 ± 0.13	van der Kruit & de Grijs (1999)	photometry	at 1 scale length
ESO-LV 505-G02	Sd	0.46 ± 0.07	van der Kruit & de Grijs (1999)	photometry	at 1 scale length
ESO-LV 506-G02	Sbc	0.47 ± 0.07	van der Kruit & de Grijs (1999)	photometry	at 1 scale length
ESO-LV 509-G19	Sbc	0.77 ± 0.12	van der Kruit & de Grijs (1999)	photometry	at 1 scale length
ESO-LV 531-G22	Sbc	0.50 ± 0.07	van der Kruit & de Grijs (1999)	photometry	at 1 scale length
ESO-LV 564-G27	Scd	0.48 ± 0.07	van der Kruit & de Grijs (1999)	photometry	at 1 scale length
NGC488	Sb	0.70 ± 0.16	Shapiro et al. (2003)	long-slit, σ_{lOS} model	disk region
NGC1068	Sb	0.58 ± 0.07	Shapiro et al. (2003)	long-slit, σ_{lOS} model	disk region
NGC2460	Sa	0.83 ± 0.35	Shapiro et al. (2003)	long-slit, σ_{lOS} model	disk region
NGC2775	Sa-Sab	$< 1.02 \pm 0.11$	Shapiro et al. (2003)	long-slit, σ_{lOS} model	disk region
NGC2985	Sab	0.75 ± 0.09	Shapiro et al. (2003)	long-slit, σ_{lOS} model	disk region
NGC4030	Sbc	0.64 ± 0.28	Shapiro et al. (2003)	long-slit, σ_{lOS} model	disk region
NGC2280	Scd	0.25 ± 0.20	Gerssen & Shapiro Griffin (2012)	long-slit, σ_{lOS} model	disk region
NGC3810	Sc	0.29 ± 0.12	Gerssen & Shapiro Griffin (2012)	long-slit, σ_{lOS} model	disk region
NGC3223	Sb	1.21 ± 0.14	Gentile et al. (2015)	long-slit, σ_{lOS} model	disk region
NGC3949	Sbc	$1.18^{+0.36}_{-0.28}$	Westfall et al. (2005)	IFS, σ_{lOS} model	disk region
NGC3982	Sb	$0.73^{+0.13}_{-0.11}$	Westfall et al. (2005)	IFS, σ_{lOS} model	disk region
NGC0234	Sc	0.48 ± 0.09	Westfall et al. (2011)	IFS, σ_{lOS} model	disk region
NGC524	$S0^+$	< 0.91	Cappellari et al. (2007)	IFS, Schwarzschild models	within 1 $R_e^{(4)}$
NGC3156	S0	< 0.78	Cappellari et al. (2007)	IFS, Schwarzschild models	within 1 $R_e^{(4)}$
NGC3414	S0	< 0.97	Cappellari et al. (2007)	IFS, Schwarzschild models	within 1 $R_e^{(4)}$
NGC4150	$S0^0$	< 0.82	Cappellari et al. (2007)	IFS, Schwarzschild models	within 1 $R_e^{(4)}$
NGC4459	$S0^+$	< 0.97	Cappellari et al. (2007)	IFS, Schwarzschild models	within 1 $R_e^{(4)}$
NGC4526	$S0^0$	< 0.94	Cappellari et al. (2007)	IFS, Schwarzschild models	within 1 $R_e^{(4)}$
NGC4550	$S0^0$	< 0.75	Cappellari et al. (2007)	IFS, Schwarzschild models	within 1 $R_e^{(4)}$
NGC7457	$S0^-$	< 0.79	Cappellari et al. (2007)	IFS, Schwarzschild models	within 1 $R_e^{(4)}$
NGC3115	$S0^-$ (5)	1.2 ± 0.1	Emsellem et al. (1999)	Three-integral models	outer disk
M104	Sa	0.57 ± 0.12	Tempel & Tenjes (2006)	Jeans equations	disk
M31	Sb (5)	0.73 ± 0.13	Kipper et al. (2016)	Jeans equations	disk

Notes. (1) Uncertainties are indicated only when available. (2) e.g. `http://messier.seds.org/more/mw_type.html`. (3) See § 2.2 and § 2.3. (4) Including bulge stars, these results are upper limits. (5) `https://ned.ipac.caltech.edu`.

TABLE A.2— SVE shapes for the solar neighborhood.

σ_z/σ_R (1)	N_*	Region	References	Comments
0.45 ± 0.06	11865	local solar nbhd	Dehnen & Binney (1998)	$B-V$ from -0.238 to 0.719
0.42 ± 0.07	15113	local solar nbhd	Aumer & Binney (2009)	$B-V$ from ~ 0 to ~ 0.8
0.70 ± 0.07	7280	$\lvert z\rvert < 2$ kpc	Smith et al. (2012)	dwarfs, [Fe/H]=[-1.5,0.5]
0.58 ± 0.04	372 768	$\lvert z\rvert < 2$ kpc	Binney et al. (2014b)	red-clump and non-clump giants, hot and cool dwarfs
0.64 ± 0.08	16 276	$\lvert z\rvert < 3$ kpc	Büdenbender et al. (2015)	G-dwarfs, [Fe/H]=[-0.89,-0.07]

Notes. (1) Averages have been computed weighting with the number of stars (N_*), in the second column. Errors have been estimated as the weighted standard deviation of the different samples.

TABLE A.3— SVE shape for 26 galaxies from zoom-in cosmological simulations.

Galaxy name	Hubble type	Stellar mass (10^{10} $M_\odot$)	Merger mass ratio(1)	Bar(2)	σ_z/σ_R
galaxy_31	Sbc	1.2	$1:10-1:20$	strong	$0.46^{+0.05}_{-0.00}$
galaxy_35	$S0^+$	1.4	$1:3-1:10$	strong	$0.53^{+0.17}_{-0.05}$
galaxy_36	Scd	1.2	$1:3-1:10$	strong	$0.42^{+0.05}_{-0.01}$
galaxy_37	Scd	1.2	$<1:20$	strong	$0.52^{+0.03}_{-0.02}$
galaxy_38	Sc	1.1	$1:3-1:10$	strong	$0.51^{+0.06}_{-0.03}$
galaxy_44	Sbc	1.2	$1:3-1:10$	strong	$0.59^{+0.06}_{-0.04}$
galaxy_47	Sb	8.6	$1:10-1:20$	absent/weak	$0.68^{+0.03}_{-0.02}$
galaxy_48	Sbc	1.1	$1:3-1:10$	absent/weak	$0.73^{+0.12}_{-0.04}$
galaxy_53	S0a	9.1	$1:3-1:10$	strong	$0.71^{+0.05}_{-0.04}$
galaxy_56	Sab	1.1	$1:3-1:10$	absent/weak	$0.77^{+0.09}_{-0.02}$
galaxy_57	Sb	1.2	$1:10-1:20$	strong	$0.49^{+0.16}_{-0.07}$
galaxy_59	Sc	7.2	$1:3-1:10$	strong	$0.69^{+0.12}_{-0.04}$
galaxy_60	Sa	4.5	$1:3-1:10$	absent/weak	$0.75^{+0.02}_{-0.04}$
galaxy_62	Sb	6.7	$1:10-1:20$	absent/weak	0.63 ± 0.02
galaxy_72	Sbc	4.6	$1:3-1:10$	absent/weak	0.89 ± 0.02
galaxy_82	Sc	3.8	$<1:20$	strong	$0.56^{+0.04}_{-0.07}$
galaxy_83	Sb	4.2	$1:10-1:20$	strong	$0.84^{+0.05}_{-0.02}$
galaxy_86	S0a	4.2	$<1:20$	absent/weak	$0.70^{+0.03}_{-0.08}$
galaxy_92	Sbc	4.4	$<1:20$	strong	$0.43^{+0.12}_{-0.06}$
galaxy_102	Sa	3.3	$1:10-1:20$	absent/weak	$0.60^{+0.07}_{-0.09}$
galaxy_106	Sc	4.3	$1:3-1:10$	strong	$0.47^{+0.13}_{-0.06}$
galaxy_125	Sbc	2.4	$1:3-1:10$	strong	$0.65^{+0.03}_{-0.07}$
galaxy_126	Sa	3.3	$1:3-1:10$	absent/weak	$0.57^{+0.07}_{-0.04}$
galaxy_128	Sc	2.7	$<1:20$	strong	$0.37^{+0.09}_{-0.02}$
galaxy_146	Sab	1.7	$<1:20$	absent/weak	$0.59^{+0.04}_{-0.03}$
galaxy_147	Sb	2.6	$1:3-1:10$	strong	$0.85^{+0.02}_{-0.01}$

Notes. (1) Estimated, for each galaxy, from its mass evolution plot from the age of 5 Gyr on.
(2) *Strong* bars have a bar-to-total light ratio above 10%. *Absent/weak* bars are below 6%.

TABLE A.4— Axis ratio of the SVE for 6 galaxies from idealized N-body simulations.

Galaxy id	DM (%)[1]	Bar	Interaction[2]	σ_z/σ_R
I0_no_bar	80	no	no	$0.84^{+0.16}_{-0.02}$
I0_inter	80	yes	yes	$0.53^{+0.26}_{-0.21}$
I1	57	yes	no	$0.59^{+0.08}_{-0.09}$
I1_inter	57	yes	yes	$0.38^{+0.16}_{-0.05}$
I2	38	yes	no	0.42 ± 0.09
I3	7	yes	no	0.53 ± 0.08

Notes. (1) This is the dark matter fraction within a central sphere of 5 kpc of radius. (2) The interaction consists in a fly-by, coplanar with the galaxy disk.

B

Appendix B: additional maps for Chapter 3 and Chapter 4

B.1 Bi-dimensional view of the SFH

A two-dimensional view of the SFH is given by the maps in Figs. B.1, B.2 and B.3. Here, the stellar populations are divided into three age bins: 11.5 – 14 Gyr, 9 – 11 Gyr and 0 – 8.5 Gyr for FCC 170 and 11.5 – 14 Gyr, 6 – 11 Gyr and 0 – 5.5 Gyr for FCC 153 and FCC 177. In each map, we have color coded the mass density contained in the corresponding age bin. Populations more than 11.5 Gyr-old (top panel of Fig. B.1) contribute about the 87 % of the mass in FCC 170, the 48 % in FCC 153 and the 44 % in FCC177. They are distributed everywhere, but the central region (box/peanut and nuclear disk) is clearly dominated by these very old populations in FCC 170. In FCC 153 they are less dense right in the midplane but aligned in the central region of the thin disk.

The ∼ 10 Gyr-old populations are plotted in the middle-panel map in Fig. B.1. They are present over all the galaxy, although mainly in the most massive structural components. The middle panels of Figs. B.2 and B.3 include populations in a broader age range, mainly concentrated in the thin disks. Few stars are younger than 8.5 Gyr in FCC 170, since the mass contained in this age-bin populations is almost two orders of magnitude lower than the mass in very old stars. They are distributed mostly in the thin disk (bottom panel of Fig B.1). In FCC 153 (Fig. B.2), stars younger than 5.5 Gyr are present only in the dynamically coldest region of the thin disk, but with a flaring in the outer part. In FCC 177 (Fig. B.3), this effect is less pronounced and this young stars are mainly in the nuclear star cluster region.

B.2 Spatial distribution of metallicity in different ranges

Dividing our metallicity range into three bins, we can map the mass density of populations with different metallicities in our three galaxies. In the top panel of Fig. B.4, B.5 and B.6 we see the most metal poor stars in the three galaxies. These stars give the lowest contribution to the total mass: about the 3 – 4 % of the total mass in the three galaxies. They are absent in numerous spatial bins of the outer regions of the three galaxies. Subsolar metallicities (top and middle

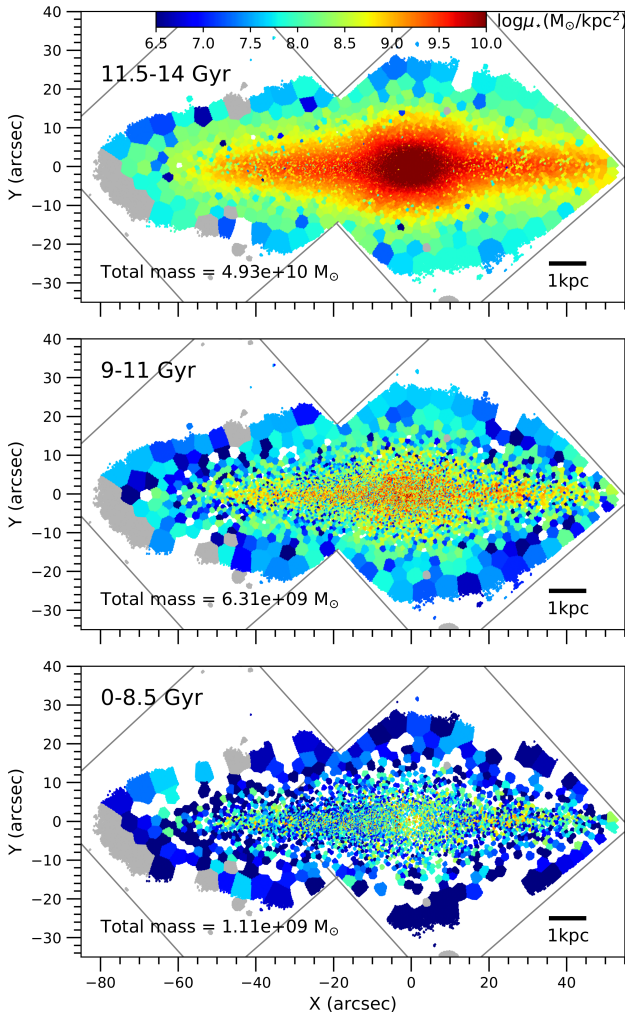

FIGURE B.1— Two-dimensional view of the star formation history in FCC 170. Stellar populations are mapped according to their age. Each map corresponds to a specific age bin: 11.5 – 14 Gyr in the top panel, 9 – 11 Gyr in the middle panel and 0 – 8.5 Gyr in the bottom panel. The color scale shows the mass density corresponding to the populations in the specific age bin. The total mass in the age bin is indicated on bottom-left of each map. The position of the two MUSE pointings is plotted in grey. A scale bar on bottom-right of each map indicates the correspondence with physical units.

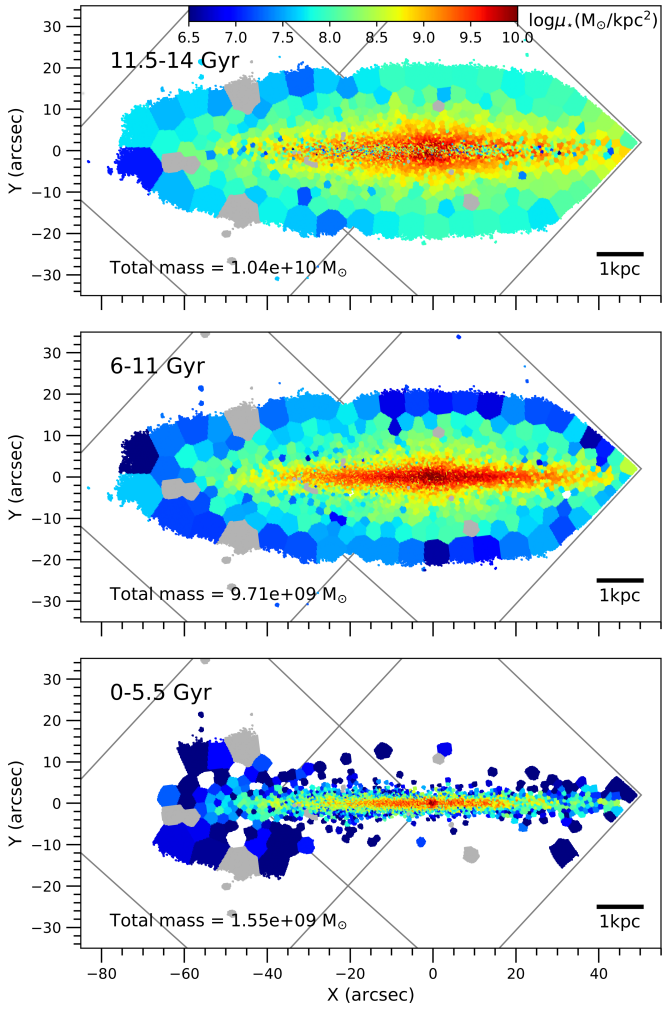

FIGURE B.2— Two-dimensional view of the star formation history in FCC 153. Stellar populations are mapped according to their age. Each map corresponds to a specific age bin: 11.5 – 14 Gyr in the top panel, 6 – 11 Gyr in the middle panel and 0 – 5.5 Gyr in the bottom panel. The color scale shows the mass density corresponding to the populations in the specific age bin. The total mass in the age bin is indicated on bottom-left of each map. The position of the two MUSE pointings is plotted in grey. A scale bar on bottom-right of each map indicates the correspondence with physical units.

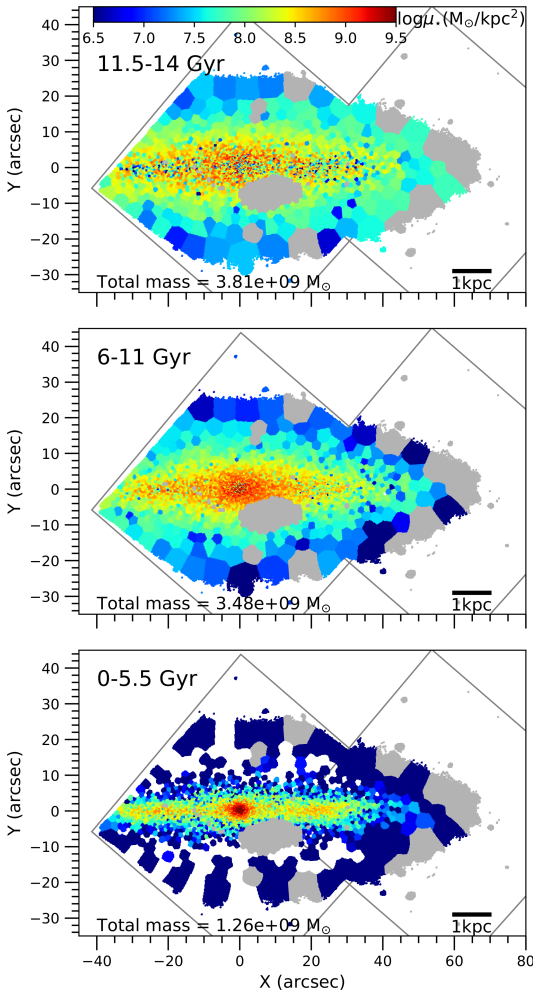

FIGURE B.3— Two-dimensional view of the star formation history in FCC 177. Stellar populations are mapped according to their age. Each map corresponds to a specific age bin: 11.5 – 14 Gyr in the top panel, 6 – 11 Gyr in the middle panel and 0 – 5.5 Gyr in the bottom panel. The color scale shows the mass density corresponding to the populations in the specific age bin. The total mass in the age bin is indicated on bottom-left of each map. The position of the two MUSE pointings is plotted in grey. A scale bar on bottom-right of each map indicates the correspondence with physical units.

panels) are present everywhere but are much denser towards the central region, especially in FCC 170, where a spherical symmetry is suggested. In FCC 153, they are absent in a narrow band lying on the midplane. Populations in the supersolar metallicity range (bottom panels) contribute most of the mass. They follow the shape of the thin disks, dominated by these metal-rich stars, in the three galaxies. The box/peanut in FCC 170 is also completely dominated by these most metal-rich stars, as well as the central mass concentration in FCC 177 (including the boxy bulge and the NSC).

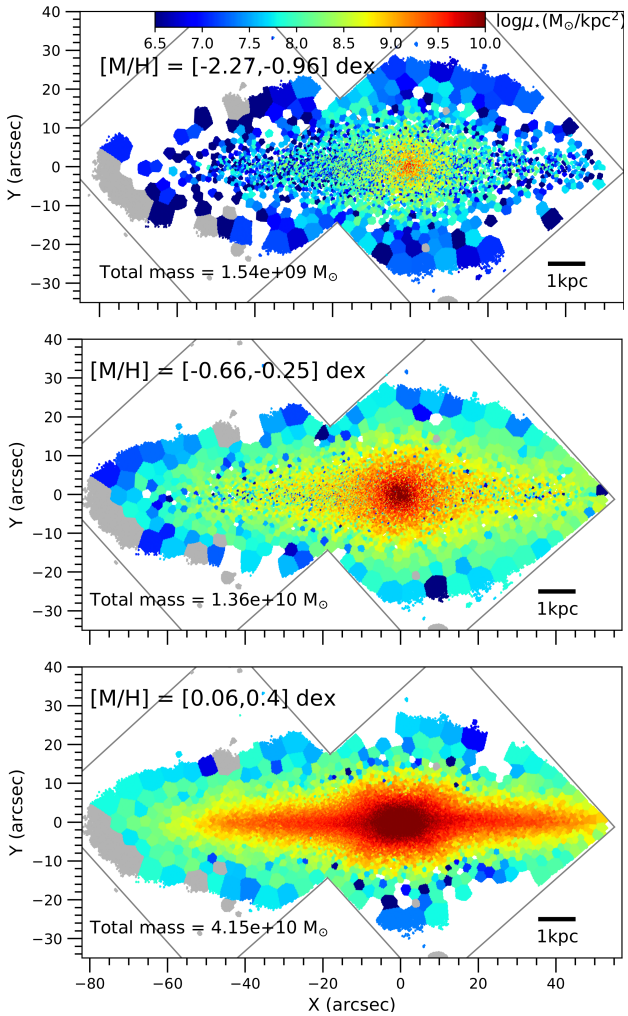

FIGURE B.4— Maps of stellar populations in FCC 170 with metallicities in three different bins: [M/H] = [-2.27,-0.96] dex in the top panel, [-0.66,-0.25] dex in the middle panel and [0.06,0.4] dex in the bottom panel. The color scale shows the mass density corresponding to the populations in the specific metallicity bin. The total mass in the metallicity bin is indicated on bottom-left of each map. The position of the two MUSE pointings is plotted in grey. A scale bar on bottom-right of each map indicates the correspondence with physical units.

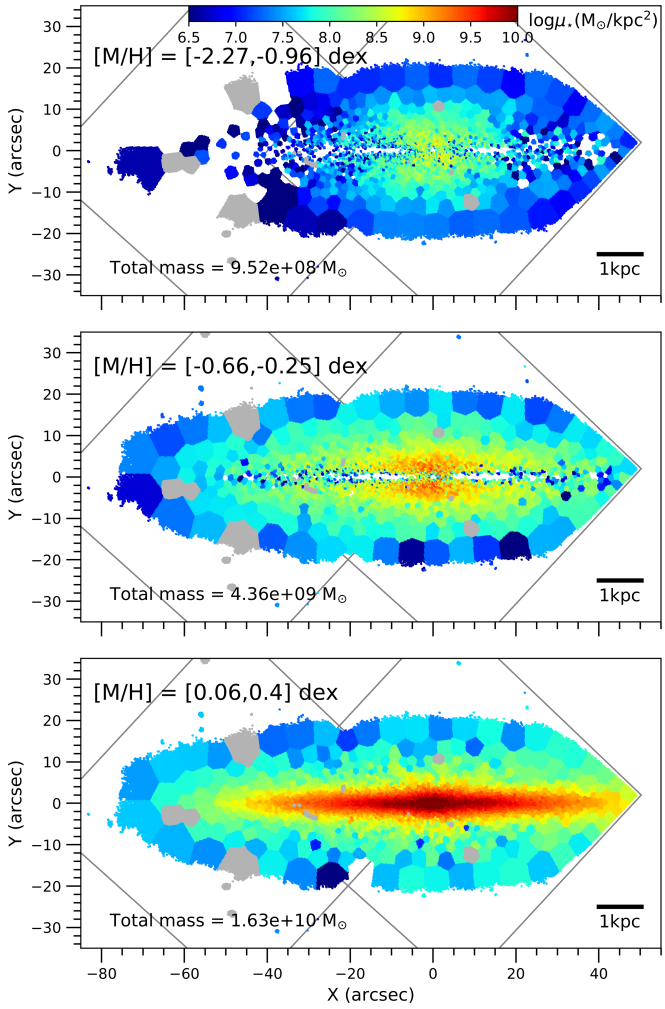

FIGURE B.5— Maps of stellar populations in FCC 153 with metallicities in three different bins: [M/H] = [-2.27,-0.96] dex in the top panel, [-0.66,-0.25] dex in the middle panel and [0.06,0.4] dex in the bottom panel. The color scale shows the mass density corresponding to the populations in the specific metallicity bin. The total mass in the metallicity bin is indicated on bottom-left of each map. The position of the two MUSE pointings is plotted in grey. A scale bar on bottom-right of each map indicates the correspondence with physical units.

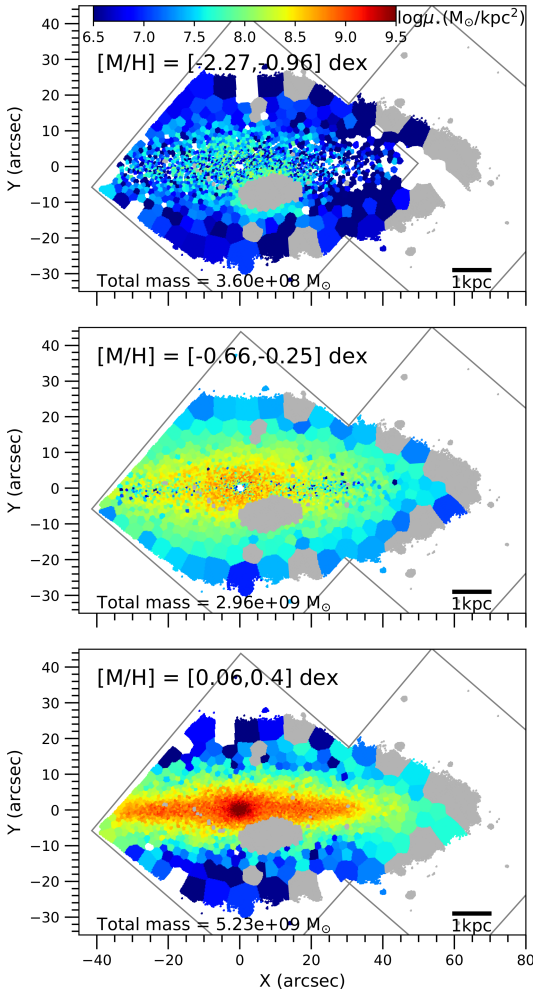

FIGURE B.6— Maps of stellar populations in FCC 177 with metallicities in three different bins: [M/H] = [-2.27,-0.96] dex in the top panel, [-0.66,-0.25] dex in the middle panel and [0.06,0.4] dex in the bottom panel. The color scale shows the mass density corresponding to the populations in the specific metallicity bin. The total mass in the metallicity bin is indicated on bottom-left of each map. The position of the two MUSE pointings is plotted in grey. A scale bar on bottom-right of each map indicates the correspondence with physical units.

Bibliography

Abadi M. G., Moore B., Bower R. G., 1999, MNRAS, 308, 947

Abadi M. G., Navarro J. F., Steinmetz M., Eke V. R., 2003, ApJ, 597, 21

Arribas S., Mediavilla E., Rasilla J. L., 1991, ApJ, 369, 260

Arribas S., et al., 1998, in D'Odorico S., ed., SPIEVol. 3355, Optical Astronomical Instrumentation. pp 821–827, doi:10.1117/12.316795

Athanassoula E., 2003, MNRAS, 341, 1179

Athanassoula E., 2005, MNRAS, 358, 1477

Aumer M., Binney J. J., 2009, MNRAS, 397, 1286

Aumer M., Binney J., Schönrich R., 2016, MNRAS, 462, 1697

Bacon R., 1995, in Comte G., Marcelin M., eds, Astronomical Society of the Pacific Conference Series Vol. 71, IAU Colloq. 149: Tridimensional Optical Spectroscopic Methods in Astrophysics. p. 239

Bacon R., et al., 2001, MNRAS, 326, 23

Bacon R., et al., 2004, in Moorwood A. F. M., Iye M., eds, SPIEVol. 5492, Ground-based Instrumentation for Astronomy. pp 1145–1149, doi:10.1117/12.549009

Bacon R., et al., 2010, in Ground-based and Airborne Instrumentation for Astronomy III. p. 773508, doi:10.1117/12.856027

Balogh M. L., Morris S. L., 2000, MNRAS, 318, 703

Balogh M. L., Morris S. L., Yee H. K. C., Carlberg R. G., Ellingson E., 1999, ApJ, 527, 54

Balogh M. L., Navarro J. F., Morris S. L., 2000, ApJ, 540, 113

Bassino L. P., Faifer F. R., Forte J. C., Dirsch B., Richtler T., Geisler D., Schuberth Y., 2006, A&A, 451, 789

Bastian N., Covey K. R., Meyer M. R., 2010, ARA&A, 48, 339

Beasley M. A., San Roman I., Gallart C., Sarajedini A., Aparicio A., 2015, MNRAS, 451, 3400

Bedregal A. G., Aragón-Salamanca A., Merrifield M. R., Milvang-Jensen B., 2006, MNRAS, 371, 1912

Bedregal A. G., Aragón-Salamanca A., Merrifield M. R., Cardiel N., 2008, MNRAS, 387, 660

Bekki K., 2009, MNRAS, 399, 2221

Bekki K., Couch W. J., 2003, ApJL, 596, L13

Bekki K., Couch W. J., 2010, MNRAS, 408, L11

Bell E. F., et al., 2004, ApJ, 608, 752

Bell E. F., Monachesi A., Harmsen B., de Jong R. S., Bailin J., Radburn-Smith D. J., D'Souza R., Holwerda B. W., 2017, ApJL, 837, L8

Benson A. J., Lacey C. G., Frenk C. S., Baugh C. M., Cole S., 2004, MNRAS, 351, 1215

Bershady M. A., Martinsson T. P. K., Verheijen M. A. W., Westfall K. B., Andersen D. R., Swaters R. A., 2011, ApJL, 739, L47

Binney J., Tremaine S., 1987, Galactic Dynamics. Princeton series in astrophysics, Princeton University Press

Binney J., et al., 2014a, MNRAS, 437, 351

Binney J., et al., 2014b, MNRAS, 439, 1231

Bird J. C., Kazantzidis S., Weinberg D. H., Guedes J., Callegari S., Mayer L., Madau P., 2013, ApJ, 773, 43

Blumenthal G. R., Faber S. M., Primack J. R., Rees M. J., 1984, Natur, 311, 517

Bond N. A., et al., 2010, ApJ, 716, 1

Bongiorno A., et al., 2016, A&A, 588, A78

Bosma A., van der Kruit P. C., 1979, A&A, 79, 281

Bottema R., 1993, A&A, 275, 16

Bournaud F., Combes F., 2002, A&A, 392, 83

Bournaud F., Jog C. J., Combes F., 2005, A&A, 437, 69

Bournaud F., Elmegreen B. G., Martig M., 2009, ApJL, 707, L1

Bovy J., Rix H.-W., Liu C., Hogg D. W., Beers T. C., Lee Y. S., 2012, ApJ, 753, 148

Braine J., Lisenfeld U., Due P.-A., Leon S., 2000, Natur, 403, 867

Bramich D. M., et al., 2008, MNRAS, 386, 887

Brook C. B., Kawata D., Gibson B. K., Freeman K. C., 2004, ApJ, 612, 894

Büdenbender A., van de Ven G., Watkins L. L., 2015, MNRAS, 452, 956

Bureau M., Athanassoula E., 2005, ApJ, 626, 159

Bureau M., Freeman K. C., 1999, AJ, 118, 126

Bureau M., Aronica G., Athanassoula E., Dettmar R.-J., Bosma A., Freeman K. C., 2006, MNRAS, 370, 753

Burkert A., 1995, ApJL, 447, L25

Burstein D., 1979, ApJ, 234, 829

Burton W. B., Elmegreen B. G., Genzel R., Pfenniger D., Bartholdi P., eds, 1992, The galactic interstellar medium

Byrd G., Valtonen M., 1990, ApJ, 350, 89

Camm G. L., 1950, MNRAS, 110, 305

Cantiello M., et al., 2017, preprint, (arXiv:1711.00750)

Cappellari M., 2017, MNRAS, 466, 798

Cappellari M., Copin Y., 2003, MNRAS, 342, 345

Cappellari M., Emsellem E., 2004, PASP, 116, 138

Cappellari M., et al., 2006, MNRAS, 366, 1126

Cappellari M., et al., 2007, MNRAS, 379, 418

Carlberg R. G., Dawson P. C., Hsu T., Vandenberg D. A., 1985, ApJ, 294, 674

Carter D., Jenkins C. R., 1993, MNRAS, 263, 1049

Casagrande L., Schönrich R., Asplund M., Cassisi S., Ramírez I., Meléndez J., Bensby T., Feltzing S., 2011, A&A, 530, A138

Cebrián M., Trujillo I., 2014, MNRAS, 444, 682

Chabrier G., 2003, PASP, 115, 763

Cheng J. Y., et al., 2012, ApJ, 752, 51

Chiang Y.-K., Overzier R., Gebhardt K., 2013, ApJ, 779, 127

Chiappini C., Matteucci F., Gratton R., 1997, ApJ, 477, 765

Chung A., Bureau M., 2004, AJ, 127, 3192

Claudi R. U., et al., 2008, in Ground-based and Airborne Instrumentation for Astronomy II. p. 70143E, doi:10.1117/12.788366

Cohen S. A., Hickox R. C., Wegner G. A., Einasto M., Vennik J., 2014, ApJ, 783, 136

Cole S., 1991, ApJ, 367, 45

Cole D. R., Debattista V. P., Erwin P., Earp S. W. F., Roškar R., 2014, MNRAS, 445, 3352

Combes F., Sanders R. H., 1981, A&A, 96, 164

Comerón S., et al., 2011a, ApJ, 729, 18

Comerón S., et al., 2011b, ApJ, 741, 28

Comerón S., et al., 2012, ApJ, 759, 98

Comerón S., Elmegreen B. G., Salo H., Laurikainen E., Holwerda B. W., Knapen J. H., 2014, A&A, 571, A58

Comerón S., Salo H., Janz J., Laurikainen E., Yoachim P., 2015, A&A, 584, A34

Comerón S., Salo H., Peletier R. F., Mentz J., 2016, A&A, 593, L6

Comerón S., Salo H., Knapen J. H., 2018, A&A, 610, A5

D'Abrusco R., et al., 2016, ApJL, 819, L31

D'Onofrio M., Zaggia S. R., Longo G., Caon N., Capaccioli M., 1995, A&A, 296, 319

Dalcanton J. J., Bernstein R. A., 2002, AJ, 124, 1328

Debattista V. P., Ness M., Gonzalez O. A., Freeman K., Zoccali M., Minniti D., 2017, MNRAS, 469, 1587

Dehnen W., Binney J. J., 1998, MNRAS, 298, 387

Di Matteo P., Lehnert M. D., Qu Y., van Driel W., 2011, A&A, 525, L3

Di Matteo P., et al., 2014, A&A, 567, A122

Dierickx M., Klement R., Rix H.-W., Liu C., 2010, ApJL, 725, L186

Dodelson S., 2003, Modern cosmology

Dorman C. E., et al., 2015, ApJ, 803, 24

Dressler A., 1984, ARA&A, 22, 185

Drinkwater M. J., Gregg M. D., Colless M., 2001, ApJL, 548, L139

Eggen O. J., Lynden-Bell D., Sandage A. R., 1962, ApJ, 136, 748

Eisenhauer F., et al., 2003, in Iye M., Moorwood A. F. M., eds, SPIEVol. 4841, Instrument Design and Performance for Optical/Infrared Ground-based Telescopes. pp 1548–1561, doi:10.1117/12.459468

Elmegreen D., Elmegreen B., 1987, ApJ, 314

Elmegreen B. G., Elmegreen D. M., 2006, ApJ, 650, 644

Elmegreen B. G., Elmegreen D. M., Tompkins B., Jenks L. G., 2017, ApJ, 847, 14

Emsellem E., Bacon R., Monnet G., Poulain P., 1996, A&A, 312, 777

Emsellem E., Dejonghe H., Bacon R., 1999, MNRAS, 303, 495

Emsellem E., Greusard D., Combes F., Friedli D., Leon S., Pécontal E., Wozniak H., 2001, A&A, 368, 52

Evrard A. E., 1991, MNRAS, 248, 8P

Faber S. M., Gallagher J. S., 1979, ARA&A, 17, 135

Falcón-Barroso J., Sánchez-Blázquez P., Vazdekis A., Ricciardelli E., Cardiel N., Cenarro A. J., Gorgas J., Peletier R. F., 2011, A&A, 532, A95

Fall S. M., Efstathiou G., 1980, MNRAS, 193, 189

Faltenbacher A., Allgood B., Gottlöber S., Yepes G., Hoffman Y., 2005, MNRAS, 362, 1099

Ferguson H. C., 1989, AJ, 98, 367

Font J., et al., 2017, ApJ, 835, 279

Forbes J., Krumholz M., Burkert A., 2012, ApJ, 754, 48

Fragkoudi F., Di Matteo P., Haywood M., Gómez A., Combes F., Katz D., Semelin B., 2017a, A&A, 606, A47

Fragkoudi F., Di Matteo P., Haywood M., Khoperskov S., Gomez A., Schultheis M., Combes F., Semelin B., 2017b, A&A, 607, L4

Fragkoudi F., Di Matteo P., Haywood M., Schultheis M., Khoperskov S., Gómez A., Combes F., 2018, preprint, (`arXiv:1802.00453`)

Freeman K. C., 1970, ApJ, 160, 811

Freeman K. C., 2007, Astrophysics and Space Science Proceedings, 3, 3

Frenk C. S., White S. D. M., Efstathiou G., Davis M., 1985, Natur, 317, 595

Frenk C. S., White S. D. M., Davis M., Efstathiou G., 1988, ApJ, 327, 507

Fuhrmann K., 1998, A&A, 338, 161

Fuhrmann K., 2011, MNRAS, 414, 2893

Fujita Y., Nagashima M., 1999, ApJ, 516, 619

Gaia Collaboration et al., 2018, preprint, (arXiv:1804.09380)

Garrison-Kimmel S., et al., 2017, preprint, (arXiv:1712.03966)

Gentile G., et al., 2015, A&A, 576, A57

Gerhard O. E., 1993, MNRAS, 265, 213

Gerhard O., Martinez-Valpuesta I., 2012, ApJL, 744, L8

Gerssen J., Shapiro Griffin K., 2012, MNRAS, 423, 2726

Gerssen J., Kuijken K., Merrifield M. R., 1997, MNRAS, 288, 618

Gerssen J., Kuijken K., Merrifield M. R., 2000, MNRAS, 317, 545

Gilmore G., Reid N., 1983, MNRAS, 202, 1025

Gilmore G., Wyse R. F. G., Kuijken K., 1989, ARA&A, 27, 555

Gonzalez O. A., et al., 2016, A&A, 591, A7

Gonzalez O. A., Debattista V. P., Ness M., Erwin P., Gadotti D. A., 2017, MNRAS, 466, L93

Grand R. J. J., Springel V., Gómez F. A., Marinacci F., Pakmor R., Campbell D. J. R., Jenkins A., 2016, MNRAS, 459, 199

Gray P. M., Phillips M. M., Turtle A. J., Ellis R., 1982, Proceedings of the Astronomical Society of Australia, 4, 477

Guedes J., Callegari S., Madau P., Mayer L., 2011, ApJ, 742, 76

Guérou A., Emsellem E., Krajnović D., McDermid R. M., Contini T., Weilbacher P. M., 2016, A&A, 591, A143

Haines C. P., et al., 2012, ApJ, 754, 97

Haines C. P., et al., 2015, ApJ, 806, 101

Hänninen J., Flynn C., 2002, MNRAS, 337, 731

Haywood M., Di Matteo P., Lehnert M. D., Katz D., Gómez A., 2013, A&A, 560, A109

Haywood M., Di Matteo P., Snaith O., Lehnert M. D., 2015, A&A, 579, A5

Heller C. H., 1995, ApJ, 455, 252

Heller C. H., Shlosman I., 1994, ApJ, 424, 84

Helmi A., 2008, A&A Rev., 15, 145

Henault F., et al., 2004, in Moorwood A. F. M., Iye M., eds, SPIEVol. 5492, Ground-based Instrumentation for Astronomy. pp 909–920, doi:10.1117/12.554096

Hes R., Peletier R. F., 1993, A&A, 268, 539

Holmberg J., Nordström B., Andersen J., 2009, A&A, 501, 941

Hopkins P. F., et al., 2018, MNRAS,

House E. L., et al., 2011, MNRAS, 415, 2652

Hubble E. P., 1926, ApJ, 64

Hubble E. P., 1929a, Leaflet of the Astronomical Society of the Pacific, 1, 93

Hubble E., 1929b, Proceedings of the National Academy of Science, 15, 168

Hubble E. P., 1936, Realm of the Nebulae

Hwang J.-S., Park C., Banerjee A., Hwang H. S., 2018, ApJ, 856, 160

Immeli A., Samland M., Gerhard O., Westera P., 2004, A&A, 413, 547

Iodice E., et al., 2016, ApJ, 820, 42

Iodice E., et al., 2017a, ApJ, 839, 21

Iodice E., et al., 2017b, ApJ, 851, 75

Jayaraman A., Gilmore G., Wyse R. F. G., Norris J. E., Belokurov V., 2013, MNRAS, 431, 930

Jenkins A., Binney J., 1990, MNRAS, 245, 305

Johnston E. J., Aragón-Salamanca A., Merrifield M. R., Bedregal A. G., 2012, MNRAS, 422, 2590

Jones B. J. T., Wyse R. F. G., 1983, A&A, 120, 165

Jordán A., et al., 2007, ApJS, 169, 213

Kasparova A. V., Katkov I. Y., Chilingarian I. V., Silchenko O. K., Moiseev A. V., Borisov S. B., 2016, MNRAS, 460, L89

Kauffmann G., White S. D. M., Guiderdoni B., 1993, MNRAS, 264, 201

Kazantzidis S., Bullock J. S., Zentner A. R., Kravtsov A. V., Moustakas L. A., 2008, ApJ, 688, 254

Kazantzidis S., Zentner A. R., Kravtsov A. V., Bullock J. S., Debattista V. P., 2009, ApJ, 700, 1896

Kelz A., et al., 2006, PASP, 118, 129

Kenney J. D. P., Koopmann R. A., 1999, AJ, 117, 181

Kennicutt Jr. R. C., 1998, ApJ, 498, 541

Kent S. M., Dame T. M., Fazio G., 1991, ApJ, 378, 131

Kipper R., Tenjes P., Tihhonova O., Tamm A., Tempel E., 2016, MNRAS, 460, 2720

Kirby E. N., Cohen J. G., Guhathakurta P., Cheng L., Bullock J. S., Gallazzi A., 2013, ApJ, 779, 102

Knapen J. H., Shlosman I., Peletier R. F., 2000, ApJ, 529, 93

Koleva M., Prugniel P., De Rijcke S., Zeilinger W. W., 2011, MNRAS, 417, 1643

Kormendy J., 1982, Morphology and dynamics of galaxies; Proceedings of the Twelfth Advanced Course, Saas-Fee, Switzerland, March 29-April 3, 1982 (A84-15502 04-90). Sauverny, Switzerland, Observatoire de Geneve, 1983, p. 113-288., 12, 113

Kormendy J., 1988, ApJ, 325, 128

Kormendy J., 1993, in Dejonghe H., Habing H. J., eds, IAU Symposium Vol. 153, Galactic Bulges. p. 209

Kormendy J., Bender R., 1999, ApJ, 522, 772

Kormendy J., Illingworth G., 1982, ApJ, 256, 460

Kormendy J., Kennicutt Jr. R. C., 2004, ARA&A, 42, 603

Kormendy J., et al., 1996, ApJL, 473, L91

Kosmalski J., Parès L., Seifert W., Xu W., Olaya J. C., Delabre B., 2011, in Optical Design and Engineering IV. p. 816715, doi:10.1117/12.896821

Krajnović D., et al., 2008, MNRAS, 390, 93

Kraljic K., Bournaud F., Martig M., 2012, ApJ, 757, 60

Kregel M., van der Kruit P. C., 2005, MNRAS, 358, 481

Kregel M., van der Kruit P. C., Freeman K. C., 2004, MNRAS, 351, 1247

Kregel M., van der Kruit P. C., Freeman K. C., 2005, MNRAS, 358, 503

Kronberger T., Kapferer W., Ferrari C., Unterguggenberger S., Schindler S., 2008, A&A, 481, 337

Kroupa P., 2002a, Science, 295, 82

Kroupa P., 2002b, MNRAS, 330, 707

Kuntschner H., 2000, MNRAS, 315, 184

La Barbera F., Vazdekis A., Ferreras I., Pasquali A., Cappellari M., Martín-Navarro I., Schönebeck F., Falcón-Barroso J., 2016, MNRAS, 457, 1468

Lacey C. G., 1984, MNRAS, 208, 687

Lacey C. G., Ostriker J. P., 1985, ApJ, 299, 633

Larson R. B., 1974, MNRAS, 166, 585

Larson R. B., 1976, MNRAS, 176, 31

Leaman R., et al., 2017, MNRAS, 472, 1879

Lin C. C., Shu F. H., 1964, ApJ, 140, 646

Lindblad B., 1963, Stockholms Observatoriums Annaler, 22

Lindblad B., 1964, Astrophysica Norvegica, 9, 103

Lintott C. J., et al., 2008, MNRAS, 389, 1179

Liu C., van de Ven G., 2012, MNRAS, 425, 2144

Lütticke R., Dettmar R.-J., Pohlen M., 2000, A&AS, 145, 405

Lyubenova M., et al., 2016, MNRAS, 463, 3220

Martig M., Bournaud F., Teyssier R., Dekel A., 2009, ApJ, 707, 250

Martig M., Bournaud F., Croton D. J., Dekel A., Teyssier R., 2012, ApJ, 756, 26

Martig M., Minchev I., Flynn C., 2014a, MNRAS, 442, 2474

Martig M., Minchev I., Flynn C., 2014b, MNRAS, 443, 2452

Martig M., Minchev I., Ness M., Fouesneau M., Rix H.-W., 2016, ApJ, 831, 139

Martín-Navarro I., 2016, MNRAS, 456, L104

Martín-Navarro I., La Barbera F., Vazdekis A., Falcón-Barroso J., Ferreras I., 2015a, MNRAS, 447, 1033

Martín-Navarro I., et al., 2015b, ApJL, 806, L31

Martinet L., Friedli D., 1997, A&A, 323, 363

Martinez-Valpuesta I., Gerhard O., 2011, ApJL, 734, L20

Martinez-Valpuesta I., Gerhard O., 2013, ApJL, 766, L3

Martinez-Valpuesta I., Shlosman I., Heller C., 2006, ApJ, 637, 214

Martinez-Valpuesta I., Aguerri J. A. L., González-García A. C., Dalla Vecchia C., Stringer M., 2017, MNRAS, 464, 1502

Martinsson T. P. K., Verheijen M. A. W., Westfall K. B., Bershady M. A., Schechtman-Rook A., Andersen D. R., Swaters R. A., 2013, A&A, 557, A130

McDermid R. M., et al., 2015, MNRAS, 448, 3484

McElroy D. B., 1983, ApJ, 270, 485

Merrifield M. R., Gerssen J., Kuijken K., 2001, in Funes J. G., Corsini E. M., eds, Astronomical Society of the Pacific Conference Series Vol. 230, Galaxy Disks and Disk Galaxies. pp 221–224 (arXiv:astro-ph/0008290)

Minchev I., Quillen A. C., 2006, MNRAS, 368, 623

Minchev I., Famaey B., Quillen A. C., Dehnen W., 2012a, in European Physical Journal Web of Conferences. p. 07002 (arXiv:1111.0195), doi:10.1051/epjconf/20121907002

Minchev I., Famaey B., Quillen A. C., Di Matteo P., Combes F., Vlajić M., Erwin P., Bland-Hawthorn J., 2012b, A&A, 548, A126

Minchev I., Famaey B., Quillen A. C., Dehnen W., Martig M., Siebert A., 2012c, A&A, 548, A127

Minchev I., Chiappini C., Martig M., 2013, A&A, 558, A9

Minchev I., Chiappini C., Martig M., 2014, A&A, 572, A92

Minchev I., Martig M., Streich D., Scannapieco C., de Jong R. S., Steinmetz M., 2015, ApJL, 804, L9

Mo H., van den Bosch F. C., White S., 2010, Galaxy Formation and Evolution

Molaeinezhad A., Falcón-Barroso J., Martínez-Valpuesta I., Khosroshahi H. G., Balcells M., Peletier R. F., 2016, MNRAS, 456, 692

Molaeinezhad A., Falcón-Barroso J., Martínez-Valpuesta I., Khosroshahi H. G., Vazdekis A., La Barbera F., Peletier R. F., Balcells M., 2017, MNRAS, 467, 353

Moore B., Katz N., Lake G., Dressler A., Oemler A., 1996, Natur, 379, 613

Morelli L., Cesetti M., Corsini E. M., Pizzella A., Dalla Bontà E., Sarzi M., Bertola F., 2010, A&A, 518, A32

Morrison H. L., Flynn C., Freeman K. C., 1990, AJ, 100, 1191

Naab T., Burkert A., 2001, ApJL, 555, L91

Naab T., Burkert A., 2003, ApJ, 597, 893

Naab T., Burkert A., Hernquist L., 1999, ApJL, 523, L133

Narayan C. A., Jog C. J., 2002a, A&A, 390, L35

Narayan C. A., Jog C. J., 2002b, A&A, 394, 89

Navarro J. F., Frenk C. S., White S. D. M., 1996, ApJ, 462, 563

Navarro J. F., Frenk C. S., White S. D. M., 1997, ApJ, 490, 493

Noh Y., Cohn J. D., 2011, MNRAS, 413, 301

Noordermeer E., Merrifield M. R., Aragón-Salamanca A., 2008, MNRAS, 388, 1381

Nordström B., et al., 2004, A&A, 418, 989

Norris J., 1987, in Gilmore G., Carswell B., eds, The Galaxy. pp 297–320

Ordenes-Briceño Y., et al., 2018, ApJ, 860, 4

Oser L., Ostriker J. P., Naab T., Johansson P. H., Burkert A., 2010, ApJ, 725, 2312

Ostriker J. P., Peebles P. J. E., 1973, ApJ, 186, 467

Ostriker J. P., Peebles P. J. E., Yahil A., 1974, ApJL, 193, L1

Overzier R. A., 2016, A&A Rev., 24, 14

Paolillo M., Fabbiano G., Peres G., Kim D.-W., 2002, ApJ, 565, 883

Peletier R. F., 2013, Stellar Populations. p. 353

Penzias A. A., Wilson R. W., 1965, ApJ, 142, 419

Perryman M. A. C., et al., 1997, A&A, 323, L49

Pfenniger D., 1984, A&A, 134, 373

Pinna F., Falcón-Barroso J., Martig M., Martínez-Valpuesta I., Méndez-Abreu J., van de Ven G., Leaman R., Lyubenova M., 2018, MNRAS, 475, 2697

Plummer H. C., 1911, MNRAS, 71, 460

Prochaska J. X., Naumov S. O., Carney B. W., McWilliam A., Wolfe A. M., 2000, AJ, 120, 2513

Qu Y., Di Matteo P., Lehnert M. D., van Driel W., 2011, A&A, 530, A10

Quilis V., Moore B., Bower R., 2000, Science, 288, 1617

Quillen A. C., et al., 2018, preprint, (`arXiv:1805.10236`)

Quinn P. J., Hernquist L., Fullagar D. P., 1993, ApJ, 403, 74

Read J. I., Mayer L., Brooks A. M., Governato F., Lake G., 2009, MNRAS, 397, 44

Rejkuba M., Mouhcine M., Ibata R., 2009, MNRAS, 396, 1231

Robin A. C., Reylé C., Fliri J., Czekaj M., Robert C. P., Martins A. M. M., 2014, A&A, 569, A13

Robin A. C., Bienaymé O., Fernández-Trincado J. G., Reylé C., 2017, A&A, 605, A1

Roškar R., Debattista V. P., 2012, Science, 338, 333

Roškar R., Debattista V. P., Loebman S. R., 2013, MNRAS, 433, 976

Rubin V. C., Ford Jr. W. K., 1970, ApJ, 159, 379

Rutten R. J., 2003, Radiative Transfer in Stellar Atmospheres, Lecture Notes Utrecht University

Saha K., Naab T., 2013, MNRAS, 434, 1287

Saha K., Tseng Y.-H., Taam R. E., 2010, ApJ, 721, 1878

Saha K., Pfenniger D., Taam R. E., 2013, ApJ, 764, 123

Salpeter E. E., 1955, ApJ, 121, 161

Samland M., Gerhard O. E., 2003, A&A, 399, 961

Sarzi M., et al., 2018, preprint, (arXiv:1804.06795)

Savage B. D., et al., 2000, ApJL, 538, L27

Scalo J. M., 1986, Fund. of Cosmic Phys., 11, 1

Schawinski K., et al., 2014, MNRAS, 440, 889

Schaye J., et al., 2015, MNRAS, 446, 521

Schwarzschild K., 1907, Göttingen Nachr., 614

Schwarzschild M., 1979, ApJ, 232, 236

Schweizer F., Seitzer P., Kelson D. D., Villanueva E. V., Walth G. L., 2013, ApJ, 773, 148

Searle L., Zinn R., 1978, ApJ, 225, 357

Seidel M. K., Falcón-Barroso J., Martínez-Valpuesta I., Díaz-García S., Laurikainen E., Salo H., Knapen J. H., 2015, MNRAS, 451, 936

Seidel M. K., Falcón-Barroso J., Martínez-Valpuesta I., Sánchez-Blázquez P., Pérez I., Peletier R., Vazdekis A., 2016, MNRAS, 460, 3784

Sellwood J. A., Carlberg R. G., 1984, ApJ, 282, 61

Sellwood J. A., Wilkinson A., 1993, Reports on Progress in Physics, 56, 173

Sellwood J. A., Nelson R. W., Tremaine S., 1998, ApJ, 506, 590

Sersic J. L., 1968, Atlas de galaxias australes

Shapiro K. L., Gerssen J., van der Marel R. P., 2003, AJ, 126, 2707

Silk J., 1977, ApJ, 211, 638

Smith M. C., Whiteoak S. H., Evans N. W., 2012, ApJ, 746, 181

Snaith O. N., Haywood M., Di Matteo P., Lehnert M. D., Combes F., Katz D., Gómez A., 2014, ApJL, 781, L31

Sommer-Larsen J., Götz M., Portinari L., 2003, ApJ, 596, 47

Sparke L. S., Gallagher III J. S., 2007, Galaxies in the Universe: An Introduction. Cambridge University Press

Spiniello C., Trager S. C., Koopmans L. V. E., 2015, ApJ, 803, 87

Spitzer Jr. L., Schwarzschild M., 1951, ApJ, 114, 385

Spitzer Jr. L., Schwarzschild M., 1953, ApJ, 118, 106

Spolaor M., Hau G. K. T., Forbes D. A., Couch W. J., 2010a, MNRAS, 408, 254

Spolaor M., Kobayashi C., Forbes D. A., Couch W. J., Hau G. K. T., 2010b, MNRAS, 408, 272

Steinmetz M., Navarro J. F., 2002, New Astron., 7, 155

Steinmetz M., et al., 2006, AJ, 132, 1645

Strömberg G., 1946, ApJ, 104, 12

Sybilska A., et al., 2017, MNRAS, 470, 815

Tamm A., Tempel E., Tenjes P., Tihhonova O., Tuvikene T., 2012, A&A, 546, A4

Tempel E., Tenjes P., 2006, MNRAS, 371, 1269

Terlevich A. I., Kuntschner H., Bower R. G., Caldwell N., Sharples R. M., 1999, MNRAS, 310, 445

Teyssier R., 2002, A&A, 385, 337

Toomre A., 1963, ApJ, 138, 385

Toomre A., 1964, ApJ, 139, 1217

Toomre A., 1977, in Tinsley B. M., Larson D. Campbell R. B. G., eds, Evolution of Galaxies and Stellar Populations. p. 401

Toomre A., 1981, in Fall S. M., Lynden-Bell D., eds, Structure and Evolution of Normal Galaxies. pp 111–136

Toth G., Ostriker J. P., 1992, ApJ, 389, 5

Treu T., Auger M. W., Koopmans L. V. E., Gavazzi R., Marshall P. J., Bolton A. S., 2010, ApJ, 709, 1195

Tully R. B., et al., 2013, AJ, 146, 86

Turner M. L., Côté P., Ferrarese L., Jordán A., Blakeslee J. P., Mei S., Peng E. W., West M. J., 2012, ApJS, 203, 5

Vaddi S., O'Dea C. P., Baum S. A., Whitmore S., Ahmed R., Pierce K., Leary S., 2016, ApJ, 818, 182

Van der Swaelmen M., Hill V., Primas F., Cole A. A., 2013, A&A, 560, A44

Vanderriest C., Lemonnier J. P., 1988, in Robinson L. B., ed., Instrumentation for Ground-Based Optical Astronomy. p. 304

Vazdekis A., Casuso E., Peletier R. F., Beckman J. E., 1996, ApJS, 106, 307

Vazdekis A., Sánchez-Blázquez P., Falcón-Barroso J., Cenarro A. J., Beasley M. A., Cardiel N., Gorgas J., Peletier R. F., 2010, MNRAS, 404, 1639

Vazdekis A., et al., 2015, MNRAS, 449, 1177

Velazquez H., White S. D. M., 1999, MNRAS, 304, 254

Vera-Ciro C., D'Onghia E., Navarro J., Abadi M., 2014, ApJ, 794, 173

Verdugo C., Combes F., Dasyra K., Salomé P., Braine J., 2015, A&A, 582, A6

Villalobos Á., Helmi A., 2008, MNRAS, 391, 1806

Villalobos Á., Helmi A., 2009, MNRAS, 399, 166

Villumsen J. V., 1985, ApJ, 290, 75

Vogelsberger M., et al., 2014, MNRAS, 444, 1518

Walker I. R., Mihos J. C., Hernquist L., 1996, ApJ, 460, 121

Weilbacher P. M., Streicher O., Urrutia T., Jarno A., Pécontal-Rousset A., Bacon R., Böhm P., 2012, in Software and Cyberinfrastructure for Astronomy II. p. 84510B, doi:10.1117/12.925114

Weilbacher P. M., Streicher O., Palsa R., 2016, MUSE-DRP: MUSE Data Reduction Pipeline, Astrophysics Source Code Library (ascl:1610.004)

Westfall K. B., Bershady M. A., Verheijen M. A. W., Andersen D. R., Swaters R. A., 2005, in de Jong R. S., ed., Islandic Universes: Structure and Evolution of Disc Galaxies. pp 157–160 (`arXiv:astro-ph/0508552`)

Westfall K. B., Bershady M. A., Verheijen M. A. W., Andersen D. R., Martinsson T. P. K., Swaters R. A., Schechtman-Rook A., 2011, ApJ, 742, 18

Wielen R., 1977, A&A, 60, 263

Williams M. J., Zamojski M. A., Bureau M., Kuntschner H., Merrifield M. R., de Zeeuw P. T., Kuijken K., 2011, MNRAS, 414, 2163

Wisnioski E., et al., 2015, ApJ, 799, 209

Wolf C., Meisenheimer K., Rix H.-W., Borch A., Dye S., Kleinheinrich M., 2003, A&A, 401, 73

Worthey G., Faber S. M., Gonzalez J. J., 1992, ApJ, 398, 69

Wouterloot J. G. A., Brand J., Burton W. B., Kwee K. K., 1990, A&A, 230, 21

Wyse R. F. G., 2004, preprint, (arXiv:astro-ph/0402636)

Wyse R. F. G., Gilmore G., 1988, AJ, 95, 1404

Yanny B., et al., 2009, AJ, 137, 4377

Yoachim P., Dalcanton J. J., 2005, ApJ, 624, 701

Yoachim P., Dalcanton J. J., 2006, AJ, 131, 226

Yoachim P., Dalcanton J. J., 2008a, ApJ, 682, 1004

Yoachim P., Dalcanton J. J., 2008b, ApJ, 683, 707

Zacharias N., Finch C. T., Girard T. M., Henden A., Bartlett J. L., Monet D. G., Zacharias M. I., 2013, AJ, 145, 44

de Carvalho R. R., da Costa L. N., 1987, A&A, 171, 66

de Grijs R., 1998, MNRAS, 299, 595

de Vaucouleurs G., 1959, Handbuch der Physik, 53, 275

de Zeeuw P. T., et al., 2002, MNRAS, 329, 513

van Albada T. S., Bahcall J. N., Begeman K., Sancisi R., 1985, ApJ, 295, 305

van Dokkum P. G., Conroy C., 2010, Natur, 468, 940

van Dokkum P. G., et al., 2008, ApJL, 677, L5

van Dokkum P., Conroy C., Villaume A., Brodie J., Romanowsky A. J., 2017, ApJ, 841, 68

van Leeuwen F., 2007, Hipparcos, the New Reduction of the Raw Data. Astrophysics and Space Science Library, Springer Netherlands

van de Weygaert R., Bertschinger E., 1996, MNRAS, 281, 84

van der Kruit P. C., 1988, A&A, 192, 117

van der Kruit P. C., Freeman K. C., 1984, ApJ, 278, 81

van der Kruit P., Freeman K., 2011, Annu. Rev. Astron. Astrophys., 49, 301

van der Kruit P. C., Searle L., 1981, A&A, 95, 105

van der Kruit P. C., de Grijs R., 1999, A&A, 352, 129

van der Marel R. P., 2006, in Livio M., Brown T. M., eds, Vol. 17, The Local Group as an Astrophysical Laboratory. pp 47–71 (arXiv:astro-ph/0404192)

van der Marel R. P., Franx M., 1993, ApJ, 407, 525

van der Marel R. P., Rix H. W., Carter D., Franx M., White S. D. M., de Zeeuw T., 1994, MNRAS, 268, 521